Flanders
State of
the Art

00_147_1
FHR reports

COHERENS

Validation report

DEPARTMENT
**MOBILITY &
PUBLIC
WORKS**

www.flandershydraulicsresearch.be

COHERENS

Validation report

Schramkowski, G. P.; Heredia Gomez, M.; Rauwoens, P.; Van Oyen, T.; Monbaliu, J.; Komijani, H.; Breugem, A.; Delecluyse, K.; Chu, K.; Lee, B. J.; Vanlede, J.; Luyten, P.; Baetens, K.; Verwaest, T.; Mostaert, F.

Cover figure © Google, 2017

Legal notice

Flanders Hydraulics Research is of the opinion that the information and positions in this report are substantiated by the available data and knowledge at the time of writing.
The positions taken in this report are those of Flanders Hydraulics Research and do not reflect necessarily the opinion of the Government of Flanders or any of its institutions.
Flanders Hydraulics Research nor any person or company acting on behalf of Flanders Hydraulics Research is responsible for any loss or damage arising from the use of the information in this report.

Copyright and citation

© The Government of Flanders, Department of Mobility and Public Works, Flanders Hydraulics Research 2017
D/2017/3241/242

This publication should be cited as follows:

Schramkowski, G. P.; Heredia Gomez, M.; Rauwoens, P.; Van Oyen, T.; Monbaliu, J.; Komijani, H.; Breugem, A.; Delecluyse, K.; Chu, K.; Lee, B. J.; Vanlede, J.; Luyten, P.; Baetens, K.; Verwaest, T.; Mostaert, F. (2017). COHERENS: Validation report. Version 3.0. FHR Reports, 00_147_1. Flanders Hydraulics Research: Antwerp.

Reproduction of and reference to this publication is authorised provided the source is acknowledged correctly.

Document identification

Customer:	Maritime Access Division	Ref.:	WL2017R00_147_1
Keywords (3-5):	Numerical modeling, hydraulics, tides, sediment transport, morphology		
Text (p.):	183	Appendices (p.):	0
Confidentiality:	☒ No	☒ Available online	

Author(s):	Schramkowski, G. P.; Heredia Gomez, M.; Rauwoens, P.; Van Oyen, T.; Monbaliu, J.; Komijani, H.; Breugem, A.; Delecluyse, K.; Chu, K.; Lee, B. J.

Control

	Name	Signature
Revisor(s):	Luyten, P.; Baetens, K.	
Project leader:	Vanlede, J.	

Approval

Coordinator research group:	Verwaest, T.	
Head of division:	Mostaert, F.	

Abstract

This document discusses the activities that have been performed to validate various functionalities of the COHERENS modeling system. Specifically the following aspects have been considered:

1. Hydrodynamics;
2. Inundation schemes;
3. Structures;
4. Additional boundary conditions;
5. Sediment transport
6. Morphology;

Each of these topics is presented in a self-contained way.

Contents

Abstract III

1 Introduction 1

2 Hydrodynamics 2
2.1 Introduction 2
2.2 Flow in a 1D short tidal channel 3
2.2.1 Introduction 3
2.2.2 Model setup 5
2.2.3 Results 6
2.2.4 Conclusions 13
2.2.5 Derivation of the semi-analytical solution 13
2.3 Flow in a long tidal embayment 17
2.3.1 Introduction 17
2.3.2 Model setup 19
2.3.3 Results 22
2.3.4 Conclusions 27
2.3.5 Derivation of the semi-analytical solution 27
2.4 Wind generated 2DH flow in a closed basin 29
2.4.1 Introduction 29
2.4.2 Model setup 31
2.4.3 Results 32
2.4.4 Conclusions 37
2.4.5 Derivation of semi-analytical solution 37
2.5 Stationary 2DV wind driven flow 40
2.5.1 Introduction 40
2.5.2 Model setup 41
2.5.3 Results 42
2.5.4 Conclusion 45
2.5.5 Derivation of the semi-analytical solution 45
2.6 Conclusions 48

3 Inundation 49
3.1 Introduction 49
3.2 Overflowing dyke 49
3.2.1 Introduction 49
3.2.2 Model setup 50
3.2.3 Results 51
3.2.4 Conclusions 54
3.3 Test case of Thacker, 1981 55
3.3.1 Introduction 55
3.3.2 Model setup 56
3.3.3 Results 57
3.3.4 Conclusions 61
3.4 Conclusions 64

4 Structures 65

4.1 Introduction ... 65
4.2 Validation of “dry cells” model unit ... 65
4.2.1 Model setup ... 65
4.2.2 Results ... 65
4.2.3 Conclusions ... 68
4.3 Validation of “THIN dams” model unit ... 70
4.3.1 Model setup ... 70
4.3.2 Results ... 70
4.3.3 Conclusions ... 72
4.4 Validation of “weirs/barriers” model unit ... 75
4.4.1 Model setup ... 75
4.4.2 Results ... 76
4.4.3 Conclusions ... 88
4.5 Validation of “discharges” model unit ... 88
4.5.1 Model setup ... 88
4.5.2 Results ... 88
4.5.3 Conclusions ... 93
4.6 Conclusions ... 95

5 Additional boundary conditions ... 96
5.1 Introduction ... 96
5.1.1 Overview and claims ... 96
5.1.2 Verification of the mass conservation ... 96
5.2 Validation of distributed discharge condition ... 98
5.2.1 Introduction ... 98
5.2.2 Model setup ... 98
5.2.3 Results ... 98
5.2.4 Conclusions ... 102
5.3 Validation of Neumann condition ... 105
5.3.1 Introduction ... 105
5.3.2 Model setup ... 105
5.3.3 Discussion of results ... 106
5.3.4 Conclusions ... 109
5.4 Validation of Thatcher-Harleman condition ... 110
5.4.1 Introduction ... 110
5.4.2 Model setup ... 110
5.4.3 Results ... 112
5.4.4 Conclusions ... 115
5.5 Validation of Tangential Components boundary condition ... 119
5.5.1 Introduction ... 119
5.5.2 Model setup ... 119
5.5.3 Results ... 121
5.5.4 Conclusions ... 124
5.6 Conclusions ... 127

6 Sediment ... 128
6.1 Introduction ... 128
6.2 Rouse profile ... 128
6.2.1 Introduction ... 128
6.2.2 Model setup ... 129
6.2.3 Results ... 130
6.2.4 Conclusions ... 133

6.3 Density stratification 136
6.3.1 Introduction 136
6.3.2 Model setup 137
6.3.3 Results 137
6.3.4 Conclusions 137
6.4 Hindered settling 149
6.4.1 Introduction 149
6.4.2 Model setup 150
6.4.3 Results 150
6.4.4 Conclusions 150
6.5 Comparison 2D/3D simulation 152
6.5.1 Introduction 152
6.5.2 Model setup 152
6.5.3 Results 154
6.5.4 Conclusion 154
6.6 Gravity current 155
6.6.1 Introduction 155
6.6.2 Model setup 156
6.6.3 Results 157
6.6.4 Conclusion 157
6.7 Bend flow 162
6.7.1 Introduction 162
6.7.2 Model setup 162
6.7.3 Results 162
6.7.4 Conclusions 162
6.8 Conclusions 169

7 Morphology 170
7.1 Introduction 170
7.2 Gaussian hump 170
7.2.1 Introduction 170
7.2.2 Model setup 172
7.2.3 Results 172
7.2.4 Conclusions 173
7.3 Vertical sorting 173
7.3.1 Introduction 173
7.3.2 Model setup 174
7.3.3 Results 175
7.3.4 Conclusions 175
7.4 Conclusions 182

References 183

List of Figures

Figure 1 Sketch (vertical slice) of the one-dimensional model domain. 3
Figure 2 Comparison between computed tidally averaged water level and semi-analytical result. 7
Figure 3 Comparison between computed tidally averaged velocity and semi-analytical result. 8
Figure 4 Comparison between computed S_2 water level and semi-analytical result. 9
Figure 5 Comparison between computed S_2 velocity and semi-analytical result. 10
Figure 6 Comparison between computed S_4 water level and semi-analytical result. 11
Figure 7 Comparison between computed S_4 velocity and semi-analytical result. 12
Figure 8 Sketch of the 2DV model domain. 17
Figure 9 Relative magnitude of the maximum horizontal velocity at the bed, scaled with the local amplitude of the S_2 depth averaged velocity. 21
Figure 10 Comparison between the computed S_2 water level and semi-analytical result (49). 22
Figure 11 Comparison between the computed S_2 depth averaged velocity and semi-analytical result (52). 23
Figure 12 Comparison between the computed residual depth averaged velocity and semi-analytical result (53). 24
Figure 13 Comparison of velocity profiles at three different times at $x = 10.5$ km (top row), $x = 50.5$ km (middle row) and $x = 90.5$ km (bottom row). 25
Figure 14 Relative rms deviation between the computed COHERENS velocity profiles and their semi-analytical approximation. 26
Figure 15 Panel (a): problem sketch, panel (b): indicative representation of flow direction for a radially increasing bottom depth. 29
Figure 16 Adopted curvilinear grid. 31
Figure 17 Water level as computed by COHERENS (top panel) and the semi-analytical model (middle panel) for modest bottom steepness ($p = 0.25$). 32
Figure 18 Radial component of transport velocity as computed by COHERENS (top panel) and the semi-analytical model (middle panel) for modest bottom steepness ($p = 0.25$). 33
Figure 19 Azimuthal component of transport velocity as computed by COHERENS (top panel) and the semi-analytical model (middle panel) for modest bottom steepness ($p = 0.25$). 33
Figure 20 Water level as computed by COHERENS (top panel) and the semi-analytical model (middle panel) for the steep bed variation ($p = 2$). 34
Figure 21 Radial component of transport velocity as computed by COHERENS (top panel) and the semi-analytical model (middle panel) for the steep bed variation ($p = 2$). 35
Figure 22 Azimuthal component of transport velocity as computed by COHERENS (top panel) and the semi-analytical model (middle panel) for the steep bed variation ($p = 2$). 36
Figure 23 Sketch of the model geometry. 40
Figure 24 Along-channel level variation for the wind testcase (left) and the difference between COHERENS result and analytical approximation (112). 42
Figure 25 The top panel shows the along-channel velocity component u as computed by COHERENS, while the middle panel shows the approximated solution (113). 43
Figure 26 Vertical velocity as computed by COHERENS. 44

Figure 27 Longitudinal scheme of the overflowing dyke 50
Figure 28 Relative change of mass between two time steps for 2D computation 52
Figure 29 Relative change of mass between two time steps for 3D computation 52
Figure 30 Total depth before, at and after the dyke for 2D and 3D computations. 53
Figure 31 Change in depth (Δd) between two time steps for 2D computation 54
Figure 32 Change in depth (Δd) between two time steps for 3D computation 55

Figure 33 Parabolic cross section of the canal with the initial water surface 57
Figure 34 Relative change of volume compared to the initial volume for 2D mode 58
Figure 35 Relative change of volume compared to the initial volume for 3D mode 58
Figure 36 Relative change of volume compared to the initial volume for 3D mode with salinity 59
Figure 37 Verification of the Flip Flop behaviour for 2D mode 60
Figure 38 Verification of the Flip Flop behaviour for 3D mode 60
Figure 39 Verification of the Flip Flop behaviour for 3D mode with salinity 61
Figure 40 Mass conservation (schemes 2, 5 and 10) as function of time..... 61
Figure 41 Mass conservation (scheme 3) as function of time 63
Figure 42 Mass conservation (schemes 1, 4, 6, 7, 9 and 11) as function of time 63

Figure 43 Shallow lateral expansion in a channel (Talstra, 2011)..... 65
Figure 44 Comparison of water depths and flow velocities calculated by COHERENS and by using the equation of Bresse for open channel flow 67
Figure 45 Calculated flow velocities and water depths after 20 minutes (experiments: A, B, C and D) 67
Figure 46 Calculated mass balance for water (experiments: A, B, C and D) and salinity (experiment: C) ... 67
Figure 47 Calculated transport of salinity for experiment C 68
Figure 48 Calculated transport of temperature for experiment D 69
Figure 49 Comparison of water depths and flow velocities calculated by COHERENS and by using the equation of Bresse for open channel flow 71
Figure 50 Calculated flow velocities and water depths after 20 minutes (experiments: A, B, C and D) 71
Figure 51 Calculated mass balance for water (experiments: A, B, C and D) and salinity (experiment: C) ... 72
Figure 52 Calculated transport of salinity for experiment C 73
Figure 53 Calculated transport of temperature for experiment D 74
Figure 54 Calculated water depths along the channel for experiments A, B, C and D (not in scale)..... 77
Figure 55 Calculated water depths at the U-node where the structure is prescribed for experiments A, B, C and D (not in scale) 77
Figure 56 Vertical view of the calculated flow velocities for experiments B, C and D (not in scale) 78
Figure 57 Vertical view of the calculated transport of salinity and temperature for experiments C and D (not in scale) 78
Figure 58 Calculated mass balance for the transport of water and salinity for experiments A, B, C and D . 79
Figure 59 Calculated water depths along the channel for experiments E, F, G and H (not in scale)..... 79
Figure 60 Calculated water depths at the U-node where the structure is prescribed for experiments E, F, G and H (not in scale) 80
Figure 61 Vertical view of the calculated flow velocities for experiments F, G and H (not in scale) 80
Figure 62 Vertical view of the calculated transport of salinity and temperature for experiments G and H (not in scale)..... 81
Figure 63 Calculated mass balance for the transport of water and salinity for experiments E, F, G and H .. 81
Figure 64 Calculated water depths along the channel for experiments I, J, and K (not in scale) 82
Figure 65 Calculated mass balance for the transport of water and salinity for experiments I, J, and K 82
Figure 66 Vertical view of the calculated flow velocities for experiments I, J and K (not in scale)..... 83
Figure 67 Vertical view of the calculated transport of salinity and temperature for experiments J and K (not in scale) 83
Figure 68 Calculated water depths along the channel for experiments L, M, and N (not in scale) 84
Figure 69 Calculated mass balance for the transport of water and salinity for experiments L, M, and N ... 84
Figure 70 Vertical view of the calculated flow velocities for experiments L, M and N (not in scale) 85
Figure 71 Vertical view of the calculated transport of salinity and temperature for experiments M and N (not in scale) 85
Figure 72 Calculated water depths along the channel for experiments O, P, and Q (not in scale)..... 86
Figure 73 Calculated mass balance for the transport of water and salinity for experiments O, P, and Q ... 86
Figure 74 Vertical view of the calculated flow velocities for experiments O, P and Q (not in scale) 87

Figure 75 Vertical view of the calculated transport of salinity and temperature for experiments P and Q (not in scale) 87
Figure 76 Calculated flow velocities with the presence of the discharge for experiments A, B, C, D, E and F (not in scale) 90
Figure 77 Calculated transport of scalars due to the presence of the discharge for experiments C, D, E and F (not in scale) 90
Figure 78 Calculated mass balance for the transport of water and salinity, experiments A, B,C, D, E and F 90
Figure 79 Calculated flow velocities with the presence of the discharge for experiments G, H, I, J, K and L (not in scale) 92
Figure 80 Calculated transport of scalars due to the presence of the discharge for experiments I, J, K and L (not in scale) 92
Figure 81 Calculated mass balance for the transport of water and salinity, experiments G, H,I, J, K and L.. 92
Figure 82 Calculated flow velocities at different moments, experiments M, N, O, P, Q and R 93
Figure 83 Calculated mass balance for water and salinity, experiments M, N, O, P, Q and R 94

Figure 84 Scheme of the tidal basin with one open boundary: top view 98
Figure 85 Cross section of the tidal basin 99
Figure 86 Calculated total discharge at the open boundary 100
Figure 87 Calculated flow velocities at the open boundary: cross section view.....100
Figure 88 Longitudinal profile of the water level after 3 hours 101
Figure 89 Calculated depth mean currents and water level after 3 hours.....101
Figure 90 Calculated depth mean currents and salinity after 40 min. 102
Figure 91 Longitudinal view of the flow velocities and salinity after 40 min. 103
Figure 92 Calculated mass balance for water, experiments A, B and C 103
Figure 93 Calculated mass balance for salinity, experiment C 104
Figure 94 Scheme of the open channel with two open boundaries: top view 105
Figure 95 Scheme of the open channel flow with a backward facing step: side view 105
Figure 96 Calculated water level gradient at the downstream boundary 107
Figure 97 Calculated water surface at the upstream open boundary.....107
Figure 98 Calculated flow velocity at the upstream open boundary. 108
Figure 99 Calculated mass balance for water, experiments A, B and C 108
Figure 100 Calculated mass balance for salinity, experiment C 109
Figure 101 Memory effect for open boundary (Deltares, 2011;SIMONA,2009).....110
Figure 102 Scheme of the estuary 2DV model: mother model 111
Figure 103 Scheme of the reduced estuary 2DV model: daughter model.....112
Figure 104 Prescribed water level at the sea boundary: S2 tide.....113
Figure 105 Calculated flow velocities and salinity at 30km from the sea boundary: tide.....114
Figure 106 Calculated flow velocities and salinity at 30km from the sea boundary: ebb.....114
Figure 107 Calculated salinity at 30 km from the sea boundary: last 3 days 115
Figure 108 Comparison of the calculated salinity at 30 km (mother model with the Thatcher-Harleman condition (last 3 days) 116
Figure 109 Calculated flow velocities and salinity at 30km from the sea boundary: tide.....117
Figure 110 Calculated flow velocities and salinity at 30km from the sea boundary: ebb.....117
Figure 111 Calculated mass balance for water.....118
Figure 112 Calculated mass balance for salinity 118
Figure 113 Scheme of the prescription of normal and tangential components of flow transports at open boundaries 119
Figure 114 Scheme of a smaller model superimposed on a larger model for the prescription of tangential and normal components 120
Figure 115 Top view of the non uniform bathymetry of the mother model.....122
Figure 116 Calculated flow velocities and water levels after 1 hour.....122
Figure 117 Longitudinal view of the calculated flow velocities after 1 hour.....123

Figure 118 Top view of the non uniform bathymetry of the daughter model 123
Figure 119 Calculated flow velocities and water levels after 1 hour 124
Figure 120 Comparison of the calculated water levels of the mother and daughter model 125
Figure 121 Longitudinal view of the flow velocity in the X-direction 125
Figure 122 Longitudinal view of the flow velocity in the Y-direction 126
Figure 123 Calculated mass balance for water, experiments A and B 126

Figure 124 COHERENS velocity profile versus the theoretical law of the wall 131
Figure 125 COHERENS suspended sediment concentration profile versus the theoretical Rouse profile for $u_*/w_s = 5$ and bed boundary condition of Smith and McLean 131
Figure 126 COHERENS suspended sediment concentration profile versus the theoretical Rouse profile for $u_*/w_s = 5$ and bed boundary condition of Van Rijn 132
Figure 127 COHERENS suspended sediment concentration profile versus the theoretical Rouse profile for $u_*/w_s = 10$ 133
Figure 128 COHERENS suspended sediment concentration profile versus the theoretical Rouse profile for $u_*/w_s = 1$ 134
Figure 129 Temporal evolution of the net sediment transport flux through the bed ($n_z = 50$ layers) 135
Figure 130 Comparison of velocity profile without and with stratification effects (model settings of section 6.2 with $nz = 50$) 137
Figure 131 Comparison of diffusion profile without and with stratification effects (model settings of section 6.2 with $nz = 50$) 138
Figure 132 Comparison of concentration profile without and with stratification effects (model settings of section 6.2 with $nz = 50$) 139
Figure 133 Comparison velocity profiles of stratification test case 1 (w_s = cst) and stratification test case 2 (w_s = calculated) for $\tau_{cr} = 1/15\,10^{-4}\,m^2/s^2$ 140
Figure 134 Comparison diffusion profiles of stratification test case 1 (w_s = cst) and stratification test case 2 (w_s = calculated) for $\tau_{cr} = 1/15\,10^{-4}\,m^2/s^2$ 141
Figure 135 Comparison concentration profiles of stratification test case 1 (w_s = cst) and stratification test case 2 (w_s = calculated) for $\tau_{cr} = 1/15\,10^{-4}\,m^2/s^2$ 142
Figure 136 Velocity profiles in case of stratification, with w_s = cst 143
Figure 137 Diffusion profiles in case of stratification, with w_s = cst 144
Figure 138 Concentration profiles in case of stratification, with w_s = cst 145
Figure 139 Velocity profiles in case of stratification, with w_s = calculated 146
Figure 140 Diffusion profiles in case of stratification, with w_s = calculated 147
Figure 141 Concentration profiles in case of stratification, with w_s = calculated 148
Figure 142 The effect of hindered settling on the suspended sediment concentration 151
Figure 143 The effect of varying critical shear stress on hindered settling 151
Figure 144 Depth averaged concentration as function of distance from the boundary (for different sediment transport models). Equilibrium concentrations are shown with a dotted line 154
Figure 145 Calculated sediment concentration profiles (3D calculation; green) and analytical solution (black) 155
Figure 146 Schematic picture of a particle-laden gravity current flowing along a horizontal boundary, under a deep and otherwise quiescent ambient fluid (Hogg *et al.*, 2000) 156
Figure 147 Numerical profiles of the gravity current height 158
Figure 148 Profiles of the gravity current height derived from the similarity solution 158
Figure 149 Numerical longitudinal depth-averaged velocity profiles 159
Figure 150 Longitudinal depth-averaged velocity profiles derived from the similarity solution 159
Figure 151 Gravity current height for the similarity solution (red curve) and the numerical solution (green curve) at $t = 10s$ 160
Figure 152 Longitudinal depth-averaged velocity profiles for the similarity solution (red curve) and the numerical solution (green curve) at $t = 10s$ 160
Figure 153 Proportion of sediment that has deposited out of the density current 161

Figure 154 Vector plot of average velocity in channel 163
Figure 155 Contour plot of average velocity in channel 164
Figure 156 Secondary current at 45° bend angle 164
Figure 157 Secondary current at 135° bend angle.....165
Figure 158 Direction of bed load transport.....165
Figure 159 Detailed view of the bed load transport direction 166
Figure 160 Contour plot of depth-averaged suspended sediment concentration 166
Figure 161 Detailed view of the depth-average suspended sediment concentration 167
Figure 162 Distribution of suspended sediment concentration at 45° bend angle 167
Figure 163 Distribution of suspended sediment concentration at 135° bend angle.....168

Figure 164 Gaussian Hump Evolution under a constant discharge of $10\ \mathrm{m}^2/\mathrm{s}$ for different time steps.....173
Figure 165 Armouring simulation results in Cell 1 (case I).....176
Figure 166 Armouring simulation results in Cell 2 (case I).....177
Figure 167 Armouring simulation results in Cell 3 (case I).....177
Figure 168 Armouring simulation results in Cell 4 (case I).....178
Figure 169 Armouring simulation results in Cell 5 (case I).....178
Figure 170 Filtering simulation results in Cell 1 (case II) 179
Figure 171 Filtering simulation results in Cell 2 (case II) 179
Figure 172 Filtering simulation results in Cell 3 (case II) 180
Figure 173 Filtering simulation results in Cell 4 (case II) 180
Figure 174 Filtering simulation results in Cell 5 (case II) 181

List of Tables

Table 1 Contributions of various tidal constituents. 4
Table 2 Model parameters as adopted for the validation runs. 5
Table 3 Contribution of harmonic components to the solution at various orders: p = contributes, × = does not contribute. 18
Table 4 Model parameters as adopted for the validation run. 20
Table 5 Model parameter settings used for the COHERENS validation runs. 31
Table 6 Parameter settings of the wind validation testcase. 41

Table 7 Matrix of claims 49
Table 8 Comments of the results of the inundation schemes 62

Table 9 Data for the setup of the test case 66
Table 10 Data for the setup of the test case 70
Table 11 List of configurations 75
Table 12 Data for the setup of the test case 76
Table 13 List of configurations 89
Table 14 Data for the setup of the test case 91

Table 15 Claims matrix for the validation tests 96
Table 16 Data for the setup of the test case 99
Table 17 Data for the setup of the test case 106
Table 18 Data for the setup of the mother model 111
Table 19 Data for the setup of the daughter model 112
Table 20 Data for the setup of the mother model 120
Table 21 Data for the setup of the daughter model 121

Table 22 Model setup for suspended sediment concentration test cases 130
Table 23 Comparison of total amount of suspended sediment with total net transport through the bed .. 135
Table 24 Model setup for density stratification test case 136
Table 25 Model setup for hindered settling test case 149
Table 26 Overview of model set up 153
Table 27 Overview of the 2D simulations 153
Table 28 Model setup for gravity current test case 157
Table 29 Model setup for bend flow test case 163

Table 30 Model setup for vertical sorting test case 1a and 1b 175

1 Introduction

COHERENS is an ocean circulation model that was originally developed at the Management Unit of the North Sea Mathematical Models and the Scheldt estuary (MUMM, now OD Nature) which is a scientific institute of the Belgian Federal Government. The first version (COHERENS V1) was completed in 1998 and was funded by several European projects.

In the period between 2003 and 2009 further developments were done within the framework of European Projects ODON and ECOOP. This version (called COHERENS V2) had noticable extensions like the use of curvilinear grids and the possibility of parallel computing.

Next, from 2008 to 2015 the COHERENS V2 version was extended greatly within the project "Expansion of the numerical modeling tools for the North Sea Harbors". This project was funded by by the Maritime Access division (aMT) of the Department of Mobility and Public Works of the Flemish Government. The code developments involved several partners: IMDC n.v, Antea Group n.v., Leuven Catholic University, Ghent University and Flanders Hydraulic Research.

The code extensions were considerable and added major functionalities to COHERENS. These new functionalities have been validated and the results of these validation activities have been compiled in the current document. Each chapter is a (more or less standalone) account of a validation of a specific part of the COHERENS code.

This validation document is organised as follows. In Chapter 2 the validation of hydrodynamics is considered. In Chapter 3 several new algorithms for inundation (drying & flooding) are discussed. Chapter 4 is devoted to the implementation of structures, which mostly deal with the schematization of engineering works like weirs. Next, Chapter 5 considers the use of several new boundary conditions that were not included included in the original COHERENS V2 code, like Neumann and Thatcher-Harleman conditions. In Chapter 6 several test cases of the sediment transport module are discussed. Finally, Chapter 7 is devoted to the morphological functionality of COHERENS and includes, amongst others, the use of tidal averaging and the effect of vertical sorting in the bed.

The structure per chapter is roughly the same. First, the contents of a chapter are outlined in an introduction. Next, several test cases (or groups of test cases) that focus on specific aspects of functionalies are discussed in sections. Conclusions regarding the validation of the functionalities are mentioned at the end of each section. At the end of each chapter, the main conclusions are summarised once again.

All testcases have been validated with COHERENS version 2.8.

2 Hydrodynamics

2.1 Introduction

In this chapter we will validate the hydrodynamics of the COHERENS model by considering cases for which a near-analytical solution is a priori known. One justification for this approach is obvious, in that any good numerical code should be able to reproduce (semi)-analytical results before it is applied to more complex real-life situations for which the outcome is much harder to judge. In addition, the use of (semi)-analytical models is the best way to judge the internal working of a numerical model. For instance, by using analytical results it can be investigated whether advective processes are treated in a reliable way. If a comparison between numerical model and (semi)-analytical models is not satisfactory, there is a clear reason for concern.

As we will see the use of semi-analytical models can be fully exploited by using a mathematical technique called assymptotic approximation. Basically, this means that one can rewrite the full set of model equations in a way that specifically identifies small contributions. These rewritten equations can then be solved in such a way, that the solution of the original problem is obtained as a series that contains successively smaller contribution. For tidal flows, this gives solutions for both the dominant tidal component (e.g. M_2) as well as the residual and overtides.

Below the following test cases will be elaborated:

1. one-dimensional short tidal channel, a case for which very accurate approximate solutions to the tidal flow can be achieved,
2. long tidal channel: a cross-channel averaged test case for which the main tidal water motion is solved. Also the Stokes return flow is validated,
3. two-dimensional wind drived flow. This is primarily a test case to check the curvilinear grid functionality of COHERENS,
4. vertical wind driven circulation.

For each of these cases a derivation of the approximate solution is included after the presentation of conclusions.

2.2 Flow in a 1D short tidal channel

2.2.1 Introduction

In this chapter, we consider tidal flow in a short one-dimensional tidal basin $0 \leq x \leq L$ with uniform bottom depth H (see Fig. 1). The boundary at $x = L$ is closed. At $x = 0$, a prescribed vertical tide (water level ζ) with

Figure 1 – Sketch (vertical slice) of the one-dimensional model domain.

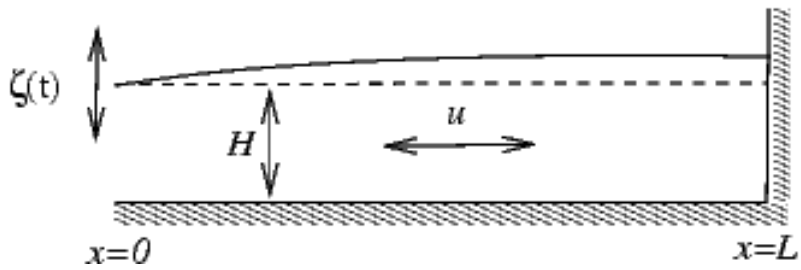

a single harmonic component (circular frequency σ, period $P = 2\pi/\sigma$) is imposed, i.e.

$$\zeta(x = 0, t) = A\cos(\sigma t)\ . \tag{1}$$

This external forcing drives the tidal flow inside the basin.
It is assumed that the embayment is short in the sense that its length L is small compared to the wavelength of the dominant tidal constituent. This condition can be expressed in terms of the dimensionless parameter

$$\delta \equiv \frac{(\sigma L)^2}{gH}\ ,$$

which is to be much smaller than unity. An advantage of the short tidal channel testcase is that it is relatively easy to obtain accurate semi-analytical solutions for water level and water motion.

Claims

The purpose of this case is to investigate the following claims:

1. appropriate description of the generation of internal overtides
2. appropriate description of water motion under the influence of linear bottom friction

Summary of semi-analytical results

It is assumed that the relative amplitude $\varepsilon \equiv A/H$ of the vertical tide at the entrance is small, i.e. $\varepsilon \ll 1$. Additionally, the channel length L is chosen such that the parameter δ (which is usually small compared to ε) is exactly equal to ε^2.
Finally, the semi-analytical results were obtained by adopting a linear law for the bottom friction τ, i.e.

$$\tau = ru\ ,$$

where r is the linear friction coefficient.

The semi-analytical expressions for water level and water motion are expressed as a truncated series expansion in ε, e.g.

$$\zeta(x, t) = \zeta_0(x, t) + \varepsilon\zeta_1(x, t) + \dots\ ,$$

and similarly for water motion. For this test case, the series expansion includes terms up to $O(\varepsilon^3)$.
Using the notation $\tilde{x} = x/L$, $\tilde{t} = \sigma t$ and $\tilde{r} = r/(\sigma H)$, the explicit expressions for water level, transport velocity U and depth averaged velocity u thus obtained read

$$\zeta(\tilde{x},\tilde{t}) = A\left[\cos(\tilde{t}) + \varepsilon^2\left(\tilde{x} - \frac{\tilde{x}^2}{2}\right)[\cos(\tilde{t}) + \tilde{r}\sin(\tilde{t})] + \varepsilon^3\left(\tilde{x} - \frac{\tilde{x}^2}{2}\right)\left(\frac{1}{2} - \frac{3}{2}\cos(2\tilde{t}) - \tilde{r}\sin(2\tilde{t})\right)\right] , \tag{2}$$

$$\begin{aligned} U(\tilde{x},\tilde{t}) = (H+\zeta)u = \sigma AL\Bigg[&-(1-\tilde{x})\sin(\tilde{t}) + \varepsilon^2\left(\frac{1}{3} - \frac{\tilde{x}^2}{2} + \frac{\tilde{x}^3}{6}\right)[-\sin(\tilde{t}) + \tilde{r}\cos(\tilde{t})] \\ &+ \varepsilon^3\left(\frac{1}{3} - \frac{\tilde{x}^2}{2} + \frac{\tilde{x}^3}{6}\right)[3\sin(2\tilde{t}) - 2\tilde{r}\cos(2\tilde{t})]\Bigg] , \end{aligned} \tag{3}$$

$$\begin{aligned} u(\tilde{x},\tilde{t}) = \frac{\sigma AL}{H}\Bigg[&(\tilde{x}-1)\sin(\tilde{t}) + \frac{\varepsilon}{2}(1-\tilde{x})\sin(2\tilde{t}) \\ &+ \frac{\varepsilon^2}{12}\left\{2\tilde{r}[\tilde{x}^3 - 3\tilde{x}^2 + 2]\cos(\tilde{t}) + [-2\tilde{x}^3 + 6\tilde{x}^2 + 3\tilde{x} - 7]\sin(\tilde{t}) + 3[\tilde{x}-1]\sin(3\tilde{t})\right\} \\ &+ \frac{\varepsilon^3}{6}(1-\tilde{x})\Bigg\{-\tilde{r}(1-\tilde{x})^2 + \tilde{r}(4\tilde{x}^2 - 8\tilde{x} - 5)\cos(2\tilde{t}) + \frac{1}{2}(-10\tilde{x}^2 + 20\tilde{x} + 17)\sin(2\tilde{t}) \\ &+ \frac{3}{4}\sin(4\tilde{t})\Bigg\}\Bigg] , \end{aligned} \tag{4}$$

respectively. Since the series includes terms up to $O(\varepsilon^3)$, the relative error of these expression is expected to be $O(\varepsilon^4)$.

Contributions of tidal components

Some more insight into the tidal dynamics can be obtained by identifying the contributions of individual harmonic components to the time variation of water level and flow velocity. These contributions may occur at specific orders of the solution. This frequency information is summarised in Table 1. From this table, we observe that the dominant tidally averaged (S_0) water level and velocity only enter at $O(\varepsilon^3)$ and that there are no S_6 or S_8 components in the water level field.
The S_2 tidal component inside the basin is predominantly a result of the external diurnal forcing at the boundary (Eq. 1). The other components, however, are entirely generated internally and thus reflect the tidal dynamics of the basin itself.

Table 1 – Contributions of various tidal constituents.

	$O(1)$	$O(\varepsilon)$	$O(\varepsilon^2)$	$O(\varepsilon^3)$
S_0 (tidal average)	×	×	×	ζ, u
S_2	ζ, U, u	×	ζ, U, u	×
S_4	×	u	×	ζ, U, u
S_6	×	×	u	×
S_8	×	×	×	u

Finally, note also that the tidally averaged transport velocity vanishes. This is due to the fact that there is no net transfer of water into (or out of) the basin. This does not imply that there is no tidally averaged velocity. Indeed, since $U = (H+\zeta)u$ we have

$$< U >= H < u > + < \zeta u >= 0 ,$$

where $< >$ denotes tidal averaging. From this we find that $< u >= - < \zeta u > /H$ so that residual flows will exist if there are nonzero correlations between water level and velocity. In the case of a short tidal basin these correlations are small but do exist because of the presence of friction.

2.2.2 Model setup

The short tidal channel testcase has been used to validate the COHERENS model for one-dimensional tidal propagation. To this end, the model domain was represented by a one-dimensional grid with $nc = 51$ points and a single computational layer ($nz = 1$). Furthermore, a specific model with $\varepsilon = 0.1$ has been adopted. The explicit parameter settings are listed in Table 2.

Table 2 – Model parameters as adopted for the validation runs.

Symbol	Meaning	Value
L	Channel length	6810 m
H	Bottom depth	10 m
σ	S_2 circular frequency	1.45×10^{-4} r$ad\ s^{-1}$
A	Water level forcing	1 m
r	Linear friction coefficient	0.001 m s^{-1}
ε	Relative amplitude of vertical tide	0.1
δ	Shortness parameter	0.01
nc	Number of grid points (along-channel)	51
nr	Number of grid points (cross-channel)	2
nz	Number of computational layers	1
Δt	Time step	6 s

The channel length is tuned such that $\delta = \varepsilon^2 = 0.01$. The bottom friction is linear so that the bed shear stress τ is given by $\tau = ru$. Note that the model is forced with a diurnal solar component (S_2) rather than the semi-diurnal lunar tide (M_2). This choice is made because the diurnal tide has an exact twelve hour period that is more convenient for an accurate harmonic analysis of the results.

Boundary and initial conditions

Three types of boundary conditions (labeled Type A-C) were used, namely

- Type A: specification of water level ζ, which is implemented in COHERENS by setting ityp2dobu=3 at the open boundary (Eq. 5),
- Type B: specification of transport velocity U, which requires ityp2dobu=4 (Eq. 6),
- Type C: specification of both ζ and U, which is implemented when ityp2dobu=11 is adopted.

The tidal components for the open boundary condition were obtained by evaluating Eqs. (2) and (3) at $\tilde{x} = 0$, which gives the time series

$$\zeta(\tilde{x} = 0, \tilde{t}) = A\cos(\tilde{t}) \,, \tag{5}$$

$$U(\tilde{x} = 0, \tilde{t}) = \sigma A L \left[-\left\{ 1 + \frac{\varepsilon^2}{3} \right\} \sin(\tilde{t}) + \frac{\varepsilon^2}{3} \tilde{r} \cos(\tilde{t}) + \varepsilon^3 \left\{ \sin(2\tilde{t}) - \frac{2}{3} r \cos(2\tilde{t}) \right\} \right] \,, \tag{6}$$

from which the amplitude and phase of tidal components is readily computed.
Similarly, one obtains the following expressions for the initial ditribution of water level and transport velocity,

which can be used for an accurate specification of an initial condition:

$$\zeta(\tilde{x}, \tilde{t} = 0) = A \left[1 + \varepsilon^2 \left(\tilde{x} - \frac{\tilde{x}^2}{2} \right) - \varepsilon^3 \left(\tilde{x} - \frac{\tilde{x}^2}{2} \right) \right] , \tag{7}$$

$$U(\tilde{x}, \tilde{t} = 0) = \frac{AL}{H^2} r \left(\frac{1}{3} - \frac{\tilde{x}^2}{2} + \frac{\tilde{x}^3}{6} \right) [\varepsilon^2 - 2\varepsilon^3] . \tag{8}$$

Quantitative measure for difference between COHERENS and semi-analytical model

The water levels and fluid velocity as computed by COHERENS and the semi-analytical formulae (2) and (4) are compared per harmonic component. To this end, we introduce the relative root mean square (rms) difference. Let $\mathscr{A}_1(x)$ and $\varphi_1(x)$ denote amplitude and phase of a harmonic component of a quantity Q as computed by COHERENS. Let $\mathscr{A}_2(x)$ and φ_2 denote amplitude and phase according to the semi-analytical results; their explicit form can be obtained per tidal component from Eqns. (2) and (4). We then define the absolute rms difference $\Delta^Q_{\text{abs}}(x)$ between numerical and semi-analytical model as

$$\begin{aligned} \Delta^Q_{\text{abs}}(x) &= \sqrt{\frac{1}{P} \int_0^{\text{P}} \{\mathscr{A}_1(x) \cos[\omega t - \varphi_1(x)] - \mathscr{A}_2(x) \cos[\omega t - \varphi_2(x)]\}^2 \, dt} \\ &= \sqrt{\frac{[\mathscr{A}_1(x) - \mathscr{A}_2(x)]^2}{2} + \mathscr{A}_1(x)\mathscr{A}_2(x) \cos[\varphi_1(x) - \varphi_2(x)]} , \end{aligned} \tag{9}$$

where P denotes the S_2 tidal period. Note that $\Delta^Q_{\text{abs}}(x)$ depends on location. If amplitudes and phases coincide perfectly (i.e. $\mathscr{A}_1(x) = \mathscr{A}_2(x)$ and $\varphi_1(x) = \varphi_2(x)$, then we have $\Delta^Q_{\text{abs}}(x) = 0$ by definition.
We now define the relative rms difference for water level and fluid velocity as

$$\Delta^\zeta_{\text{rel}}(x) = \frac{\Delta^\zeta_{\text{abs}}(x)}{A} \quad \text{and} \quad \Delta^u_{\text{rel}}(x) = \frac{H \Delta^u_{\text{abs}}(x)}{\sigma A L} ,$$

respectively, where the factors A and $\sigma AL/H$ stem from the scaling analysis that is used to obtain the semi-analytical approximation (see Sect. 2.2.5). Typically, these factors are a measure for the magnitude of water level and tidal flow velocity.
Since the semi-analytical expressions (2) and (4) include terms up to $O(\varepsilon^3)$, we expect the relative deviations $\Delta^\zeta_{\text{rel}}$ and Δ^u_{rel} to be $O(\varepsilon^4) \sim 10^{-4}$ or less. This gives a direct way to judge the quality of tidal components that are computed with COHERENS.

2.2.3 Results

Tidally averaged component

First we consider the results for the tidally averaged or S_0 water level and fluid motion, which are obtained by taking the time average over a tidal period. This tidal consitituent is generated internally (see Sect 2.2.1). Figures 2 and 3 show the distribution of the tidally water level and flow velocity for all three types of boundary conditions as well as their relative rms differences with the analytical result.

We see that the relative rms differences for the tidal mean water level and velocity are $\sim 10^{-5}$ or less. Hence we conclude that the tidally averaged quantities are well decribed by COHERENS.

Figure 2 – Comparison between computed tidally averaged water level and semi-analytical result.

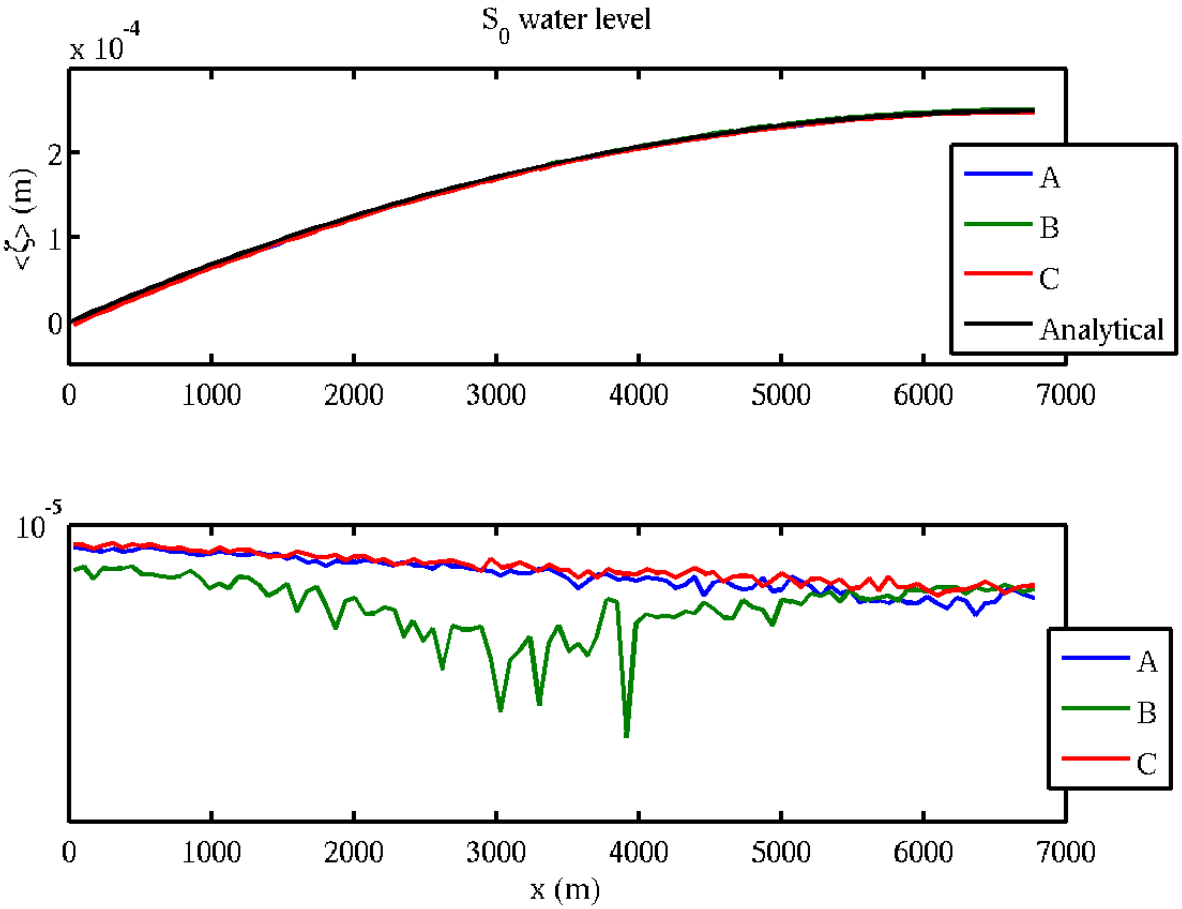

Top panel: spatial distribution, bottom panel: spatial distribution of relative rms differences with the analytical results.

Figure 3 – Comparison between computed tidally averaged velocity and semi-analytical result.

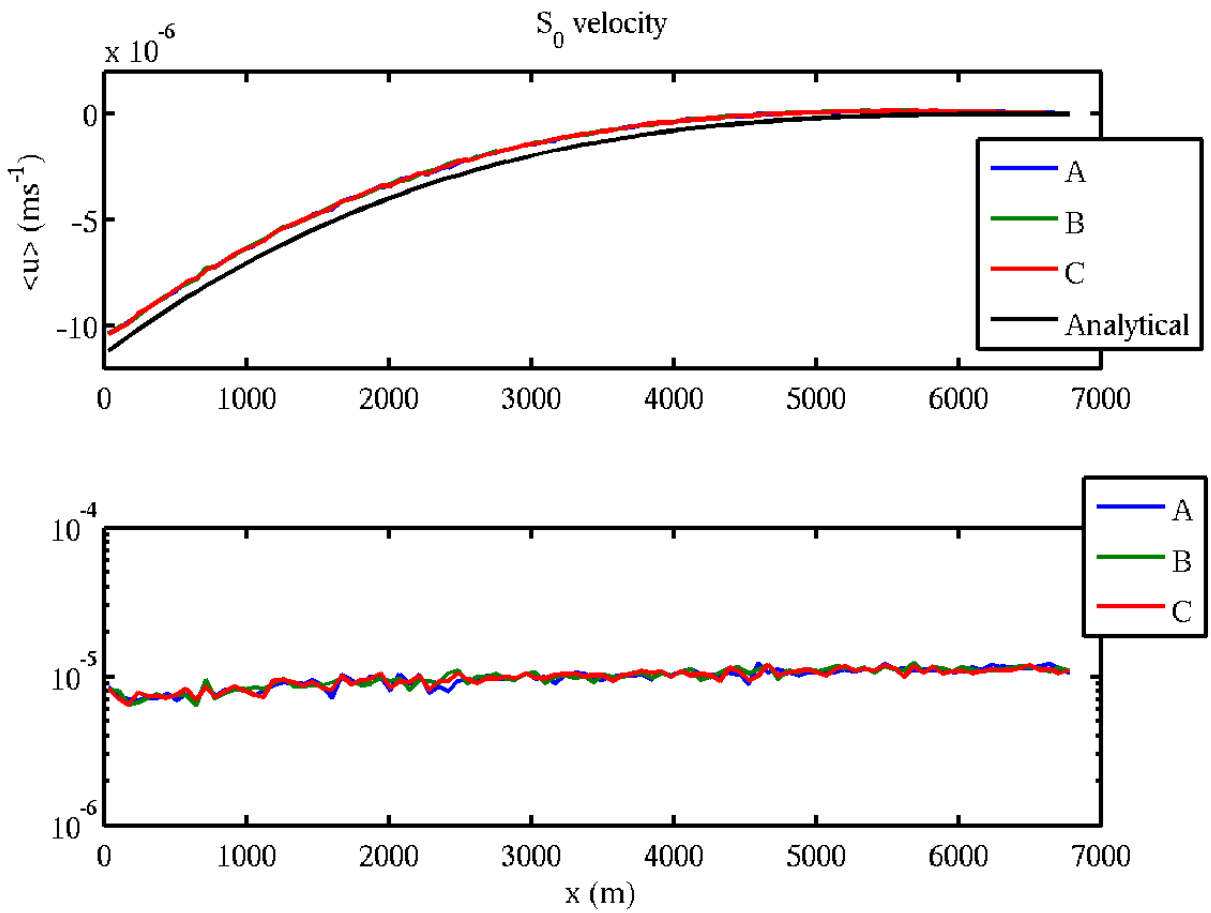

Top panel: spatial distribution, bottom panel: spatial distribution of relative rms differences with the analytical results.

S_2 component

A comparison between the S_2 contribution to water level and the analytical approximation is displayed in Fig. 4. Figure 5 shows the comparison between COHERENS and the semi-analytical solution for the S_2 component of velocity. For both water level and velocity we find a maximum relative difference $\sim 2 \times 10^{-4}$. From this we conclude that COHERENS gives an adequate description of the diurnal tidal dynamics.
For completeness we note that the use of the transport velocity boundary condition (boundary condition B) leads to a non-zero phase angle for the water level at the entrance (see Fig. 4b). Hence for this condition the water level forcing (1) is not reproduced exactly.

Figure 4 – Comparison between computed S_2 water level and semi-analytical result.

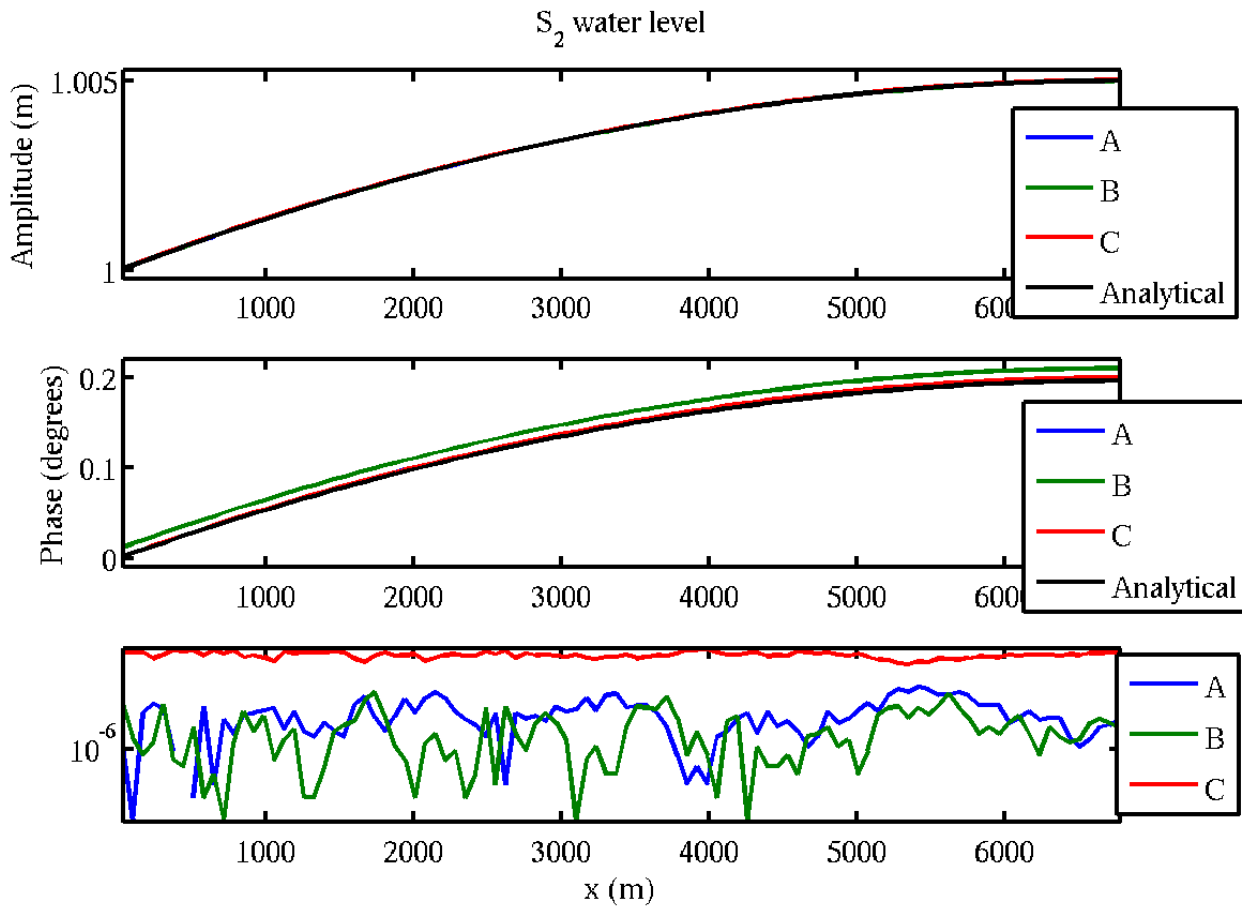

Figure 5 – Comparison between computed S_2 velocity and semi-analytical result.

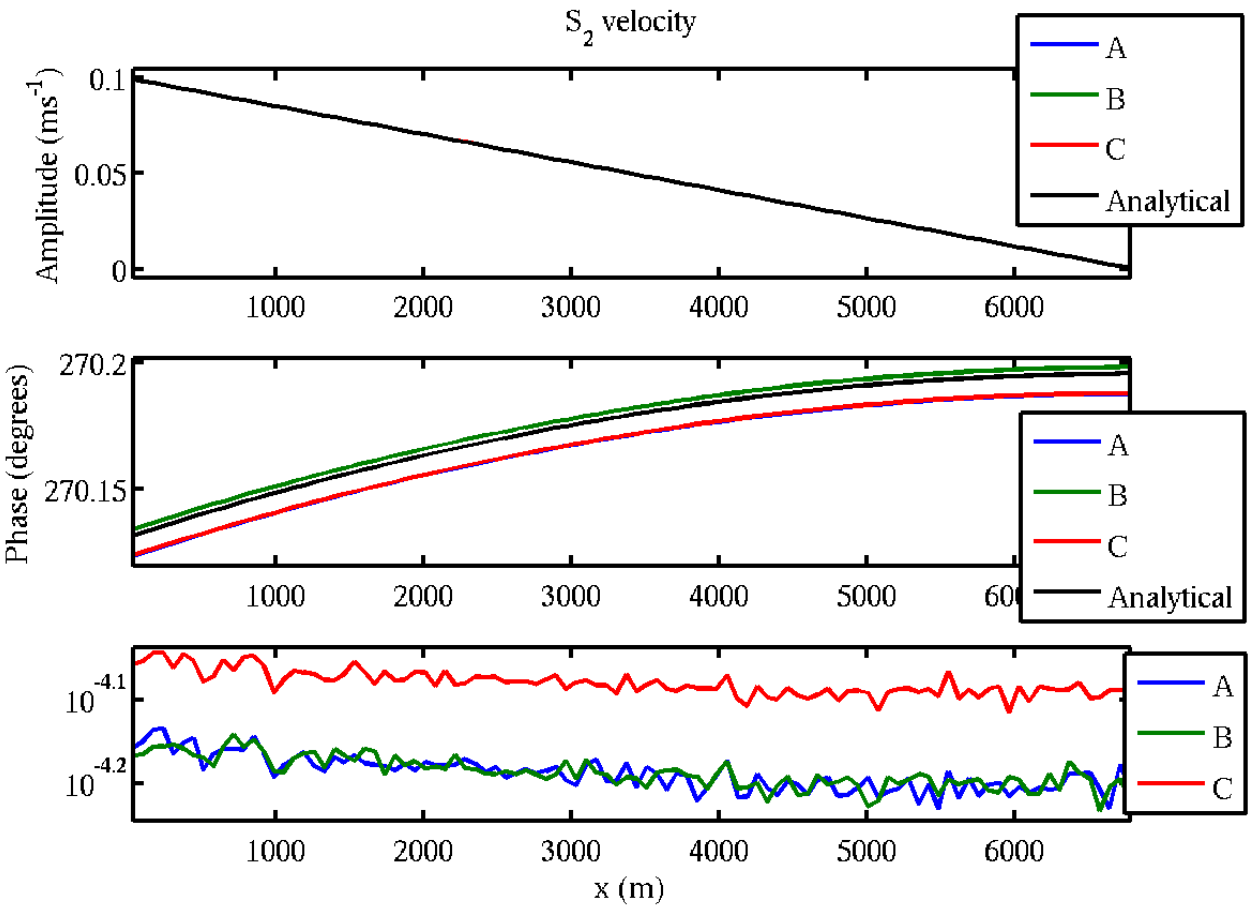

S_4 component

This tidal consitituent is generated internally (see Sect 2.2.1). The comparison between the S_4 dynamics from COHERENS and the semi-analytical model is displayed in Figs. 6 and 7 which refer to water level and velocity, respectiely. From both figures, we see that the relative difference is below 10^{-4} so that the S_4 dynamics as computed by COHERENS is in good agreement with the semi-analytical approximation.
It should be noted that COHERENCE results regarding the the tidal phase of the S_4 water level tend to diverge towards the entrance of the basin. While this behaviour does not affect the accuracy of the computed solution, is has not been possible to identify its origin. The current hypothesis is that the phase angle divergence is due to relatively small deviations amongst the solutions in the region near the open boundary. While the solution for runs A–C goes to zero near $x = 0$, the small differences amongst the three simulations may amount to large differences in phase angle. More explicitly, computation of the phase angle involves the arctangent of the ratio of two numbers. Near $x = 0$, the value of this ratio may be very sensitive to deviations in the value of the denominator (which becomes very small), thus resulting in a possibly large variation of the value of the phase angle.

Figure 6 – Comparison between computed S_4 water level and semi-analytical result.

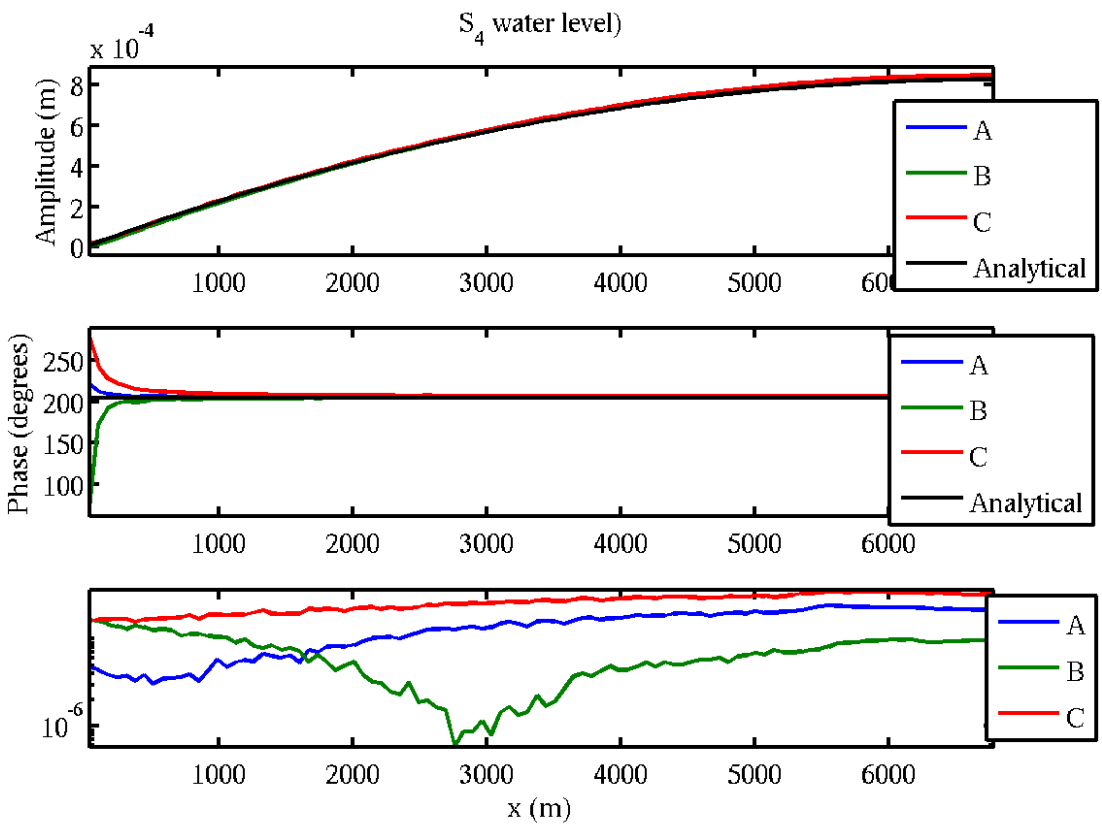

Figure 7 – Comparison between computed S_4 velocity and semi-analytical result.

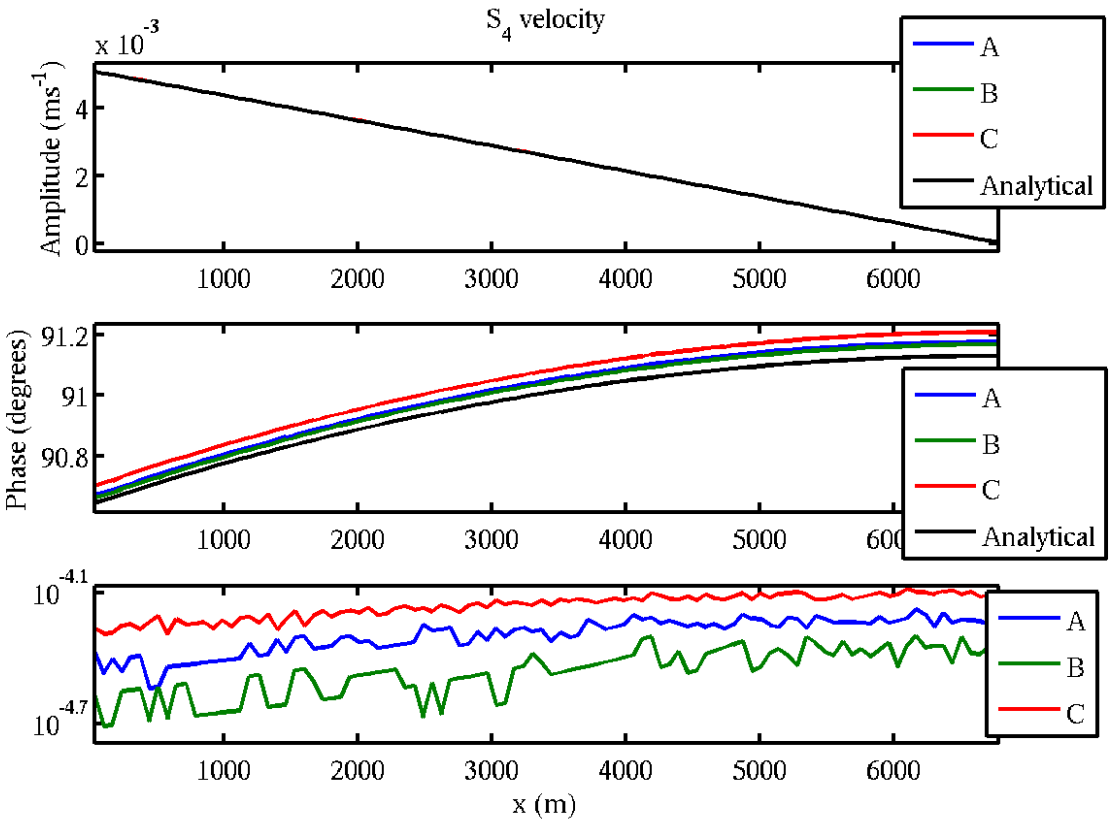

2.2.4 Conclusions

1. COHERENS gives an accurate description of internally generated overtides in a short tidal basin
2. COHERENS is able to compute tidal flow in a short tidal accurately for the case of linear bottom friction

2.2.5 Derivation of the semi-analytical solution

Dimensional model equations

The full set of model equations are given by the one-dimensional shallow water equations for flow and sediment which read

$$\frac{\partial u}{\partial t} + u\frac{\partial u}{\partial x} = -g\frac{\partial \zeta}{\partial x} - r\frac{u}{h}\,, \tag{10}$$

$$\frac{\partial \zeta}{\partial t} + \frac{\partial}{\partial x}(hu) = 0\,, \tag{11}$$

respectively. Note that the bed shear stress is assumed to be a linear function of velocity.
The hydrodynamics inside the basin is forced externally by a prescribed water level at the seaward side ($x = 0$), i.e.

$$\zeta(x = 0, t) = A\zeta_{\mathrm{e}}(t)\,, \tag{12}$$

where $\zeta_{\mathrm{e}}(t)$ is a harmonic signal and A denotes the typical amplitude of the imposed vertical tide. The analysis below will give expressions for water level and tidal flow velocity in terms of $\zeta_{\mathrm{e}}(t)$. From these expressions, can obtain the solution for boundary condition (1) a posteriori by putting $\zeta_{\mathrm{e}}(t) = \cos(\sigma t)$. The boundary condition at the landward side ($x = L$) is given by impermeability of the solid wall, i.e.

$$u(x = L, t) = 0\,. \tag{13}$$

Scaled model equations

The full set of model equations (10)–(13) can be reduced by adopting the following scaling for the model variables:

$$x = L\tilde{x}\,,\ t = \tilde{t}/\sigma\,,\ \zeta = A\tilde{\zeta}\,,\ h = H\tilde{h}\,,\ u = \frac{\sigma AL}{H}\tilde{u}\,,\ r = \sigma H\tilde{r}\,, \tag{14}$$

where variables with a tilde ($\sim$) denote scaled variables. The scaling for velocity stems from mass balance (tidal filling and emptying). Inserting this scaling into Eqs. (10) and (11) gives

$$\frac{\partial \tilde{\zeta}}{\partial \tilde{x}} = -\delta\left[\frac{\partial \tilde{u}}{\partial \tilde{t}} + \varepsilon\tilde{u}\frac{\partial \tilde{u}}{\partial \tilde{x}} + \tilde{r}\frac{\tilde{u}}{1+\varepsilon\tilde{\zeta}}\right]\,, \tag{15}$$

$$\frac{\partial \tilde{\zeta}}{\partial \tilde{t}} + \frac{\partial}{\partial \tilde{x}}[(1+\varepsilon\tilde{\zeta})\tilde{u}] = 0\,, \tag{16}$$

where ε and δ are parameters which are defined as

$$\varepsilon = \frac{A}{H}, \quad \delta = \frac{(\sigma L)^2}{gH} = 4\pi^2\left(\frac{L}{\Lambda}\right)^2\,, \tag{17}$$

We will assume that the amplitude of the vertical tide is small in the sense that $\varepsilon \ll 1$. The parameter δ is related to the ratio of basin length to tidal wavelength, which is small because we consider a short tidal

embayment. In the the remainder of this chapter it will be assumed that the model parameters are chosen such that $\delta = \varepsilon^2$. The main advantage of this choice is that the successive approximation to the solution of the model equations involves an expansion in the single parameter ε rather than a double series in ε and δ.

The scaled versions of the boundary conditions (12) and (13) read

$$\tilde{\zeta}(\tilde{x} = 0, \tilde{t}) = \tilde{\zeta}_{\mathrm{e}}(\tilde{t}) \,, \tag{18}$$

and

$$\tilde{u}(\tilde{x} = 1, \tilde{t}) = 0 \,, \tag{19}$$

respectively.

$O(1)$ solution

The equation for flow and sediment at zeroth order are given by

$$\frac{\partial \tilde{\zeta}_0}{\partial \tilde{x}} = 0 \,, \tag{20}$$

$$\frac{\partial \tilde{\zeta}_0}{\partial \tilde{t}} + \frac{\partial \tilde{u}_0}{\partial \tilde{x}} = 0 \,, \tag{21}$$

while the boundary conditions read

$$\tilde{\zeta}_0(\tilde{x} = 0, \tilde{t}) = \tilde{\zeta}_{\mathrm{e}}(\tilde{t}) \,,\ \tilde{u}(\tilde{x} = 1, \tilde{t}) = 0 \,. \tag{22}$$

From Eq. (20) and (22) we obtain

$$\tilde{\zeta}_0(\tilde{x}, \tilde{t}) = \tilde{\zeta}_{\mathrm{e}}(\tilde{t}) \,, \tag{23}$$

i.e. the zeroth order water level does not vary throughout the basin. From continuity (Eq. 21) it is found that the only flow that obeys impermeability at $x = 1$ is

$$\tilde{u}_0(\tilde{x}, \tilde{t}) = (1 - \tilde{x}) \frac{d\tilde{\zeta}_{\mathrm{e}}}{d\tilde{t}} \,. \tag{24}$$

$O(\varepsilon)$ solution

The first order flow equations and boundary conditions are as follows

$$\frac{\partial \tilde{\zeta}_1}{\partial \tilde{x}} = 0 \,, \tag{25}$$

$$\frac{\partial \tilde{\zeta}_1}{\partial \tilde{t}} + \frac{\partial \tilde{u}_1}{\partial \tilde{x}} + \frac{\partial (\tilde{\zeta}_0 \tilde{u}_0)}{\partial \tilde{x}} = 0 \,, \tag{26}$$

$$\tilde{\zeta}_1(\tilde{x} = 0, \tilde{t}) = \tilde{u}_1(\tilde{x} = 1, \tilde{t}) = 0 \,. \tag{27}$$

From Eqs. (25) and (27) we find that

$$\tilde{\zeta}_1(\tilde{x}, \tilde{t}) = 0 \,, \tag{28}$$

while the first order velocity $\tilde{u}_1(\tilde{x}, \tilde{t})$ is found from mass conservation (Eq. 26) as

$$\tilde{u}_1(\tilde{x}, \tilde{t}) = -\tilde{u}_0 \tilde{\zeta}_0 = -(1 - \tilde{x}) \tilde{\zeta}_{\mathrm{e}} \frac{d\tilde{\zeta}_{\mathrm{e}}}{d\tilde{t}} \,. \tag{29}$$

$O(\varepsilon^2)$ solution

At $O(\varepsilon^2)$, the model equations are given by

$$\frac{\partial \tilde{\zeta}_2}{\partial \tilde{x}} = -\frac{\partial \tilde{u}_0}{\partial \tilde{t}} - \tilde{r}\tilde{u}_0 \,, \tag{30}$$

$$\frac{\partial \tilde{\zeta}_2}{\partial \tilde{t}} + \frac{\partial \tilde{u}_2}{\partial \tilde{x}} + \frac{\partial(\tilde{\zeta}_0 \tilde{u}_1)}{\partial \tilde{x}} = 0 \,, \tag{31}$$

$$\tilde{\zeta}_2(\tilde{x}=0,\tilde{t}) = \tilde{u}_2(\tilde{x}=1,\tilde{t}) = 0 \,. \tag{32}$$

From these expressions we find that the water level $\zeta_2(x,t)$ is given by

$$\tilde{\zeta}_2(\tilde{x},\tilde{t}) = \left[\frac{\tilde{x}^2}{2} - \tilde{x}\right]\left[\frac{d^2\tilde{\zeta}_\mathrm{e}}{d\tilde{t}^2} + \tilde{r}\frac{d\tilde{\zeta}_\mathrm{e}}{d\tilde{t}}\right] \,, \tag{33}$$

while the second order velocity contribution $u_2(x,t)$ reads

$$\begin{aligned}\tilde{u}_2(\tilde{x},\tilde{t}) &= -\tilde{\zeta}_0\tilde{u}_1 + \int_{\tilde{x}}^{1} \frac{\partial \tilde{\zeta}_2}{\partial x'}(x',\tilde{t})dx' \\ &= (1-\tilde{x})\left[\tilde{\zeta}_\mathrm{e}^2\frac{d\tilde{\zeta}_\mathrm{e}}{d\tilde{t}} + \frac{1}{6}(-2-2\tilde{x}+\tilde{x}^2)\left\{\frac{d^3\tilde{\zeta}_\mathrm{e}}{d\tilde{t}^3} + \tilde{r}\frac{d^2\tilde{\zeta}_\mathrm{e}}{d\tilde{t}^2}\right\}\right]\end{aligned} \tag{34}$$

$O(\varepsilon^3)$ solution

The flow at $O(\varepsilon^3)$ is governed by the following equations and boundary conditions:

$$\frac{\partial \tilde{\zeta}_3}{\partial \tilde{x}} = -\frac{\partial \tilde{u}_1}{\partial \tilde{t}} - \tilde{u}_0\frac{\partial \tilde{u}_0}{\partial \tilde{x}} - \tilde{r}\tilde{u}_1 + \tilde{r}\tilde{u}_0\tilde{\zeta}_0 \,, \tag{35}$$

$$\frac{\partial \tilde{\zeta}_3}{\partial \tilde{t}} + \frac{\partial \tilde{u}_3}{\partial \tilde{x}} + \frac{\partial(\tilde{\zeta}_0\tilde{u}_2 + \tilde{\zeta}_2\tilde{u}_0)}{\partial \tilde{x}} = 0 \,, \tag{36}$$

$$\tilde{\zeta}_3(\tilde{x}=0,\tilde{t}) = \tilde{u}_3(\tilde{x}=1,\tilde{t}) = 0 \,. \tag{37}$$

From this, we find that the third order contribution $\zeta_3(x,t)$ to water level is given by

$$\tilde{\zeta}_3(x,t) = \left[\tilde{x} - \frac{\tilde{x}^2}{2}\right]\left[\frac{1}{2}\frac{d^2\tilde{\zeta}_\mathrm{e}^2}{d\tilde{t}^2} + \left(\frac{d\tilde{\zeta}_\mathrm{e}}{d\tilde{t}}\right)^2 + \tilde{r}\frac{d\tilde{\zeta}_\mathrm{e}^2}{d\tilde{t}}\right] \,, \tag{38}$$

while the third order velocity $u_3(x,t)$ reads

$$\begin{aligned}\tilde{u}_3 &= -\tilde{u}_0\tilde{\zeta}_2 - \tilde{u}_2\tilde{\zeta}_0 + \int_{\tilde{x}}^{1}\frac{\partial \tilde{\zeta}_3}{\partial \tilde{t}}\,\mathrm{d}x' \\ &= -\frac{1}{6}(1-\tilde{x})\left[6\tilde{\zeta}_\mathrm{e}^3\frac{d\tilde{\zeta}_\mathrm{e}}{d\tilde{t}} + \tilde{r}(5\tilde{x}^2-10\tilde{x}-4)\left(\frac{d\tilde{\zeta}_\mathrm{e}}{d\tilde{t}}\right)^2 + 2(4\tilde{x}^2-8\tilde{x}-5)\frac{d\tilde{\zeta}_\mathrm{e}}{d\tilde{t}}\frac{d^2\tilde{\zeta}_\mathrm{e}}{d\tilde{t}^2}\right. \\ &\quad \left. +(\tilde{x}^2-2\tilde{x}-2)\left\{2\tilde{\zeta}_\mathrm{e}\frac{d^3\tilde{\zeta}_\mathrm{e}}{d\tilde{t}^3} + 3\tilde{r}\tilde{\zeta}_\mathrm{e}\frac{d^2\tilde{\zeta}_\mathrm{e}}{d\tilde{t}^2}\right\}\right] \,.\end{aligned} \tag{39}$$

Explicit expressions for a monochromatic tidal forcing

The scaled solution for the monochromatic forcing (1) is obtained by putting $\tilde{\zeta}_e(t) = \cos(\tilde{t})$. This gives the following expressions for the various contributions to water level and tidal velocity

$$\tilde{\zeta}_0(\tilde{x},\tilde{t}) = \cos\tilde{t}\,, \tag{40}$$

$$\tilde{\zeta}_1(\tilde{x},\tilde{t}) = 0\,, \tag{41}$$

$$\tilde{\zeta}_2(\tilde{x},\tilde{t}) = \left[\tilde{x} - \frac{\tilde{x}^2}{2}\right](\cos\tilde{t} + \tilde{r}\sin\tilde{t})\,, \tag{42}$$

$$\tilde{\zeta}_3(\tilde{x},\tilde{t}) = \left[\tilde{x} - \frac{\tilde{x}^2}{2}\right]\left[\frac{1}{2} - \frac{3}{2}\cos(2\tilde{t}) - \tilde{r}\sin(2\tilde{t})\right]\,, \tag{43}$$

$$\tilde{u}_0(\tilde{x},\tilde{t}) = -(1-\tilde{x})\sin\tilde{t}\,, \tag{44}$$

$$\tilde{u}_1(\tilde{x},\tilde{t}) = \frac{1}{2}(1-\tilde{x})\sin(2\tilde{t})\,, \tag{45}$$

$$\tilde{u}_2(\tilde{x},\tilde{t}) = -\frac{1}{12}(1-\tilde{x})\left\{2\tilde{r}[\tilde{x}^2 - 2\tilde{x} - 2]\cos\tilde{t} + [-2\tilde{x}^2 + 4\tilde{x} + 7]\sin\tilde{t} + 3\sin(3\tilde{t})\right\}\,, \tag{46}$$

$$\begin{aligned}\tilde{u}_3(\tilde{x},\tilde{t}) = \frac{1}{6}(1-\tilde{x})\Big[&-\tilde{r}(1-\tilde{x})^2 + \tilde{r}(4\tilde{x}^2 - 8\tilde{x} - 5)\cos(2\tilde{t}) + \frac{1}{2}(-10\tilde{x}^2 + 20\tilde{x} + 17)\sin(2\tilde{t}) \\ &+\frac{3}{4}\sin(4\tilde{t})\Big]\,.\end{aligned} \tag{47}$$

The dimensional forms of these formulae are obtained by "reversing" the scaling adopted in Sect. 2.2.5. To this end, $\tilde{x}$, $\tilde{t}$ and $\tilde{r}$ should be replaced by x/L, σt and $r/(\sigma H)$, respectively, while the water level and velocity should be multiplied by A and $\sigma AL/H$, respectively.

2.3 Flow in a long tidal embayment

2.3.1 Introduction

In this chapter, we consider the horizontal and vertical structures of the tidal flow in a semi-enclosed embayment of length L. Contrary to the short tidal channel tetscase, L is not small compared to the tidal wavelength. The bottom z_b is taken to be horizontal at bottom depth H, i.e. $z_b = -H$. (see Fig. 8). The boundary at $x = L$

Figure 8 – Sketch of the 2DV model domain.

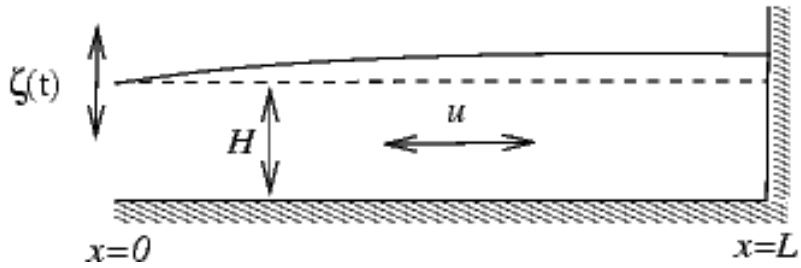

is closed. At $x = 0$, a prescribed vertical tide (water level ζ) with a single harmonic component (circular frequency σ, period $P = 2\pi/\sigma$) is imposed, i.e.

$$\zeta(x = 0, t) = A\cos(\sigma t)\ . \tag{48}$$

This external forcing drives the tidal flow inside the basin.

Claims

The purpose of this case is to investigate the following claims:

1. appropriate description of the propagation of the dominant tidal component
2. appropriate description of 2DV water motion for constant vertical viscosity
3. appropriate description of the depth averaged residual (Stokes) flow

Summary of semi-analytical results

It is assumed that the relative amplitude $\varepsilon \equiv A/H$ of the vertical tide at the entrance is small, i.e. $\varepsilon \ll 1$. The vertical coefficient of viscosity A_v is taken to be constant while the flow velocity is assumed to vanish at the true bed (located at $z = -H$).

The semi-analytical expressions for water level and water motion are expressed as a truncated series expansion in ε, e.g.

$$\zeta(x,t) = \zeta_0(x,t) + \varepsilon\zeta_1(x,t) + \dots\ ,$$

and similarly for the flow components u and w. For this test case, only the leading order (i.e. zeroth) order solution has been considered up to now. The solution for the flow variables thus obtained reads

$$\zeta(x,t) = A\,\mathscr{R}\left[\frac{\cosh[\mu(L-x)]}{\cosh(\mu L)}\ \exp(i\sigma t)\right]\ , \tag{49}$$

$$u(x,z,t) = \varepsilon\sqrt{gH}\,\mathscr{R}\left[-i\mu L\frac{\sinh[\mu(L-x)]}{\cosh(\mu L)}\ \left\{1 - \frac{\cosh(\lambda z)}{\cosh(\lambda H)}\right\}\ \exp(i\sigma t)\right]\ , \tag{50}$$

$$w(x,z,t) = 0\ . \tag{51}$$

Here $\mathscr{R}$ denotes the real part of a complex expression. Furthermore, the complex parameters λ and μ are defined as follows:

$$\lambda = (1+i)\sqrt{\frac{\sigma}{2A_{\mathrm{v}}}}\,,$$

$$\mu = \frac{i}{L}\sqrt{\frac{\lambda H\cosh(\lambda H)}{\lambda H\cosh(\lambda H)-\sinh(\lambda H)}}\,.$$

respectively. The leading order depth averaged along-channel flow $\overline{u}$ is given by

$$\overline{u}(x,t) = \varepsilon\sqrt{gH}\,\mathscr{R}\left[-i\mu L\frac{\sinh[\mu(L-x)]}{\cosh(\mu L)}\left\{1-\frac{1}{\lambda H}\frac{\sinh(\lambda H)}{\cosh(\lambda H)}\right\}\exp(i\sigma t)\right]\,, \tag{52}$$

and this result will be used for validation purposes as well.
While higher order contributions the tidal flow have so far not been incorporated, depth averaged mass balance readily gives the residual depth averaged velocity $\left\langle\overline{u}(x)\right\rangle$ which is given by

$$\begin{aligned}\left\langle\overline{u}(x)\right\rangle &= -\frac{1}{H}\left\langle\zeta\overline{u}\right\rangle\\ &= \frac{\varepsilon^2}{2}\sqrt{gH}\mathscr{R}\left[-i\mu L\frac{\cosh[\mu^\star(L-x)]\sinh[\mu(L-x)]}{\|\cosh(\mu L)\|^2}\left\{1-\frac{1}{\lambda H}\frac{\sinh(\lambda z)}{\cosh(\lambda H)}\right\}\right]\,,\end{aligned} \tag{53}$$

where * denotes complex conjugation. The residual depth averaged flow will also be used to validate the COHERENS model results.

Contributions of tidal components

For validation, only the zeroth order solution for water level and tidal flow have been obtained explicitly. However, the structure of the $O(\varepsilon)$ model equations (which have not been solved) reveal that the $O(\varepsilon)$ solution contains only the residual S_0 and S_4 harmonic component. Hence the occurence of tidal components can ba summarised as in Table 3.

Table 3 – Contribution of harmonic components to the solution at various orders: p = contributes, × = does not contribute.

	$O(1)$	$O(\varepsilon)$
S_0 (tidal average)	×	p
S_2	p	×
S_4	×	p

Accuracy

The information in Table 3 can be used to put a stricter limit on the expected accuracy of the diurnal and residual components as predicted by the depth averaged of the zeroth order S_2 approximation. Explicitly, S_2 only occurs at $O(1)$, not at $O(\varepsilon)$ and presumably again at $O(\varepsilon^2)$. This implies that the expected relative accuracy of the S_2 solution as given by Eqs. (49)-(51) and (52) is in fact $O(\varepsilon^2)$.
Similarly, the residual depth averaged velocity $\left\langle\overline{u}\right\rangle$ is obtained from the depth avreraged continuity equation as

$$\begin{aligned}\left\langle\overline{u}\right\rangle &= -\frac{1}{H}\left\langle\zeta_0+\varepsilon\zeta_1)(\overline{u}_0+\varepsilon\overline{u}_1)\right\rangle+\ldots\\ &= -\frac{1}{H}[\left\langle\zeta_0\overline{u}_0\right\rangle+\varepsilon\left\langle\zeta_0\overline{u}_1+\zeta_1\overline{u}_0\right\rangle]+\ldots\,.\end{aligned}$$

The term $\sim \left\langle \zeta_0 \overline{u}_0 \right\rangle$ gives solution (53), but the next contribution vanishes since $O(1)$ and $O(\varepsilon)$ contributions have no harmonic frequency in common. Hence we expect the next contribution to $\left\langle \overline{u} \right\rangle$ at $O(\varepsilon^2)$. Thus we expect the relative accuracy of expression (53) to be $O(\varepsilon^2)$ as well.
Regarding *temporal* behaviour, on the other hand, the difference between the zeroth order solution and the full solution does contain the residual and S_4 constituent. As a result, the expected relative accuracy of (49)-(51), (52) is then $O(\varepsilon)$.

2.3.2 Model setup

No slip boundary condition

The testcase is compared with a semi-analytical solution that assumes the velocity to vanish at the true bed (no slip condition), i.e.

$$u(z = -H) = 0 \,. \tag{54}$$

However, the near-bed boundary condition in COHERENS is formulated as a flux condition at the lowest velocity point (situated at $z = z_1$). For linear bottom friction this expression reads

$$A_{\mathrm{v}} \left.\frac{\partial u}{\partial z}\right|_{\mathrm{z=z_1}} = r u(z = z_1) \,. \tag{55}$$

The no slip condition can be reformulated in terms of a flux by an appropriate choice of the linear bottom friction parameter r, as will now be explained. First, we define $\Delta z = z_1 + H$ as the heigth of the near-bed velocity point above the bottom. Next, one can rewrite (54) as follows

$$u(-H) = 0 = u(z_1 - \Delta z) \approx u(z_1) - \Delta z \left.\frac{\partial u}{\partial z}\right|_{\mathrm{z=z_1}} + \dots \,,$$

where the last step follows from a first order Taylor expansion around $z = z_1$. Neglecting higher order contributions to this expansion we thus find that

$$\left.\frac{\partial u}{\partial z}\right|_{\mathrm{z=z_1}} = \frac{1}{\Delta z} u(z_1) \,.$$

This is a flux condition at level $z = z_1$, which is identical to (55) provided that

$$r = \frac{A_{\mathrm{v}}}{\Delta z} \,. \tag{56}$$

Note that this method for implementing a no slip condition in COHERENS only works if the near bed boundary condition adopts a linear bottom friction (i.e. shear stress scaling linearly with the velocity). Also expression (56) gives an estimate for the bottom friction parameter by using a first order Taylor approximation to the near bed flow. As a result, it is not accurate for logarithmic flow profiles so that this method works best for constant vertical viscosity A_{v}. Finally, time and space dependence in Δz (due to water level variations) is ignored: Δz will be solely related to the mean bottom depth H.
Whether the no slip condition is reproduced adequately by adopting (56) has to be checked a posteriori for each new choice of model parameters.

Geometry and parameter settings

The long tidal channel testcase has been used to validate the COHERENS model for 2DV dimensional tidal propagation. To this end, the model domain was represented by a grid with $nc = 101$ points and ten equidistant

computational layers ($nz = 10$). The bottom depth H was taken equal to 10 m, while the amplitude of the vertical tide A was one meter, giving $\varepsilon = 0.1$. The coefficient of vertical viscosity A_v is taken sufficiently high ($A_\mathrm{v} = 0.01\ \mathrm{m}^2\ s^{-1}$) so that the vertical variation of the tidal flow could be described accurately by the adopted vertical grid. For consistency with the no slip boundary condition $r = 0.02\ \mathrm{m\ s}^{-1}$ was adopted (see Sect. 2.3.2). A full list of model parameter settings is found in Table 4.

Table 4 – Model parameters as adopted for the validation run.

Symbol	Meaning	Value
L	Channel length	100 km
H	Bottom depth	10 m
σ	S_2 circular frequency	$1.45 \times 10^{-4}\ \mathrm{rad\ s}^{-1}$
A	Water level forcing	1 m
A_v	Vertcal coefficient of viscosity	$0.01\ \mathrm{m\ s}^{-1}$
r	Linear friction coefficient	$0.02\ \mathrm{m\ s}^{-1}$
ε	Relative amplitude of vertical tide (A/H)	0.1
nc	Number of grid points (along-channel)	101
nr	Number of grid points (cross-channel)	2
nz	Number of computational layers	10
Δt	Time step	30 s
Δz	Height of near-bed velocity point	0.5 m

Note that the model is forced with a diurnal solar component (S_2) rather than the semi-diurnal lunar tide (M_2). This choice is made because the diurnal tide has an exact twelve hour period that is more convenient for an accurate harmonic analysis of the results.

Validity of the no slip boundary condition

As discussed in sect. 62 the validity of the no slip condition has to be verified a posteriori. To this end, the following approach was adopted. First for every horizontal location x, velocity profiles were extrapolated to the true bed. From these extrapolated values the maximum absolute value over a tidal period ($u_{\mathrm{max,b}}(x)$) was determined. Next, $u_{\mathrm{max,b}}(x)$ was scaled with the local value of the S_2 amplitude of the depth averaged velocity $\overline{u}(x)$. The result is shown in Fig. 9. We see that the magnitude of $u_{\mathrm{max,b}}(x)$ is ~ 0.01 relative to the depth averaged S_2 flow. Since $\varepsilon = 0.1$ we conclude that the velocity at the bed is $O(\varepsilon^2)$ so that the no slip condition is valid if we compare COHERENS results with $O(1)$ or $O(\varepsilon)$ analytical approximations. For the present validation, this is sufficient.

Method of comparison

The S_2 water level and the S_2 and residual depth averaged velocity as obtained from COHERENS are compared with analytical approximations (49), (52) and (53), respectively. For this comparison, we use the following the relative root mean square (rms) difference method.
Let $\mathscr{A}_1(x)$ and $\varphi_1(x)$ denote amplitude and phase of a harmonic component of a quantity Q as computed by COHERENS. Let $\mathscr{A}_2(x)$ and φ_2 denote amplitude and phase according to the semi-analytical results. We then

Figure 9 – Relative magnitude of the maximum horizontal velocity at the bed, scaled with the local amplitude of the S_2 depth averaged velocity.

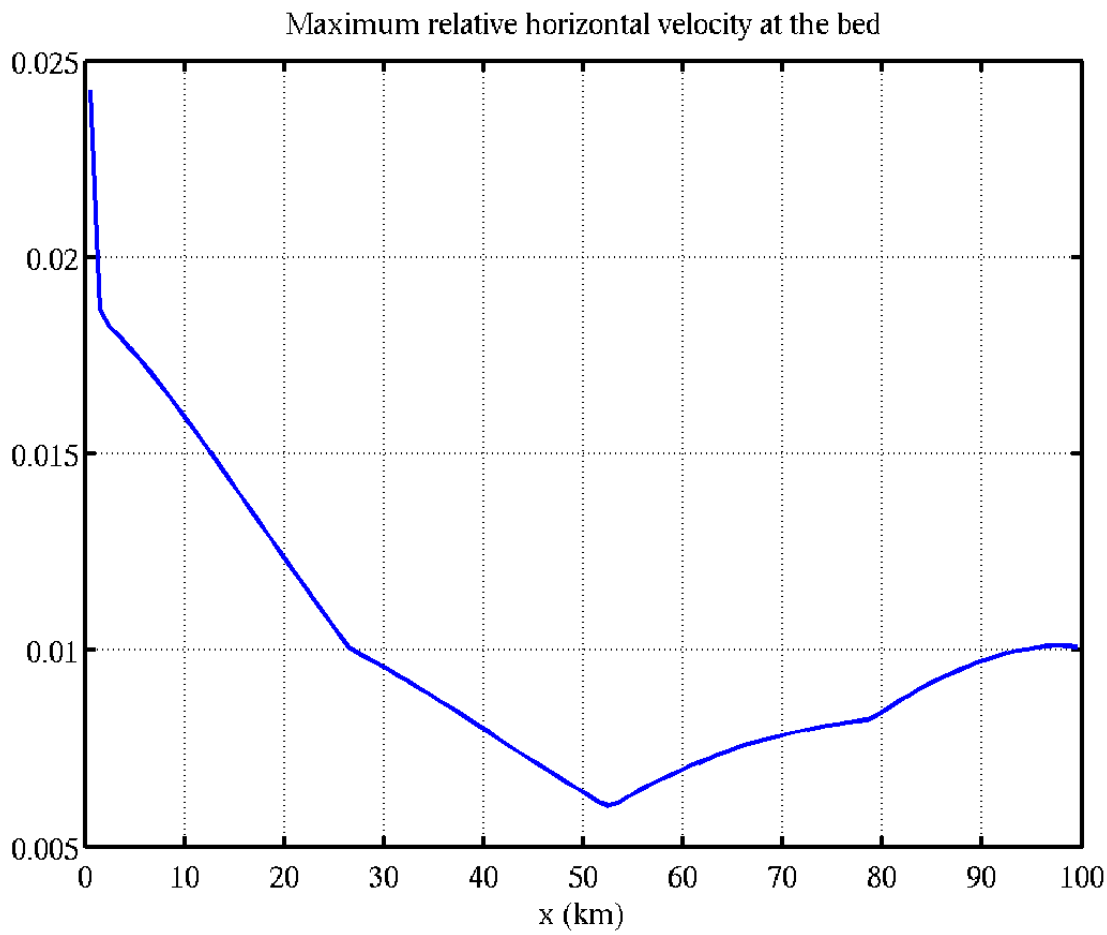

define the absolute rms difference $\Delta^{Q}_{\text{abs}}(x)$ between numerical and semi-analytical model as

$$\Delta^{Q}_{\text{abs}}(x) = \sqrt{\frac{1}{P}\int_0^{\text{P}} \{\mathscr{A}_1(x)\cos[\omega t - \varphi_1(x)] - \mathscr{A}_2(x)\cos[\omega t - \varphi_2(x)]\}^2\, dt}$$
$$= \sqrt{\frac{[\mathscr{A}_1(x) - \mathscr{A}_2(x)]^2}{2} + \mathscr{A}_1(x)\mathscr{A}_2(x)\cos[\varphi_1(x) - \varphi_2(x)]}\,, \tag{57}$$

where P denotes the S_2 tidal period. Note that $\Delta^{Q}_{\text{abs}}(x)$ depends on location. If amplitudes and phases coincide perfectly (i.e. $\mathscr{A}_1(x) = \mathscr{A}_2(x)$ and $\varphi_1(x) = \varphi_2(x)$, then we have $\Delta^{Q}_{\text{abs}}(x) = 0$ by definition. From this absolute rms difference we define a relative error for water level and velocity by dividing $\Delta^{Q}_{\text{abs}}(x)$ by A and $\varepsilon\sqrt{gH}$, respectively.
Since the semi-analytical expressions (2) and (4) include terms up to $O(\varepsilon^3)$, we expect the relative deviations $\Delta^{\zeta}_{\text{rel}}$ and Δ^{u}_{rel} to be $O(\varepsilon^4) \sim 10^{-4}$ or less. This gives a direct way to judge the quality of tidal components that are computed with COHERENS.

Regarding the vertical variation of tidal flow velocity, the comparison between COHERENS and semi-analytical results is done in two ways. First, a comparison between the computed velocity profile $u(x, z, t)$ and the corresponding analytical approximation is shown graphically for several locations and times. Second, the relative difference is quantified in an rms way similar to (57), except that now also integration over depth is applied.

2.3.3 Results

Diurnal (S_2) water level and depth averaged velocity

A comparison between the S_2 contribution to water level and the analytical approximation is displayed in Fig. 10. Figure 11 shows the comparison between COHERENS and the semi-analytical solution for the S_2 component of the depth averaged velocity. For both water level and velocity we find a maximum relative difference $\sim O(\epsilon^2) = 0.01$ or even less, which agrees with the expected accuracy anticipated in Sect. 2.3.1. From this we conclude that COHERENS gives an adequate description of the diurnal depth averaged tidal dynamics.

Figure 10 – Comparison between the computed S_2 water level and semi-analytical result (49).

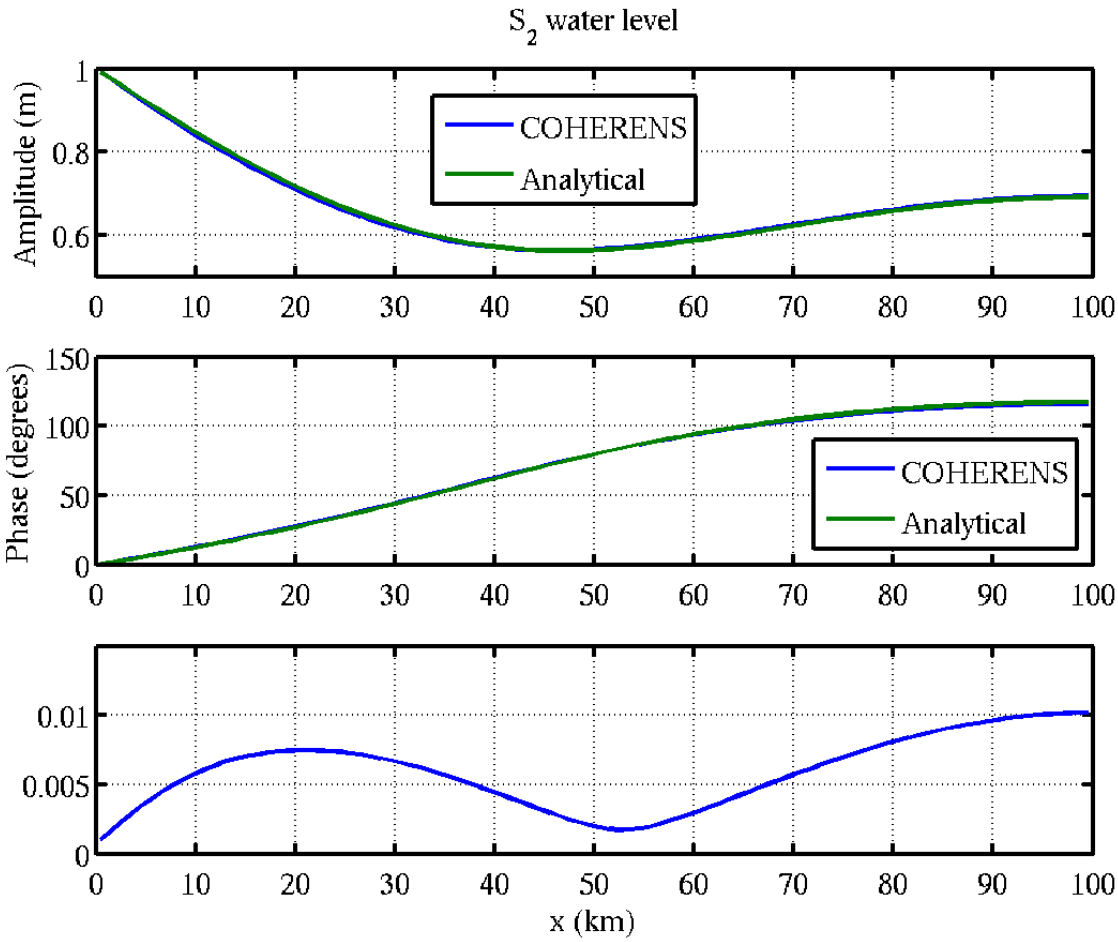

The bottom panel shows the relative rms deviation.

Figure 11 – Comparison between the computed S_2 depth averaged velocity and semi-analytical result (52).

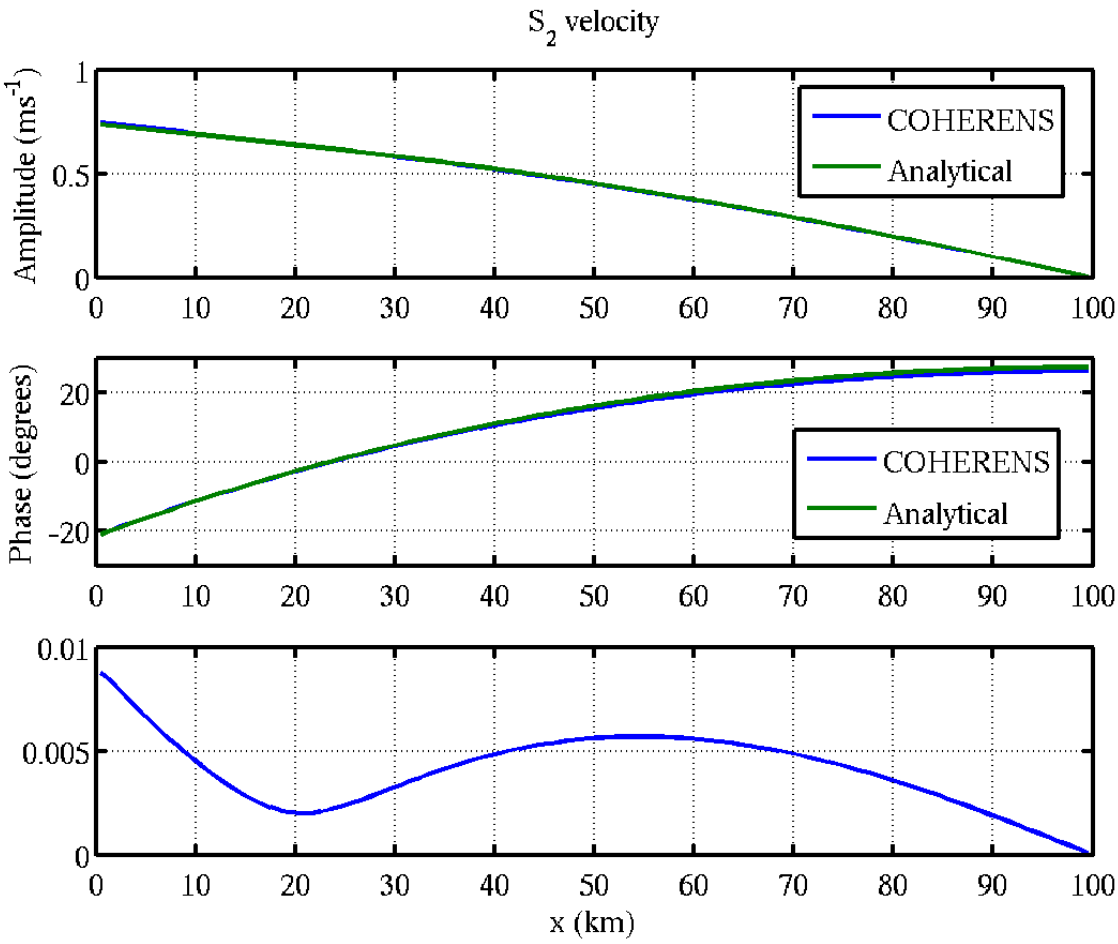

The bottom panel shows the relative rms deviation.

Residual (S_0) depth averaged flow

Figure 12 shows the comparison between COHERENS and the semi-analytical solution for the residual component of the depth averaged velocity. The bottom figure shows the relative rms deviation, but this relative

Figure 12 – Comparison between the computed residual depth averaged velocity and semi-analytical result (53).

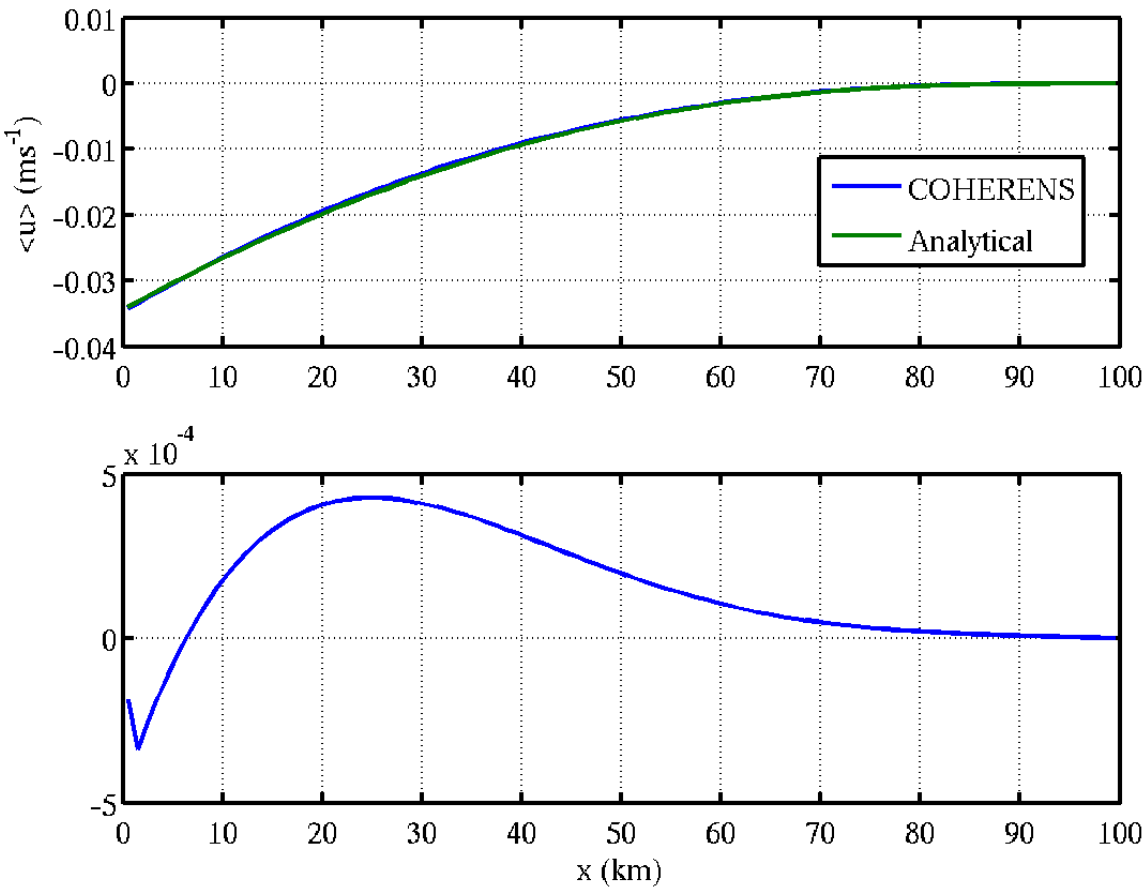

The bottom panel shows the relative rms deviation.

to the zeroth order flow which is $\sim O(1\ \mathrm{m\ s^{-1}})$ so the absolute error in $\langle \overline{u} \rangle$ is $\sim 1 - 5 \times 10^{-4}\ \mathrm{m\ s^{-1}}$), which in turn is $\sim 0.01 = O(\varepsilon^2)$ relative to typical value of $\langle \overline{u} \rangle$ ($\sim 0.01 - 0.03\ \mathrm{m\ s^{-1}}$), see top panel). We thus find that COHERENS computes the residual depth averaged flow to expected accuracy.

Comparison of temporal behaviour

Figure 13 shows a comparison of vertical profiles of the horizontal velocity at a location near the entrance, near the center of the basin and near the wall. These profiles are show at moments that coincide with high water, mid tide and low water at the entrance. The qualitative agreement between the COHERENS model and semi-analytical approximation (50) appears to be reasonable although no conclusion about quantitative agreement can be infered from these plots.

Figure 13 – Comparison of velocity profiles at three different times at $x = 10.5$ km (top row), $x = 50.5$ km (middle row) and $x = 90.5$ km (bottom row).

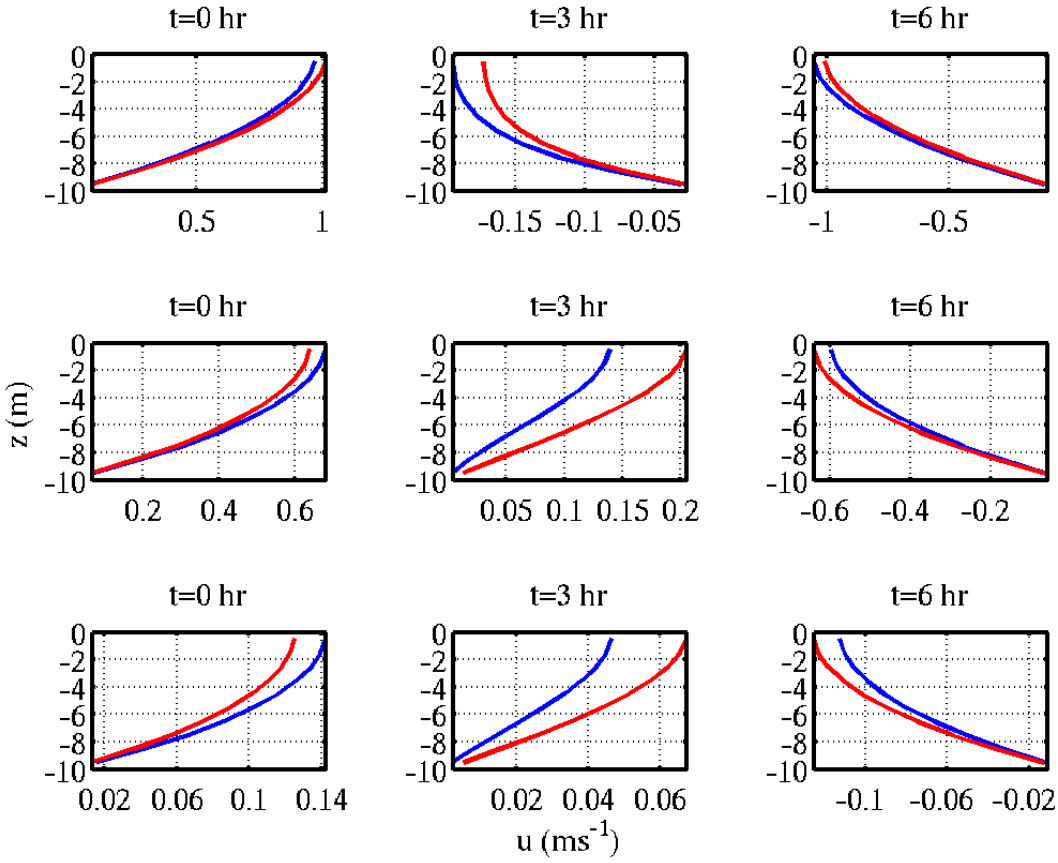

Time is relative to high water at the entrance. Blue profiles correspond to COHERENS, red to approximation (50).

Figure 14 shows the relative rms difference between the COHERENS profiles and semi-analytical approximation as function of location throughout the embayment. We find a relative deviation $\sim 0.1 - 0.2$ which is on the order of $\varepsilon = 0.1$, which is the expected accuracy of approximation (50). From this we conclude that the 2DV structure of tidal flow is computed adequately by COHERENS.

Figure 14 – Relative rms deviation between the computed COHERENS velocity profiles and their semi-analytical approximation.

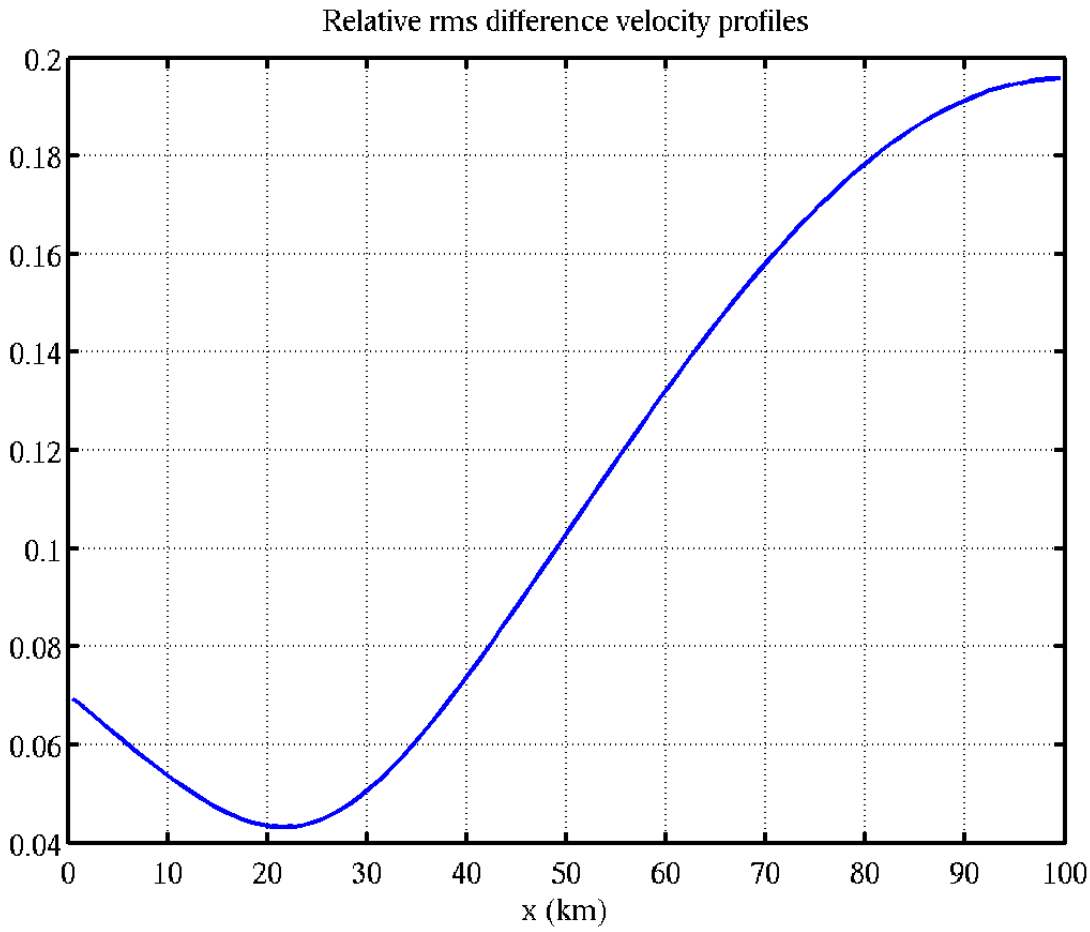

2.3.4 Conclusions

1. COHERENS gives an accurate description of the main tidal water motion and the residual Stokes return flow in a long tidal channel of finite length.
2. COHERENS is able to compute the vertical variation of the tidal flow accurately for the case of linear bottom friction.

2.3.5 Derivation of the semi-analytical solution

Dimensional model equations

The full set of model equations are given by the 2DV shallow water equations for water motion which read

$$\frac{\partial u}{\partial t} + u\frac{\partial u}{\partial x} + w\frac{\partial u}{\partial z} = -g\frac{\partial \zeta}{\partial x} + \frac{\partial}{\partial z}\left(A_{\mathrm{v}}\frac{\partial u}{\partial z}\right) , \tag{58}$$

$$\frac{\partial u}{\partial x} + \frac{\partial w}{\partial z} = 0 , \tag{59}$$

respectively. Hereafter, the vertical coefficient of viscosity A_{v} is assumed to be constant.
The hydrodynamics inside the basin is forced externally by a prescribed S_2 water level at the seaward side ($x = 0$), i.e.

$$\zeta(x = 0, t) = A\cos(\sigma t) , \tag{60}$$

where A and σ denote the amplitude and the circular frequency of the vertical S_2 tide, respectively. The boundary condition at the landward side ($x = L$) is given by impermeability of the solid wall, i.e.

$$u(x = L, t) = 0 . \tag{61}$$

At the bed ($z = -H$) a no slip condition is imposed so that

$$u(z = -H) = w(z = -H) = 0, \tag{62}$$

while at the surface ($z = \zeta$) a free slip condition is used in conjunction with the kinematic requirement that a water parcel at the surface will remain there for all time. These conditions are expressed by the relations

$$A_{\mathrm{v}}\frac{\partial u}{\partial z}\bigg|_{z=\zeta} = 0 , \tag{63}$$

$$w(z = \zeta) = \frac{\partial \zeta}{\partial t} + u(z = \zeta)\frac{\partial \zeta}{\partial x} , \tag{64}$$

respectively.

Scaled model equations

The full set of model equations (58)–(64) can be reduced by adopting the following scaling for the model variables:

$$x = \tilde{x}/k \ , \ t = \tilde{t}/\sigma \ , \ \zeta = A\tilde{\zeta} \ , \ z = H\tilde{z} \ , \ u = \varepsilon\sqrt{gH}\tilde{u} \ , A_{\mathrm{v}} = \sigma H^2\tilde{A}_{\mathrm{v}}, \tag{65}$$

where variables with a tilde (~) denote scaled variables. The quantity $k = \sigma/\sqrt{gH}$ denotes the wave number of the tide while $\varepsilon = A/H$ is a measure of the relative magnitude of the vertical tide. Inserting the scaling into

Eqs. (58) and (59) gives the following scaled form for the momentum and mass conservation equations:

$$\frac{\partial u}{\partial t} + \varepsilon \left[u\frac{\partial u}{\partial x} + w\frac{\partial u}{\partial z} \right] = -\frac{\partial \zeta}{\partial x} + \frac{\partial}{\partial z}\left(A_{\mathrm{v}} \frac{\partial u}{\partial z} \right) , \tag{66}$$

$$\frac{\partial u}{\partial x} + \frac{\partial w}{\partial z} = 0 . \tag{67}$$

The scaled form of the boundary conditions (60)-(64) read

$$\zeta(x = 0, t) = \cos t , \tag{68}$$

$$u(x = L, t) = 0 , \tag{69}$$

$$u(z = -1) = w(z =_1) = 0, \tag{70}$$

$$A_{\mathrm{v}} \frac{\partial u}{\partial z}\bigg|_{z=\varepsilon\zeta} = 0 , \tag{71}$$

$$w(z = \varepsilon\zeta) = \frac{\partial \zeta}{\partial t} + \varepsilon u(z = \varepsilon\zeta)\frac{\partial \zeta}{\partial x} , \tag{72}$$

We will assume that the amplitude of the vertical tide is small in the sense that $\varepsilon \ll 1$. This is a common situation for tidal wave propagation in deep channels. Because $\varepsilon \ll 1$ the solution for the flow variables $\{\zeta, u, w\}$ can be expanded as a series, i.e.

$$\zeta(x, t) = \zeta_0(x, t) + \varepsilon\zeta_1(x, t) + \varepsilon^2\zeta_2(x, t) + \ldots$$

and similarly for u and w. Upon inserting these expansions in the model equations and equating terms of equal order in ε one obtains a hierarchy of equations from which zeroth and higher order contributions to the series solution can be obtained successively.

$O(1)$ solution

The equation for flow and sediment at zeroth order are given by

$$\frac{\partial u_0}{\partial t} = -\frac{\partial \zeta_0}{\partial x} + \frac{\partial}{\partial z}\left(A_{\mathrm{v}} \frac{\partial u_0}{\partial z} \right) , \tag{73}$$

$$\frac{\partial u_0}{\partial x} + \frac{\partial w_0}{\partial z} = 0 . \tag{74}$$

while the boundary conditions read

$$\zeta_0(x = 0, t) = \cos(t) = \mathscr{R}[\exp(it)] , \tag{75}$$

$$u_0(x = L, t) = 0 , \tag{76}$$

$$w_0(z = -1) = 0 , \tag{77}$$

$$A_{\mathrm{v}} \frac{\partial u_0}{\partial z}\bigg|_{z=0} = 0 , \tag{78}$$

$$w_0(z = 0) = \frac{\partial \zeta_0}{\partial t} . \tag{79}$$

The solution to these equations is given by

$$\zeta_0(x, t) = \mathscr{R}\left[\frac{\cosh[\mu(L - x)]}{\cosh(\mu L)} \exp(it) \right] , \tag{80}$$

$$u_0(x, z, t) = \mathscr{R}\left[-i\mu L \frac{\sinh[\mu(L - x)]}{\cosh(\mu L)} \left\{ 1 - \frac{\cosh(\lambda z)}{\cosh(\lambda)} \right\} \exp(it) \right] , \tag{81}$$

$$w_0(x, z, t) = 0 . \tag{82}$$

2.4 Wind generated 2DH flow in a closed basin

2.4.1 Introduction

In this chapter we investigate the stationary flow that occurs when a stationary uniform wind is blowing over a closed basin with curved boundaries and a non-horizontal bottom. This testcase can be used to validate wind driven horizontal circulation as well as the curvilinear grid functionality in COHERENS.

Claims

The purpose of this case is to investigate the following claims:

1. accurate description of wind driven flow
2. the ability to predict accurate results when using orthogonal curvilinear grids

Testcase description

The explicit situation that is considered is shown in panel (a) of Fig. 15. A uniform wind is blowing along the positive x-axis over a domain that is enclosed between two concentric semi-circles of radii R_1 and $R_2 > R_1$, respectively. The region is bounded by solid vertical walls.
The bathymetry $H(R)$ inside the domain varies radially according to a power law, i.e.

$$H(R) = H_2 \left(\frac{R}{R_2} \right)^{\mathrm{p}} , \tag{83}$$

where H_2 is the bottom depth at $R = R_2$. The parameter p will hereafter be referred to as the (bottom) steepness parameter.
The wind stress will generate a torque on the water mass inside the domain because the bottom depth gradi-

Figure 15 – Panel (a): problem sketch, panel (b): indicative representation of flow direction for a radially increasing bottom depth.

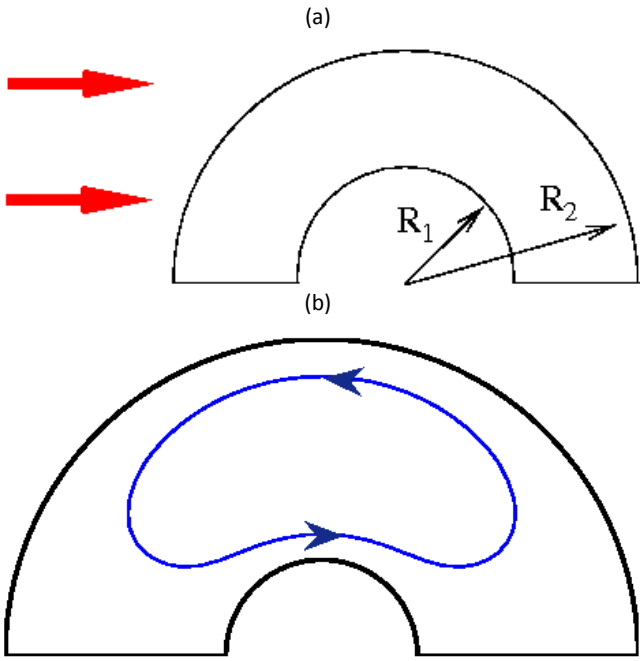

ent has a component perpendicular to the direction of the wind. This will give rise to a single, stationary cell with anti-clockwise circulation for radially increasing bottom depth ($p > 0$, Fig. 15, panel (b)). For a radially decreasing bottom depth ($p < 0$), a clockwise rotation will ensue.
For completeness, we mention that the situation as depicted in Fig. 15 can be extended to consider the wind driven flow within two full circles (i.e. spanning a full azimuthal revolution). The flow solution for this problem is obtained by taking the solutions presented in Sect. 2.4.1 and reflection thereoff with respect to the x axis.

Summary of semi-analytical expressions

In deriving a semi-analytical expression for water level and fluid flow, several assumptions have been made. It has been assumed that the depth to size ratio $\varepsilon \equiv \hat{H}/R_2$ is small ($\varepsilon \ll 1$). This is not really a constraint since it is merely a restatement of the shallow water approximation.
Next, the magnitude of the dynamic wind shear stress τ_{w} is chosen such that

$$u_{\star\mathrm{w}} = \frac{\tau_{\mathrm{w}}}{\rho} = \varepsilon^2 g \hat{H} \ .$$

where $u_{\star\mathrm{w}}$ is the friction velocity associated with the wind stress exerted on the water surface. This assumption is required keep the water level variation small compared to the bottom depth.
Two further assumptions are made for mathematical simplicity. First, a linear law for bottom friction τ is adopted, i.e.

$$\tau = r\mathrm{u} \ ,$$

where the linear friction coefficient r is chosen such that $r \approx \varepsilon u_{\star\mathrm{w}} \hat{H}$, which gives realistic numerical values ($r \sim 0.0001 - 0.01\ \mathrm{m\,s^{-1}}$). Finally, advection of momentum was neglected a priori (in COHERENS this is done by setting the switch iopt_adv_2D zero). Neither of these two simplifications are essential for the current testcase.

For this stationary testcase problem, semi-analytical solutions for water level and transport (i.e. vertically integrated) velocity can be obtained as expansion series in ε, i.e.

$$\zeta(R,\theta) = \zeta_0(R,\theta) + \varepsilon\zeta_1(R,\theta) + \dots \ ,$$

and similarly for the radial and azimuthal component of transport velocity (U_{R} and U_θ, respectively). For validation, only the leading order contributions (e.g. ζ_0) have been used.
The approximate variation of the water level $\zeta(R,\theta)$ thus obtained is given by

$$\zeta(R,\theta) = \frac{\varepsilon\hat{H}}{p}\left[\frac{1}{n_-}\frac{R_1^{\mathrm{p}+1} - R_1^{\mathrm{n}_-}}{R_1^{\mathrm{n}_-} - R_1^{\mathrm{n}_+}}\left(\frac{R}{R_2}\right)^{-\mathrm{n}_-} + \frac{1}{n_+}\frac{R_1^{\mathrm{n}_+} - R_1^{\mathrm{p}+1}}{R_1^{\mathrm{n}_-} - R_1^{\mathrm{n}_+}}\left(\frac{R}{R_2}\right)^{-\mathrm{n}_+} - \left(\frac{R}{R_2}\right)^{1-\mathrm{p}}\right]\cos\theta \ . \tag{84}$$

where $n_\pm = -p \pm \sqrt{p^2+1}$. The water motion is described by the so-called transport (i.e. depth integrated) velocity of which the radial and azimuthal components are approximately given by

$$U_{\mathrm{R}}(R,\theta) = \frac{u_{\star\mathrm{w}}^2\hat{H}}{pr}\left[\frac{R_1^{\mathrm{p}+1} - R_1^{\mathrm{n}_-}}{R_1^{\mathrm{n}_-} - R_1^{\mathrm{n}_+}}\left(\frac{R}{R_2}\right)^{\mathrm{n}_+} + \frac{R_1^{\mathrm{n}_+} - R_1^{\mathrm{p}+1}}{R_1^{\mathrm{n}_-} - R_1^{\mathrm{n}_+}}\left(\frac{R}{R_2}\right)^{\mathrm{n}_-} + \left(\frac{R}{R_2}\right)^{\mathrm{p}+1}\right]\cos\theta \ , \tag{85}$$

$$U_\theta(R,\theta) = -\frac{u_{\star\mathrm{w}}^2\hat{H}}{pr}\left[n_+\frac{R_1^{\mathrm{p}+1} - R_1^{\mathrm{n}_-}}{R_1^{\mathrm{n}_-} - R_1^{\mathrm{n}_+}}\left(\frac{R}{R_2}\right)^{\mathrm{n}_+-1} + n_-\frac{R_1^{\mathrm{n}_+} - R_1^{\mathrm{p}+1}}{R_1^{\mathrm{n}_-} - R_1^{\mathrm{n}_+}}\left(\frac{R}{R_2}\right)^{\mathrm{n}_--1} + \right.$$
$$\left. +(p+1)\left(\frac{R}{R_2}\right)^{\mathrm{p}}\right]\sin\theta \ , \tag{86}$$

respectively.
Since the above expressions only include the lowest order contribution, the expected relative error of the above expressions is $O(\varepsilon)$.

2.4.2 Model setup

The semi-analytical expression (84)-(86) have been used to validate the COHERENS model. To this end, the domain depicted in Fig. 83 was used with $R_2 = 1$ km and $R_2 = 300$ m. The bottom depth $\hat{H}$ at the outer boundary was equal to 10 m., so that $\varepsilon = 0.01$. Two bottom steepness parameter values were considered: $p = 0.25$, which represents a modest bottom variation and $p = 2$ which is fairly steep for typical coastal environments. Note that both these cases correspond to radially increasing bottom depth and will give a counter-clockwise rotating gyre. A wind shear stress with friction velocity $u_{\star \mathrm{w}} = \epsilon\sqrt{g\hat{H}} \approx 9.9\ \mathrm{cm\ s^{-1}}$ was imposed.
The grid was constructed by using polar coordinates and consisted of nearly square grid cells. The number of grid points in the radial and azimuthal direction were $nc = 20$ and $nr = 51$, respectively. Since polar coordinates are orthogonal, COHERENS should be able to compute the wind driven flow accurately. The adopted grid is displayed in Fig. 16.

Figure 16 – Adopted curvilinear grid.

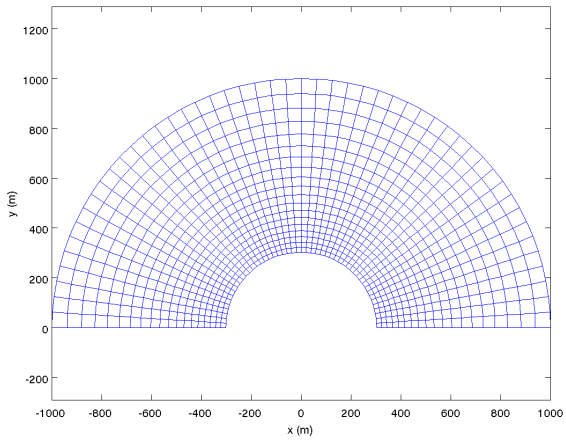

The time step was taken to be 0.8 s., which is slightly below the Courant limit. The model parameter settings are summerised in Table 5.
Starting from an initial condition with horizontal water level and with fluid at rest (i.e. $\zeta = 0$ and $\mathrm{U} = 0$) a five day period was simulated. After this period, the model had settled to a stationary state that could be compared to the semi-analytical solution.

Table 5 – Model parameter settings used for the COHERENS validation runs.

R_1	radius of outer ring	1000 m
R_2	radius of inner ring	300 m
H_2	bottom depth at $R = R_2$	10 m.
ε	depth to size ratio: $\varepsilon = \hat{H}/R_1$	0.01
r	coefficient of linear friction	$0.001\ \mathrm{m\ s^{-1}}$
nc	Number of grid points (radial)	20
nr	Number of grid points (azimuthal)	51
Δt	time step	0.8 s
p	bottom steepness parameter	$p = 0.25$ (modest) or $p = 2$ (steep)
iopt_adv_2D	advection switch	0 (i.e no advection of momentum)

Method of comparison

The quality of the results as computed by COHERENS is judged by comparison by the semi-analytical approximations (84)-(86). Since these approximations have a relative accuracy of $\sim \varepsilon = 0.01$, we define the results of COHERENS to be acceptable if their relative deviation from the semi-analytical result is a few percent or less.

2.4.3 Results

Modest bottom steepness ($p = 0.25$)

Figure 17 shows the water level as obtained from COHERENS and the semi-analytical expression (84). Typical values of water level are ~ 0.1m, while the difference between COHERENS result and semi-analytical approximation is $\sim 5 \times 10^{-4}$. Hence the relative deviation ($\sim 5 \times 10^{-3}$) is less than $\varepsilon = 0.01$, which implies that the COHERENS result and expression (84) agree within the expected accuracy. We thus conclude that the water level is well reproduced by COHERENS.

Figure 17 – Water level as computed by COHERENS (top panel) and the semi-analytical model (middle panel) for modest bottom steepness ($p = 0.25$).

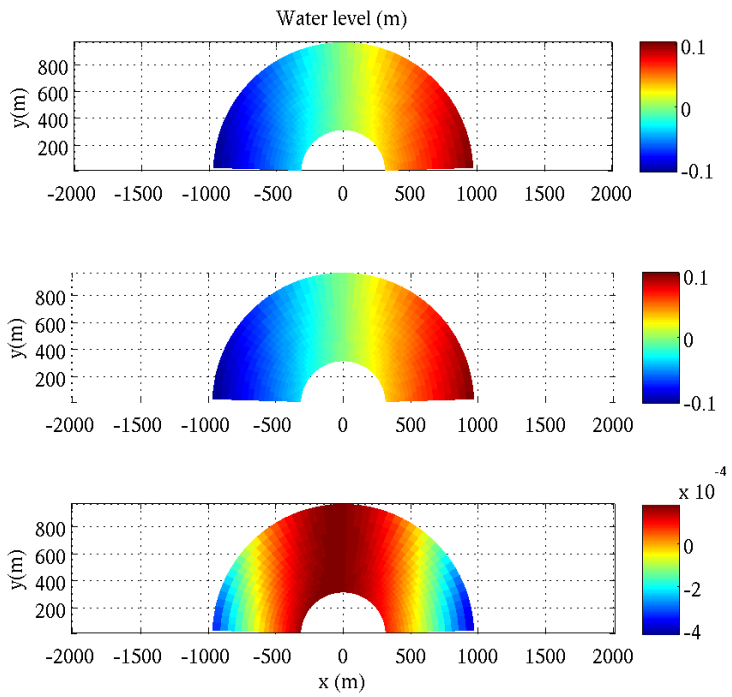

The bottom panel shows the absolute difference.

Similar to Fig. 17, Figs. 18 and 19 give a comparison for the radial and azimuthal components of transport velocity, respectively. The radial transport velocity is typically $\sim 2\ \mathrm{m^2\,s^{-1}}$ while the differences between numerical and semi-analytical results are typically $0.01\ \mathrm{m^2\,s^{-1}}$. For the azimuthal component U_θ one finds $U_\theta \sim 5 - 10\ \mathrm{m\,s^{-1}}$ while deviations are again $\sim 0.01\ \mathrm{m^2\,s^{-1}}$. For both components, we thus find that the difference between COHERENS and expressions is comparable to $\varepsilon = 0.01$ or less. From this, we conclude that COHERENS gives an accurate description of the transport velocity.

Figure 18 – Radial component of transport velocity as computed by COHERENS (top panel) and the semi-analytical model (middle panel) for modest bottom steepness ($p = 0.25$).

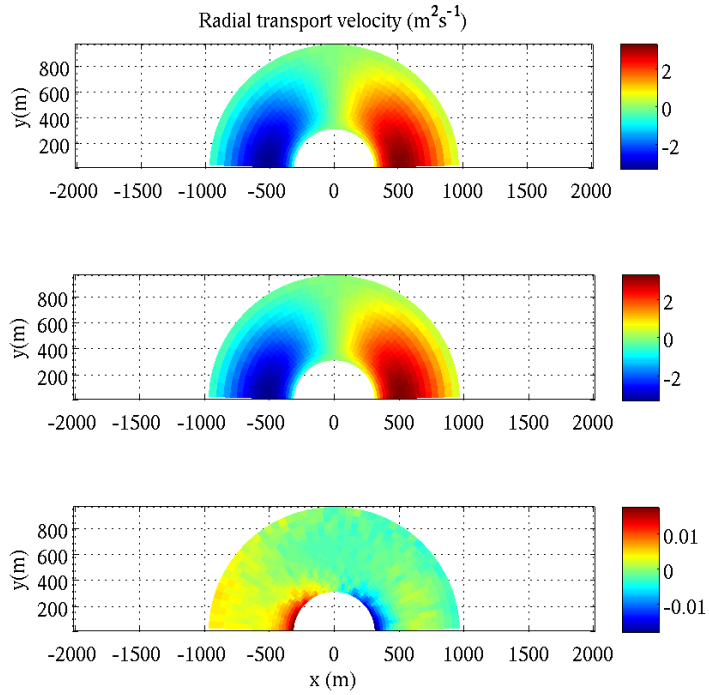

The bottom panel shows the absolute difference.

Figure 19 – Azimuthal component of transport velocity as computed by COHERENS (top panel) and the semi-analytical model (middle panel) for modest bottom steepness ($p = 0.25$).

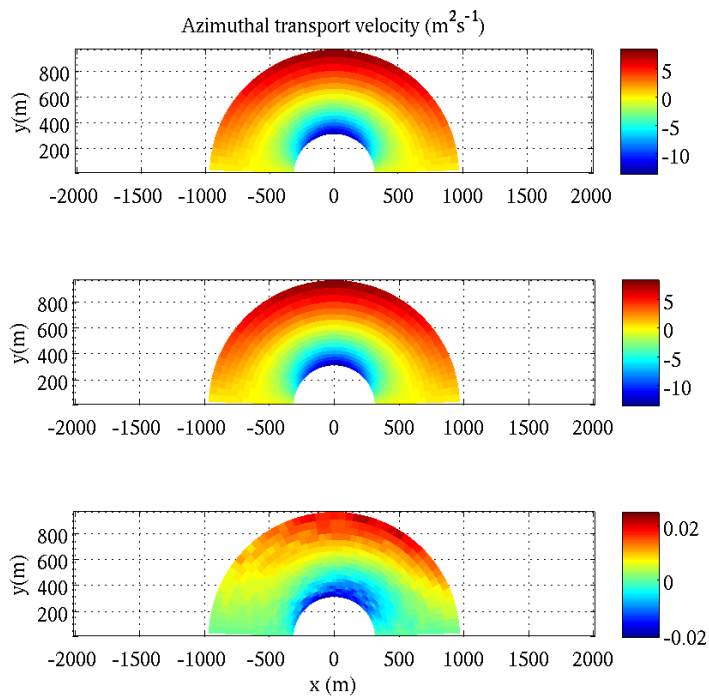

The bottom panel shows the absolute difference.

Considerable bottom steepness ($p = 2$)

We now turn to the case of a fairly steep radial bottom variation ($p = 2$). This indicates that the bottom depth at the inner part of the domain (near $R = R_1$) is 0.9 m, so that there is a bottom variation of almost ten meters over a distance of less than a kilometer. This is steeper than typical realistic situations.
It is to be expected that this case will be a stronger test for curvilinearity since. Indeed for a given curvilinear grid, larger bottom gradients will occur if p is higher and these gradients will be more difficult to compute accurately. Since the gyre is generated by wind stress torques that are related to bottom variations, it is to be expected that the water motion will also be calculated less accurately.

Figure 20 shows the water level for $p = 2$ as obtained from COHERENS and the semi-analytical expression (84). We find that the water level is of the same order of magnitude as for the modest bed slope (Fig. 17). The difference between numerical result and analytical approximation is slightly higher (~ 1 mm). Thus the typical relative deviation is still $\sim 0.01 \sim \varepsilon$ so that we conclude that COHERENS gives an accurate description of water level.

Figure 20 – Water level as computed by COHERENS (top panel) and the semi-analytical model (middle panel) for the steep bed variation ($p = 2$).

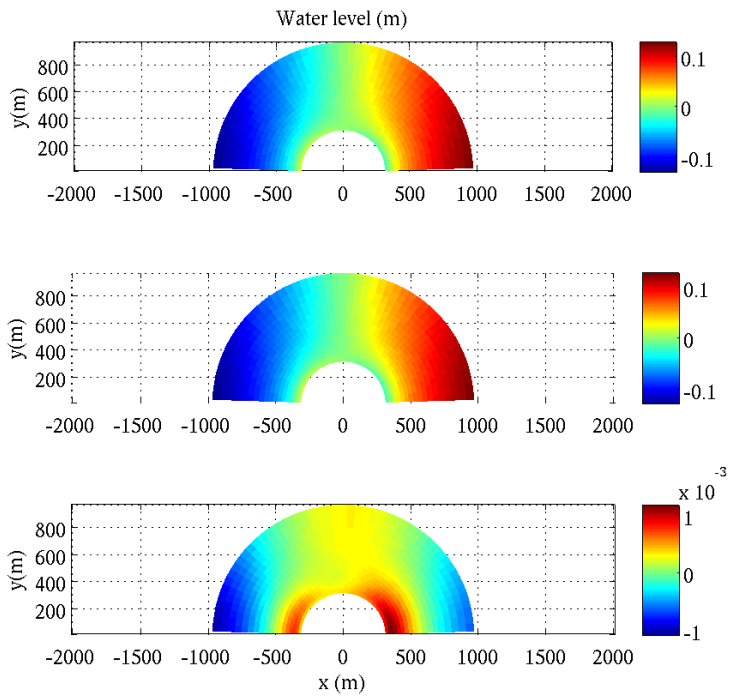

The bottom panel shows the absolute difference.

We find that both radial (Fig. 21) and azimuthal (Fig. 22) component of the transport velocity are higher as compared to the modest bottom slope case ($\sim 5\ \mathrm{m}^2\ \mathrm{s}^{-1}$ and $\sim 20\ \mathrm{m}^2\ \mathrm{s}^{-1}$, respectively). This reflects the fact that the the gyre is a result of wind driven bottom torques the magnitude of which scales with the steepness of the bed.
The absolute deviations between COHERENS result and analytical approximation are approximately $0.1\ \mathrm{m}^2\ \mathrm{s}^{-1}$ for both transport velocity components. We thus find that while the flow is increased by a factor $2 - 3$, the absolute difference between numerical and analytical result has increased by a factor $2 - 5$. Hence, in relative terms COHERENS results show a lesser agreement with the analytical approximation.
Nonetheless, the relative error ~ 0.02 for the radial flow and ~ 0.005 for the azimuthal components are still

of the the order of $\varepsilon = 0.01$ or less. Hence we conclude that COHERENS is also able to give an acceptable description of the water motion for the case of considerable bottom steepness.

Figure 21 – Radial component of transport velocity as computed by COHERENS (top panel) and the semi-analytical model (middle panel) for the steep bed variation ($p = 2$).

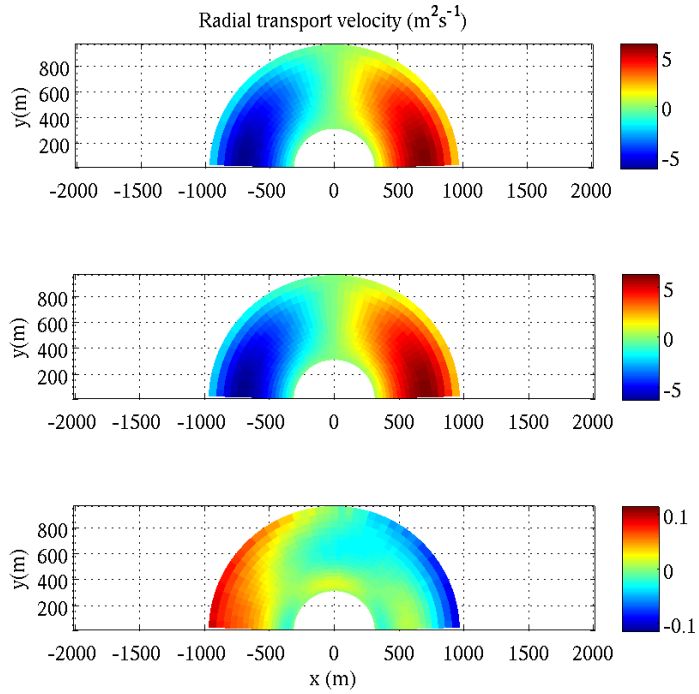

The bottom panel shows the absolute difference.

Figure 22 – Azimuthal component of transport velocity as computed by COHERENS (top panel) and the semi-analytical model (middle panel) for the steep bed variation ($p = 2$).

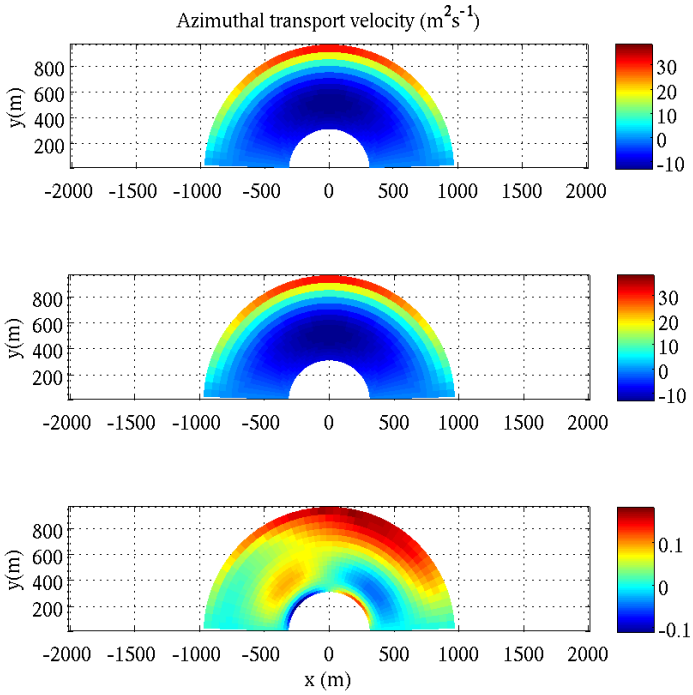

The bottom panel shows the absolute difference.

2.4.4 Conclusions

From the results of this testcase we conclude the following:

1. wind driven flow over a non-horizontal bed is computed adequately by COHERENS.
2. COHERENS is able to perform sufficiently accurate computations on an orthogonal curvilinear grid.

2.4.5 Derivation of semi-analytical solution

Model equations

The dynamics of the system is determined by the time-independent 2DH shallow water equations with excluded Coriolis force and advection and assumed uniform water density, i.e.

$$g\nabla\zeta + r\frac{\mathrm{u}}{h} = \frac{\tau_{\mathrm{w}}}{\rho h}\,, \tag{87}$$

$$\nabla\cdot(h\mathrm{u}) = 0\,, \tag{88}$$

where linear bottom friction has been adopted and τ_{w} denotes the wind shear stress that is exerted on the water surface. The quantity $h = H + \zeta$ is the total water depth. The boundary conditions are given by the impermeability of the solid walls which implies

$$u_{\mathrm{R}}(R_1,\theta) = u_{\mathrm{R}}(R_2,\theta) = u_\theta(R,0) = u_\theta(R,\pi) = 0\,. \tag{89}$$

Because the flow is stationary, the transport velocity $\mathrm{U} = h\mathrm{u}$ is divergence free so that there exists a stream function Ψ such that $\mathrm{U} = \nabla\Psi\times\hat{z}$. Hence the problem is more conveniently expressed by using the transport velocity rather than the depth averaged flow. In terms of U, the equation of motion (87) can be expressed as

$$g\nabla\zeta + r\frac{\mathrm{U}}{h^2} = \frac{\tau_{\mathrm{w}}}{\rho h}\,. \tag{90}$$

The curl of Eq. (90) gives a Poisson equation for Ψ, from which eventually U can be solved. In terms of the stream function $\Psi(R,\theta)$, boundary conditions (89) correspond to $\Psi = 0$, i.e.

$$\Psi(R_1,\theta) = \Psi(R_2,\theta) = \Psi(R,0) = \Psi(R,\theta) = 0\,. \tag{91}$$

The divergence of Eq. (90) gives a Poisson equation for the water level $\zeta(R,\theta)$. The boundary conditions for the latter problem are given by

$$g\frac{\partial\zeta}{\partial R} = \frac{\tau_{\mathrm{w}}\cdot\hat{R}}{\rho h} = \frac{\tau_{\mathrm{w}}\cos\theta}{\rho h} \qquad \text{at } R = R_1, R_2\,, \tag{92}$$

$$\frac{\partial\zeta}{\partial\theta} = 0 \qquad \text{at } \theta = 0,\pi\,, \tag{93}$$

and express force balance at the solid walls under the constraint of impermeability. The quantity $\hat{R}$ is the unit vector in the radial direction.

Scaling and reduced model equations

The following scaling is adopted for the model variables:

$$\mathrm{U} = u_{\star\mathrm{w}}H_2\tilde{\mathrm{U}}\ ,\ \ R = R_2\tilde{R}\ ,\ \ \zeta = Fr^2\frac{R_2}{H_2}H_2\tilde{\zeta} = \frac{Fr^2}{\varepsilon}H_2\tilde{\zeta}\ ,\ \ H = H_2\tilde{H}\ ,\ \ r = \varepsilon u_{\star\mathrm{w}}\tilde{r}\,, \tag{94}$$

where $u_{\star\mathrm{w}} = \sqrt{\tau_\mathrm{w}/\rho}$ is the friction velocity associated with the wind stress and $Fr = u_{\star\mathrm{w}}^2/(gH_2)$ is the Froude number. The scaling for ζ stems from a balance between barotropic pressure gradient and wind stress.
Next, we define the parameter $\varepsilon \equiv H_2/R_2$ which is assumed to be small ($\varepsilon \ll 1$). It is also assumed that the Froude number equals ε^2 so that $\zeta/H_2 = O(\varepsilon)$. With these assumptions and scaling (94) the full equation of motion (90) becomes (˜ will be dropped on scaled quantities for the remainder of this section)

$$\nabla\zeta + \varepsilon r \frac{\mathrm{U}}{(H+\varepsilon\zeta)^2} = \frac{\hat{x}}{H+\varepsilon\zeta} \,. \tag{95}$$

The scaled versions of the boundary conditions for stream function (Eq. 91) and water level (92-93) are given by

$$\Psi(R_1,\theta) = \Psi(1,\theta) = \Psi(R,0) = \Psi(R,\pi) = 0 \,, \tag{96}$$

$$\frac{\partial\zeta}{\partial R} = \frac{\cos\theta}{H+\varepsilon\zeta} \qquad \text{at } R = R_1, 1 \,, \tag{97}$$

$$\frac{\partial\zeta}{\partial\theta} = 0 \qquad \text{at } \theta = 0, \pi \,. \tag{98}$$

Solution method

The scaled model equations (95)-(98) can be solved approximately by adopting the following expansion of the model variables:

$$\zeta = \zeta_0 + \varepsilon\zeta_1 + \varepsilon^2\zeta_2 + \dots \,, \tag{99}$$

$$\mathrm{U} = \frac{1}{\varepsilon}[\mathrm{U}_0 + \varepsilon\mathrm{U}_1 + \varepsilon^2\mathrm{U}_2 + \dots] \,, \tag{100}$$

$$\Psi = \frac{1}{\varepsilon}[\Psi_0 + \varepsilon\Psi_1 + \varepsilon^2\Psi_2 + \dots] \,, \tag{101}$$

where

$$\mathrm{U_i} = \nabla\Psi_\mathrm{i} \times \hat{z}, \quad (i = 0, 1, 2, \dots) \,.$$

Note that the dominant component of transport velocity (and hence stream function Ψ) is $O(\varepsilon^{-1})$. This is necessary in order to have a consistent model formulation and can be understood as follows. Suppose the leading order of U were $O(1)$ then the $O(1)$ equation of motion would read

$$\nabla\zeta_0 = \frac{\hat{x}}{H} \,.$$

However, this is not consistent since the left hand side is irrotational ($\nabla \times \nabla\zeta_0 = 0$) while the right hand side is not ($\nabla \times (\hat{x}/H) \sim \nabla H \times \hat{x} \sim \hat{R} \times \hat{x} \sim \sin\theta\hat{z}$). Hence bottom friction must be included in the dominant $O(1)$ force balance, which implies that the leading order contribution to (100) is $O(\varepsilon^{-1})$.
Below, only the leading order components ζ_0, U_0 and Ψ_0 will be derived.

$O(1)$ solution

At zeroth order, the scaled equation of motion reads

$$\nabla\zeta_0 + r\frac{\mathrm{U}_0}{H^2} = \frac{\hat{x}}{H} \tag{102}$$

The curl of this expression gives the following Poisson equation for the zeroth order stream function $\Psi_0(R,\theta)$

$$r\left[\frac{\partial^2}{\partial R^2} + \frac{1-2p}{R}\frac{\partial}{\partial R} + \frac{1}{R^2}\frac{\partial^2}{\partial\theta^2}\right]\Psi_0 = -\sin\theta\frac{dH}{dR} = -p\sin\theta R^{\mathrm{p}-1} \,, \tag{103}$$

which is subject to the boundary condition

$$\Psi_0(R_1,\theta) = \Psi_0(1,\theta) = \Psi_0(R,0) = \Psi_0(R,\pi) = 0\,. \tag{104}$$

The solution to Eqs. (103)–(104) reads

$$\Psi_0(R,\theta) = \frac{1}{pr}\left[\frac{R_1^{\mathrm{p}+1} - R_1^{\mathrm{n}_-}}{R_1^{\mathrm{n}_-} - R_1^{\mathrm{n}_+}} R^{\mathrm{n}_+} + \frac{R_1^{\mathrm{n}_+} - R_1^{\mathrm{p}+1}}{R_1^{\mathrm{n}_-} - R_1^{\mathrm{n}_+}} R^{\mathrm{n}_-} + R^{\mathrm{p}+1}\right]\sin\theta\,, \tag{105}$$

where $n_\pm = p \pm \sqrt{p^2+1}$. The zeroth order radial and azimuthal transport velocity component are readily obtained as

$$U_{\mathrm{R}0}(R,\theta) = \frac{1}{R}\frac{\partial\Psi_0}{\partial\theta} = \frac{1}{prR}\left[\frac{R_1^{\mathrm{p}+1} - R_1^{\mathrm{n}_-}}{R_1^{\mathrm{n}_-} - R_1^{\mathrm{n}_+}} R^{\mathrm{n}_+} + \frac{R_1^{\mathrm{n}_+} - R_1^{\mathrm{p}+1}}{R_1^{\mathrm{n}_-} - R_1^{\mathrm{n}_+}} R^{\mathrm{n}_-} + R^{\mathrm{p}+1}\right]\cos\theta\,, \tag{106}$$

$$\begin{aligned} U_{\theta 0}(R,\theta) &= -\frac{\partial\Psi_0}{\partial R} \\ &= \frac{1}{prR}\left[n_+\frac{R_1^{\mathrm{p}+1} - R_1^{\mathrm{n}_-}}{R_1^{\mathrm{n}_-} - R_1^{\mathrm{n}_+}} R^{\mathrm{n}_+} + n_-\frac{R_1^{\mathrm{n}_+} - R_1^{\mathrm{p}+1}}{R_1^{\mathrm{n}_-} - R_1^{\mathrm{n}_+}} R^{\mathrm{n}_-} + (p+1)R^{\mathrm{p}+1}\right]\sin\theta\,, \end{aligned} \tag{107}$$

respectively.
The divergence of Eq. (103) yields the following Poisson equation for the zeroth order water level ζ_0:

$$\begin{aligned} \left[\frac{\partial^2}{\partial R^2} + \frac{1}{R}\frac{\partial}{\partial R} + \frac{1}{R^2}\frac{\partial^2}{\partial\theta^2}\right]\zeta_0 &= \frac{2r}{H^3}\mathrm{U}_0\cdot\nabla H - \frac{1}{H^2}\frac{\partial H}{\partial x} = \\ &= \left[\frac{2r}{H^3(R)R}\frac{\partial\Psi_0}{\partial\theta} - \frac{1}{H^2(R)}\cos\theta\right]\frac{dH}{dR} \\ &= \left[2\frac{R_1^{\mathrm{p}+1} - R_1^{\mathrm{n}_-}}{R_1^{\mathrm{n}_-} - R_1^{\mathrm{n}_+}} R^{-\mathrm{n}_- -2} + 2\frac{R_1^{\mathrm{n}_+} - R_1^{\mathrm{p}+1}}{R_1^{\mathrm{n}_-} - R_1^{\mathrm{n}_+}} R^{-\mathrm{n}_+ -2}\right. \\ &\quad \left. +(2-p)R^{-\mathrm{p}-1}\right]\cos\theta\,, \end{aligned} \tag{108}$$

which is subject to the boundary conditions

$$\left.\frac{\partial\zeta_0}{\partial R}\right|_{\mathrm{R}=1} = \cos\theta\ ,\quad \left.\frac{\partial\zeta_0}{\partial R}\right|_{\mathrm{R}=\mathrm{R}_1} = \cos\theta R_1^{-\mathrm{p}}\ ,\quad \left.\frac{\partial\zeta_0}{\partial\theta}\right|_{\theta=0,\pi} = 0\,. \tag{109}$$

The solution to (108) and (109) is given by

$$\zeta_0(R,\theta) = \frac{1}{p}\left[\frac{R_1^{\mathrm{p}+1} - R_1^{\mathrm{n}_-}}{R_1^{\mathrm{n}_-} - R_1^{\mathrm{n}_+}}\frac{R^{-\mathrm{n}_-}}{n_-} + \frac{R_1^{\mathrm{n}_+} - R_1^{\mathrm{p}+1}}{R_1^{\mathrm{n}_-} - R_1^{\mathrm{n}_+}}\frac{R^{-\mathrm{n}_+}}{n_+} - R^{1-\mathrm{p}}\right]\cos\theta \tag{110}$$

2.5 Stationary 2DV wind driven flow

2.5.1 Introduction

In this chapter we study the stationary vertical circulation that arises due to wind stress stress exerted on the water surface. Tidal effects are ignored.

Figure 23 – Sketch of the model geometry.

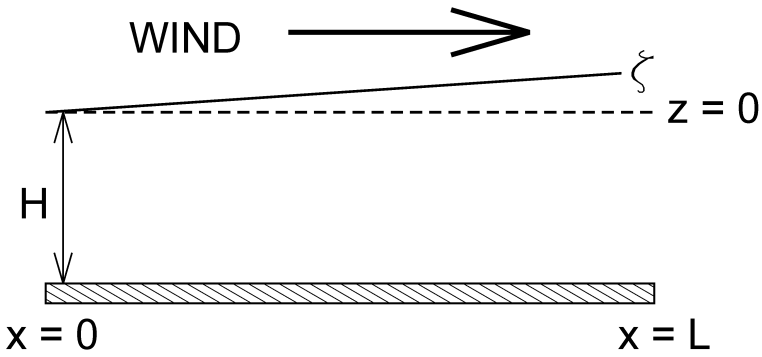

We consider the following model setup. A uniform, stationary wind blows along a channel of length L and horizontal bottom depth H (see Fig. 23). It is assumed that conditions are uniform in the cross-channel direction, which in particular implies that only the along-channel and vertical velocity components need to be considered. At the upwind boundary ($x = 0$) zero water level ζ is imposed while a zero transport (i.e. depth integrated) velocity U is specified at the downwind open end ($x = L$).

Claim

The purpose of this case is to study whether COHERENS gives an adequate description of the vertical structure of wind driven flow.

Semi-analytical solution

A semi-analytical solution for this test case has been derived under the assumptions that the depth to length ratio $\varepsilon \equiv H/L$ is much smaller than unity. Moreover, the magnitude of the dynamic wind shear stress $\tau_{\mathrm{w}} = \rho u_{\mathrm{w}\star}^2$ is tuned such that value of the wind friction velocity $u_\star$ is given by

$$u_{\mathrm{w}\star} = \epsilon\sqrt{gH} \ .$$

At the bed ($z = -H$), the shear stress is related to the local velocity by means of a linear partial slip relation, i.e.

$$\tau \equiv A_{\mathrm{v}} \left(\frac{\partial u}{\partial z}\right)_{\mathrm{z=-H}} = ru(-H) \ . \tag{111}$$

Here A_{v} and r denote the vertical viscosity coefficient and the linear friction parameter, respectively, which are both taken to be constant.

The approximate variation of the water level $\zeta(x)$ is given by

$$\zeta(x) = \varepsilon H \frac{6A_v + 3rH}{6A_v + 2rH} \frac{x}{L} \ , \tag{112}$$

while the along-channel and vertical velocity components read

$$u(z) = u_{\star\mathrm{w}} \left(\frac{u_{\star\mathrm{w}} H}{2A_\mathrm{v}} \right) \left[\frac{6A_v + 3rH}{6A_v + 2rH} \left(\frac{z}{H} \right)^2 + 2\frac{z}{H} + \frac{1}{3} \frac{12A_v + 3rH}{6A_v + 2rH} \right] , \tag{113}$$

and

$$w = 0 , \tag{114}$$

respectively.

Accuracy

The semi-analytical expressions (112)-(114) are obtained as part of a series expansion in ε. For an arbitrary quantity Q (which may denote either ζ, u or w), this expansion can be written as

$$Q = Q_0 + \varepsilon Q_1 + \varepsilon^2 Q_2 + \dots \quad .$$

The approximate solution stated above is obtained by retrieving only the leading order term in this expansion. As a result, the relative accuracy of the semi-analytical expressions is expected to be $O(\varepsilon)$.

2.5.2 Model setup

Expressions (112)–(114) have been used as a means to validate the wind driven vertical circulation as computed by COHERENS. The model domain was represented by a 2DV domain by using only one computational grid cell in the cross channel (i.e. y) direction. Furthermore, a channel of length $L = 1000$ m and depth $H = 10$ m is considered, so that $\varepsilon = H/L = 0.01$. As a consequence the value for the wind friction velocity $u_{\star\mathrm{w}}$ is set to $u_{\star\mathrm{w}} = \varepsilon\sqrt{gH} \approx 9.9\ \mathrm{cm\ s^{-1}}$. Physically, this corresponds to a wind speed of approximately $58\ \mathrm{m\ s^{-1}}$, which is characteristic of a Type II tropical cyclone. For further model parameter settings, see Table 6.

Table 6 – Parameter settings of the wind validation testcase.

Parameter	Meaning	Value	Remarks
L	Channel length (km)	1	
H	Bottom depth (m)	10	
ε	depth-to-length ratio ($= H/L$)	0.01	
$u_{\star\mathrm{w}}$	Wind friction velocity ($cm\ s^{-1}$)	9.9045	$\tau_\mathrm{w} = \rho u_{\star\mathrm{w}}^2 = 1.00556 \times 10^{-3}$ Pa
A_v	Vertical coefficient for viscosity ($m^2\ s^{-1}$)	0.1	
r	Friction parameter ($m\ s^{-1}$)	0.05	
nc	Grid size (along-channel)	51	
nr	Grid size (cross-channel)	2	
nz	Number of vertical layers	50	
Δt	Time step (s)	0.8	$\Delta t/\Delta t_\mathrm{Cour} \sim 0.8$

Initially, the water is at rest with zero water level. Fairly high values for the turbulent parameters are used ($A_\mathrm{v} = 0.1\ \mathrm{m^2\ s^{-1}}$, $r = 0.05\ \mathrm{m\ s^1}$) in order to ensure a proper convergence to a stationary flow. If the turbulent parameters are too low, the short term solution exhibits oscillatory behaviour which is propably due to the fact that the work done by the high wind stress can not be balanced by frictional forces from the (nearly unmoving) fluid. The long term dynamics for these low turbulent parameter settings has not been persued.
The simulation period is taken equal to five days, after which a steady state is achieved.

2.5.3 Results

Figure 24 – Along-channel level variation for the wind testcase (left) and the difference between COHERENS result and analytical approximation (112).

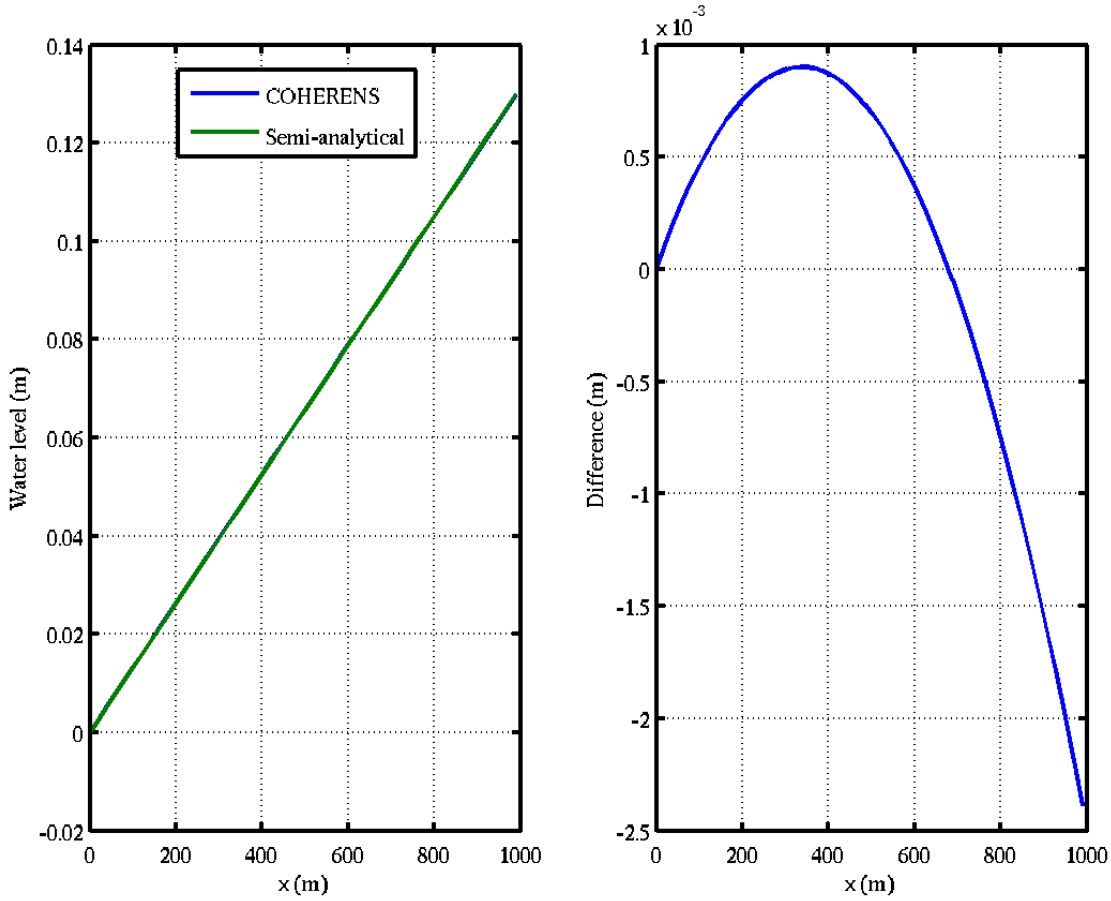

Figure 24 shows the along-channel variation of the computed water level and its difference with approximation (112). It is seen that typical values of the water level are ~ 0.1 m. while deviations from the analytical approximation are ~ 1 mm. Hence we find that the COHERENS result has a relative difference of a few procent from the analytical expression, which agrees well with the expected $O(\varepsilon) \sim 0.01$ accuracy of the approximated expression (112). We thus conclude that the water level has been computed adequately by COHERENS.

Similarly, we find a good agreement between computed and approximated along-channel velocity u (see Fig. 25). Both COHERENS and the analytical approximation (113) yield velocities $\sim 0.1\ \mathrm{m\,s^{-1}}$ while the difference between them is $\sim 1\ \mathrm{mm\,s^{-1}}$. Hence we again find an $O(\varepsilon) \sim 0.01$ relative difference between COHERENS and expression (113). Hence the conclude that the along-channel velocity is well described by COHERENS.

Finally, we consider the vertical velocity component w. Figure 26 shows this velocity component as computed by COHERENS. Typical flow velocities are $\sim 10^{-5}\ \mathrm{m\,s^{-1}}$. In comparison, the zeroth order approximation (114) is zero, which indicates that the first nonzero contribution to the analytical solution is at most an $O(\varepsilon)$ contribution. However, because $H \ll L$, the magnitude of the $O(\varepsilon)$ contribution to w (i.e. w_1) has in fact relative magnitude $O(\varepsilon^2)$ compared to u_0. Hence we expect the ratio of vertical to horizontal velocity to be at most $O(\varepsilon^2) = 10^{-4}$. With a typical along-channel velocity $\sim 0.1\ \mathrm{m\,s^{-1}}$ we thus find that the computed vertical velocity $\sim 10^{-5}\ \mathrm{m\,s^{-1}}$ is consistent with the maximum flow velocity that follows from the analytical solution procedure.

Figure 25 – The top panel shows the along-channel velocity component u as computed by COHERENS, while the middle panel shows the approximated solution (113).

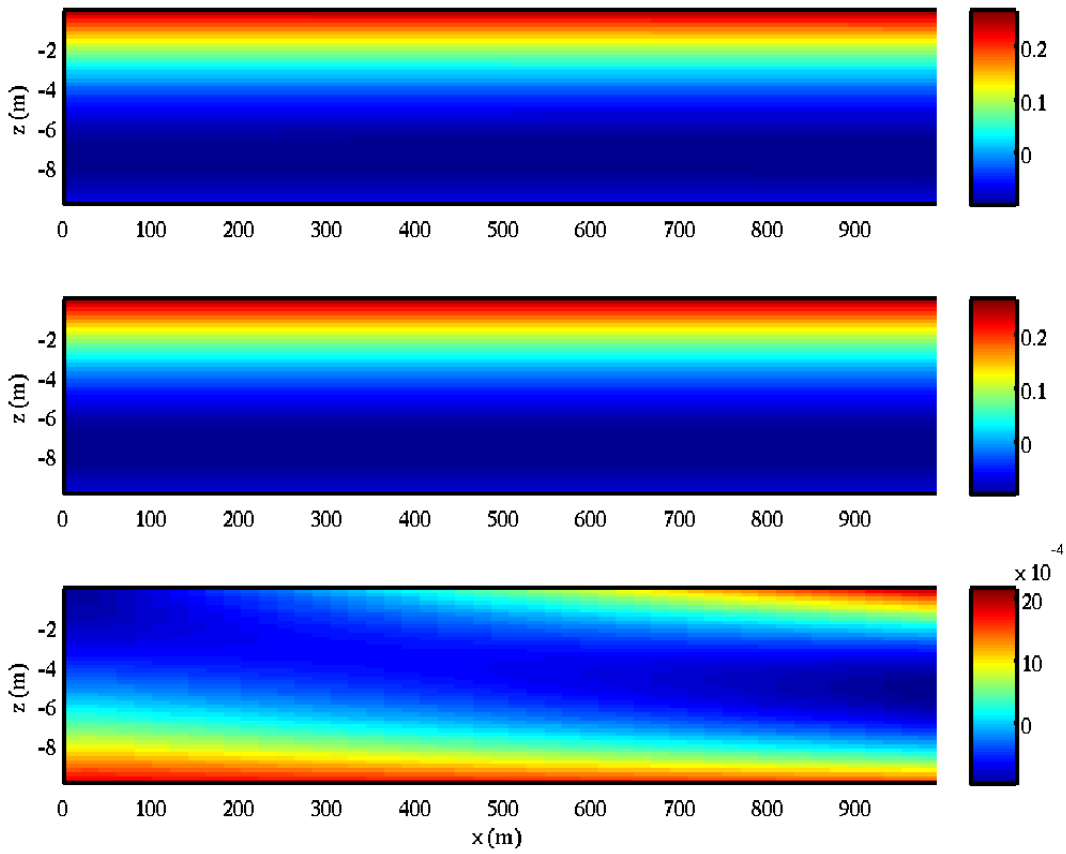

The bottom figure shows the difference between the COHERENS result and the approximation.

Figure 26 – Vertical velocity as computed by COHERENS.

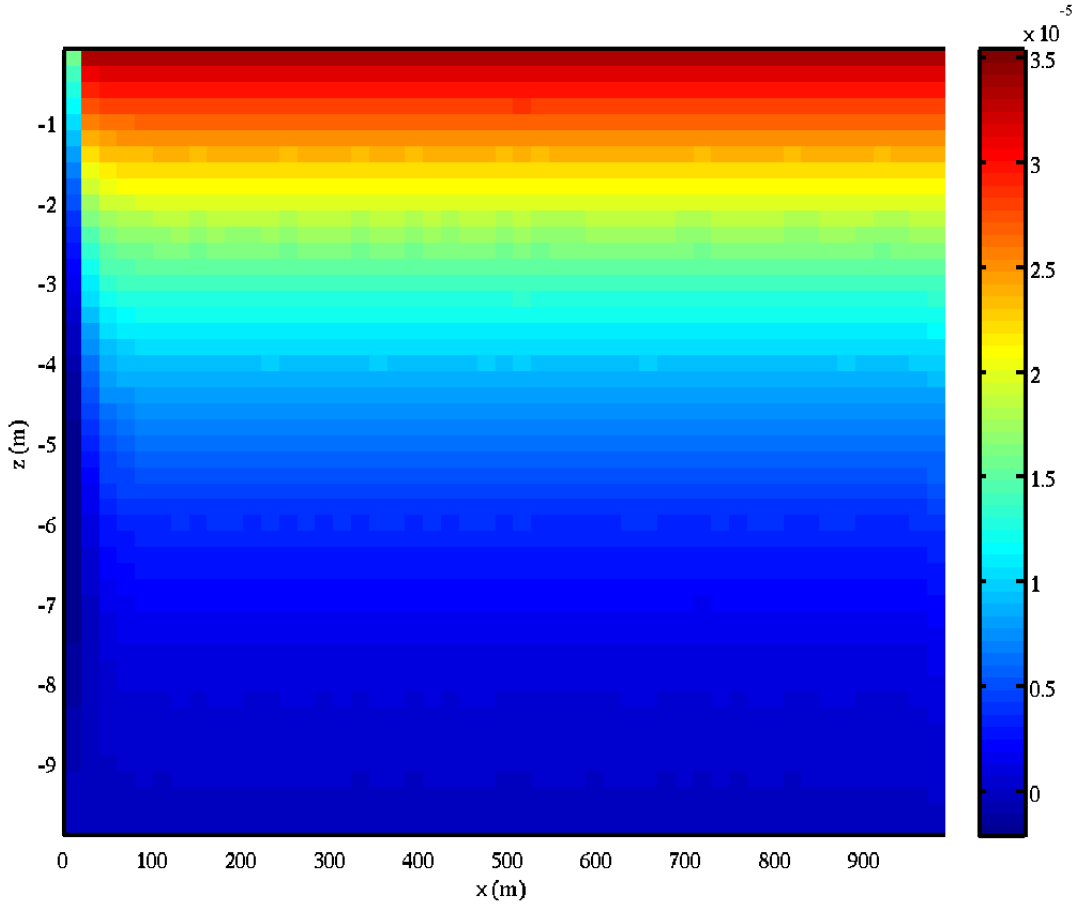

2.5.4 Conclusion

The vertical structure of wind driven flow is computed accurately by COHERENS.

2.5.5 Derivation of the semi-analytical solution

Full model equations

The 2DV flow is governed by the so-called stationary three-dimensional shallow water equations which are given by

$$u\frac{\partial u}{\partial x} + w\frac{\partial u}{\partial z} = -g\frac{\partial \zeta}{\partial x} + \frac{\partial}{\partial z}\left(A_v\frac{\partial u}{\partial z}\right) , \tag{115}$$

$$\frac{\partial u}{\partial x} + \frac{\partial w}{\partial z} = 0 , \tag{116}$$

and represent the along-channel momentum balance and the mass conservation law for incompressible fluids, respectively. The quantities u and w are the along-channel and vertical flow component, respectively while A_v is the coefficient of vertical viscosity. Hereafter A_v is assumed to be constant.

In order to solve the vertical variation of u and w, vertical boundary conditions have to be specified for Eqs. (115) and (116). At the water surface ($\zeta = 0$), the surface stress equals the kinematic wind stress τ_w/ρ while the vertical velocity follows from the kinematic boundary condition, i.e.

$$A_v\left(\frac{\partial u}{\partial z}\right)_{z=\zeta} = \frac{\tau_w}{\rho} , \tag{117}$$

$$w(z=\zeta) = u\frac{\partial \zeta}{\partial x} . \tag{118}$$

At the bottom, the vertical velocity is zero by virtue of the fact that the bed is horizontal and impermeable. Hence

$$w(z=-H) = 0 . \tag{119}$$

For the horizontal velocity component u, a so-called linear slip formulation is adopted which is a linear relation between the shear stress and flow velocity at the bed ($z = -H$), i.e.

$$A_{\mathrm{v}}\left(\frac{\partial u}{\partial z}\right)_{-\mathrm{H}} = ru(z=-H) . \tag{120}$$

Here, r denotes the so-called (linear) friction parameter which is assumed to be constant. Note that this boundary condition differs from COHERENS, where the slip formulation is applied at the lowest horizontal velocity point rather than at the true bed. For the sole derivation of the approximate zeroth order solution (112)-(114), however, this difference is not relevant.

The boundary conditions (117)-(120) determine the vertical variation of the flow components but not their magnitude since the barotropic forcing ($g\partial\zeta/\partial x$) is not yet determined. In order to specify this forcing, the local value of the transport velocity U, which is defined as

$$U = \int_{-H}^{\zeta(x)} u(x,z)dz \tag{121}$$

should be specified. It can be shown that this local value is equal to the specified downwind boundary value $U(x = L) = 0$. Indeed, vertical integration of the mass conservation equation (116) for stationary flow gives the exact result

$$\frac{\partial U}{\partial x} = 0 ,$$

from which it follows that $U(x) = U(x = L) = 0$.
Once the along-channel water level gradient $\partial\zeta/\partial x$ has been obtained, the water level variation is straightforwardly found by along-channel integration under the condition that $\zeta(x = 0) = 0$, i.e.

$$\zeta(x) = \int_0^x \frac{\partial\zeta(x')}{\partial x'} dx' \tag{122}$$

Scaled model equations and solution method

The full set of model equations can be reduced by using the following scaling:

$$x = L\tilde{x}, \quad z = H\tilde{z}, \quad u = u_*\tilde{u}, \quad w = u_*\frac{H}{L}\tilde{w}, \quad U = u_* H\tilde{U}, \quad \zeta = \frac{Fr^2}{\varepsilon}H\tilde{\zeta}, \quad A_v = u_* H\tilde{A}_v, \quad r = u_\star\tilde{r}\,, \tag{123}$$

where $u^\star = \sqrt{\tau_w/\rho}$ is the friction velocity associated with the imposed wind stress and $\epsilon = H/L \ll 1$. The Froude parameter Fr is defined as $Fr = u^\star/\sqrt{gH}$, which is in general small. Hereafter, it will be assumed that $Fr = \epsilon$ so that the scaling for ζ reads $\zeta = \epsilon H\tilde{\zeta}$.
Using the above scaling, the equations for momentum and mass conservation and can be written as

$$\varepsilon\left[\tilde{u}\frac{\partial\tilde{u}}{\partial\tilde{x}} + \tilde{w}\frac{\partial\tilde{u}}{\partial\tilde{z}}\right] = -\frac{\partial\tilde{\zeta}}{\partial\tilde{x}} + \tilde{A}_v\frac{\partial^2\tilde{u}}{\partial\tilde{z}^2}\,, \tag{124}$$

$$\frac{\partial\tilde{u}}{\partial\tilde{x}} + \frac{\partial\tilde{w}}{\partial\tilde{z}} = 0\,, \tag{125}$$

whereas boundary conditions (117)–(120) become

$$\tilde{A}_v\left(\frac{\partial\tilde{u}}{\partial\tilde{z}}\right)_{\tilde{z}=\varepsilon\tilde{\zeta}} = 1\,, \tag{126}$$

$$\tilde{w}(\tilde{z} = \varepsilon\tilde{\zeta}) = \varepsilon\tilde{u}\frac{\partial\tilde{\zeta}}{\partial\tilde{x}}\,, \tag{127}$$

$$\tilde{w}(\tilde{z} = -1) = 0\,, \tag{128}$$

$$\tilde{A}_v\left(\frac{\partial\tilde{u}}{\partial\tilde{z}}\right)_{\tilde{z}=-1} = \tilde{r}\tilde{u}(\tilde{z} = -1)\,, \tag{129}$$

respectively. Finally, the scaled condition for zero transport velocity reads

$$\tilde{U} = \int_{-1}^{\varepsilon\tilde{\zeta}} \tilde{u}(\tilde{x}, z)dz = 0\,. \tag{130}$$

The solution to the scaled model equations can be found in an approximate sense by expansion of the model variables in a series of the small parameter ε, i.e.

$$\tilde{\zeta} = \tilde{\zeta}_0 + \tilde{\varepsilon}\zeta_1 + \tilde{\varepsilon}^2\zeta_2 + \dots\,, \tag{131}$$

and similarly for $\tilde{v}$, $\tilde{w}$ and $\tilde{U}$. In this chapter, only the zeroth order solutions $\tilde{\zeta}_0$, $\tilde{u}_0$ and $\tilde{v}_0$ will be considered.

$O(1)$ solution

The zeroth order equations for momentum and mass balance are obtained by putting $\varepsilon = 0$ in the scaled model equations (124)-(130). This gives

$$-\frac{\partial \tilde{\zeta}_0}{\partial \tilde{x}} + \tilde{A}_v \frac{\partial^2 \tilde{u}_0}{\partial \tilde{z}^2} = 0 \,, \tag{132}$$

$$\frac{\partial \tilde{u}_0}{\partial \tilde{x}} + \frac{\partial \tilde{w}_0}{\partial \tilde{z}} = 0 \,. \tag{133}$$

The boundary condition at the water surface and the bed read

$$\tilde{A}_v \left(\frac{\partial \tilde{u}_0}{\partial \tilde{z}} \right)_{\tilde{z}=0} = 1 \,, \quad \tilde{w}_0(\tilde{z} = 0) = 0 \,, \tag{134}$$

and

$$\tilde{A}_v \left(\frac{\partial \tilde{u}_0}{\partial \tilde{z}} \right)_{\tilde{z}=-1} = \tilde{r}\tilde{u}_0(\tilde{z} = -1) \,, \quad \tilde{w}_0(\tilde{z} = -1) = 0 \,, \tag{135}$$

respectively, while the zero tranport velocity condition is given by

$$\int_{-1}^{0} \tilde{u}_0 dz = 0 \,. \tag{136}$$

The solution for the zeroth order flow $(\tilde{u}_0, \tilde{w}_0)$ is given by

$$\tilde{u}_0 = \tilde{u}_0(\tilde{z}) = \frac{1}{2\tilde{A}_v} \frac{\partial \tilde{\zeta}_0}{\partial \tilde{x}} \tilde{z}^2 + \frac{\tilde{z}}{\tilde{A}_v} + \frac{1}{6\tilde{A}_v} \frac{12\tilde{A}_v + 3\tilde{r}}{6\tilde{A}_v + 2\tilde{r}} \,, \tag{137}$$

$$\tilde{w}_0 = 0 \,, \tag{138}$$

where

$$\frac{\partial \tilde{\zeta}_0}{\partial \tilde{x}} = \frac{6\tilde{A}_v + 3\tilde{r}}{6\tilde{A}_v + 2\tilde{r}} \,. \tag{139}$$

From Eqs. (122) and (139) and the condition $\tilde{\zeta}_0(x = 0)$ we find that the zeroth order water level varies linearly according to

$$\tilde{\zeta}_0 = \frac{6\tilde{A}_v + 3\tilde{r}}{6\tilde{A}_v + 2\tilde{r}} \tilde{x} \,. \tag{140}$$

2.6 Conclusions

Regarding the testcases discussed in this chapter, the following conclusions can be drawn regarding the modelling of hydrodynamics in COHERENS:

1. internally generated overtides are described accurately,
2. the vertical variation of tidal flow is computed accurately for the case of linear bottom friction,
3. wind driven flow over a non-horizontal bed is computed adequately,
4. COHERENS is able to perform accurate computations on an orthogonal curvilinear grid,
5. the vertical structure of wind driven flow is computed accurately.

3 Inundation

3.1 Introduction

This report deals with the presentation of the results of the validation tests applied to the Inundation Schemes functionality implemented into the COHERENS. Two test cases were considered for this purpose: A 1D overflowing dyke and the test case proposed by Thacker, 1981.

The aim of the validation tests is to verify the fulfilment of the list of claims that is depicted in Table 7.

Table 7 – Matrix of claims

Test case/ Claim	mass conservation (water)	mass conservation (salt)	2D mode	3D mode	puddles	water depth/concentration positive	flip-flop behavior
Overflowing dike	√		√	√	√	√	√
Thaker (1981) test case	√	√	√	√		√	√

In addition, it was assessed the performance of the ten inundation schemes implemented into the COHERENS model. This assessment is not applied to the overflowing dyke because it is focused on the validation of the 11th inundation scheme. Hence, the assessment is performed only for the Thacker test case, For this purpose, a comparison between the obtained results is made, looking at the conservation of mass. Only the Thacker test case in 2D is regarded (so no salinity is applied).

3.2 Overflowing dyke

3.2.1 Introduction

This validation test case was proposed by the Laboratory of Hydraulics. It indicates that in estuarine models, structures of 1 cell wide are alternately wet and dry (overflowing dikes). In the case of staggered grids, the code has to interpolate the depth information to a location where a wetting drying condition is set (e.g. velocity point). Therefore, it was proposed to test this particular case.

3.2.2 Model setup

The set-up is chosen simple, using 100 columns and 1 row. In the case of three dimensional computations, 5 layers are used. For the grid spacing, the grid size $\Delta x = \Delta y$ is set to 10 m. Making a 1D channel with a length of 1000 m (see Figure 27).

The rectangular reservoir is closed at all sides except at the Westside. There, an open boundary condition is applied with: specified level at the velocity nodes. Hence, a tidal constituent (open_S2) is applied. The amplitude of this wave is set to 2.0 m and the phase shift at initialisation is (π). Hence a low water condition is created.

For the specification of the initial conditions. Zero initial velocities are applied: Uvel $=$ Vvel $= 0$ m/s. And a surface elevation of -2.0 m below mean sea level is forced at initialization for all the grid cells, except the grid cell which corresponds to the dyke. Therefore, at the initial condition all the grid cells are 'wet' (with the exception of the dyke). The main objective of this validation test is the verification of the behaviour of the 1D dyke during inundations and the 'filling' behind the dyke in case 'dry' grid cells were defined behind the dyke was not considered. However, preliminary tests were performed with dry grid cells behind the dyke, showing an acceptable behaviour.

Figure 27 – Longitudinal scheme of the overflowing dyke

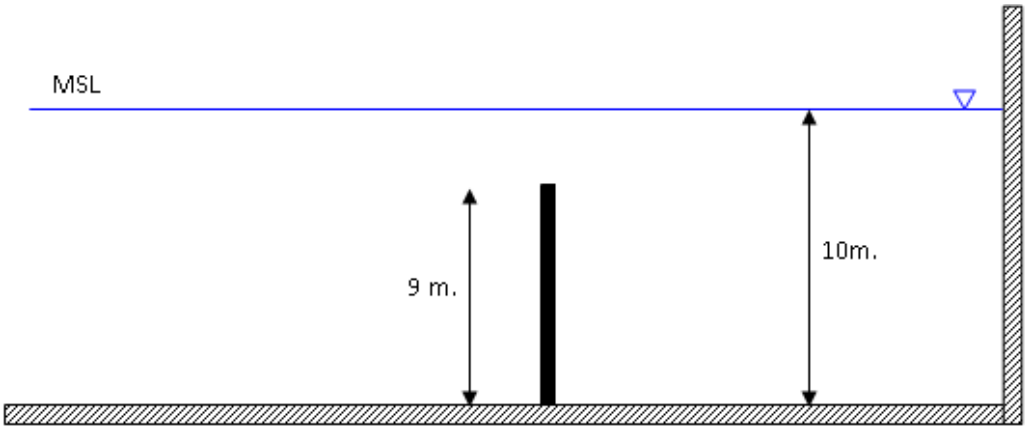

The time step Δt is set to 0.2 s and computations are made for 2 days (i.e. four high and low water conditions). This time step is less than the required for the Courant condition (~ 2.5 sec.). However, a smaller time step is chosen in order to avoid further instabilities due to the discretization.

The bathymetry is set to 10 m below the mean see level for all cells, except for the middle column (10) where the depth is set to 1 m (representing a dyke of height 9 m). Thus, only one cell is used to define the dyke.

A constant roughness length is applied to all the grid cells: $z_0 = 0.006m$. For the 3D case, the vertical viscosity is set to: $\nu = 10^{-6}$ m^2/s. The horizontal viscosity is set to $\nu_H = 10.0$ m^2/s, larger values were tested in order to suppress the presence of internal waves generated by the dyke. Finally, the eleventh inundation scheme (fld_schm(1) =11) is used with a standard threshold depth (dthd_fld) of 10 cm for the simulation of the inundation process.

3.2.3 Results

Mass conservation

Mass conservation is computed at every time step using:

$$V(t) - V(0) = \int_0^t \int_0^B U\,dy\,dt\ . \tag{141}$$

The double integral applies on the open boundary cells (in and outflow), in this simple case the first column. This is discretisized into:

$$V(t) - V(0) = B\Delta t \sum_{p=0}^{p=n-1} \frac{1}{2}\left(U_p + U_{p+1}\right)\ , \tag{142}$$

where:

- U_p = depth-mean current in U-direction at the open boundary and at $t = p\Delta t$, (m/s)
- Δy = grid spacing, (m)
- Δt = two dimensional time step, (s)
- B = width of the reservoir, (m)
- $V(0)$ = the initial volume at t=0, (m^3)
- $V(t) = i$ the volume at t, (m^3)
- t = time, (s)

The difference between both terms of the mass conservation equation should be minimum. Hence, the absolute difference (Λ_{abs}) of the two terms is calculated as:

$$\Lambda_{abs} = (V(t) - V(0)) - B\Delta t \sum_{p=0}^{p=n-1} \frac{1}{2}\left(U_p + U_{p+1}\right)\ . \tag{143}$$

It is set relative to the basin volume at mid tide, $\overline{V}$:

$$\overline{V} = H_{\text{tot}} L_{channel} \Delta y \cdot \Delta x\ . \tag{144}$$

And hence the relative change of mass between two consecutive time steps is calculated:

$$\Lambda = \frac{\Lambda_{abs}}{\overline{V}} - 1\ . \tag{145}$$

It should be noticed that $\overline{V}$ is overestimated because of neglecting the volume of the implemented dyke structure. The graphs of the relative difference of the mass are depicted in Figure 28 and Figure 29 for 2D and 3D mode respectively.

Overflow process and development of puddles

The development of puddles is verified through the comparison of the total water depth calculated at three locations: upstream of the dyke, at the dyke location and downstream of the dyke. The calculated time series of the total water depth of these three locations are compared. Figure 30 depicts the time series of the total water depth for:

1. a cell located **before** the dyke structure. This means in between the dyke and the open boundary.

Figure 28 – Relative change of mass between two time steps for 2D computation

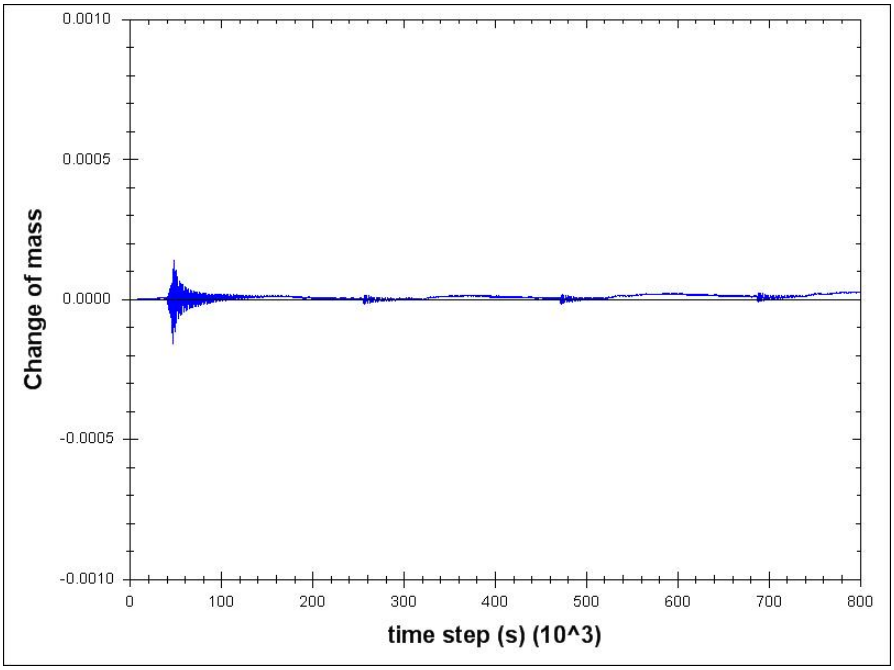

Figure 29 – Relative change of mass between two time steps for 3D computation

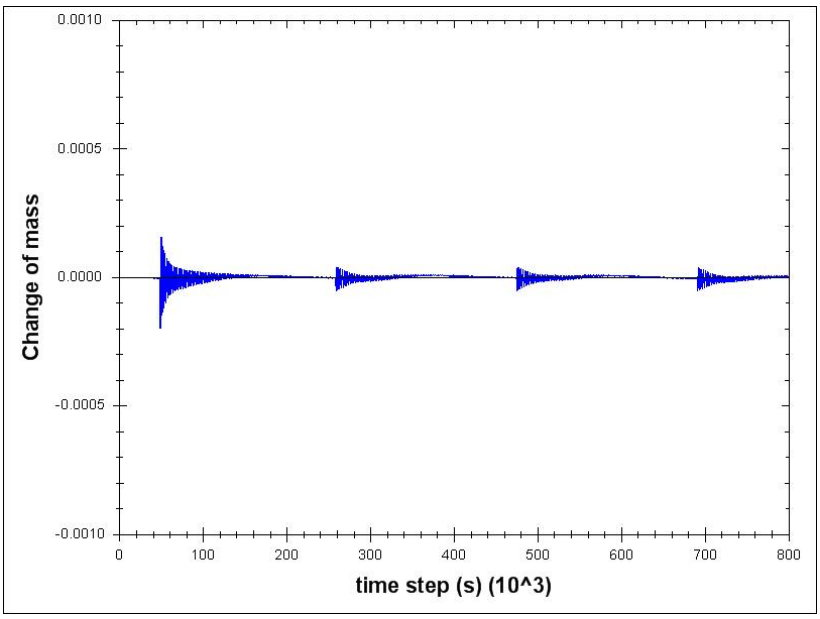

2. The cell hosting the dyke structure

3. A cell located **behind** the dyke structure, i.e. in between the dyke and the closed boundary.

As is seen from Figure 30, the water depth is always positive. When the water depth would become to low, it is set to a critical water depth. The puddle formation is clearly noticeable from this picture, as well that it reconnects when the water level before the dyke is higher than the dike height.

Figure 30 – Total depth before, at and after the dyke for 2D and 3D computations.

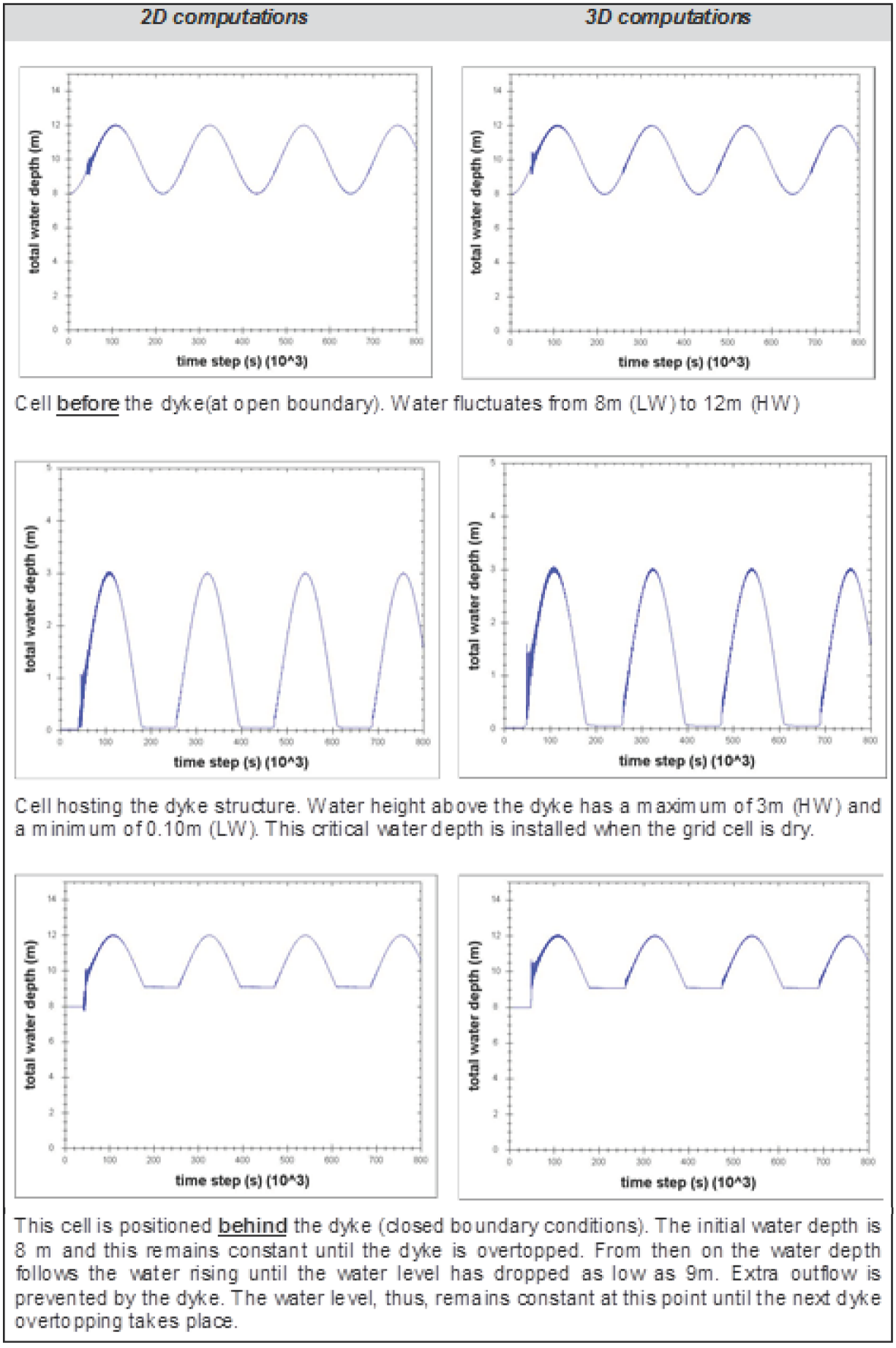

Figure 31 – Change in depth (Δd) between two time steps for 2D computation

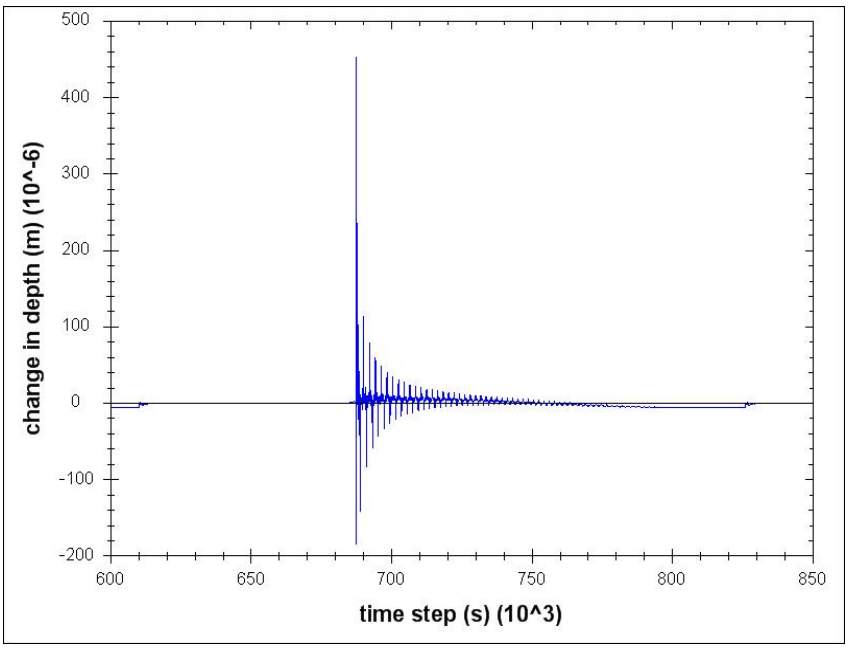

Verification of flip-flop behaviour

The verification of the flip-flop behaviour is performed by the verification of the time series of the water depths calculated at the grid cells which corresponds to the dyke. Therefore, a change of the water depth is calculated for consecutive time step, being defined as Δd:

$$\Delta d = \frac{d(t) - d(t-1)}{10}\,, \tag{146}$$

where, $d(t) - d(t-1)$ is divided by 10 (the initial depth) to scale the results. The periods where $\Delta d = 0$ correspond with water levels on the right hand side of the dyke (closed boundary) lower than the dyke height so there is no water depth change. When the water rises to the dyke height the dyke is overtopped and as a result Δd is large. It is seen that Δd shows a decreasing evolution (see Figure 31 and Figure 32).

3.2.4 Conclusions

The results of the simulation of the overflowing dyke show that there is mass conservation. Only a fluctuation around a constant average mass was noticed. The origin of this fluctuation is found in the discretization and the integration scheme used. Anyhow, the calculated relative change of mass for 2D and 3D mode are around 0.005%. The biggest fluctuation is observed at the initialization stage when the dyke is inundated for the first time, this big fluctuation is a result of the initial conditions defined for the total water depth behind the dyke.

The model worked for 2D and 3D mode. Following, the water depth is always positive (by convention). When the water depth would become too low, it is set to a critical water depth. Regarding the formation of puddles, it is verified that there is puddle formation which reconnects when the water level before the dyke is higher than the dike height.

From a flip-flop analysis it is clear that flip flop doesn't occur (or could be considered low). For this purpose, the difference of consecutive water depths are calculated for the locations of the dyke. The biggest fluctuation occurs at the initialisation of the simulation, when the dyke is flooded for the first time, with a fluctuation of

Figure 32 – Change in depth (Δd) between two time steps for 3D computation

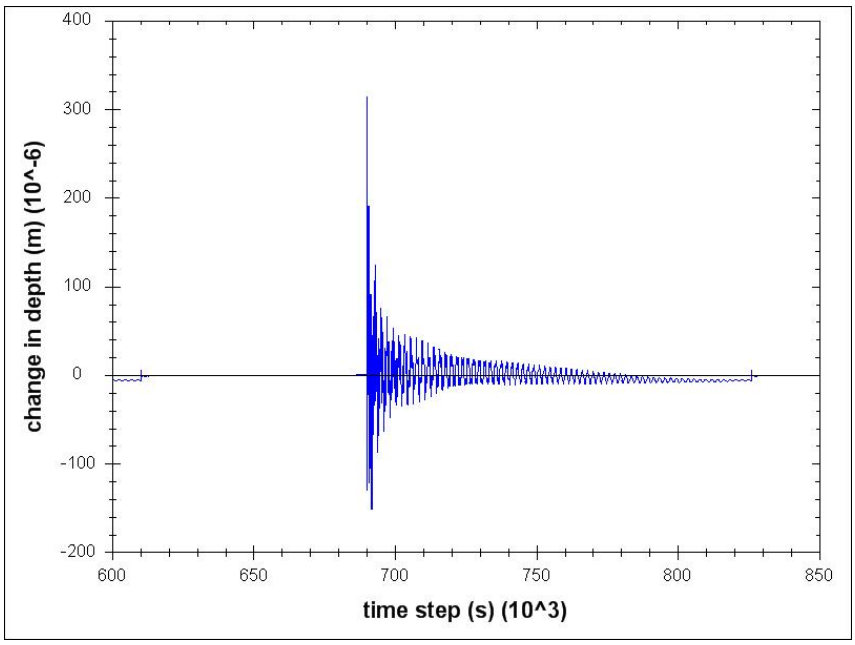

0.007m, the reason for this is the initial conditions defined for the water depth behind the dyke. Later on, much lower fluctuations are observed (around 0.0005m).

Attending a suggestion of WLB, these oscillations could be reduced by increasing the value of the horizontal viscosity which would suppress the presence of internal waves. Several values were tested from $\nu_H = 0$ to $\nu_H = 100m^2/s$. It was observed that larger values of the horizontal viscosity effectively reduce the presence of internal waves. However, the conservation of mass is affected. The reason of this was not investigated (falls beyond the aim of the present validation test). Nevertheless, lower values can reduce the presence of internal waves without affecting the conservation of mass, then the final value for the horizontal viscosity used in these simulations is $\nu_H = 10m^2/s$.

3.3 Test case of Thacker, 1981

3.3.1 Introduction

This test case was proposed by Thacker, 1981, where an analytical solution is obtained for an oscillatory motion of a water body in a closed basin, in order to establish a basis for further validation of inundation schemes. This test case was proposed by WLB to validate the implemented inundation schemes of the COHERENS model.

However, some preliminary facts have to be pointed prior to the validation test. First, the analytical solution proposed by Thacker, 1981 is applied considering an 'ideal' case, where the surface remains planar or parabolic during the oscillations. Second, the shallow water flow equations (equations 1 to 3 of Thacker paper) used for the analytical solution do not consider the presence of the bottom stress. Then, no roughness is considered nor applied in the analytical solution, confirming the fact that this solution is applicable for ideal conditions. This leads to the third fact, where the analytical solutions of (u, v, h) use the constant η, which denotes the amplitude that the motion is ideal with no roughness and the motion is permanent through the time.

Therefore, the application of the inundation schemes of the COHERENS model to reproduce this oscillatory motion is strongly constrained by the intrinsic limitations of a numerical model for 2DH and 3D flow, this mean,

roughness at the bottom that will damp the motion until it stops. As a result, the application of the inundation schemes will not be able to reflect the fully behaviour described by the analytical solution proposed by Thacker, 1981 . Instead, it will be limited to the verification of the list of claims presented in the planning (see Table 1 -1).

Three main simulations are performed for this test case:

- 2D mode
- 3D mode
- 3D mode with salinity

3.3.2 Model setup

Bathymetry and initial condition

The bathymetry used for the analytical solution corresponds to an elliptical paraboloid defined by:

$$D = D_0 \left(1 - \frac{x^2}{L^2} - \frac{y^2}{l^2} \right) , \tag{147}$$

where D denotes the bathymetry (measured positive below the mean reference level - MSL). Thacker, 1981 considers two special cases for the analytical solution: for $l = L$, where the basin is a parabola of revolution and for $l \gg L$, where the basin is a canal with a parabolic cross-section. For the present validation test, only the second case is considered. Hence, intermediate calculation are applied to the elliptical paraboloid equation in order to define the equation of a parabola. Thus, the bathymetry of the canal is defined by:

$$D = D_0 - \frac{(x-25)^2}{\left(\frac{L^2}{D_0}\right)} , \tag{148}$$

where the bathymetric value is given by D, being measured positive below the MSL level, $D_0 = 30$ is the distance between the bottom of the canal and the MSL, $L = \sqrt{750}$ (no numerical value is given in the analytical solution). For a better definition in the COHERENS code, this parabola is shifted in the horizontal direction, with a distance equals to 25, a graph of the defined bathymetry is depicted in Figure 33. Therefore, this bathymetry is used in the setup file of the COHERENS model.

The initial condition of the surface level corresponds to a linear slope defined by:

$$z = -5 - 0.8x , \tag{149}$$

where the surface level is measured negative below the MSL level. The analytical solution of Thacker, 1981 does not provide any numerical value for the initial conditions. Therefore, the initial surface level corresponds to assumed values (see Figure 33).

Model setup

The basin is discretized in 50 columns and 5 rows with square grid cells measuring 1 by 1 m. For the simulation of the 3D mode, 5 vertical layers are defined.

The simulation of the oscillatory motion is set to 10 min, assuming that this motion stops as a result of the bottom shear stress. The time step is set to $t = 0.002s$, larger values were tested leading to instabilities and the crash of the simulation. A uniform roughness height (applied to the whole domain) is set to $z_0 = 0.001m$ and a constant vertical viscosity is set to $\nu_v = 1e-06m^2/s$.

Figure 33 – Parabolic cross section of the canal with the initial water surface

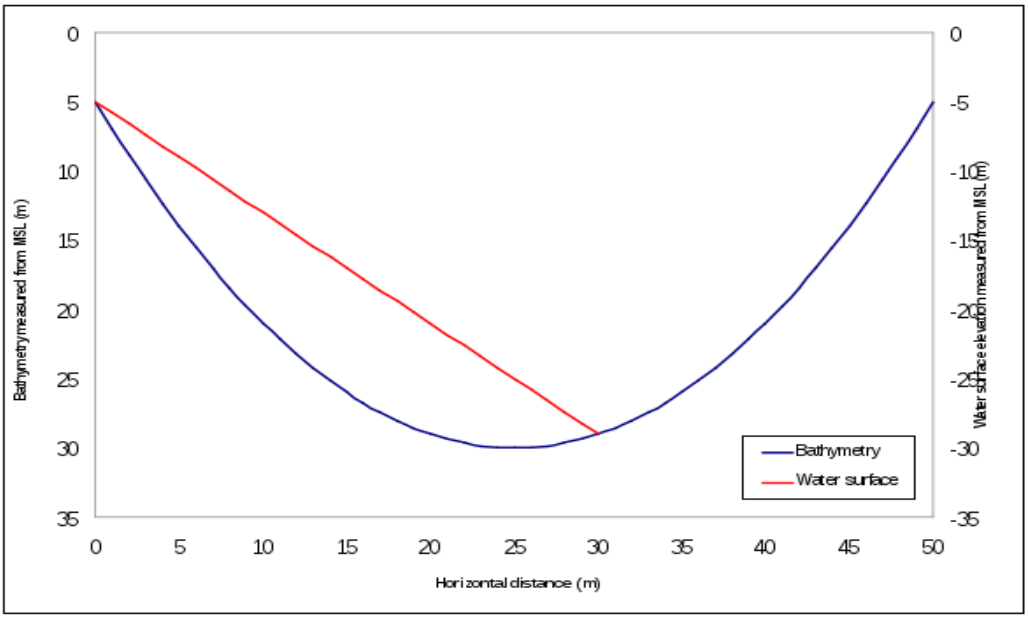

The ten inundation schemes were tested. Here are presented the verifications for the first scheme. The first inundation scheme is used with a threshold depth $h_{thd} = 0.05m$.

In case salinity is included in the computations, an initial value of 33 PSU is applied to wet grid cells and no salinity is applied to dry cells.

3.3.3 Results

Mass conservation of water and salinity

The mass conservation is verified by the calculation of the relative change of volume compared to the initial volume, $\Delta V(t)$, being given by:

$$\Delta V(t) = \frac{V(t) - V_0}{V_0} \cdot 100(\%)\,, \tag{150}$$

where V_0 denotes the initial volume inside the basin. A similar criterion is applied for the calculation of the mass conservation in the case of the simulation of salinity, where the relative change of salinity compared to the initial salinity, $\Delta S(t)$ is given by:

$$\Delta S(t) = \frac{S(t) - S_0}{S_0} \cdot 100(\%)\,, \tag{151}$$

where $S(t)$ is the total salinity calculated for all grid cells at time t, S_0 is the total salinity for all grid cells at initialisation. The graphs of the relative change of volume are depicted in Figs. 34, 35 and 36.

According to the result, for 2D mode, there is a relative change of volume of around 0.02% (with respect to the initial volume) at the initialisation time. For 3D mode, the relative change of volume is about 0.2%. Concerning the conservation of salinity, the relative change is around -3%.

Figure 34 – Relative change of volume compared to the initial volume for 2D mode

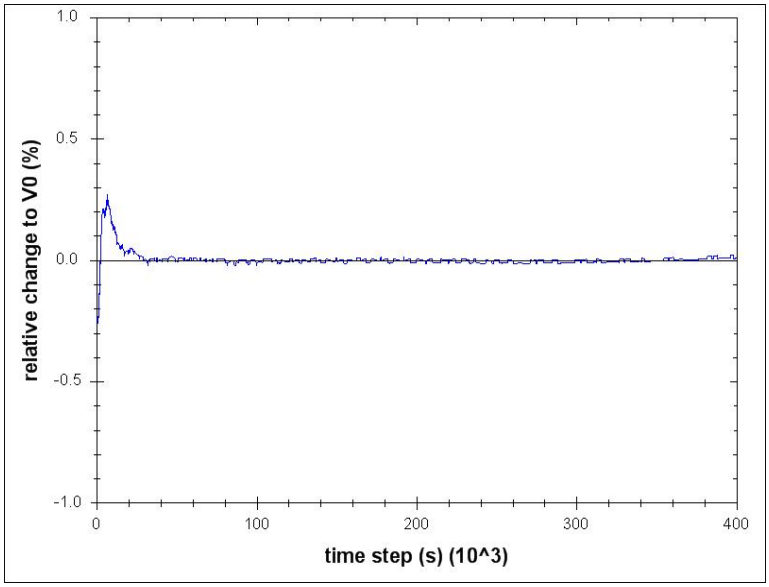

Figure 35 – Relative change of volume compared to the initial volume for 3D mode

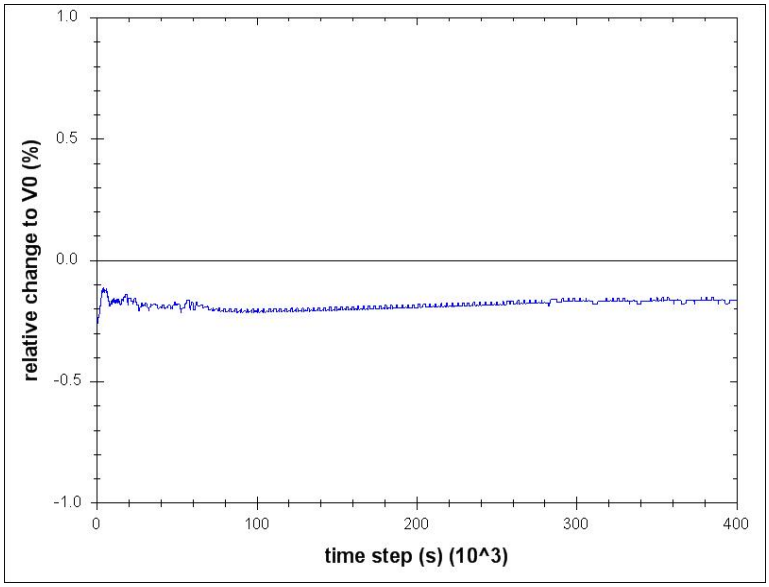

Figure 36 – Relative change of volume compared to the initial volume for 3D mode with salinity

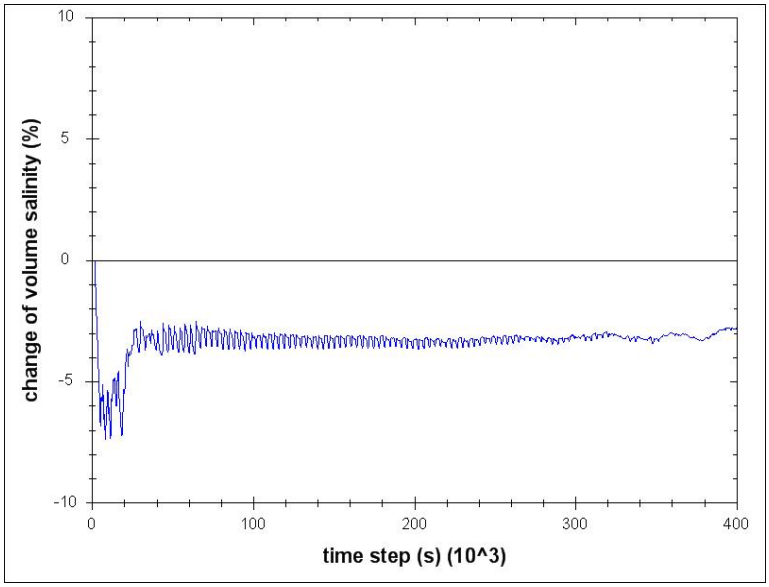

Verification of flip-flop behaviour

The presence of flip-flop is verified by the calculation of the difference of consecutive values (in time) of the total water depth, this is computed for the centre of the cross-section:

$$\Delta d = d(t) - d(t-1)(m) \,. \tag{152}$$

The obtained plots are similar for all three cases, see Figs. 37, 38 and 39. During the first time steps the values fluctuate because of the initial conditions.

Comparison of the inundation schemes

The ten inundation schemes were tested in order to determine their performance and establish a basic guideline for further simulations of inundation.

Using scheme 1 to 10, only scheme 8 causes a crash. Computations using scheme 2, 5 and 10 lead to a decrease in volume and an unrealistic water movement. The other schemes have better results: mass conservation and 'realistic' water movement. It should be mentioned that for these schemes the volume oscillates around an average volume while for scheme 3 the oscillation stops and the volume remains constant. Table 8 gives a summary of the computations for the 10 schemes. From this table it is clear that 4 different cases occur:

1. The computation crashes using scheme 8
2. Computation without conservation of mass (drop in volume) using schemes 2, 5 and 10 (Figure 40).
3. The computations take place with conservation of mass and with initial oscillation around the average volume. This oscillation, however, stops after t= 40000 (approximately). The water movement is realistic. This is only so for scheme 3. (Figure 41).
4. The computations happen with conservations of mass, but with oscillation around the average volume. The water movement is realistic. This is the case for schemes 1, 4, 6, 7 and 9. The end volume (at time step 72000) corresponds with the initial volume, only for schemes 7 and 9 (Figure 42).

Figure 37 – Verification of the Flip Flop behaviour for 2D mode

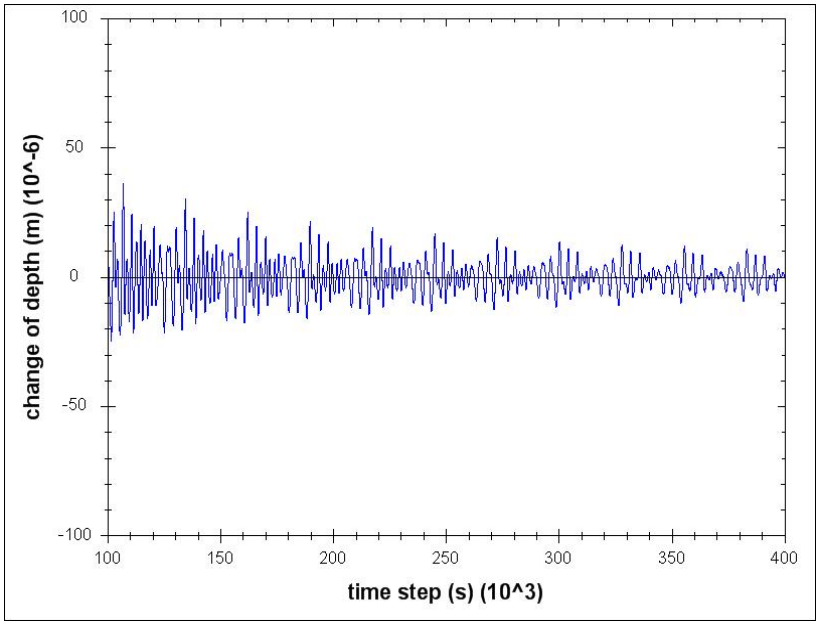

Figure 38 – Verification of the Flip Flop behaviour for 3D mode

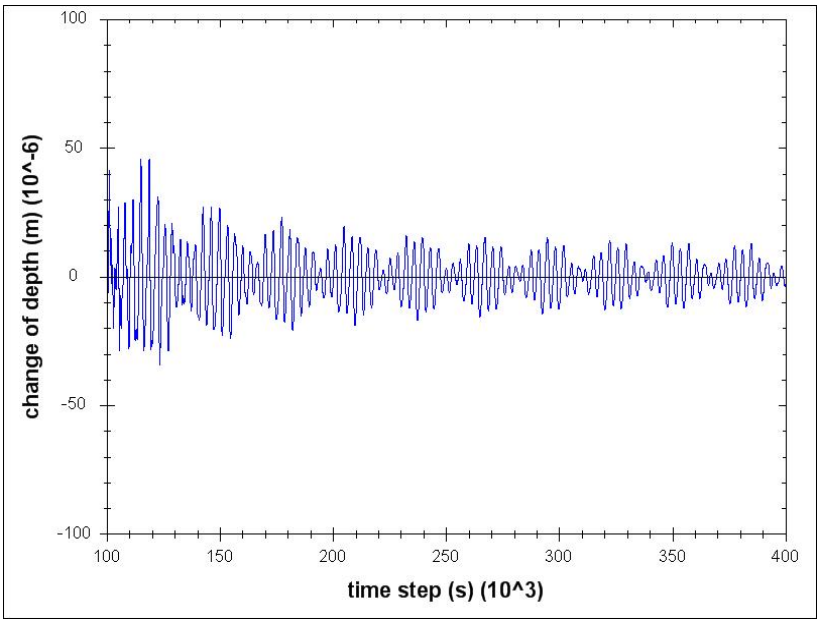

Figure 39 – Verification of the Flip Flop behaviour for 3D mode with salinity

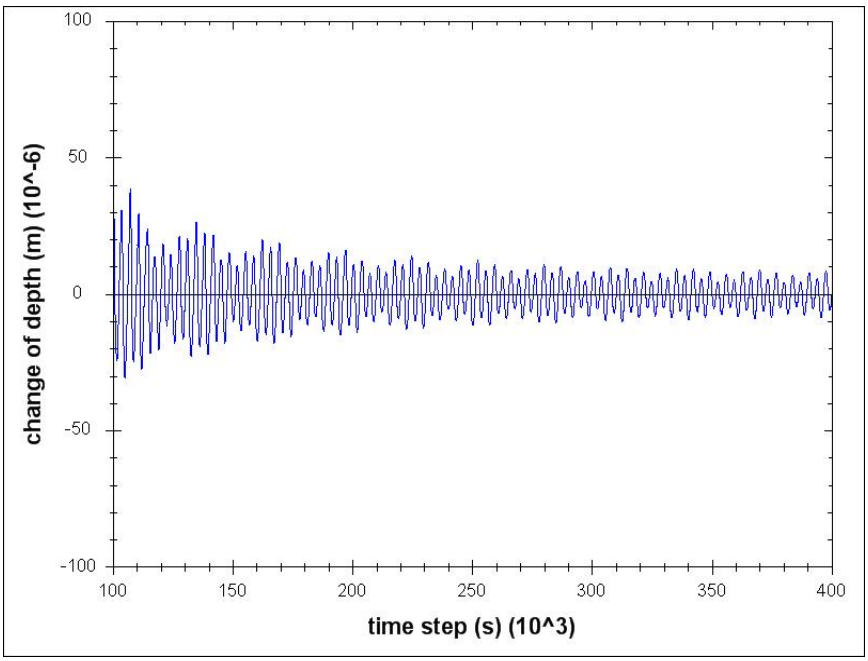

Figure 40 – Mass conservation (schemes 2, 5 and 10) as function of time

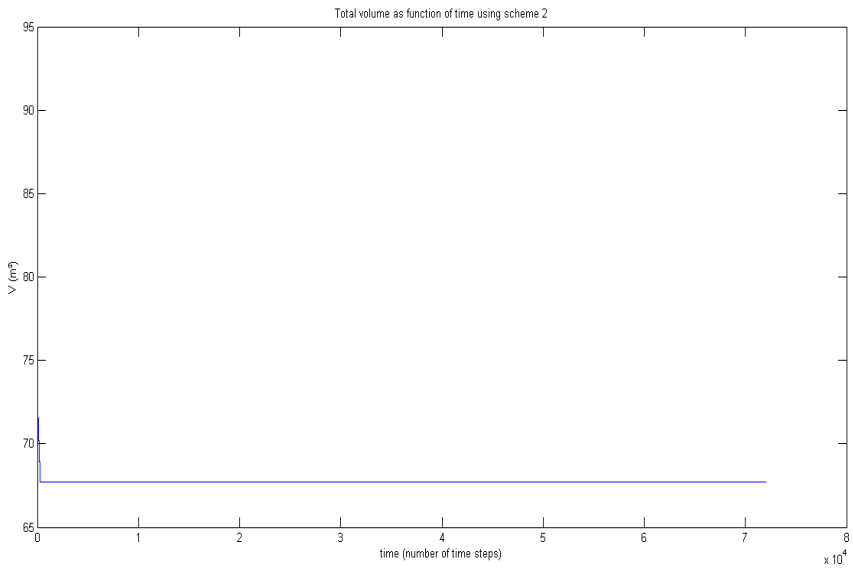

3.3.4 Conclusions

The second case of the analytical solution of Thacker was tested in this test case (canal with parabolic cross section). The mass conservation was tested showing that the relative change of volume (in relation to the initial volume) is low for 2D mode, 3D mode and Salinity, showing values of: 0.02% for 2D mode, -0.2% for 3D mode and -3% for salinity. The initial oscillations observed at the initialisation, can be explained from the initial conditions assumed for the simulation of this test case, with flow velocities equal to zero and the presence of a steep bottom gradient that has a strong influence on 3D simulations.

Moreover, the presence of flip-flop behaviour is tested by the calculation of consecutive water depths at the centre of the cross section of the canal with initial oscillations around 0.005 m and no oscillations after this

Table 8 – Comments of the results of the inundation schemes

Scheme	Mass Conservation	Comment
1	Yes	Mass conservation with fluctuation around average value water movement ok
2	No	No mass conservation (94m³ to 68 m³), Water movement not ok (not everything falls dry)
3	Yes	Mass conservation with temporary fluctuations. The fluctuations stop after t = 40000 (approximately)
4	Yes	Mass conservation with fluctuation around average value water movement ok
5	No	No mass conservation (94m³ to 68 m³), Water movement not ok (not everything falls dry)
6	Yes	Mass conservation with fluctuation around average value water movement ok
7	Yes	Mass conservation with fluctuation around average value water movement ok
8	No	Crash: volume towards 10^{32}, no computation of the water movement (crash takes place at initialisation)
9	Yes	Mass conservation with fluctuation around average value water movement ok
10	No	No mass conservation (94m³ to 89 m³), Water movement not ok (not everything falls dry)

stage.

Regarding the verification of the performance of the ten inundation schemes, only computations with scheme 8 crashed. Computations with schemes 2, 5 and 10 did result in mass conservation. Using the other schemes (1, 3, 4, 6, 7 and 9) led to a constant volume as function of time. However, only for schemes 7 and 9 this volume was the same as the initial volume. For the Thacker, 1981 test case, schemes 7 and 9 are therefore recommended.

Figure 41 – Mass conservation (scheme 3) as function of time

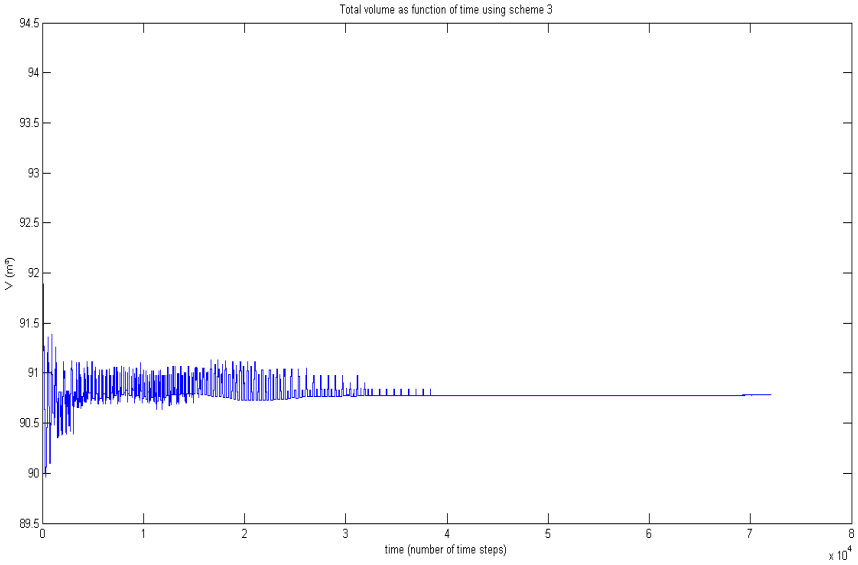

Figure 42 – Mass conservation (schemes 1, 4, 6, 7, 9 and 11) as function of time

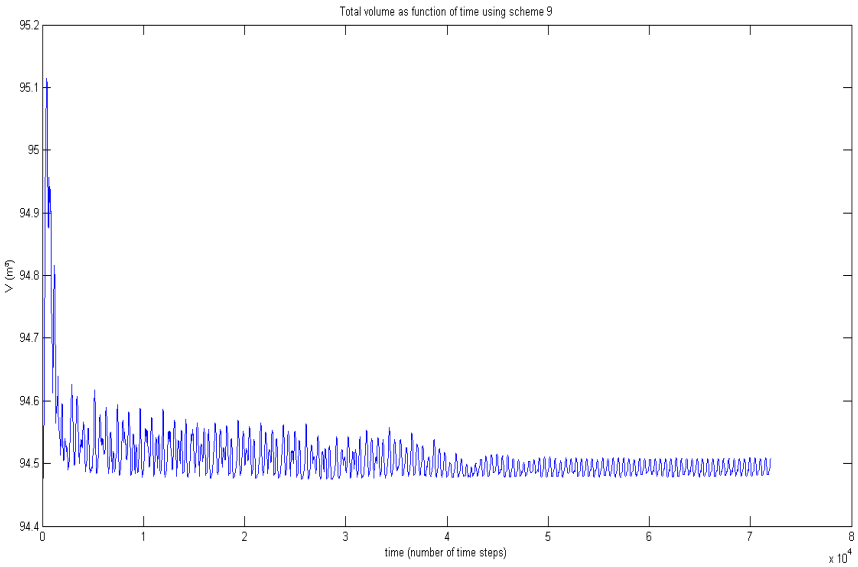

3.4 Conclusions

Regarding the testcases discussed in this chapter, the following conclusions can be drawn regarding the inundation functionalities of COHERENS:

1. effects of dyke overflow are well described by inundation scheme 11. Explicitly, both in 2D and 3D mode the relative deviations in mass conservation are approximately 0.005%.
2. the effects of puddles (i.e. wet regions that disconnect from the main flow at low water levels) are well described by using inundation scheme 11. In particular, the reconnection of such regions when the water level incraeses is modeled adequately.
3. regarding drying and flooding for intertidal flats, the Thacker, 1981 testcase indicates that inundation schemes 7 and 9 are the recommended choices as these obeys mass conservation accurately.
4. schemes $1,\ 3,\ 4$ and 6 obey mass conservation after an slight initial change of water volume. The water motion for these schemes is still realistic.
5. mass conservation for tidal flat indundation was found to be obeyed by a relative error ~ 0.02% for 2D mode, ~ 0.2% for $3D$ mode without salinity and ~ 3% for $3D$ mode with salinity.

4 Structures

4.1 Introduction

This chapter is devoted to a number of testcases that consider the functionality of structures in COHERENS. Specifically the structures that have been implemented are dry cells, thin dams, weirs/barriers and discharges. The criteria that were used to evaluate these structures are

- Mass conservation of water
- Mass conservation of scalars (salinity)
- Model units should work in 2D and 3D mode
- Fulfill the purpose of the model unit (schematization of hydraulic structures)

The following sections describe briefly the setup of the test cases and the correspondent results.

4.2 Validation of “dry cells” model unit

4.2.1 Model setup

The proposed test case is composed of a channel with a shallow lateral expansion. This test case is presented in Talstra, 2011 (see Fig. 43).

Figure 43 – Shallow lateral expansion in a channel (Talstra, 2011)

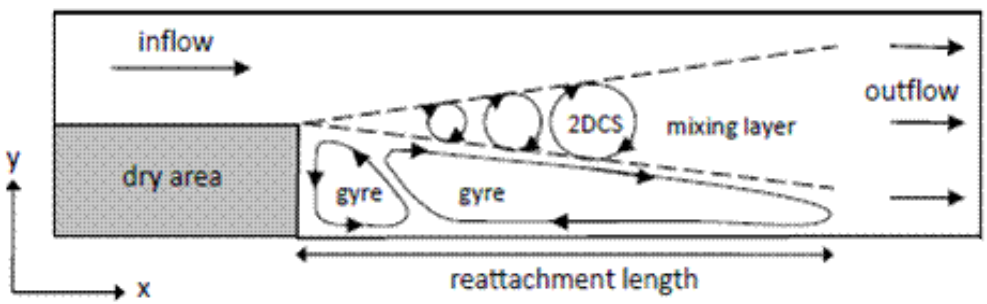

The purpose of the test case is to reproduce the dry area by the application of ‘dry cells’, it is not the purpose to reproduce the recirculation patterns of the experiment. The following table summarize the dimensions and the necessary data for the setup of this test case:

4.2.2 Results

Four test cases were developed, being identified by a letter:

- dry_cells_A: 2D test case
- dry_cells_B: 3D test case
- dry_cells_C: 3D test case with salinity

Table 9 – Data for the setup of the test case

Parameter	Value	Remarks
channel length	20 m.	
width	2.0 m.	
mean water depth simulation time length dry area width dry area	0.10 m. 20 min. 5 m. 1 m.	uniform flow
discharge	0.03 m^3/s	constant discharge
mean velocity	0.3 m/s	applied as B.C.
roughness	0.01	Manning coef. for glass
grid size dx = dy	0.10 m.	
time step	0.02 sec.	
initial flow velocity	0.0 m/s	initial condition
initial water surface initial salinity initial temperature number of rows	0.0 m. 0.0 PSU 12.0 °C 21	initial condition initial condition initial condition
number of columns	201	
number of vertical layers	10	for 3D model
B.C. upstream	type 4	specified transport
B.C. downstream	type 2	zero volume flux
B.C. salinity	1.0 PSU	upstream boundary
B.C. temperature	20.0 °C	upstream boundary
schematization dry area	500 dry cells	

- dry_cells_D: 3D test case with temperature

The first analysis corresponds to the calculation of water depths and flow velocities. The equation of Bresse for open channel flow is used for this purpose. Figure 44 depicts a comparison of the calculated water depths, showing a reasonable agreement with differences up to 1.8%. The sudden expansion was calculated in the Bresse equation by defining two different sections (i.e. expansion). The calculated flow velocities are also compared and show a considerable difference. The reason is that the equation of Bresse considers an average flow velocity for the whole transect, while COHERENS also represents secondary currents which are not included in the Bresse approach.

Figure 45 depicts the calculated flow velocities and water depths after 20 minutes. Both figures show clearly that the implemented functionality fulfils its purpose. The dry area is schematized by dry cells and no flow is calculated in this area.

The mass balance for water and salinity is applied to verify if the implemented functionality is not affecting the calculation of flow and salinity transport. The mass balance equation is used for this purpose. Figure 46 depicts the calculated mass balance for water and salinity.

Figure 44 – Comparison of water depths and flow velocities calculated by COHERENS and by using the equation of Bresse for open channel flow

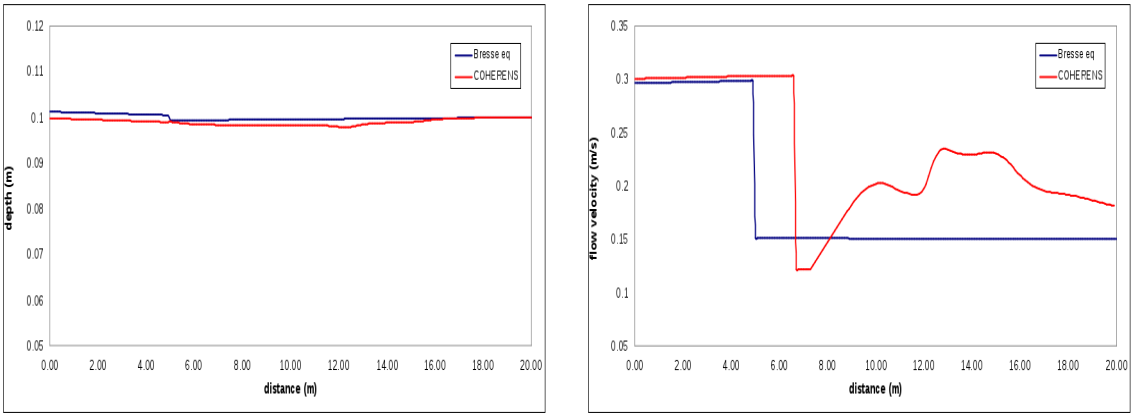

Figure 45 – Calculated flow velocities and water depths after 20 minutes (experiments: A, B, C and D)

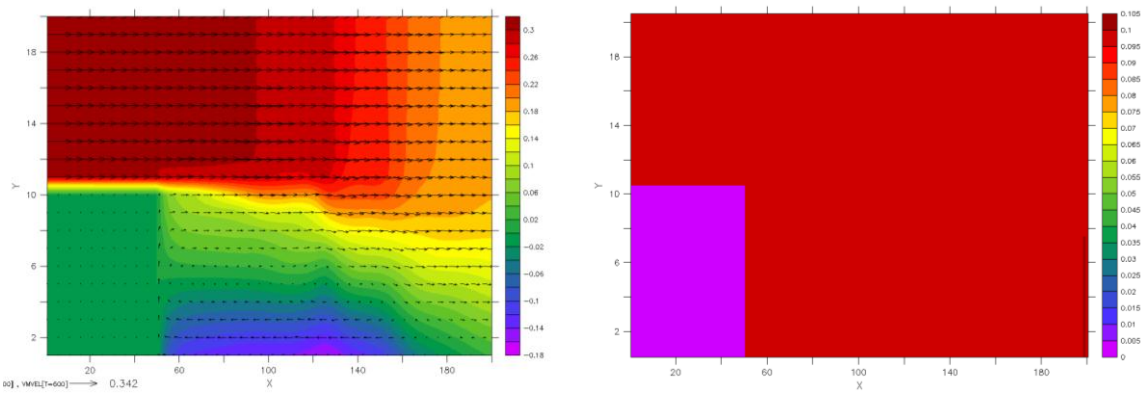

Figure 46 – Calculated mass balance for water (experiments: A, B, C and D) and salinity (experiment: C)

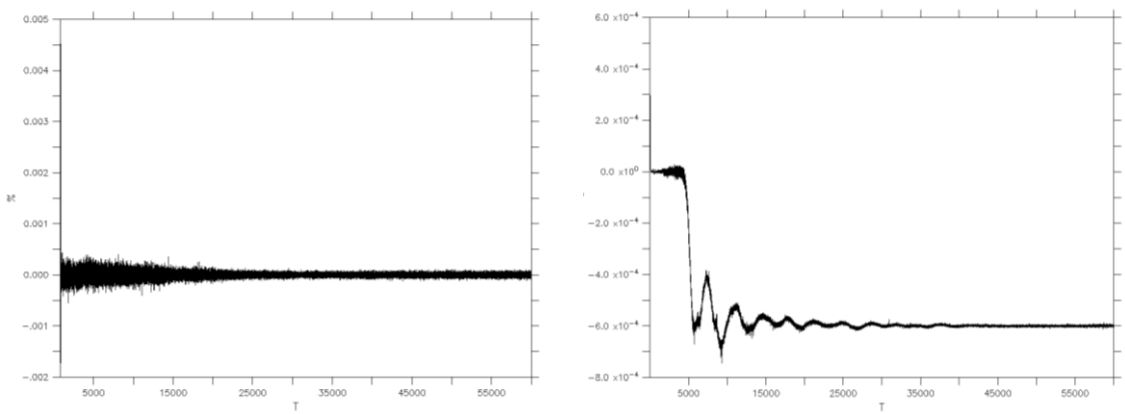

Figure 47 – Calculated transport of salinity for experiment C

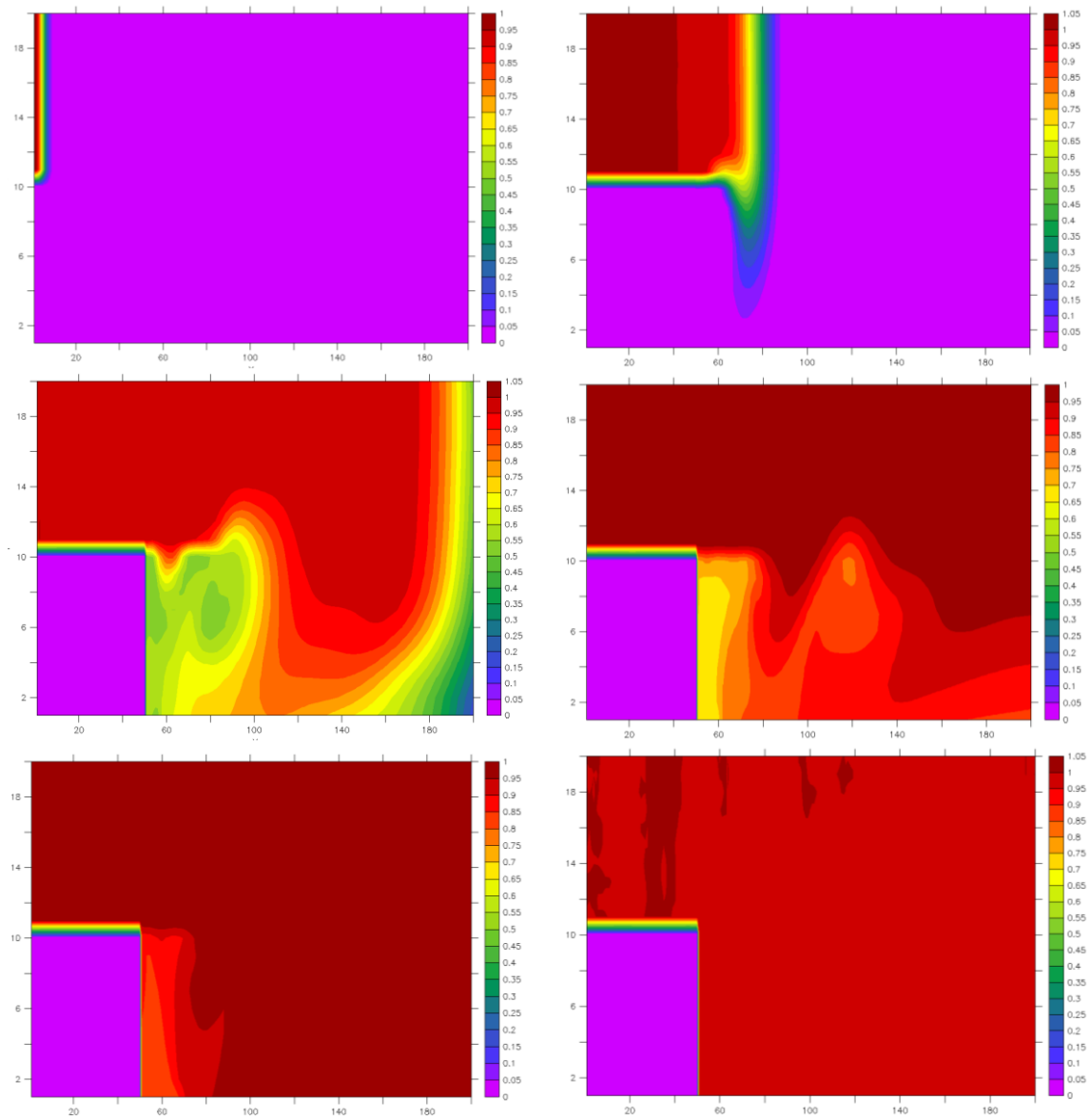

4.2.3 Conclusions

The mass balance of water shows and oscillation around 0.0005% and decreasing along the time with values around 0.0002% of the initial water volume, which is considered acceptable. Regarding the salinity, big oscillations are observed at the beginning of the simulation because the initial conditions of salinity (sal = 0.0); however, the mass balance is stabilized around -0.0006 PSU (˜0.3% of the total inflow weight).

Following, it was verified the transport of scalar within the dry area. It is supposed that this area does not have to present any kind of transport. Experiments C and D were developed to validate it. Figure 47 depicts the transport of salinity along the time. The initial concentration is set to zero for a better assessment. The calculated transport shows that no salinity is present inside the dry area during the whole simulation period (sal = 0.0 PSU).

A similar analysis is performed for the transport of temperature, inside the dry area no temperature should be present. Figure 48 depicts the calculated transport showing that no temperature is present inside the dry area for the whole simulation period.

Figure 48 – Calculated transport of temperature for experiment D

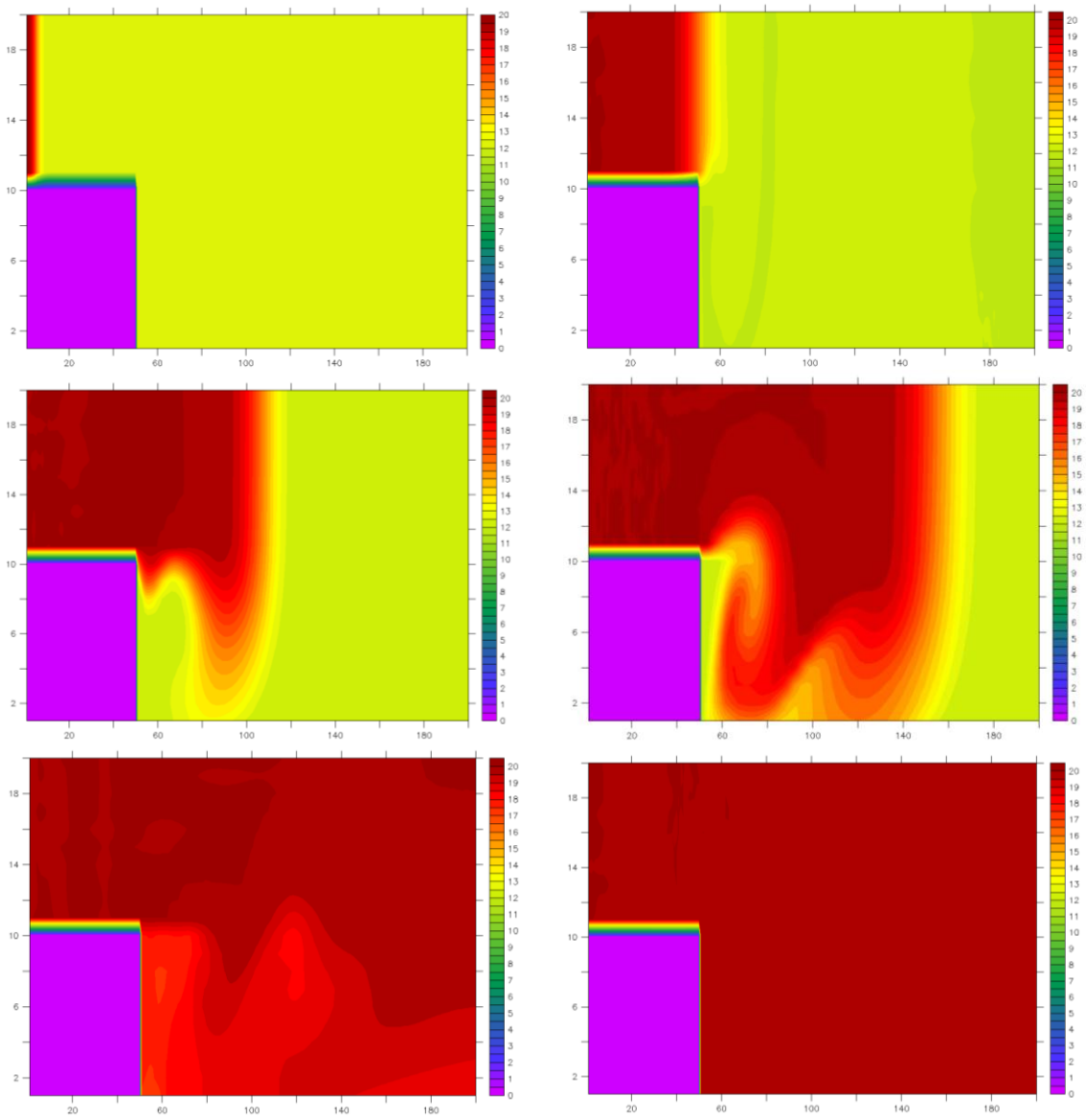

4.3 Validation of “THIN dams” model unit

4.3.1 Model setup

The proposed test case is composed of a channel with a shallow lateral expansion. This test case is presented in Talstra, 2011 (see Fig. 43).

The purpose of the test case is to reproduce the dry area by the application of ‘thin dams’, it is not the purpose to reproduce the recirculation patterns of the experiment. Tabel 10 summarizes the dimensions and the necessary data for the setup of this test case.

Table 10 – Data for the setup of the test case

Parameter	*Value*	*Remarks*
channel length	20 m.	
width	2.0 m.	
mean water depth	0.10 m.	uniform flow
simulation time	20 min.	
length dry area	5 m.	
width dry area	1 m.	
discharge	0.03 m^3/s	constant discharge
mean velocity	0.3 m/s	applied as B.C.
roughness	0.01	Manning coef. for glass
grid size dx = dy	0.20 m.	
time step	0.01 sec.	
initial flow velocity	0.0 m/s	initial condition
initial water surface	0.0 m.	initial condition
initial salinity	0.0 PSU	initial condition
initial temperature	12.0 °C	initial condition
number of rows	11	
number of columns	101	
number of vertical layers	10	for 3D model
B.C. upstream	type 4	specified transport
B.C. downstream	type 2	zero volume flux
B.C. salinity	1.0 PSU	upstream boundary
B.C. temperature	20.0 °C	upstream boundary
schematization dry area	5 U-thin dams	
schematization dry area	25 V-thin dams	

4.3.2 Results

Four test cases were developed, being identified by a letter:

- thin_dams_A: 2D test case

Figure 49 – Comparison of water depths and flow velocities calculated by COHERENS and by using the equation of Bresse for open channel flow

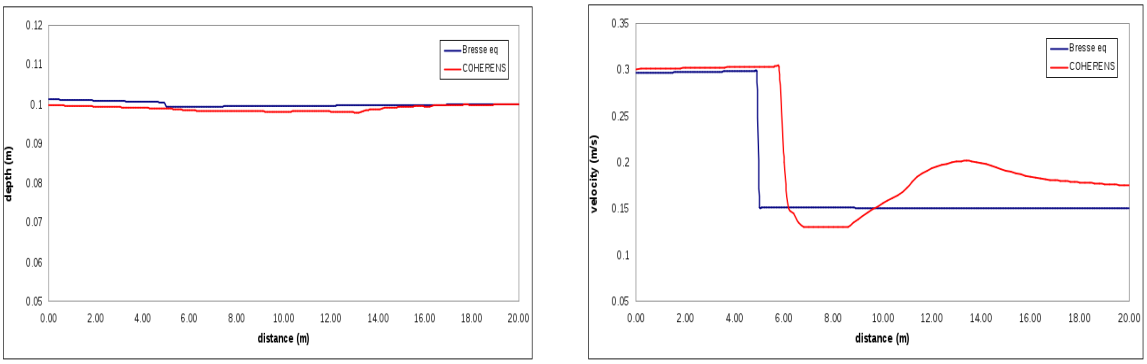

Figure 50 – Calculated flow velocities and water depths after 20 minutes (experiments: A, B, C and D)

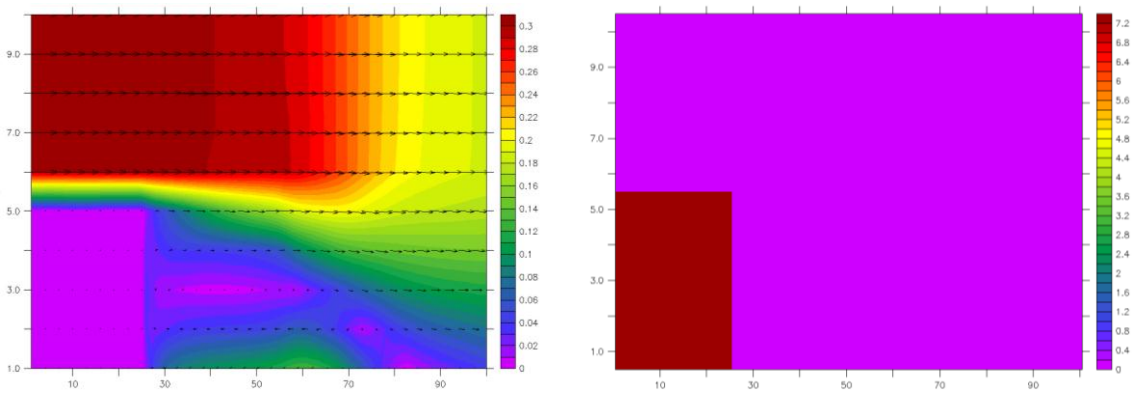

- thin_dams_B: 3D test case
- thin_dams_C: 3D test case with salinity
- thin_dams_D: 3D test case with temperature

The first analysis corresponds to the calculation of water depths and flow velocities. The equation of Brsee for open channel flow is used for this purpose. Figure 49 depicts a comparison of the calculated water depths, showing a reasonable agreement with differences up to 1.8%. The sudden expansion was calculated in the Bresse equation by defining two different sections (i.e. expansion). The calculated flow velocities are also compared showing the same behaviour as observed in the test for 'dry cells' (see Figure 49).

Figure 50 depicts the calculated flow velocities and water depths after 20 minutes. Both figures show clearly that the implemented functionality fulfils its purpose. The dry area is schematized by thin dams and no flow is calculated in this area. In addition, the flow exchange between the wet and dry area was calculated by determining the velocity values at the corresponding U- and V-nodes where the thin dams are defined, showing that no flow is calculated since 'thin dams' make use of the mask functions which are used to perform the calculations of the transport equations.

The mass balance for water and salinity is applied to verify if the implemented functionality is not affecting the calculation of flow and salinity transport. The mass balance equation is used for this purpose. Figure 51 depicts the calculated mass balance for water and salinity.

Figure 51 – Calculated mass balance for water (experiments: A, B, C and D) and salinity (experiment: C)

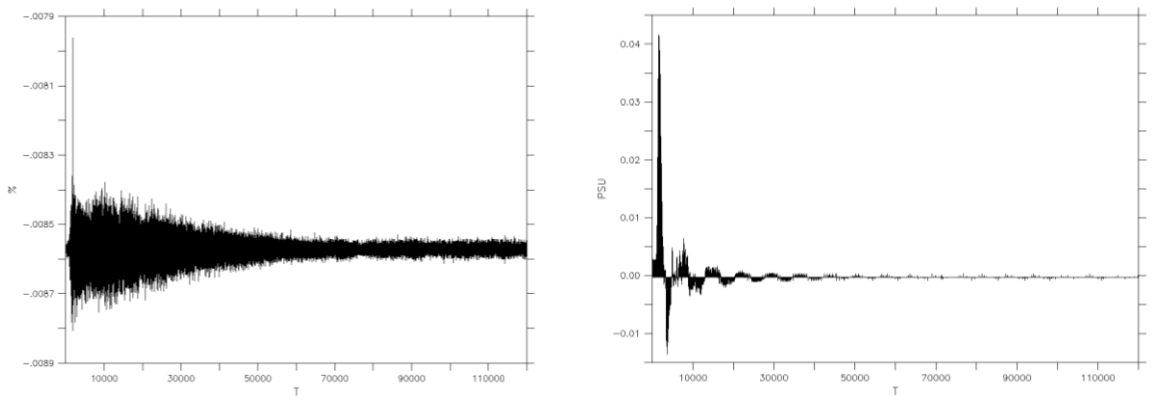

4.3.3 Conclusions

The mass balance of water shows and oscillation around 0.0001% and decreasing along the time with values around 0.00005% of the initial water volume, which is considered acceptable. Regarding the salinity, big oscillations are observed at the beginning of the simulation because the initial conditions of salinity (sal = 0.0); however, the mass balance is stabilized around -0.0001 PSU (˜0.3% of the total inflow weight).

Following, it was verified the transport of scalar within the dry area and the presence of possible transport between the dry and the wet areas. considering that this area does not have to present any kind of exchange of scalars with the wet area. The reason of this verification lies in the fact that the area delimited by the 'thin dams' contains water that does not have to interact with the water behind the 'thin dams'. Experiments C and D were developed to validate it. Figure 52 depicts the transport of salinity along the time. The initial concentration is set to zero for a better assessment. The calculated transport shows that no salinity is present inside the dry area during the whole simulation period (sal = 0.0 PSU), leading to the conclusion that no exchange of salt takes place at both sides of the defined 'thin dams'.

A similar analysis is performed for the transport of temperature, inside the dry area no temperature should be present. Figure 53 depicts the calculated transport showing that no temperature is added to the dry area (behind the thin dams) for the whole simulation period.

Figure 52 – Calculated transport of salinity for experiment C

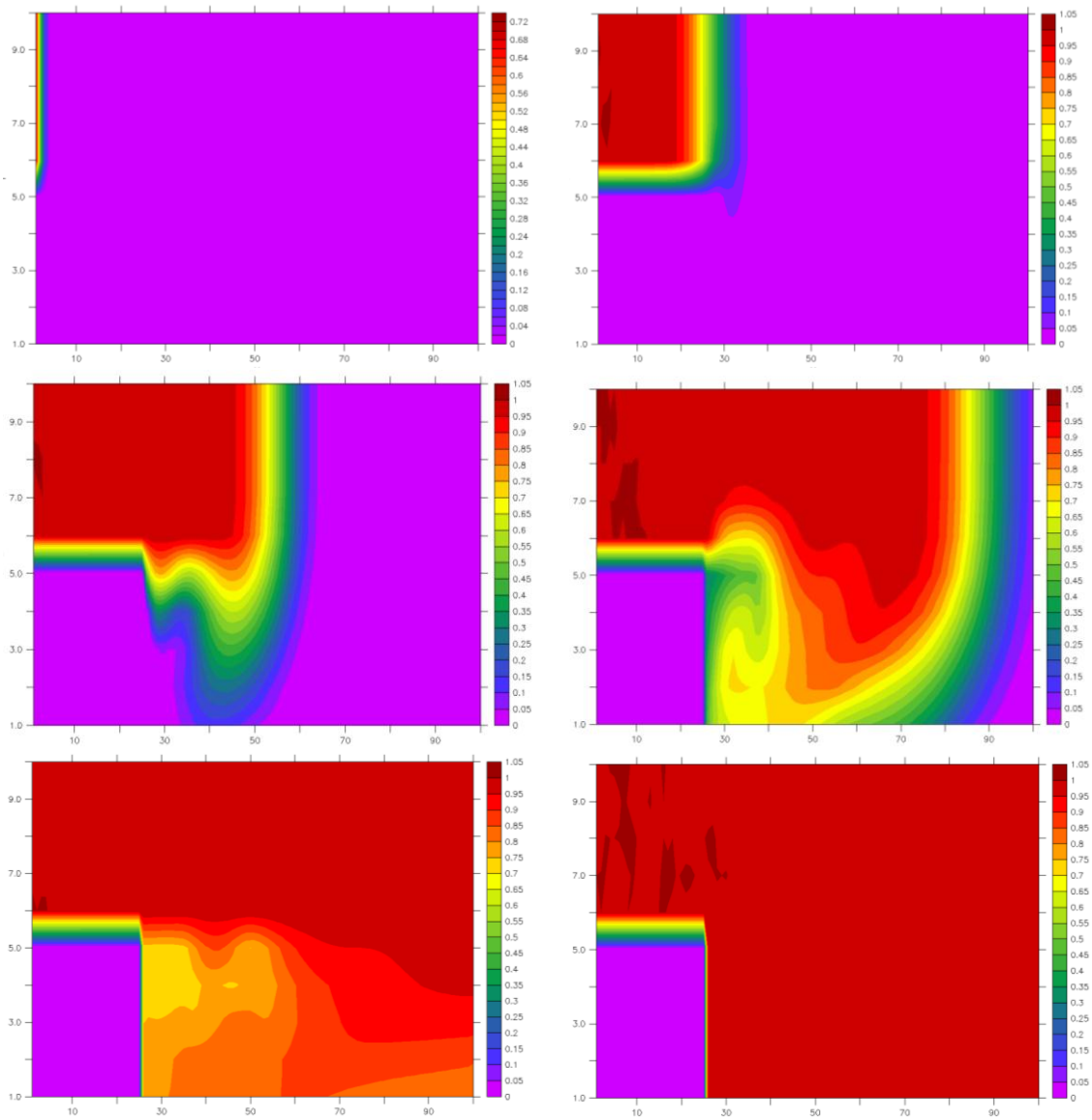

Figure 53 – Calculated transport of temperature for experiment D

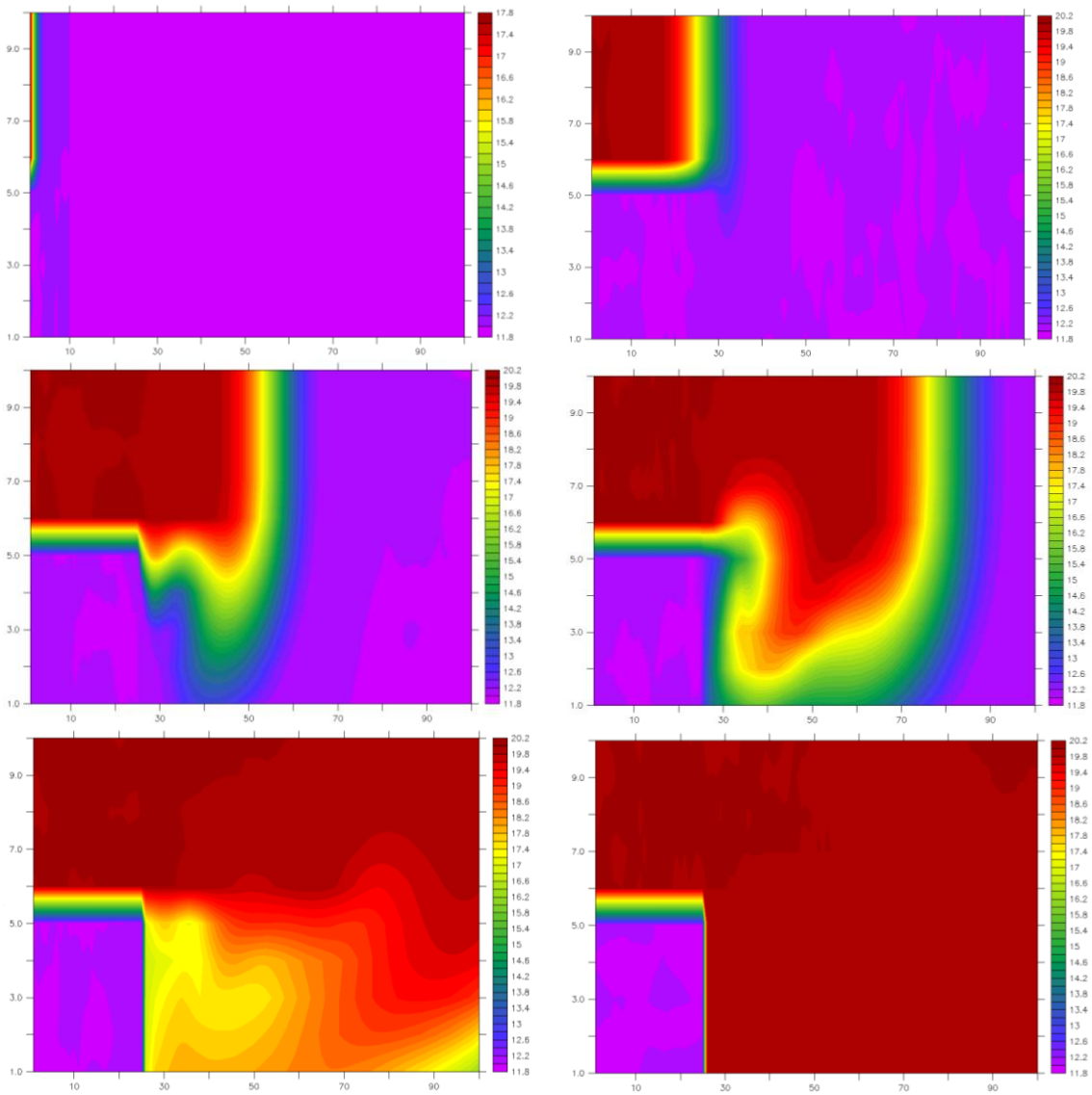

4.4 Validation of “weirs/barriers” model unit

4.4.1 Model setup

This model unit can be applied to U or V-nodes. for 2D and 3D mode simulations. This model unit focuses on the schematization of two types of structures: weirs and CDW. The validation test case will assess the blocking and the energy loss due to the definition of the model unit. Different configurations are proposed to test the model unit, they are listed in Table 11.

Table 11 – List of configurations

Description	Scheme
Open channel with a weir under tidal conditions	
Open channel with a weir under tidal conditions with a dry area	
Open channel with a CDW with one orifice under submerged conditions	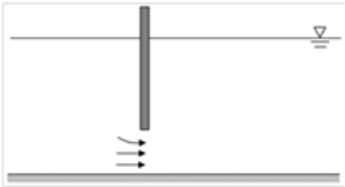
Open channel with a CDW under submerged conditions with two openings	
Open channel with a CDW with one orifice with free flow	

Table 12 summarizes the dimensions and the necessary data for the setup of this test case.

Table 12 – Data for the setup of the test case

Parameter	Value	Remarks
channel length	1000 m.	
width	10.0 m.	
mean water depth	10.0 m.	bathymetry
simulation time	1 hour	6 hour for tidal condition
crest of weir	9 m.	12 m for exp I,J and K
height of opening CDW	2 m.	5m for exp. O,P and Q
amplitude	2.0 m.	tidal condition B.C.
mean velocity	0.1 m/s	applied as B.C.
roughness grid size dx = dy	0.005 m 10.0 m.	roughness height
time step	0.02 sec.	0.5 sec. for 2D experiments
initial flow velocity initial water surface	0.0 m/s 0.0 m.	initial condition -2.00 for tidal condition
initial salinity	0.0 PSU	initial condition
initial temperature	12.0 °C	initial condition
number of rows	2	
number of columns	101	
number of vertical layers	20	for 3D model
B.C. upstream	type 4	type 3 for tidal
B.C. downstream	type 2	zero volume flux
B.C. salinity	1.0 PSU	upstream boundary
B.C. temperature location weir (CDW)	20.0 °C 500.0 m.	upstream boundary

4.4.2 Results

Several test cases were developed for the different configurations, being identified by a letter:

- weirs_barriers_A: 2D weir under tidal condition
- weirs_barriers_B: 3D weir under tidal condition
- weirs_barriers_C: 3D weir salinity under tidal condition
- weirs_barriers_D: 3D weir temperature under tidal condition
- weirs_barriers_E: 2D weir with dry area under tidal condition
- weirs_barriers_F: 3D weir with dry area under tidal condition
- weirs_barriers_G: 3D weir with dry area salinity under tidal condition
- weirs_barriers_H: 3D weir with dry area temperature under tidal condition
- weirs_barriers_I: CDW with 1 opening
- weirs_barriers_J: CDW with 1 opening salinity
- weirs_barriers_K: CDW with 1 opening temperature
- weirs_barriers_L: CDW with 2 openings
- weirs_barriers_M: CDW with 2 openings salinity
- weirs_barriers_N: CDW with 2 openings temperature
- weirs_barriers_O: CDW with free flow

Figure 54 – Calculated water depths along the channel for experiments A, B, C and D (not in scale).

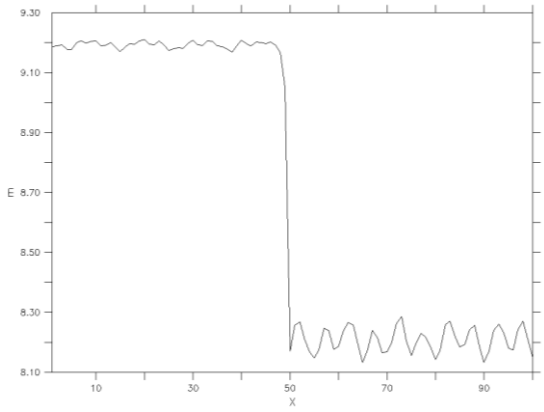

Figure 55 – Calculated water depths at the U-node where the structure is prescribed for experiments A, B, C and D (not in scale)

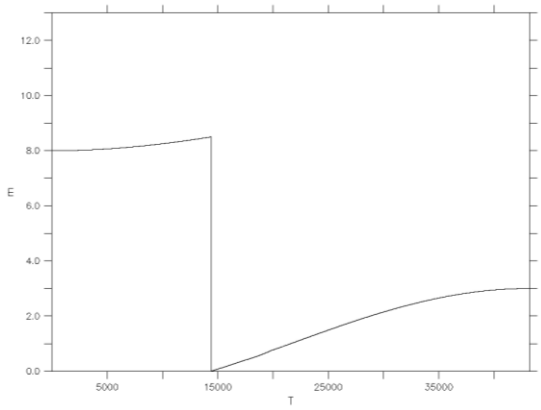

- weirs_barriers_P: CDW with free flow salinity
- weirs_barriers_Q: CDW with free flow temperature

For a better assessment the experiments are divided in 5 groups according to the configuration given in Table 11.

Weir under tidal condition (experiments: A, B, C and D)

The first validation corresponds to the verification of the application of a loss of energy. This should imposed once the corresponding U- or V-node is unblocked. Figure 54 depicts the calculated water depth along the channel, it clearly shows the difference of water depths upstream and downstream the structure.

The water depth at the location of the structure (i.e. U-node) should present the water depth measured from the crest of the structure, Figure 55 depicts the calculated water depth at the location of the structure. The initial depth (H=8) corresponds to the period when the U-node is blocked and no flow is allowed, as a consequence, COHERENS calculated the water depth based on the value of the neighbouring C-nodes. However, this value is meaningless since this node is not used in the calculations while is blocked. Once is unblocked, the graph shows how the water depth above the structure evolves according to the tidal condition.

Figure 56 depicts the calculated flow velocities in 3D mode, the figure shows the partial blocking process. The vertical layers above layer 16 are free allowing the flow over the structure, while the layers below that level are blocked, not allowing any kind of flow.

Figure 56 – Vertical view of the calculated flow velocities for experiments B, C and D (not in scale)

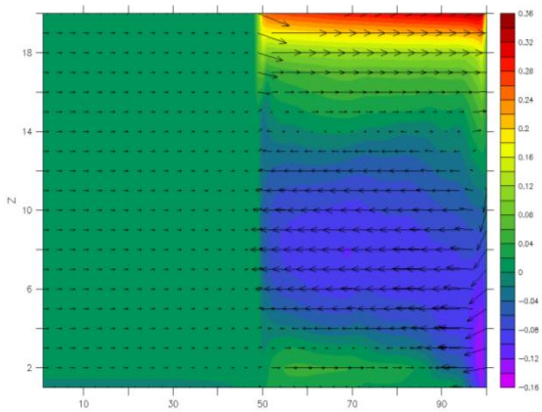

Figure 57 – Vertical view of the calculated transport of salinity and temperature for experiments C and D (not in scale)

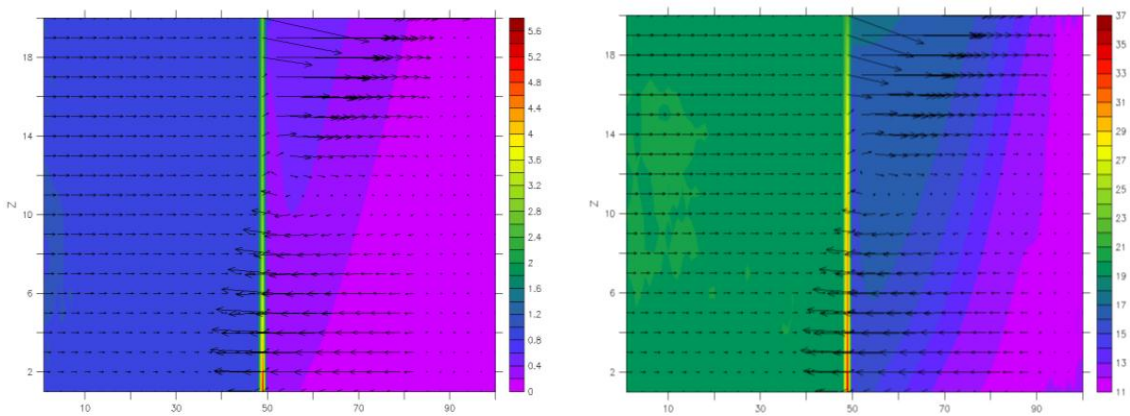

A similar analysis is performed for the transport of scalars (i.e. salinity and temperature), Figure 57 depicts the calculated transport of scalars, showing that the scalars are being transported only in the upper layers (not blocked) while the lower vertical layers are blocking the transport of the scalar.

The mass balance is calculated for the transport of water and salinity (see Figure 58). The calculated mass balance for water shows and acceptable accuracy, less than 0.0018% of the initial volume of water, this parameter was also calculated for larger simulation periods showing also acceptable values. A similar behaviour is observed for the calculation of the conservation of mass in the case of salinity. The bigger values observed at the beginning of the simulation are result of the prescribed initial conditions inside the channel (SAL = 0.0 PSU), after the system reaches an equilibrium, the mass balance decreases and show values close to zero (˜0.05 PSU).

Weir under tidal condition (experiments: E, F, G and H)

Similarly to the previous test case, the first validation corresponds to the verification of the application of a loss of energy. This should imposed once the corresponding U- or V-node is unblocked. Figure 59 depicts the calculated water depth along the channel, it clearly shows the difference of water depths upstream and downstream the structure. Bigger oscillations are observed upstream the structure since the prescribed initial condition considers a dry area behind the structure.

The water depth at the location of the structure (i.e. U-node) should present the water depth measured from the crest of the structure, Figure 60 depicts the calculated water depth at the location of the structure. The

Figure 58 – Calculated mass balance for the transport of water and salinity for experiments A, B, C and D

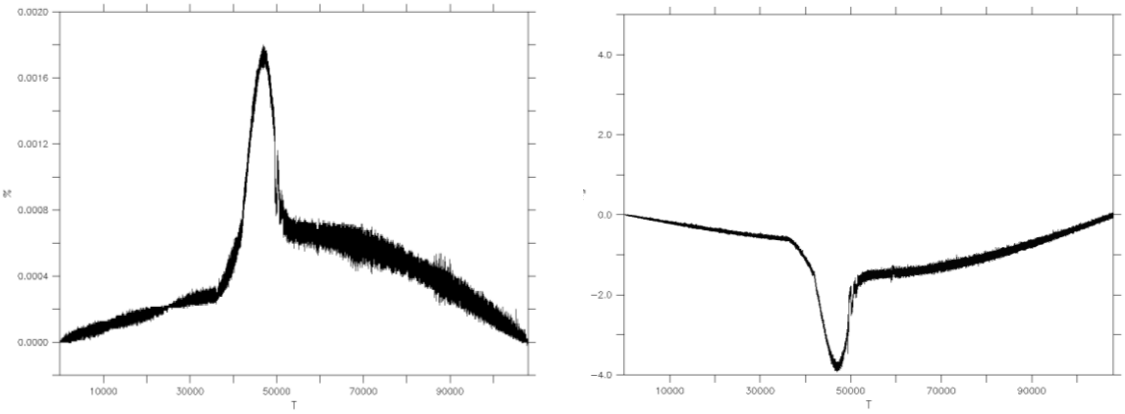

Figure 59 – Calculated water depths along the channel for experiments E, F, G and H (not in scale)

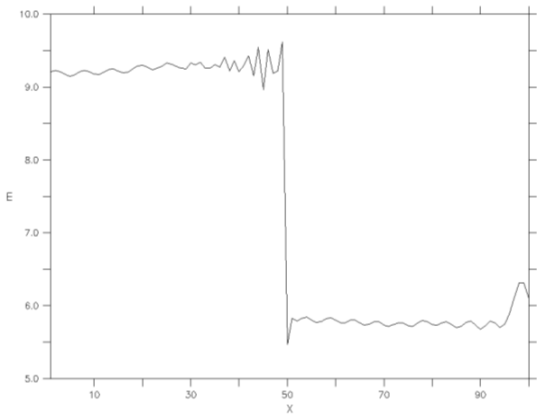

Figure 60 – Calculated water depths at the U-node where the structure is prescribed for experiments E, F, G and H (not in scale)

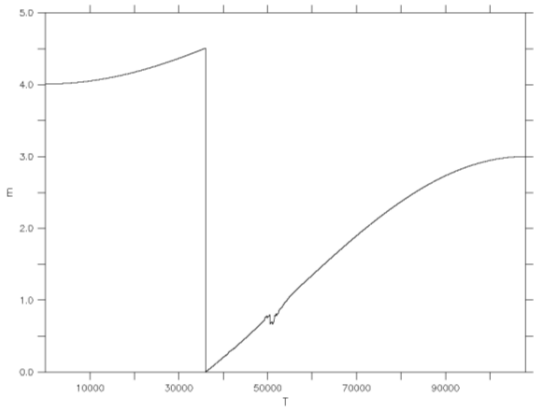

Figure 61 – Vertical view of the calculated flow velocities for experiments F, G and H (not in scale)

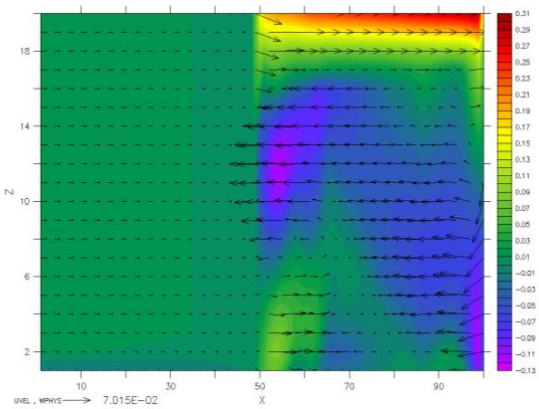

initial depth (H=4) corresponds to the period when the U-node is blocked and no flow is allowed, as a consequence, COHERENS calculated the water depth based on the value of the neighbouring C-nodes (i.e. 0.0m and 8.0m). However, this value is meaningless since this node is not used in the calculations while is blocked. Once is unblocked, the graph shows how the water depth above the structure evolves according to the tidal condition.

Figure 61 depicts the calculated flow velocities in 3D mode, the figure shows the partial blocking process. The vertical layers above layer 16 are free allowing the flow over the structure, while the layers below that level are blocked, not allowing any kind of flow.

A similar analysis is performed for the transport of scalars (i.e. salinity and temperature), Figure 62 depicts the calculated transport of scalars, showing that the scalars are being transported only in the upper layers (not blocked) while the lower vertical layers are blocking the transport of the scalar.

The mass balance is calculated for the transport of water and salinity (see Figure 63). The calculated mass balance for water shows and acceptable accuracy, less than 0.013% of the initial volume of water,. The observed bigger values and oscillations are because the prescribed initial conditions with zero flow velocity and a dry area behind the structure. However, this parameter was also calculated for larger simulation periods showing also acceptable values (˜0.00001%) once the system is stabilized. A similar behaviour is observed for the calculation of the conservation of mass in the case of salinity. The bigger values observed at the beginning of the simulation are result of the prescribed initial conditions inside the channel (SAL = 0.0 PSU), after the system reaches an equilibrium, the mass balance decreases and show values close to zero (˜0.001 PSU).

Figure 62 – Vertical view of the calculated transport of salinity and temperature for experiments G and H (not in scale)

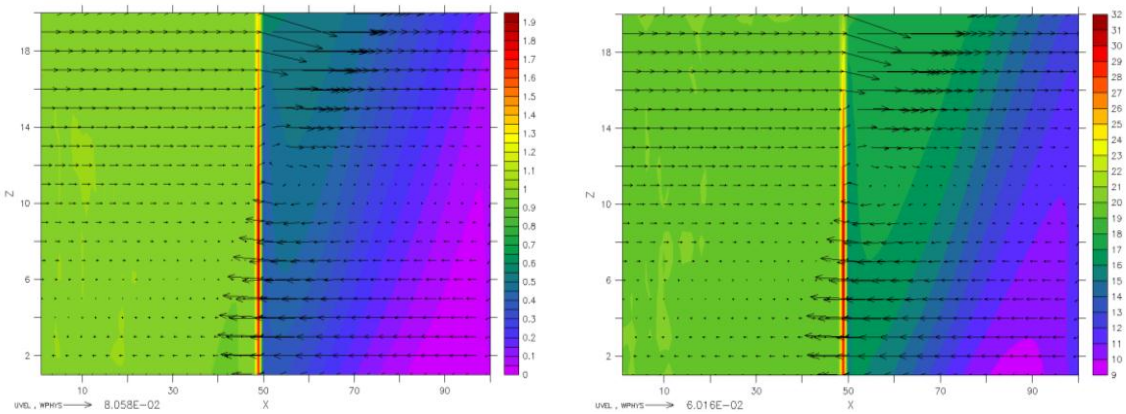

Figure 63 – Calculated mass balance for the transport of water and salinity for experiments E, F, G and H

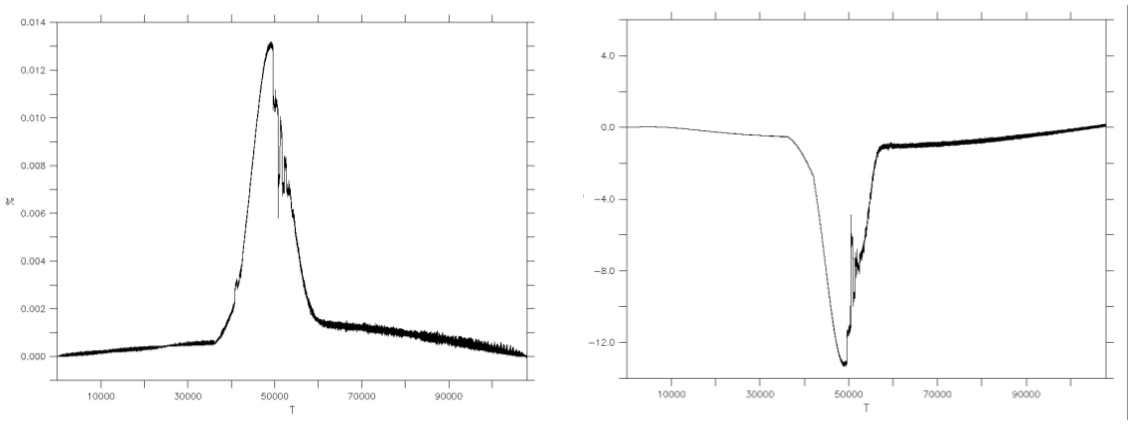

Figure 64 – Calculated water depths along the channel for experiments I, J, and K (not in scale)

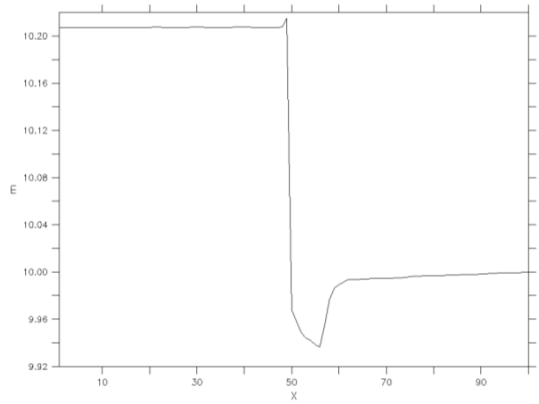

Figure 65 – Calculated mass balance for the transport of water and salinity for experiments I, J, and K

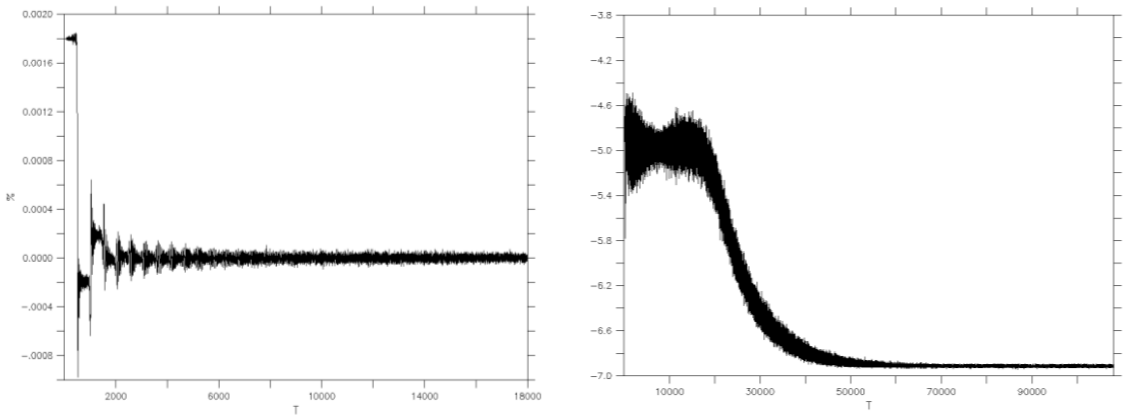

CDW with one opening (experiments: I, J and K)

The first validation corresponds to the verification of the application of a loss of energy. This should imposed due to the contraction and expansion of flow due to the opening close to the bottom. Figure 64 depicts the calculated water depth along the channel, it clearly shows the difference of water depths upstream and downstream the structure.

The mass balance is calculated for the transport of water and salinity (see Figure 65). The calculated mass balance for water shows and acceptable accuracy, less than 0.0001% of the initial volume of water,. The observed bigger values and oscillations are because the prescribed initial conditions with zero flow velocity. However, this parameter was also calculated for larger simulation periods showing also acceptable values. The calculation of the conservation of mass in the case of salinity presents bigger values at the beginning of the simulation, which are result of the prescribed initial conditions inside the channel (SAL = 0.0 PSU), after the system reaches an equilibrium with oscillations lower than 0.0005 PSU.

Figure 66 depicts the calculated flow velocities in 3D mode, the figure shows the partial blocking process. The vertical layers below layer 3 are free allowing the flow through the opening close to the bottom, while the layers

A similar analysis is performed for the transport of scalars (i.e. salinity and temperature), Figure 67 depicts the calculated transport of scalars, showing that the scalars are being transported only in the lower layers (not blocked) while the upper vertical layers are blocking the transport of the scalar.

Figure 66 – Vertical view of the calculated flow velocities for experiments I, J and K (not in scale)

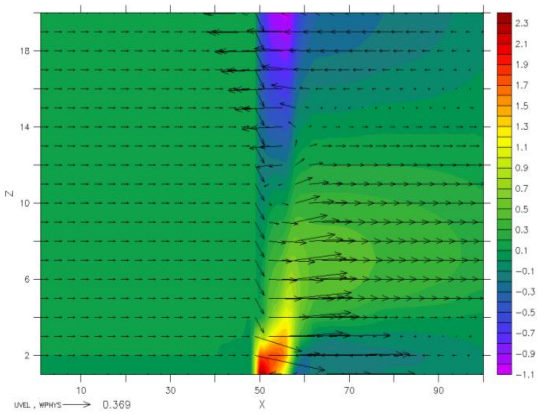

Figure 67 – Vertical view of the calculated transport of salinity and temperature for experiments J and K (not in scale)

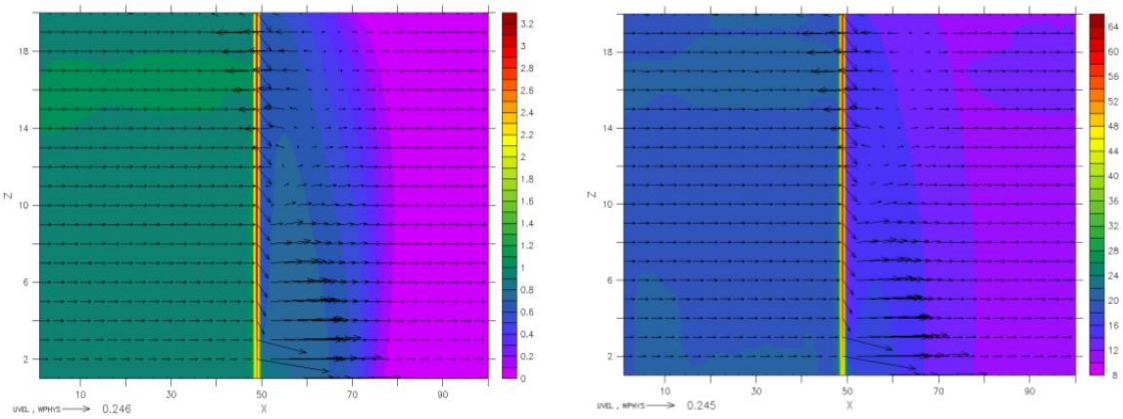

Figure 68 – Calculated water depths along the channel for experiments L, M, and N (not in scale)

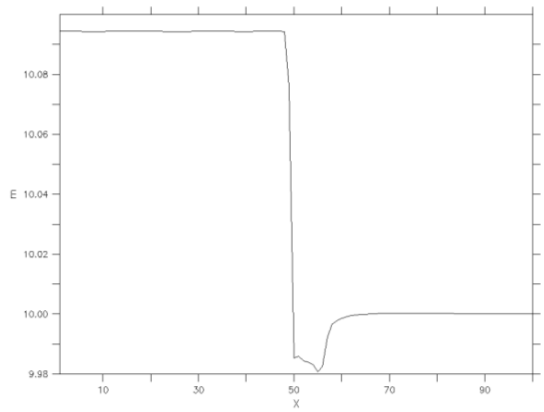

Figure 69 – Calculated mass balance for the transport of water and salinity for experiments L, M, and N

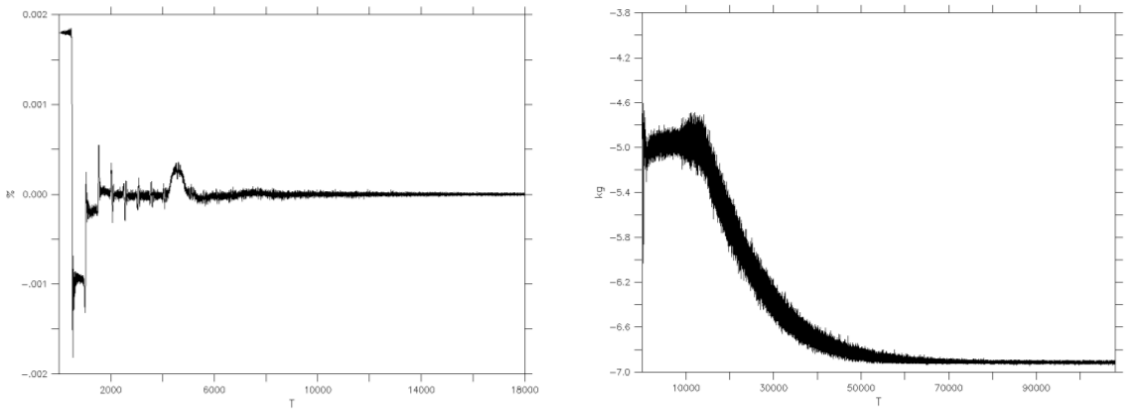

CDW with two openings (experiments: L, M and N)

The first validation corresponds to the verification of the application of a loss of energy. This should imposed due to the contraction and expansion of flow due to the openings close to the bottom and at the surface. Figure 68 depicts the calculated water depth along the channel, it clearly shows the difference of water depths upstream and downstream the structure.

The mass balance is calculated for the transport of water and salinity (see Figure 69). The calculated mass balance for water shows and acceptable accuracy, less than 0.0001% of the initial volume of water,. The observed bigger values and oscillations are because the prescribed initial conditions with zero flow velocity. However, this parameter was also calculated for larger simulation periods showing also acceptable values. The calculation of the conservation of mass in the case of salinity presents bigger values at the beginning of the simulation, which are result of the prescribed initial conditions inside the channel (SAL = 0.0 PSU), after the system reaches an equilibrium with oscillations lower than 0.0005 PSU.

Figure 70 depicts the calculated flow velocities in 3D mode, the figure shows the partial blocking process. The vertical layers below layer 3 and the upper layers above layer 16 are free allowing the flow through the opening close to the bottom and at the surface, while the rest of the layers are blocked, not allowing any kind of flow.

A similar analysis is performed for the transport of scalars (i.e. salinity and temperature), Figure 71 depicts the calculated transport of scalars, showing that the scalars are being transported only in the layers that are not blocked (close to the bottom and at the surface) while the rest of the layers are blocking the transport of the scalar.

Figure 70 – Vertical view of the calculated flow velocities for experiments L, M and N (not in scale)

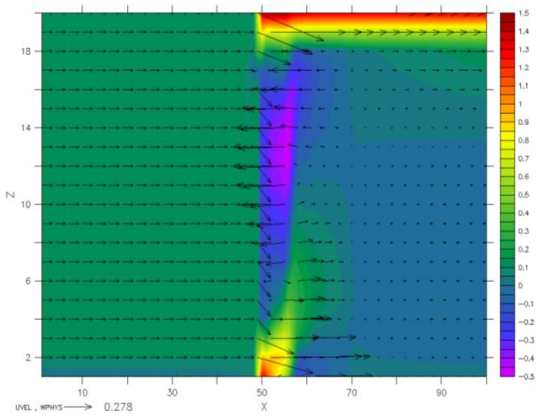

Figure 71 – Vertical view of the calculated transport of salinity and temperature for experiments M and N (not in scale)

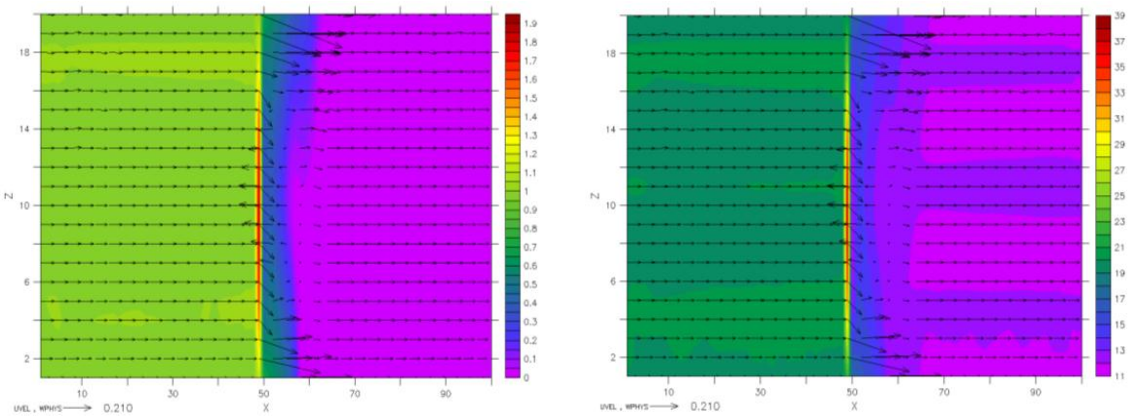

Figure 72 – Calculated water depths along the channel for experiments O, P, and Q (not in scale)

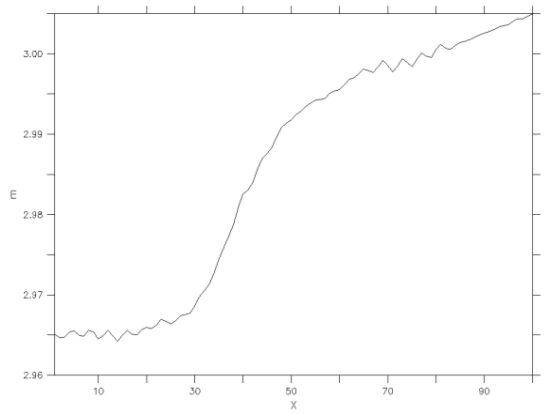

Figure 73 – Calculated mass balance for the transport of water and salinity for experiments O, P, and Q

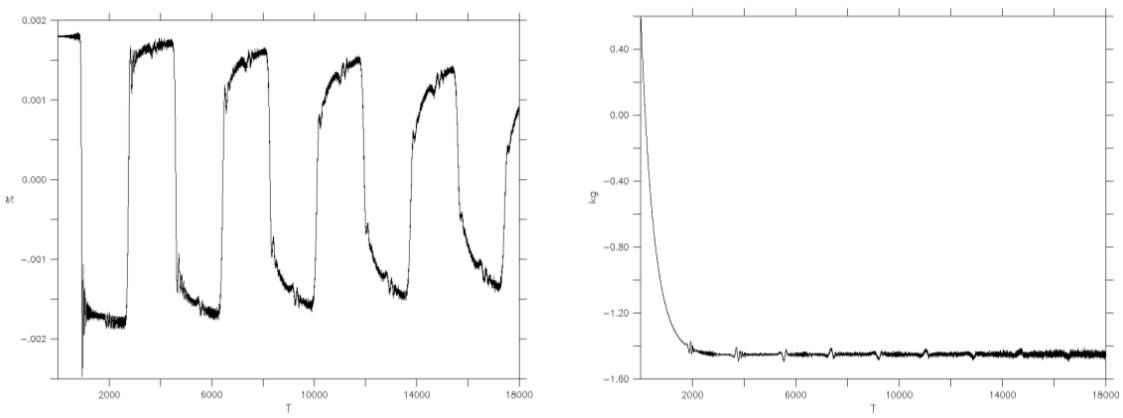

CDW under free flow (experiments: O, P and Q)

The first validation corresponds to the verification of the application of a loss of energy and the blocking of the flow. Since the opening of the structure is prescribed above of the surface level, a free flow condition should be imposed. Therefore, no blocking and no loss of energy should be observed. Figure 72 depicts the calculated water depth along the channel, it clearly shows that there is not variation in the water depth due to the structure, the observed difference is due to the boundary conditions prescribed at the downstream open boundary, with a difference of 4 cm in 1000 of length.

The mass balance is calculated for the transport of water and salinity (see Figure 73). The calculated mass balance for water shows and acceptable accuracy, with oscillations less than 0.0015% of the initial volume of water,. The observed bigger values and oscillations are because the prescribed initial conditions with zero flow velocity. However, this parameter was also calculated for larger simulation periods showing also acceptable values. The calculation of the conservation of mass in the case of salinity presents bigger values at the beginning of the simulation, which are result of the prescribed initial conditions inside the channel (SAL = 0.0 PSU), after the system reaches an equilibrium with oscillations lower than 0.01 PSU.

Figure 74 depicts the calculated flow velocities in 3D mode, the figure shows that there is no blocking process. The vertical layers are not blocked and are allowing the flow in the whole water column.

A similar analysis is performed for the transport of scalars (i.e. salinity and temperature), Figure 75 depicts the calculated transport of scalars, showing that the scalars are being transported freely without any blocking.

Figure 74 – Vertical view of the calculated flow velocities for experiments O, P and Q (not in scale)

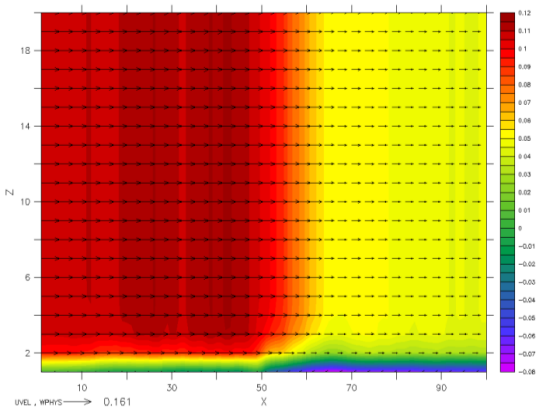

Figure 75 – Vertical view of the calculated transport of salinity and temperature for experiments P and Q (not in scale)

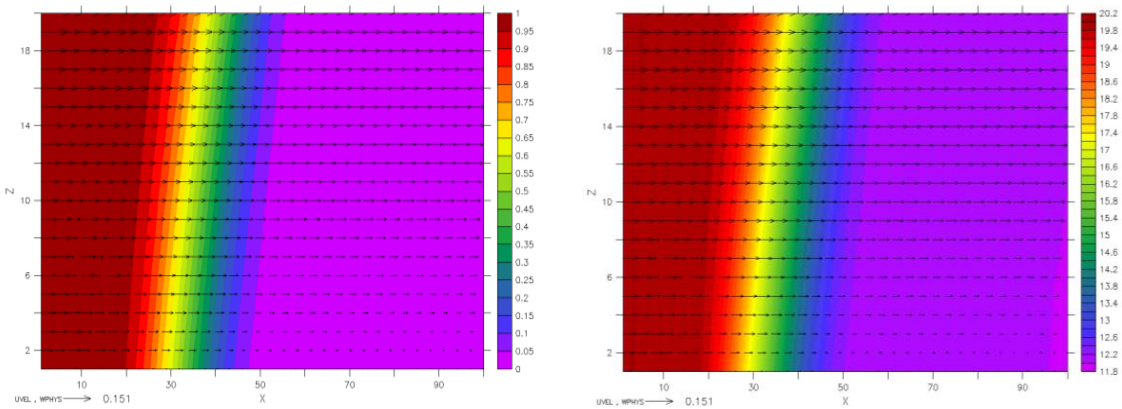

4.4.3 Conclusions

The conclusions that can be drawn from the above experiments will be grouped below, acoording to the setups displayed in Table 11.

Weir under tidal conditions (experiments A-D)

Here, the relative accuracy of water mass balance was smaller than 0.0018%. The deviations of salinity were at most 0.05 PSU.

Weir with dry area under tidal conditions (experiments E-H)

Here, the relative accuracy of water mass balance was smaller than 0.013%. The deviations of salinity were at most 0.001 PSU.

CDW with one or two openings (experiments I-K and L-N, respectively)

Here, the relative accuracy of water mass balance was smaller than 0.0001%. The deviations of salinity were at most 0.0005 PSU.

CDW with free flow (experiments O-Q)

Here, the relative accuracy of water mass balance was smaller than 0.0015%. The deviations of salinity were at most 0.01 PSU.

4.5 Validation of “discharges” model unit

4.5.1 Model setup

The discharges model unit simulates the effect of discharges (intake and outlet) in the study area. The implementation considers the discharge of clear water and the discharge of scalars (e.g. salinity, temperature). The validation test cases are applied for both types of discharges: normal discharges where no direction is considered and momentum discharges where the direction of the discharge is considered. Therefore, the validation test cases are divided in groups with a total number of 18 test cases, see Table 13.

Table 14 summarizes the dimensions and the necessary data for the setup of this test case.

4.5.2 Results

Several test cases were developed for the different configurations, being identified by a letter:

- discharges_A 2D normal discharge
- discharges_B 2D momentum discharge
- discharges_C 2D salinity normal discharge
- discharges_D 2D salinity momentum discharge
- discharges_E 2D temperature normal discharge

Table 13 – List of configurations

Model Unit	Test case	Mode	Type
Normal and Momentum Discharges	Open channel with a discharge	2D	hydrodynamic
	Open channel with a discharge	2D	salinity
	Open channel with a discharge	2D	temperature
Normal and Momentum Discharges	Open channel with a discharge	3D distrib.	hydrodynamic
	Open channel with a discharge	3D distrib.	salinity
	Open channel with a discharge	3D distrib.	temperature
Normal and Momentum Discharges	Open channel with a discharge	3D local	hydrodynamic
	Open channel with a discharge	3D local	salinity
	Open channel with a discharge	3D local	temperature

- discharges_F 2D temperature momentum discharge
- discharges_G 3D distributed normal discharge
- discharges_H 3D distributed momentum discharge
- discharges_I 3D distributed salinity normal discharge
- discharges_J 3D distributed salinity momentum discharge
- discharges_K 3D distributed temperature normal discharge
- discharges_L 3D distributed temperature momentum discharge
- discharges_M 3D local normal discharge
- discharges_N 3D local momentum discharge
- discharges_O 3D local salinity normal discharge
- discharges_P 3D local salinity momentum discharge
- discharges_Q 3D local temperature normal discharge
- discharges_R 3D local temperature momentum discharge

For a better assessment the experiments are divided in 3 groups according to the configuration given in Table 13.

Discharges 2D (experiments: A, B, C, D, E and F)

The discharge is applied to the open channel. Hence, it is expected that the flow behaviour of the channel would be affected by the added source. Figure 76 depicts the calculated flow velocity with the presence of the added discharge that affects the flow behaviour of the channel.

A similar assessment is applied to the transport of scalars, Figure 77 depicts the discharge of salinity and temperature, clearly affected by the direction of the flow.

The validation of the mass balance is important since a new source is added to the domain. Figure 78 depicts the calculated mass balance for water and salinity. The mass balance of water shows an acceptable accuracy with oscillations of the order of 0.0002% of the initial volume. The mass balance for salinity also shows an acceptable performance with oscillations lower than 0.006 PSU (˜0.06%).

Discharges 3D- distributed (experiments: G, H, I, J, K and L)

Figure 79 depicts the calculated flow velocity with the presence of the added discharge that affects the flow behaviour of the channel.

Figure 76 – Calculated flow velocities with the presence of the discharge for experiments A, B, C, D, E and F (not in scale)

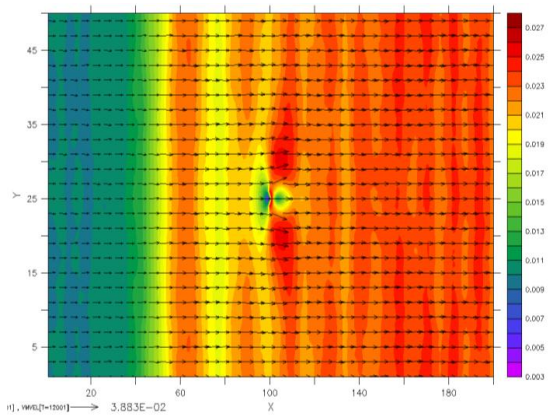

Figure 77 – Calculated transport of scalars due to the presence of the discharge for experiments C, D, E and F (not in scale)

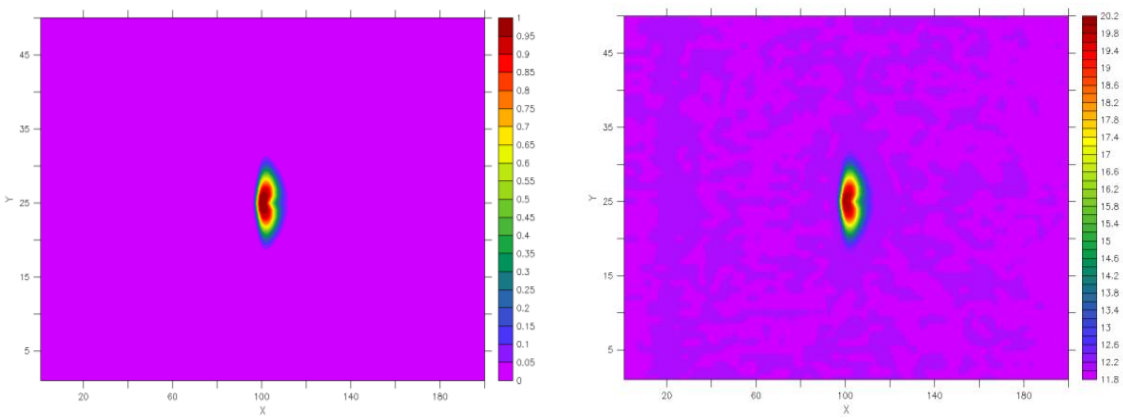

Figure 78 – Calculated mass balance for the transport of water and salinity, experiments A, B,C, D, E and F

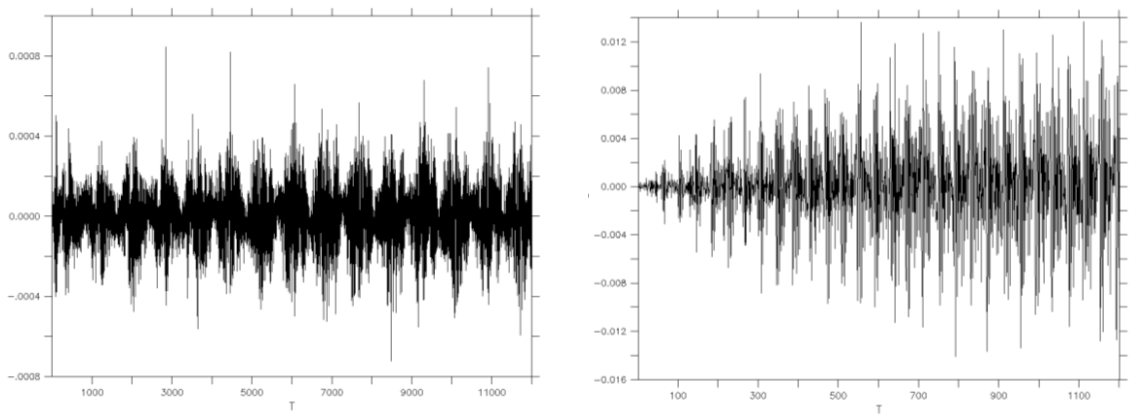

Table 14 – Data for the setup of the test case

Parameter	Value	Remarks
channel length	200 m.	2000m for tidal condition
width	50.0 m.	500m for tidal condition
mean water depth	10.0 m.	bathymetry
simulation time	10 min	6 hour for tidal condition
amplitude	2.0 m.	tidal condition B.C.
mean velocity	0.01 m/s	applied as B.C.
roughness	0.006 m	roughness height
grid size dx = dy	1.0 m.	10.0m for tidal condition
time step	0.05 sec.	0.5 sec. for tidal condition
initial flow velocity	0.0 m/s	initial condition
initial water surface	0.0 m.	2.00 for tidal condition
initial salinity	0.0 PSU	initial condition
initial temperature	12.0 °C	initial condition
number of rows	51	
number of columns	201	
number of vertical layers	10	for 3D model
B.C. upstream	type 4	type 3 for tidal
B.C. downstream	type 2	zero volume flux
X-coordinate discharge	100m	1000m for tidal condition
Y-coordinate discharge	25m	250m for tidal condition
Z-coordinate discharge	1.0m (from MSL)	for tidal condition
Discharge	1.0 m3/s	5.0 m3/s for tidal condition
Area of discharge	1.0 m2	momentum discharge
Direction discharge	90°	momentum discharge
Salinity discharge	1 PSU	
Temperature discharge	20°C	

A similar assessment is applied to the transport of scalars, Figure 80 depicts the discharge of salinity and temperature, clearly affected by the direction of the flow.

The validation of the mass balance is important since a new source is added to the domain. Figure 81 depicts the calculated mass balance for water and salinity. The mass balance of water shows an acceptable accuracy with oscillations of the order of 0.003% of the initial volume. The mass balance for salinity also shows an acceptable performance with oscillations lower than 0.01 PSU (˜0.1%).

Discharges 3D- local (experiments: M, N, O, P, Q and R)

A local discharge is applied 1m below the MSL, with the aim to be deactivated once the water surface falls below this level due to the tidal condition. Figure 82 depicts the calculated flow velocities with the presence of the discharge, the last two graphs correspond to the moments when the discharge is deactivated, it is possible to see that the calculated flow velocities that corresponds to the discharge were displaced from the original

Figure 79 – Calculated flow velocities with the presence of the discharge for experiments G, H, I, J, K and L (not in scale)

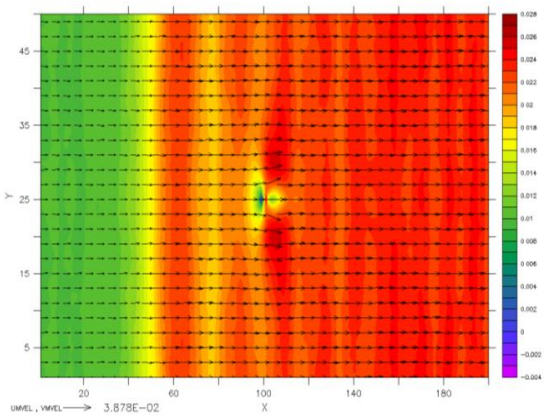

Figure 80 – Calculated transport of scalars due to the presence of the discharge for experiments I, J, K and L (not in scale)

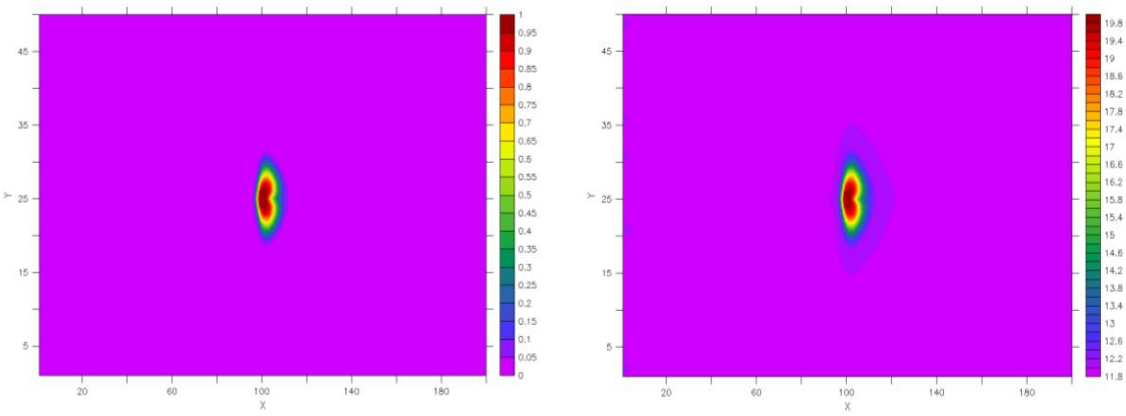

Figure 81 – Calculated mass balance for the transport of water and salinity, experiments G, H,I, J, K and L

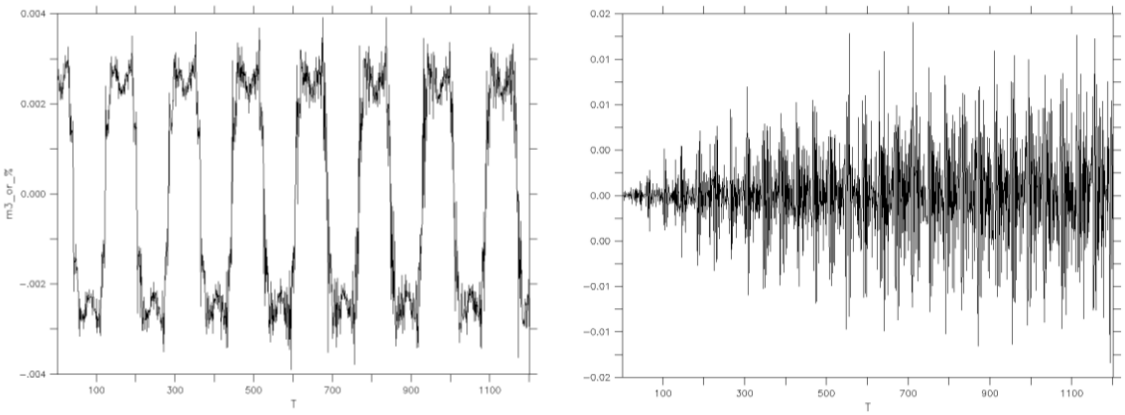

Figure 82 – Calculated flow velocities at different moments, experiments M, N, O, P, Q and R

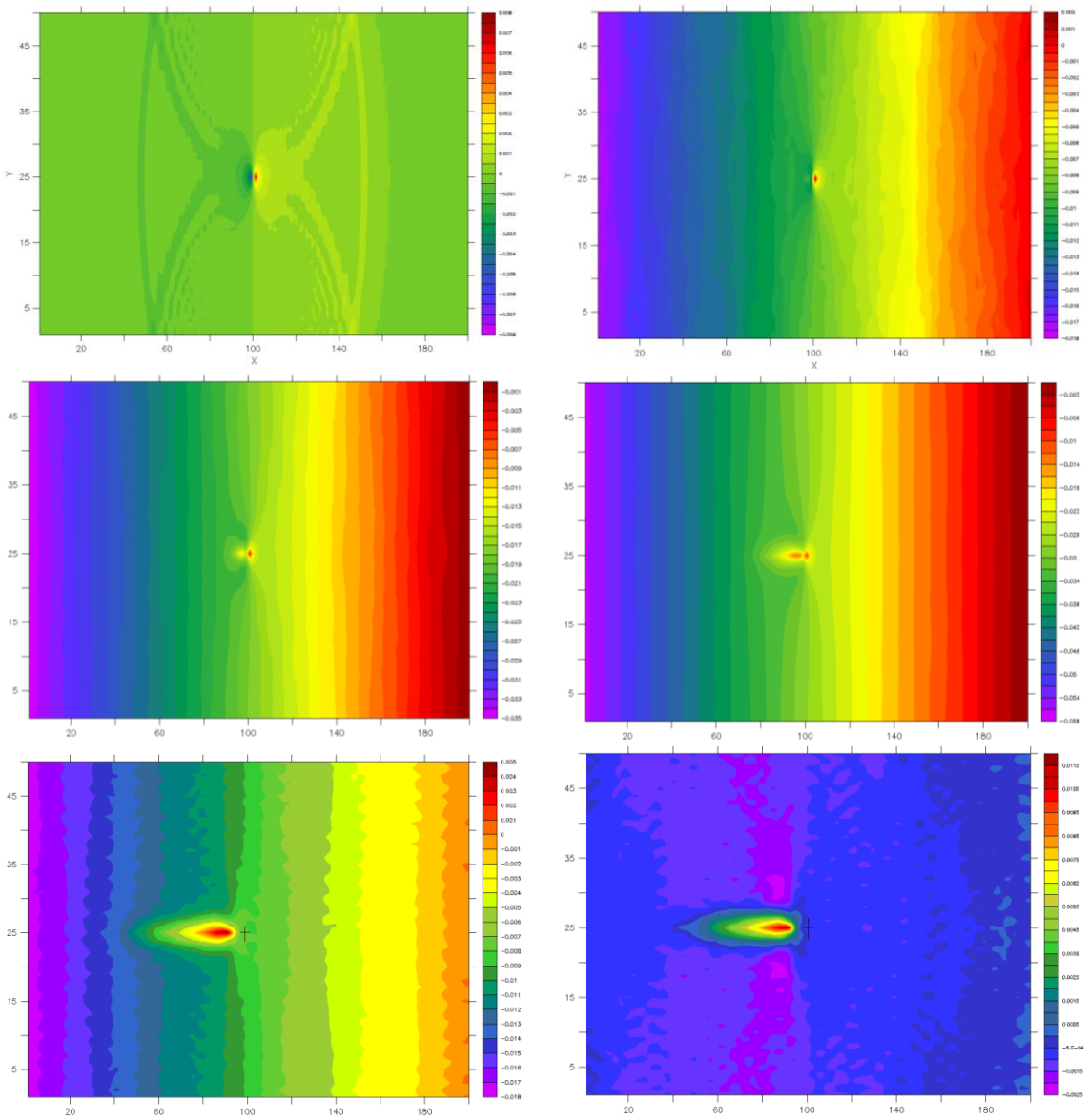

location due to the flow (˜70m).

The mass balance is also calculated to determine the influence of the added discharge. Figure 83 depicts the mass balance calculated for the transport of water and salinity. The mass balance of water presents high oscillations (˜0.02% of the original volume). This high oscillation is due to the truncation applied by the computer for the calculation of the instantaneous water volume. Moreover, the mass balance graph also shows the influence of the deactivation of the discharge at the end of the simulation presenting lower oscillations. On the other hand, the mass balance of salinity presents similar oscillations of the order of 0.05 PSU (˜0.05%), cause also by the truncation error during the calculation of the instantaneous volume.

4.5.3 Conclusions

- for 2D discharges the relative accuracies of the water mass and salinity balance are below 0.0002% and 0.06%, respectively,
- for distributed 3D discharges the relative accuracies of the water mass and salinity balance are below

Figure 83 – Calculated mass balance for water and salinity, experiments M, N, O, P, Q and R

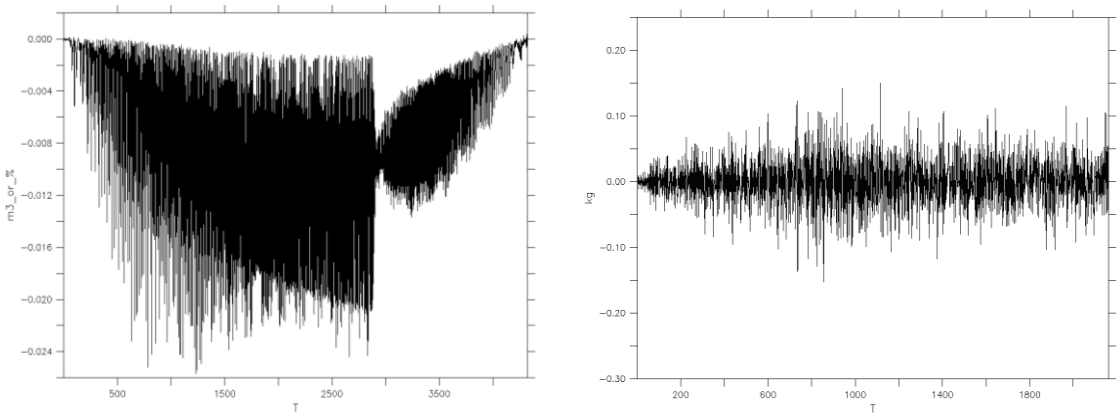

0.003% and 0.01%, respectively,

- for local 3D discharges the relative accuracies of the water mass and salinity balance are below 0.02% and 0.05%, respectively.

Five claims were assessed in the validation tests. The four model units showed an acceptable performance. They could schematize hydraulic structures fulfilling their purpose (i.e. blocking of flow, definition of dry areas or addition of sources). The model could work in 2D and 3D conditions for the transport of water and scalars (i.e. salinity and temperature) showing an acceptable performance. The conservation of mass was also assessed showing acceptable results. In conclusion, the implemented model units can be used to schematize hydraulic structures in different hydraulic conditions.

4.6 Conclusions

Regarding the testcases discussed in this chapter, the following conclusions can be drawn with respect to the structures functionality as implemented in COHERENS:

1. with dry cells the mass conservation of water is obeyed by a relative eroor $\sim 0.0002\%$ while absolute deviations in salinity are no more than 0.0006 PSU.
2. as required, no scalar is transported to dry cell regions. This is demonstrated explicitly for salinity and temperature.
3. for thin dams the mass conservation of water is obeyed with a relative error of $\sim 0.00005\%$ while absolute deviations in salinity are at most ~ 0.0001 PSU.
4. as required, thin dams prohibit transport of scalars. This is demonstrated explicitly for salinity and temperature.
5. for weirs under tidal conditions without a dry area the relative accuracy of water mass balance was smaller than 0.0018%. The deviations of salinity were at most 0.05 PSU.
6. for weirs with dry area under tidal conditions with a dry area the relative accuracy of water mass balance was smaller than 0.013%. The deviations of salinity were at most 0.001 PSU.
7. for a CDW with one or two openings the relative accuracy of water mass balance was smaller than 0.0001%. The deviations of salinity were at most 0.0005 PSU.
8. for a CDW with free flow the relative accuracy of water mass balance was smaller than 0.0015%. The deviations of salinity were at most 0.01 PSU.
9. for 2D discharges the relative accuracies of the water mass and salinity balance are below 0.0002% and 0.06%, respectively,
10. for distributed 3D discharges the relative accuracies of the water mass and salinity balance are below 0.003% and 0.01%, respectively,
11. for local 3D discharges the relative accuracies of the water mass and salinity balance are below 0.02% and 0.05%, respectively.

5 Additional boundary conditions

5.1 Introduction

This chapter considers the validation of a number of additional boubndary conditions that were implemented in COHERENS. Hereafter, testcases for the following boundary conditions are discussed:

- distributed discharge
- Neumann condition
- Thatcher-Harleman (salinity)
- tangential components of flow transport.

5.1.1 Overview and claims

The validation test cases should fulfill the objective that they are acceptable in a qualitative way.

- Mass conservation of water
- Mass conservation of salinity
- The additional boundary conditions should work in 2D and 3D mode
- Fulfill the purpose of the boundary condition (prescription of boundary values)

A list of claims of the validation tests is given in Table 15.

Table 15 – Claims matrix for the validation tests

Boundary Cond.	2D	3D	Mass Cons.	Salinity	Purpose
distributed discharge	✓	✓	✓	✓	✓
Neumann condition	✓	✓	✓	✓	✓
Thatcher-Harleman		✓	✓	✓	✓
Tangential components	✓	✓	✓		✓

5.1.2 Verification of the mass conservation

The verification of the mass conservation for water can be easily verified by calculating a water balance in an open channel (or reservoir), where an inflow and an outflow are provided. The water balance is calculated by the application of:

$$Q_{in} - Q_{out} = \frac{dV}{dt} \tag{153}$$

where Q_{in} denotes the inflow defined at the open boundary, the discharge Q_{out} denotes the outflow discharge defined at the open boundary, V denotes the total water volume inside the reservoir and t denotes the time variable. Once the discharges are know, it is possible to determine the variation of the water volume as a function of time. The analytic solution of this equation can be easily obtained for a reservoir with predefined

dimensions and with predefined discharges. This analytic solution can be compared with the model results of the variation of the water volume as a function of time. Eventually, a curve rate of water volume vs. time can be plotted for both solutions (model vs. analytic solution).

For the case of scalars, the mass balance is calculated by the application of:

$$flux_{salt}^{IN} - flux_{salt}^{OUT} = \frac{dM}{dt} \tag{154}$$

where $flux_{salt}^{IN}$ denotes the inflow of the scalar flux (discharge of water multiplied by the concentration of the scalar), $flux_{salt}^{OUT}$ denotes the outflow of the scalar flux, M denotes the total mass of the scalar inside the reservoir and t denotes the time variable. Once the discharges and concentrations of scalars are known, it is possible to determine the variation of the total mass of the scalar as a function of time.

The analytic solution of this equation can be obtained for a reservoir with predefined dimensions and with predefined discharges. This analytic solution can be compared with the model results of the variation of the total mass as a function of time. Eventually, a curve rate of total mass vs. time can be plotted for both solutions (model vs. analytic solution).

5.2 Validation of distributed discharge condition

5.2.1 Introduction

Total distributed discharges can be prescribed at open boundary sections. The aim of this type of boundary condition is to distribute the total discharge over the whole open boundary as a function of the local flow conditions avoiding the necessity in specifying discharges per grid cell. Thus, the discharge is distributed along the open boundary in the following manner derived from the Chézy equation:

$$q_i = \frac{B_i H_i^{1.5} C_i}{\sum_{j=1}^{N} B_j H_j^{1.5} C_j} Q \tag{155}$$

where B_i, H_i and C_i are the width, water depth and roughness of grid cell i respectively, N is the number of boundary grid cells, and Q is the total discharge imposed.

5.2.2 Model setup

This boundary type was tested by the simulation of a tidal basin with only one open boundary (see Figure 84) and a non-uniform bathymetry, presenting a triangular cross section (see Figure 85). The purpose of choosing a non uniform bathymetry is to test the performance of this type of boundary type. Since this boundary type is a function of the calculated water depth, it is expected to obtain higher discharges at the grid cells with higher water depths.

Figure 84 – Scheme of the tidal basin with one open boundary: top view

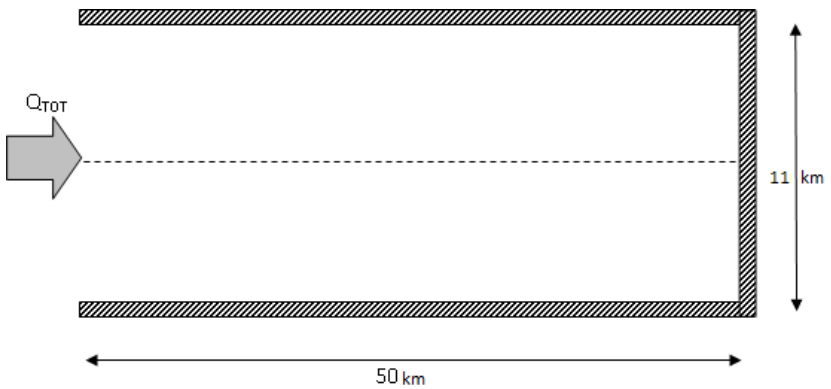

The total discharge was prescribed as constant in time to allow a better calculation of the mass conservation. Due to the geometric conditions of the computational domain with three sides defined as closed, it is expected that the water volume inside the basin will increase through the time. The purpose of this test case is to validate the prescription of the total distributed discharge as a boundary condition. Hence, in this section is provided the information of the setup of this test case:

5.2.3 Results

Three experiments were tested:

Figure 85 – Cross section of the tidal basin

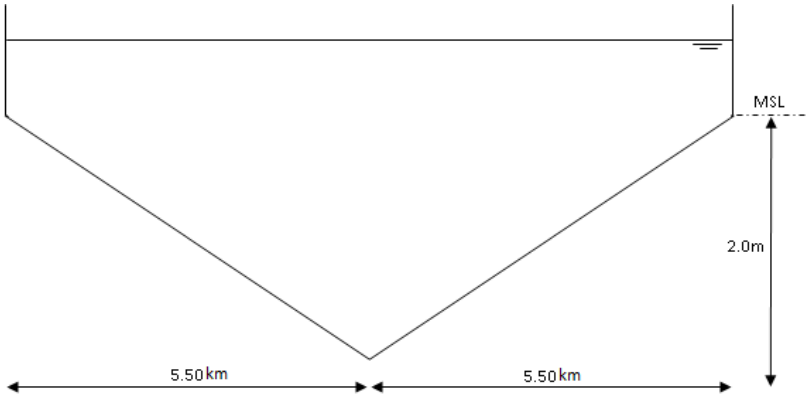

Table 16 – Data for the setup of the test case

Parameter	Value	Remarks
Basin legth	50 km.	
Basin width	11 km.	
Mean water depth	see Fig. 85	non-uniform bottom
Simulation time	6 hr.	
Number of rows	12	
Number of columns	51	
Number of vertical layers	10	only for the 3D and salinity modes
Grid size dx=dy	1000 m.	
Time step	0.1 sec.	
Roughness height	0.006 m.	
Initial flow velocity	0.00 m/s	
Initial water surface	0.00 m.	
Initial salinity	30 PSU	
Boundary condition	2.0 m^3/s	Total discharge condition
Salinity BC	32 PSU	

- qdist_A: 2D test
- qdist_B: 3D test
- qdist_C: 3D test with salinity

The discussion of the results corresponds to the five claims already defined to validate the performance of the implemented boundary condition. The first element to analyze is the verification of the value of the total discharge at the boundary points and its distribution per grid cell.

Figure 86 depicts the calculated total discharge at the open boundary. This discharge was calculated based on the calculated water depths defined at every boundary grid cell. The calculated value reaches the prescribed one (i.e. $Q = 2.0m^3/s$) with oscillations at the beginning of the simulation that corresponds to the spin-up period. Similarly to the previous test cases, no reflecting waves are observed yet, at least during the simulation time

The 3D mode simulation allowed to obtain a cross section view of the calculated flow velocities at the open boundary (see Figure 87), this view depicts the distribution of flow velocities at the open boundary. It is clearly

Figure 86 – Calculated total discharge at the open boundary

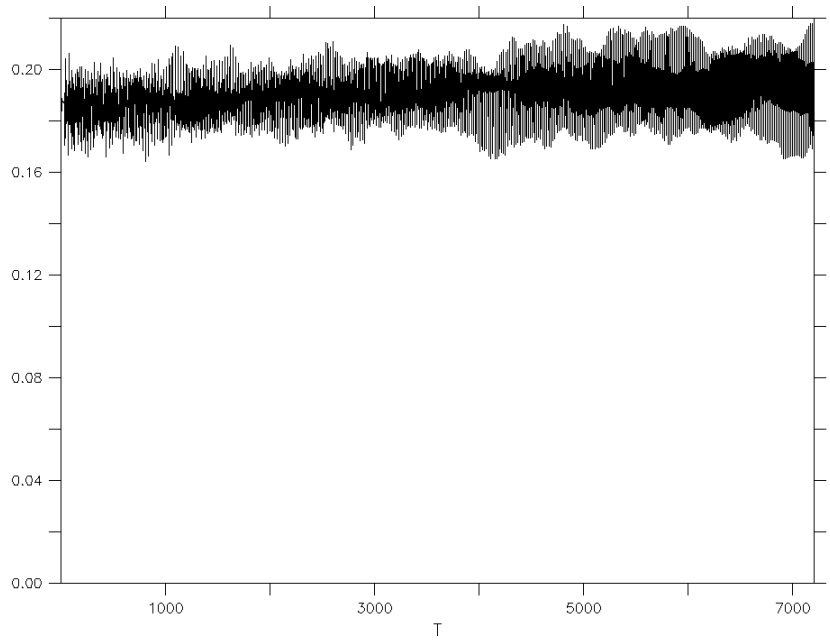

showed that higher velocities are observed at the center of the section where higher water depths are present, confirming the correct distribution of the total discharge along the boundary grid cells.

Figure 87 – Calculated flow velocities at the open boundary: cross section view

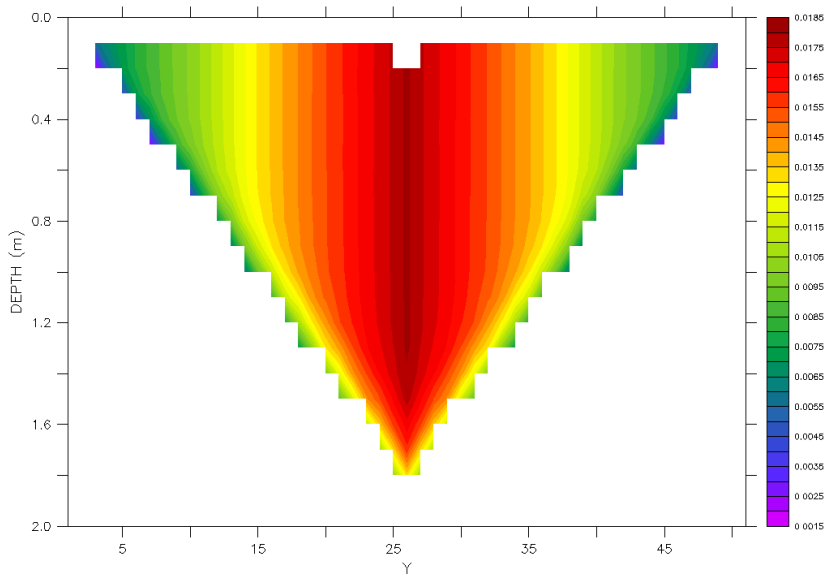

As mentioned before, the fact that he computational domain presents only one open boundary, creates the possibility that reflecting waves could be generated and affect the prescribed open boundaries. Therefore, additionally to the time series graph of the calculated total discharge, the water level and the flow velocities in the domain are also verified. Figure 88 and Figure 89 depict the longitudinal profile of the water surface level and the top view of the water level and flow velocities respectively.

The test with the presence of salinity, shows that the prescribed salinity moves towards the closed boundary due to the presence of the prescribed local discharge (advective process). Figure 90 depicts the calculated salinity and flow velocity after 40 minutes, higher flow velocities and salinity concentrations are observed at the central line of the basin, which seems to be logic since this axis presents the higher water depths. According

Figure 88 – Longitudinal profile of the water level after 3 hours

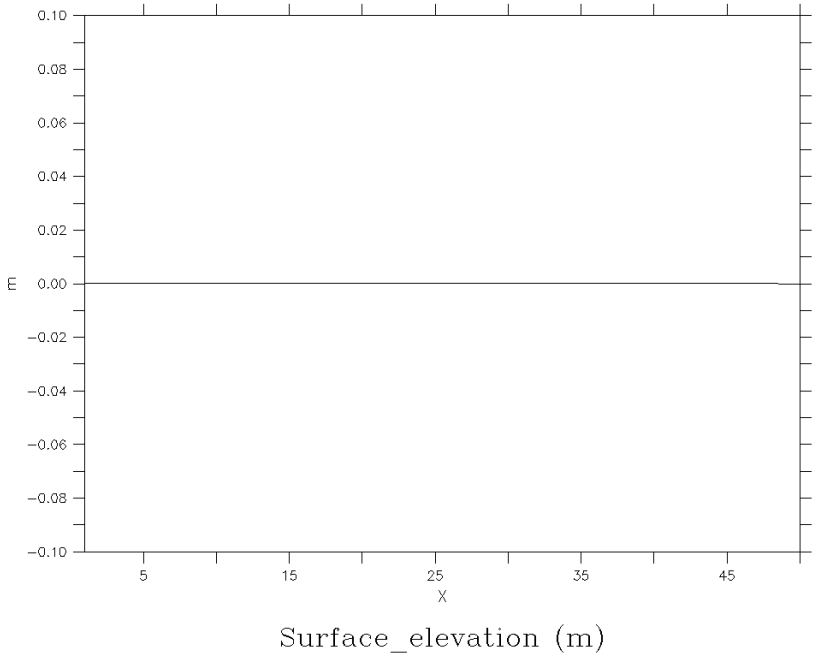

Figure 89 – Calculated depth mean currents and water level after 3 hours

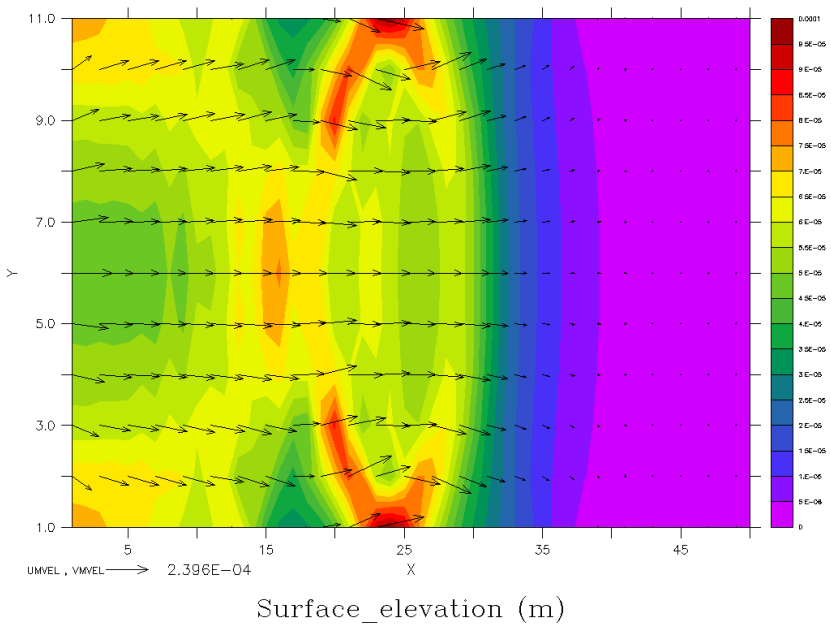

to the equation for the distribution of the total discharge, it is expected to obtain higher discharges (flow velocities as well) at points where the water depths are also higher.

Figure 90 – Calculated depth mean currents and salinity after 40 min.

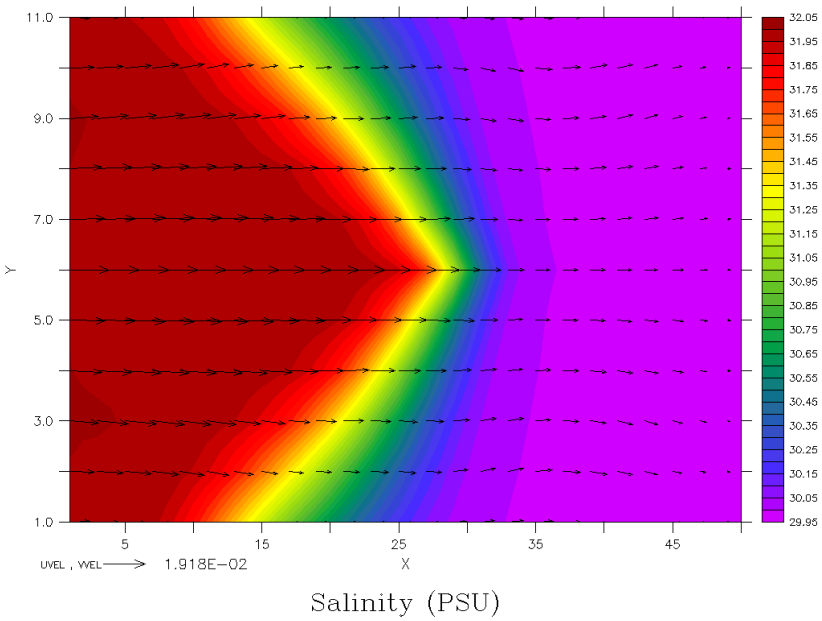

Figure 91 depicts a longitudinal view of the salinity concentration and the flow velocity at the middle axis of the basin. Here is clearly observed thatr the effect of the closed boundary is important for the generation of waves and the change of the flow direction, producing a variation in the vertical profila of salinity.

The mass conservation was verified for the two components, water and salinity. This verification was done in order to determine if the prescribed boundary condition, fulfills the requirement of the mass conservation. The mass balance for water shows (see Figure 92) an error of 0.0001% of the total water volume, which could be considered low.

On the other hand, the mass balance of the salinity, shows (see Figure 93) an error of 0.01%. which is also low, confirming that no reflecting waves are present yet that could have an influence on the mass balance.

5.2.4 Conclusions

The test case is characterized by presenting a domain with three closed boundaries and one open boundary, where a total discharge was prescribed along the open boundary to be distributed. It was also expected that no reflecting waves would be observed, at least during the simulation time (i.e. 6 hours). Hence, it was possible to obtain a stationary condition, that would allow a better verification of the prescribed boundary conditions.

The model results (2D and 3d mode) confirmed the initial assumptions that no reflecting waves were observed and that the total discharge calculated at the open boundary is equal to the prescribed boundary condition. Hence, it is possible to conclude preliminary that the prescribed boundary condition type works acceptably. Additionally, it was observed that the mass conservation for water and salinity present errors of 0.00001% and 0.01% respectively, which are low values considering that standard modeling practices suggest that mass blance errors below 1% are acceptable.

Figure 91 – Longitudinal view of the flow velocities and salinity after 40 min.

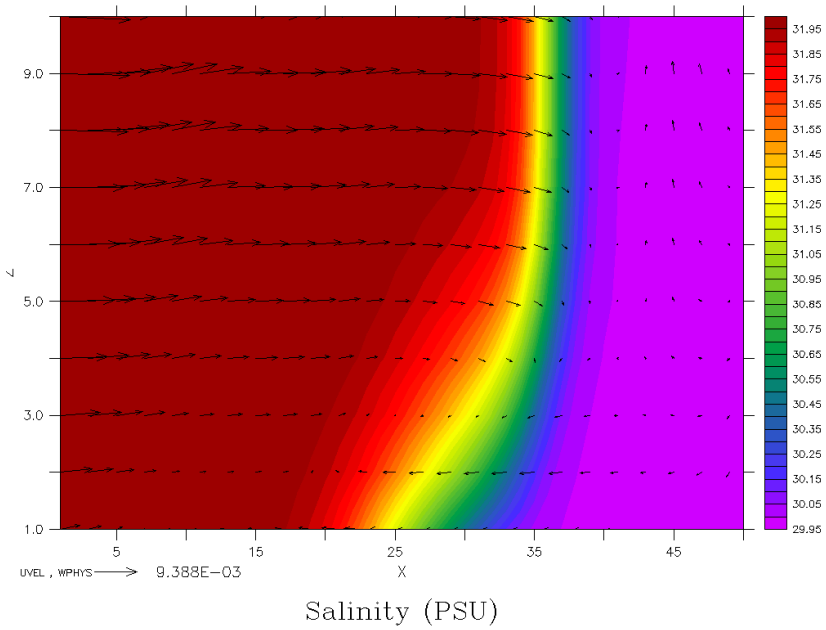

Figure 92 – Calculated mass balance for water, experiments A, B and C

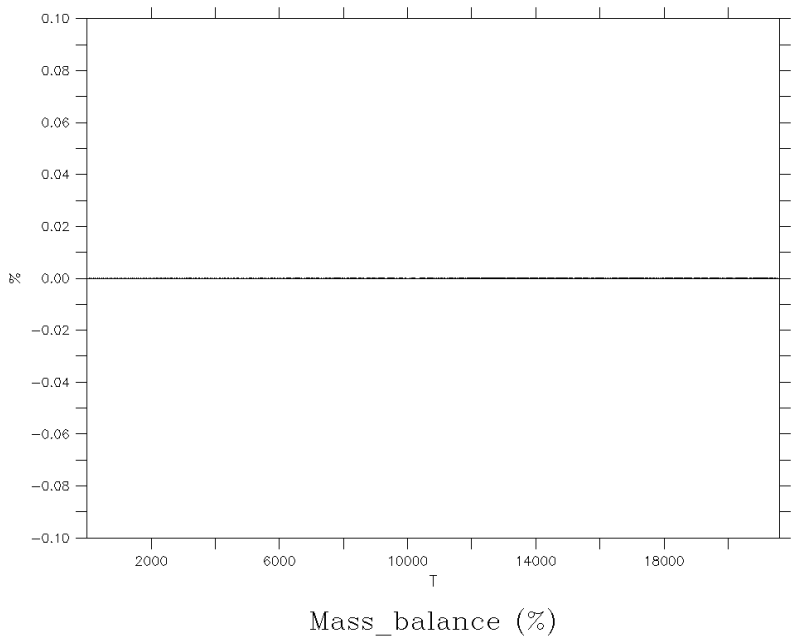

Figure 93 – Calculated mass balance for salinity, experiment C

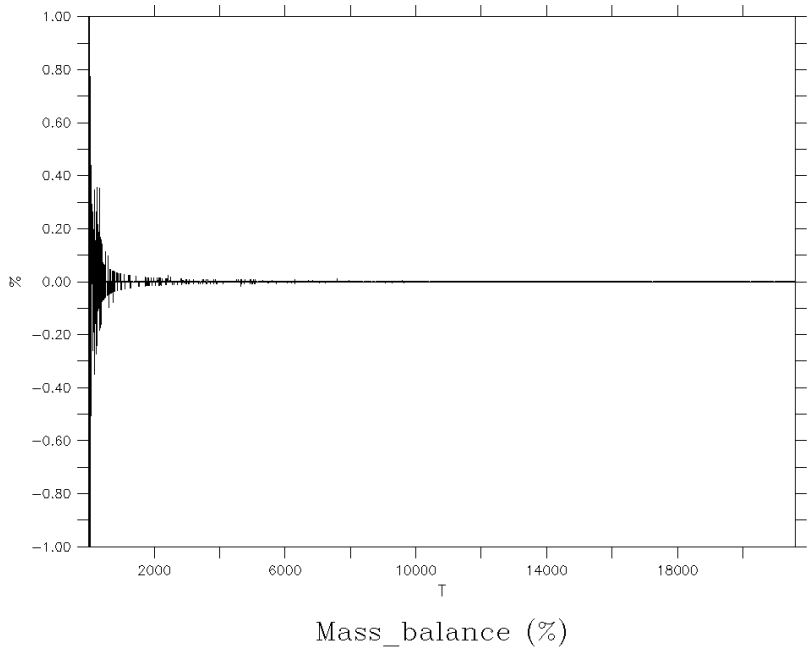

5.3 Validation of Neumann condition

5.3.1 Introduction

The Neumann boundary condition refers to the prescription of the water level gradient component that is perpendicular to the boundary. For a boundary along the V-direction this implies that $\partial\zeta/\partial\xi$ is imposed, which is related to the transport velocity component U according to

$$\frac{\partial U}{\partial t} = -\frac{c^2}{h_1}\frac{\partial \zeta^e}{\partial \xi_1}(t) + fV + HF_1^t + \tau_{s1} - \tau_{b1} \tag{156}$$

5.3.2 Model setup

This boundary type was tested by the simulation of an open channel with a backward facing step (non-uniform bathymetry) and a rectangular cross section with two open boundaries (see Figure 94 and Figure 95). The purpose of choosing an open channel with a backward facing step (non uniform bathymetry) is to test the performance of the Neumann boundary type under such conditions, it is expected that the backward facing step will have an influence on the flow. Hence, the downstream open boundary should be located far enough in order to reduce the influence of the facing step.

Figure 94 – Scheme of the open channel with two open boundaries: top view

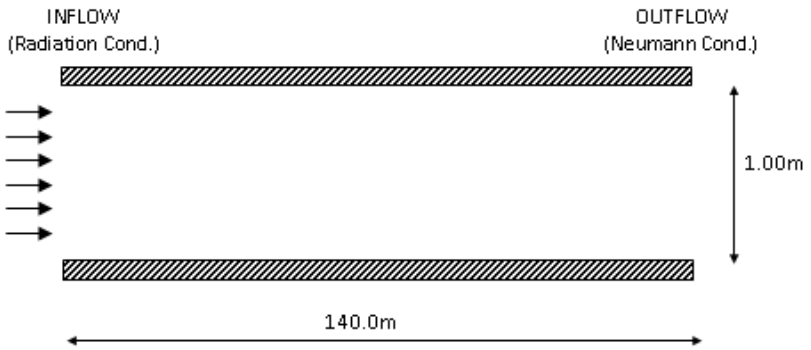

Figure 95 – Scheme of the open channel flow with a backward facing step: side view

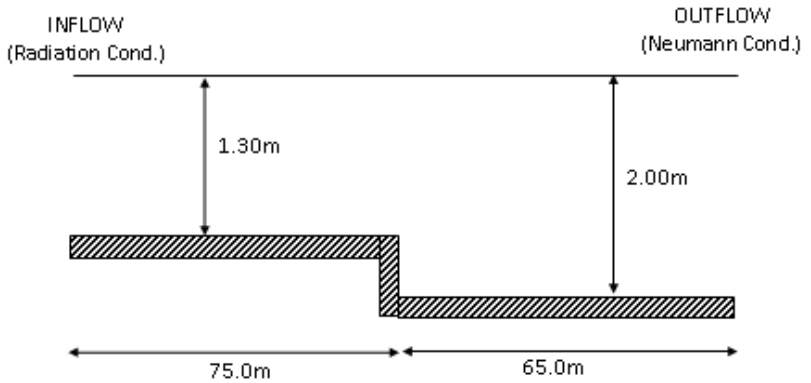

The purpose of this test case is to validate the prescription of the Neumann boundary condition. Hence, in this section is provided the information of the setup of this test case:

Table 17 – Data for the setup of the test case

Parameter	Value	Remarks
Channel legth	140 m.	
Channel width	1 m.	
Mean water depth	see Fig. 95	non-uniform bottom
Simulation time	12 hr.	
Number of rows	2	
Number of columns	141	
Number of vertical layers	10	only for the 3D and salinity modes
Grid size dx=dy	1 m.	
Time step	0.02 sec.	
Bottom drag coefficient	0.003	
Initial flow velocity	0.50 m/s	
Initial water surface	0.00 m.	
Initial salinity	30 PSU	
BC upstream	Type 5	Radiation condition
BC downstream	0.0 m/m	Neumann Condition
Salinity BC	32 PSU	

5.3.3 Discussion of results

Three experiments were tested:

- neuma_A: 2D test
- neuma_B: 3D test
- neuma_C: 3D test with salinity

The discussion of the results corresponds to the five claims already defined to validate the performance of the implemented boundary condition. The first element to analyze is the verification of the value of the gradient of the water surface at the downstream open boundary. Figure 96 depicts the calculated gradient of the water level surface (Neumann condition). This gradient presents a value oz zero, as prescribed in the boundary conditions. Some oscillations are observed at the first time steps that correspond to the spin-up process.

In order to verify this spin-up process, the calculated flow velocity and water surface are plotted as time series. Figure 97 and Figure 98 depict the time series of the mentioned variables calculated at the upstream open boundary. There is evident that a spin-up process is present for the first hours until the system reaches a stable condition.

This test case was also executed in 3D mode with the presence of salinity. The mass conservation was verified for the two components, water and salinity. This verification was done in order to determine if the prescribed boundary condition, fulfills the requirement of the mass conservation. The mass balance for water shows (see Figure 99) an error of 0.00002% of the total water volume, which could be considered low. On the other hand, the mass balance of the salinity, shows (see Figure 100) an error of 0.0001%, which is also low.

Figure 96 – Calculated water level gradient at the downstream boundary

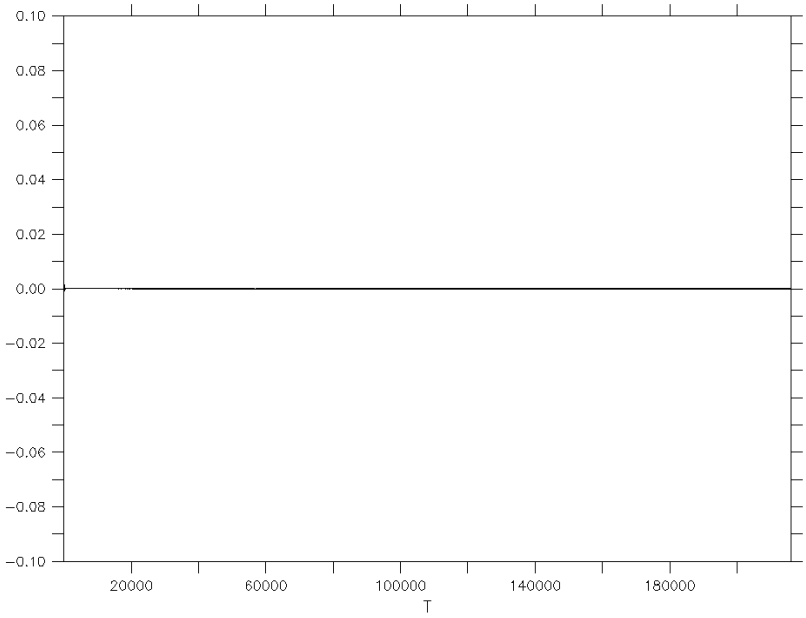

Figure 97 – Calculated water surface at the upstream open boundary

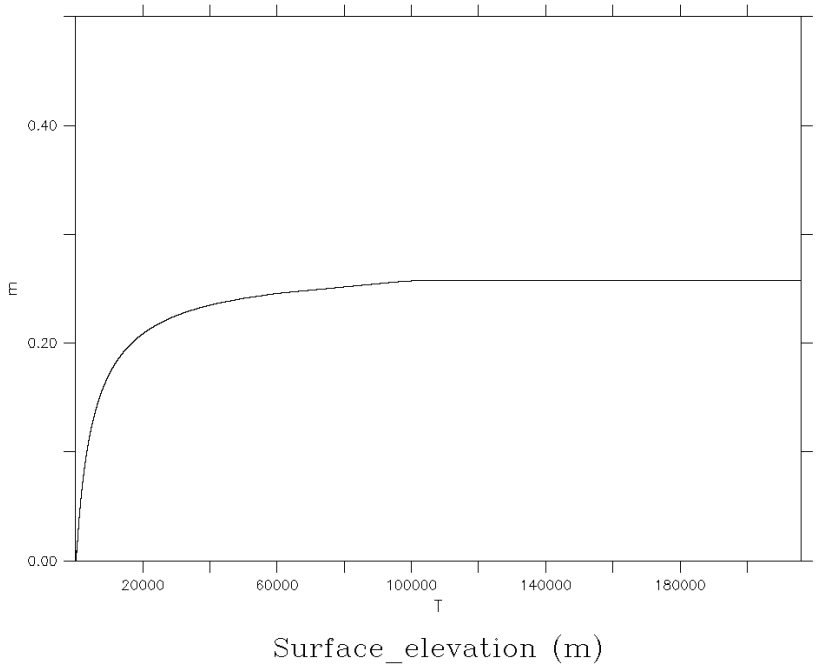

Figure 98 – Calculated flow velocity at the upstream open boundary.

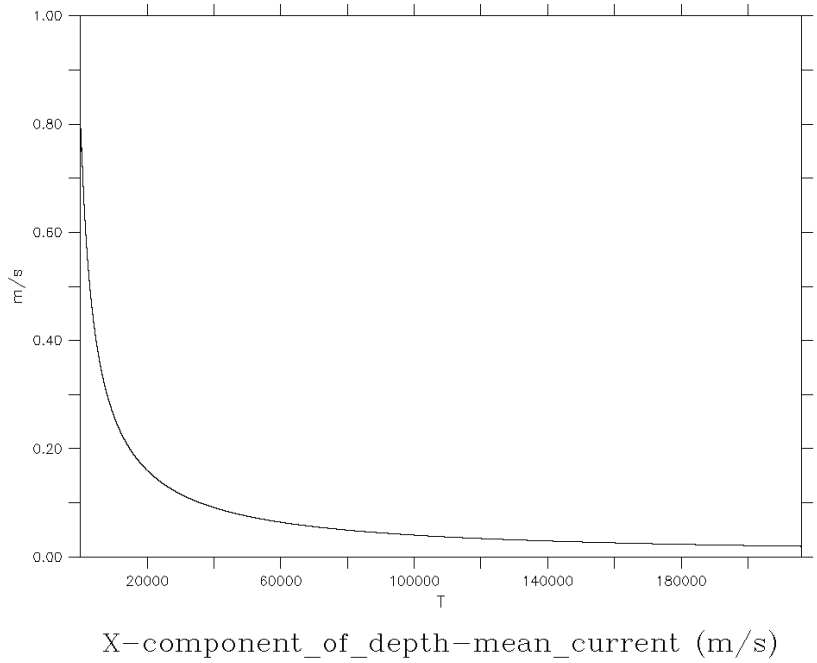

Figure 99 – Calculated mass balance for water, experiments A, B and C

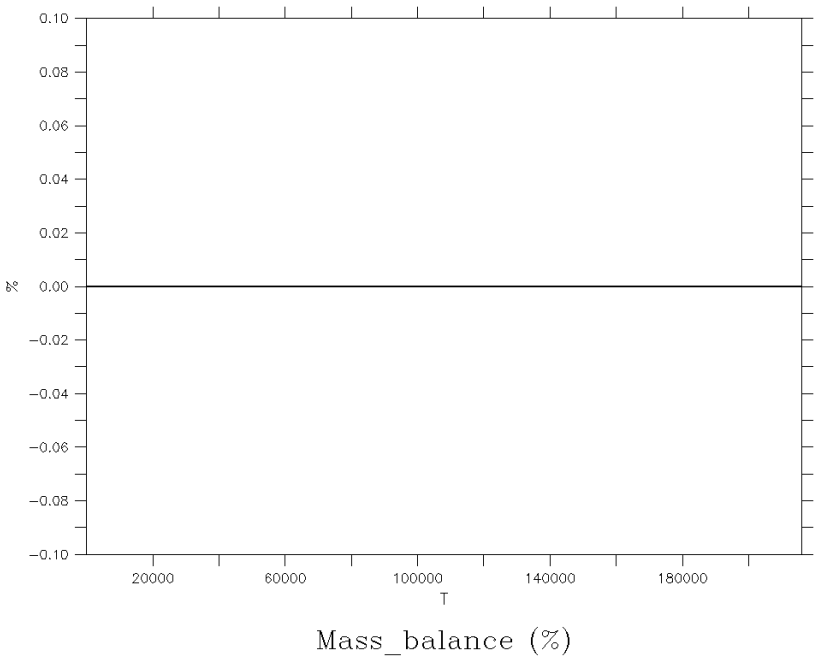

Figure 100 – Calculated mass balance for salinity, experiment C

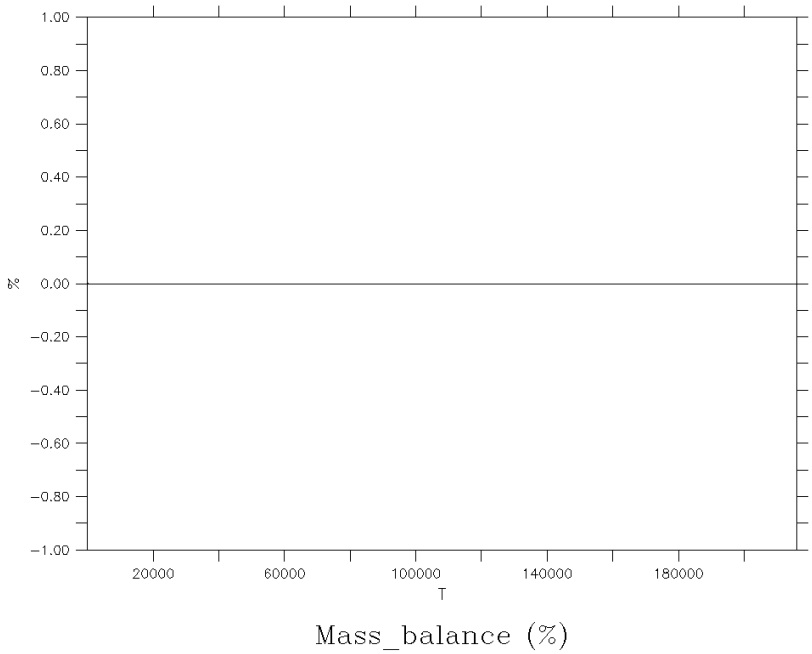

5.3.4 Conclusions

This test is characterized by presenting two open boundaries and a non-uniform bottom (i.e. backward facing step), which could generate effects on the flow behavior. Therefore, the downstream boundary condition (Neumann BC) had to be prescribed far enough from this step in order to avoid possible effects. Additionally, the Radiation condition using shallow water speed was prescribed at the upstream open boundary. This condition is considered as a reflective condition.

The results show that the presence of the reflecting condition and the backward facing step did not present a big effect on the flow behavior. However, special car should be taken when prescribing the Neumann boundary condition. This BC type cannot be combined with certain open boundary condition types. The development testing, alpha testing and validation test cases have shown that in order to have a well posed system,the Neumann condition can be used in combination with water levels and the radiation condition. However, this can be case dependent.

As a preliminary conclusion, this boundary condition type could work acceptably in 2D and 3D mode in certain conditions. special care should be taken and define a well posed system before applying this boundary condition type.

5.4 Validation of Thatcher-Harleman condition

5.4.1 Introduction

This type of boundary condition is applied to the transport of dissolved substances such as salt under tidal conditions (i.e. estuaries). It is assumed that the transition of the concentration at the boundary from the outflow value to the inflow value may take some time. This boundary condition allows the possibility that some of the water that leaves the estuary on the ebb tide may re-enter the estuary with the following flood tide. The mathematical formulation of this memory effect is given as follows:

$$C(t) = C^{out} + \frac{1}{2}\left(C^{bnd} - C^{out}\right)\left[\cos\left\{\pi \frac{T_{ret} - t_{out}}{T_{ret}}\right\} + 1\right], \quad 0 \leq t_{out} \leq T_{ret} \tag{157}$$

where C^{out} is the computed concentration at the open boundary at the last time of outward flow, C^{bnd} is the background concentration that should be prescribed by the user as a reference concentration, t_{out} is the elapsed time since the last outflow and $T_{ret}t$ is the constituent return period. When the flow turns inward ($t_{out} = 0$), the concentration is set equal to C^{out}. During the interval $0 \leq t_{out} \leq T_{ret}$the concentration will return to the background concentration C^{bnd}. After that period, the concentration will remain C^{bnd} (see Figure 101).

Figure 101 – Memory effect for open boundary (Deltares, 2011;SIMONA,2009)

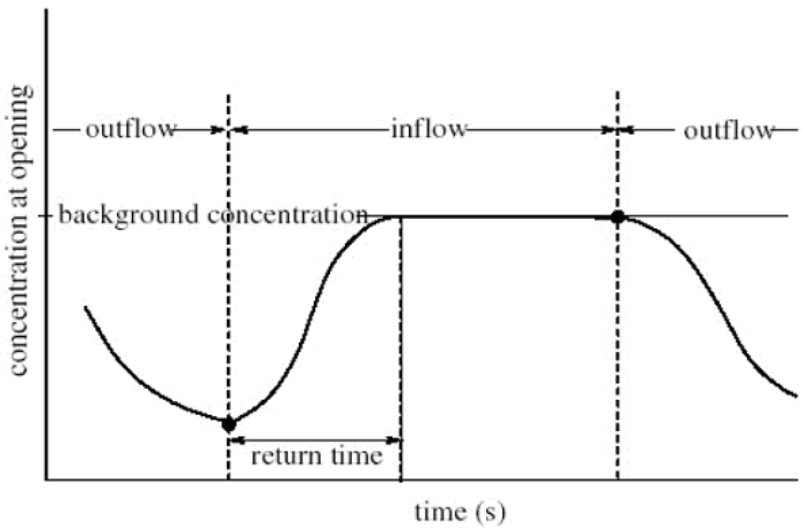

5.4.2 Model setup

Since this type of boundary condition is oriented to tidal conditions in estuaries, the validation test cases have to resemble these conditions. Therefore, the scheme of an estuary is used as a test case (see Figure 102):

This scheme is defined as a 'mother model' (2DV model). This model schematizes an estuary, where two open boundaries are defined, one for the see and the other for the river. A tidal condition with a constant salinity concentration is prescribed at the see side while a constant discharge and no salinity are prescribed at the river side. The results of this model are used for further comparisons an validations of a 'daughter model', where the Thatcher-Harleman condition is prescribed.

The setup of the model is defined according to the following data:

Figure 102 – Scheme of the estuary 2DV model: mother model

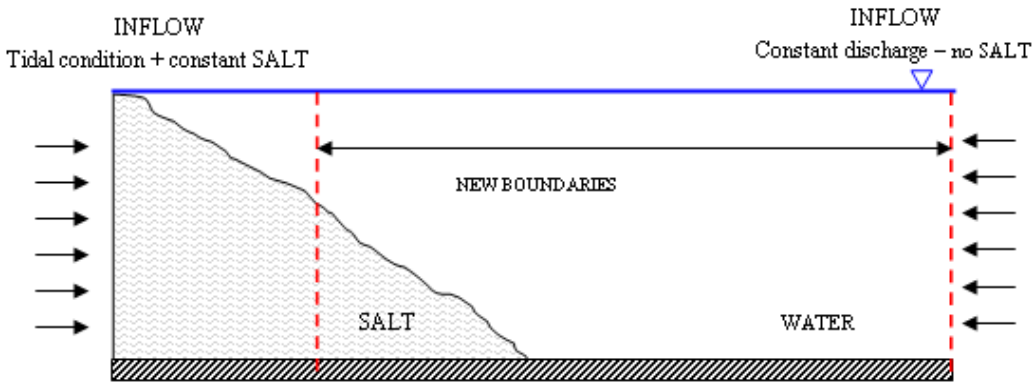

Table 18 – Data for the setup of the mother model

Parameter	Value	Remarks
Estuary length	100 km.	
Estuary width	1 km.	
Mean water depth	10 m.	uniform bottom
Simulation time	3 months	long time for spin-up
Number of rows	2	
Number of columns	101	
Number of vertical layers	20	
Grid size dx=dy	1000 m.	
Time step	30 sec.	
Roughness height	0.006 m.	
Initial flow velocity	0.00 m/s	
Initial water surface	-2.00 m.	Low water condition
Initial salinity	0 PSU	
Water Level BC	Amp=2m; Phase=PI	S2 tide
Transport BC	0.02 m/s	River side
Salinity BC	32 PSU	

The daughter model is set to simulate a portion of the mother model. It is assumed that the sea boundary is far enough from the river boundary; hence, it is possible to prescribe constant boundary values for salinity at the mother model. Due to the tidal condition, it is expected that at a certain point (close to the river boundary), salinity will behave according to the equation of Thatcher-Harleman. Therefore, this location is used to define the sea boundary of the daugther model (see Figure 103).

The daughter model is aimed to represent a reduced version of the mother model. It is also a 2DV model, where the concentration of salinity is distributed over the vertical direction. Two open boundaries are defined: one for the sea side and one for the river side. A constant discharge of clear water is prescribed at the river boundary (same of the mother model). A tidal condition (water level) is prescribed at the sea boundary (S2 tide). The Thatcher-Harleman condition is prescribed at the sea boundary. Additionally, a warming up process was defined in order to initially simulate the hydrodynamics and then the salinity is released. The setup of the model is defined according to the following data:

Figure 103 – Scheme of the reduced estuary 2DV model: daughter model

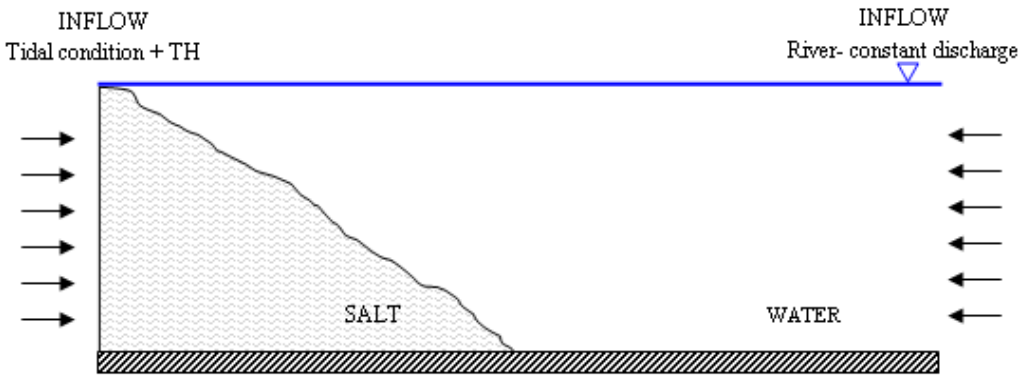

Table 19 – Data for the setup of the daughter model

Parameter	Value	Remarks
Estuary length	70 km.	from mother model results
Estuary width	1 km.	
Mean water depth	10 m.	uniform bottom
Simulation time	3 months	long time for spin-up
Number of rows	2	
Number of columns	71	
Number of vertical layers	20	
Grid size dx=dy	1000 m.	
Time step	30 sec.	
Roughness height	0.006 m.	
Initial flow velocity	0.00 m/s	
Initial water surface	2.00 m.	High water condition
Initial salinity	0 PSU	
Water Level BC	Amp=2m; Phase=PI	S2 tide
Transport BC	0.02 m/s	River side
Salinity BC	15.8 PSU	Background salinity
Return time	5.5 hrs.	Calibration parameter

The length of the model and the background salinity is obtained from the results of the mother model.

5.4.3 Results

Only one experiment was defined for the mother and daughter models which is a 3D mode with the presence of salinity.

The discussion of the results corresponds to four of the five claims already defined to validate the performance of the implemented boundary condition. Only four claims are verified since it is not a 2D model.

Mother model

In this section is discussed the results of the mother model which are used for comparison and validation of the results of the daughter model.

This is a 2DV model that resembles an estuary under tidal conditions and the presence of salinity. A S2-tide was prescribed at the sea boundary, Figure 104 depicts the prescribed water level, here is depicted a portion of the water level time series since the simulation period was set to 3 months. Hydrodynamically, the model reaches an stable solution quite quickly (spin-up).

Figure 104 – Prescribed water level at the sea boundary: S2 tide

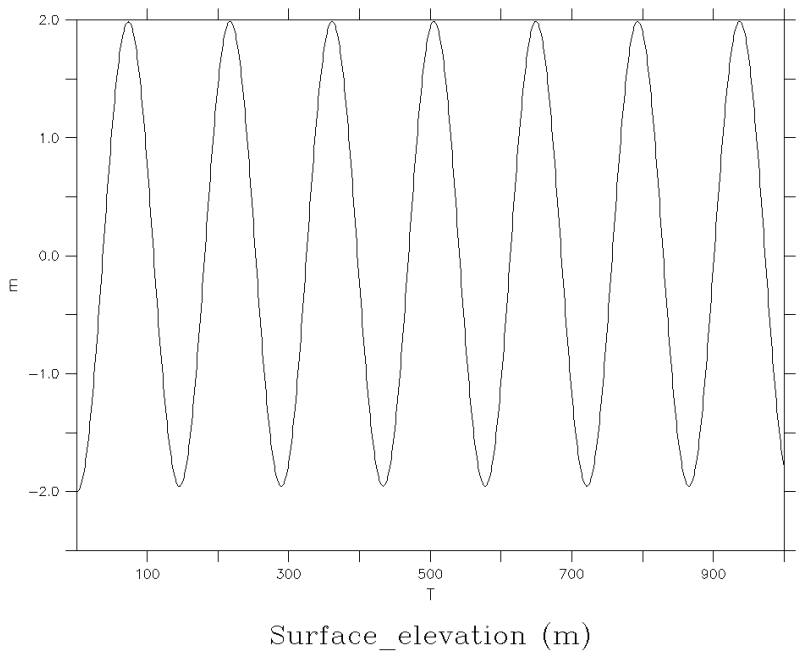

This tidal activity allows the movement of the salinity along the estuary. At the same time, the river releases fresh water to the estuary with a constant discharge, leading to a cyclical behavior of the salinity along the domain. Figure 105 and Figure 106 depict the calculated flow velocity and salinity at 30 km from the sea boundary, both graphs show the Tide and Ebb phases:

Contrary to the hydrodynamics, salinity takes longer until reaches an stable solution (spin-up), because an initial value of $0.0PSU$ was defined for salinity. Therefore, the spin-up process is longer, reaching finally an stable behavior (cyclical). This cyclical behavior of the salinity concentration is used to prescribe the boundary condition of the daughter model (Thatcher-Harleman). Figure 107 depicts the calculated salinity at 30 km from the sea boundary. This location was selected based on the comparison of the results of the salinity at different locations. This comparison allowed to determine that at 30 km from the sea boundary, salinity presents a reasonable cyclical behavior that can be simulated by the application of the Thatcher-Harleman condition.

Daugther model

In this section is discussed the results of the daughter model, where the prescribed Thatcher-Harleman condition is compared to the results of the mother model. This is a 2DV model that resembles a reduced version of the estuary simulated by the mother model. Similarly to the mother model, a S2-tide was prescribed at the sea boundary, while a constant flow velocity with fresh water (no salinity) was prescribed at the river boundary.

Figure 105 – Calculated flow velocities and salinity at 30km from the sea boundary: tide

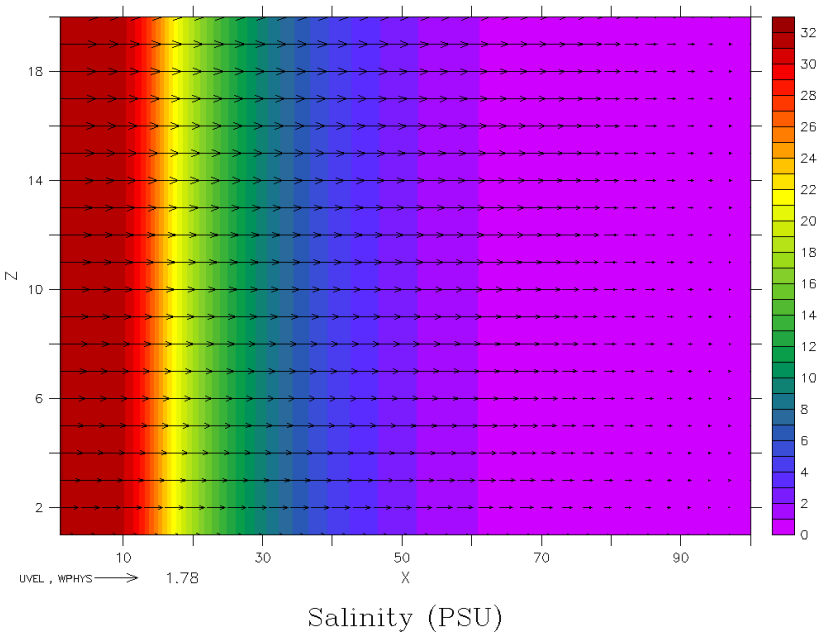

Figure 106 – Calculated flow velocities and salinity at 30km from the sea boundary: ebb

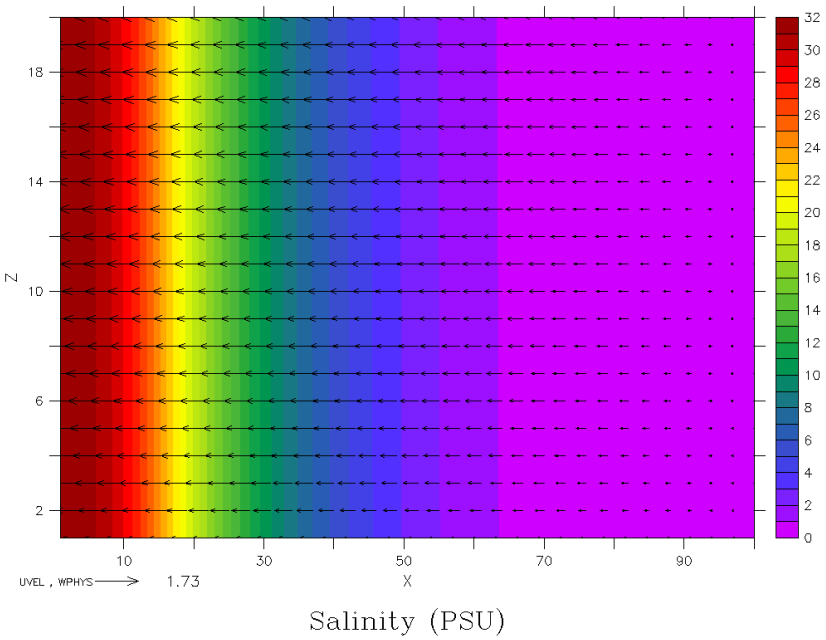

Figure 107 – Calculated salinity at 30 km from the sea boundary: last 3 days

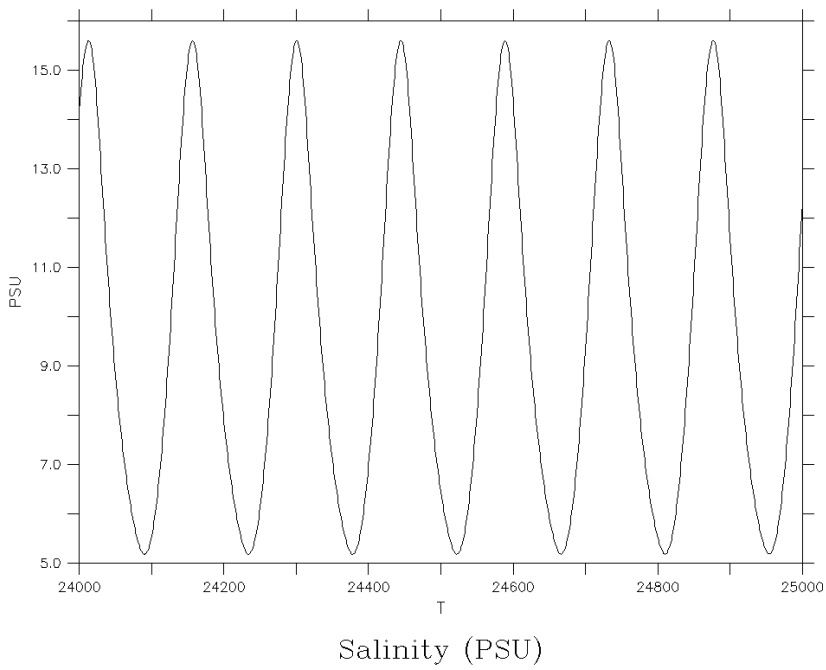

Since the aim of the daughter model is to resemble the estuary modeled by the mother model, the observed cyclical behavior of the salinity has to be reproduced by the prescription of the Thatcher-Harleman boundary condition. Hence, two parameters are necessary for the prescription of this boundary condition: the background salinity and the return time. The background salinity corresponds to the maximum salinity concentration reached during the cyclical behavior. This value was obtained from the results of the mother model being equal to $15.5PSU$. The return time is the time required by salinity to reach the background value during the Tide. This is a calibration parameter, that should be adjusted in order to resemble the observed salinity time series (result of the mother model).

Figure 108 depicts the comparison of the calculated salinity at 30 km from the boundary in the mother model and the prescribed Thatcher-Harleman boundary condition. This is the best approach obtained after the calibration of the return time. Larger values would have a strong effect on the lowest value of the salinity. Even though, a difference is observed when the boundary condition is compared to the results of the mother model (around 2 PSU).

Figure 109 and Figure 110 depict the calculated flow velocity and salinity at 30 km from the sea boundary, both graphs show the Tide and Ebb phase.

The mass conservation was verified for the two components, water and salinity. This verification was done in order to determine if the prescribed boundary condition, fulfills the requirement of the mass conservation. The mass balance for water shows (see Figure 111) that the Tatcher-Harleman boundary condition could fulfill the condition of the mass conservation. Similar results were obtained for the calculation of the mass conservation for salinity (see Figure 112).

5.4.4 Conclusions

After testing the implemented Thatcher-Harleman boundary condition for salinity, it was observed that this boundary type could reproduce the cyclical behavior of salinity observed in the mother model, when salinity enters into the domain when Tide occurs and leaves the domain at the Ebb period. The analysis of the

Figure 108 – Comparison of the calculated salinity at 30 km (mother model with the Thatcher-Harleman condition (last 3 days)

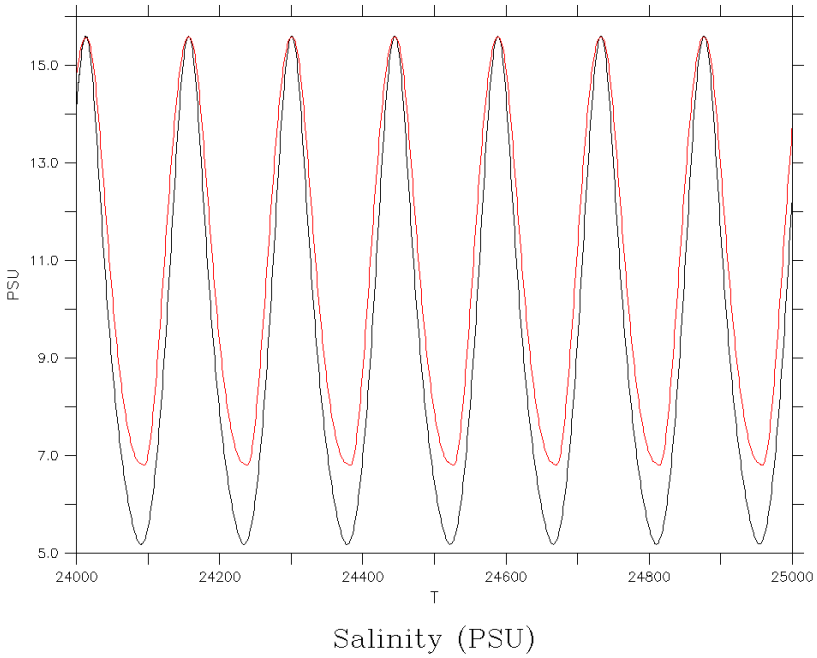

mass balance for water and salinity showed that this boundary type fulfills the requirement of mass conservation.

Figure 109 – Calculated flow velocities and salinity at 30km from the sea boundary: tide

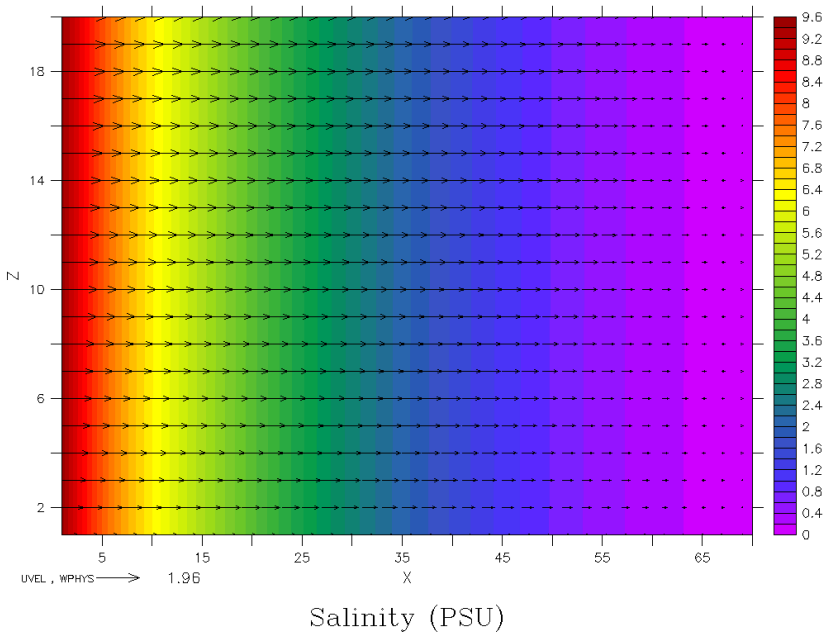

Figure 110 – Calculated flow velocities and salinity at 30km from the sea boundary: ebb

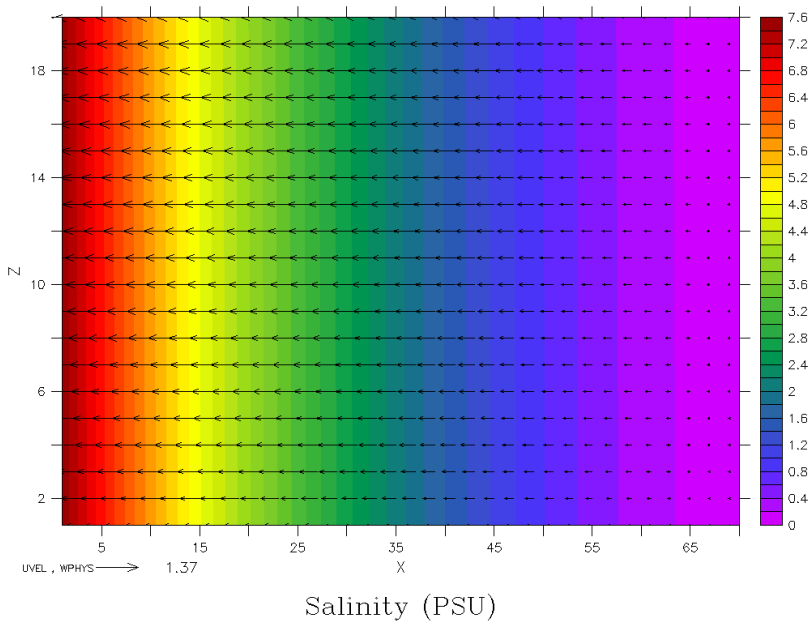

Figure 111 – Calculated mass balance for water

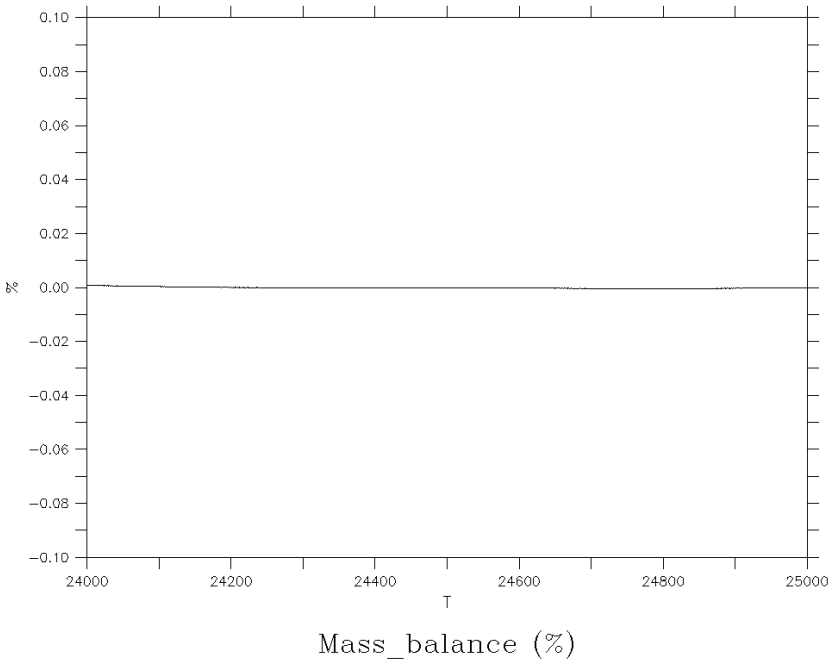

Figure 112 – Calculated mass balance for salinity

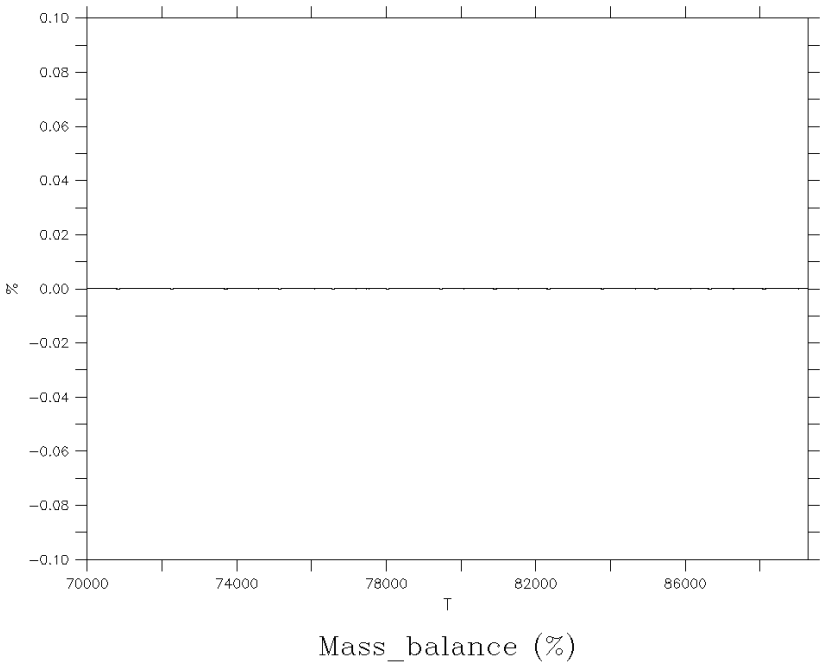

5.5 Validation of Tangential Components boundary condition

5.5.1 Introduction

The aim of this type of boundary condition is the prescription of the tangential components of the flow transport (depth-integrated velocity) at the boundaries jointly with the normal components (see Figure 113), enabling the possibility in modeling complex situations in coastal waters, where the flows entering the model domain under an angle can be represented accurately at open boundaries.

Figure 113 – Scheme of the prescription of normal and tangential components of flow transports at open boundaries

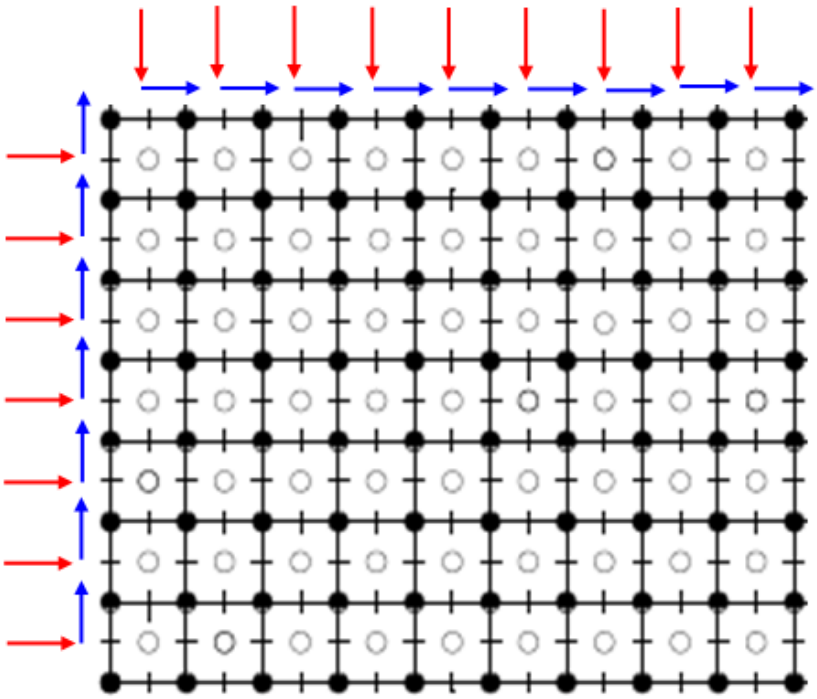

5.5.2 Model setup

The aim of this test case is to use a case proposed by Deltares (to validate the computational model Delft3D) as a basis for the validation of the implemented tangential boundary conditions.

Hence, a larger model under steady and uniform flow is the basis to generate the boundary conditions (normal and tangential) for the smaller model (see Figure 114). This procedure is fulfilled in three steps:

1. A mother model with two open boundaries with steady and uniform flow is defined, where a uniform and a constant flow velocity is prescribed at the southern open boundary and a uniform and constant water level is prescribed at the northern open boundary.
2. The results of this mother model are used to set the boundary conditions of a daughter model, i.e. the normal and tangential components of the depth-integrated currents at the southern boundaries and the water levels at the northern boundaries.
3. The results of both models (mother and daughter) are compared.

The mother model corresponds to a basin with two open boundaries under steady and uniform flow. The basin presents a non uniform bathymetry with a depth of 10m at the southern boundary and 29m at the northern boundary (both measured from the MSL). A constant depth-integrated velocity condition is prescribed at the

Figure 114 – Scheme of a smaller model superimposed on a larger model for the prescription of tangential and normal components

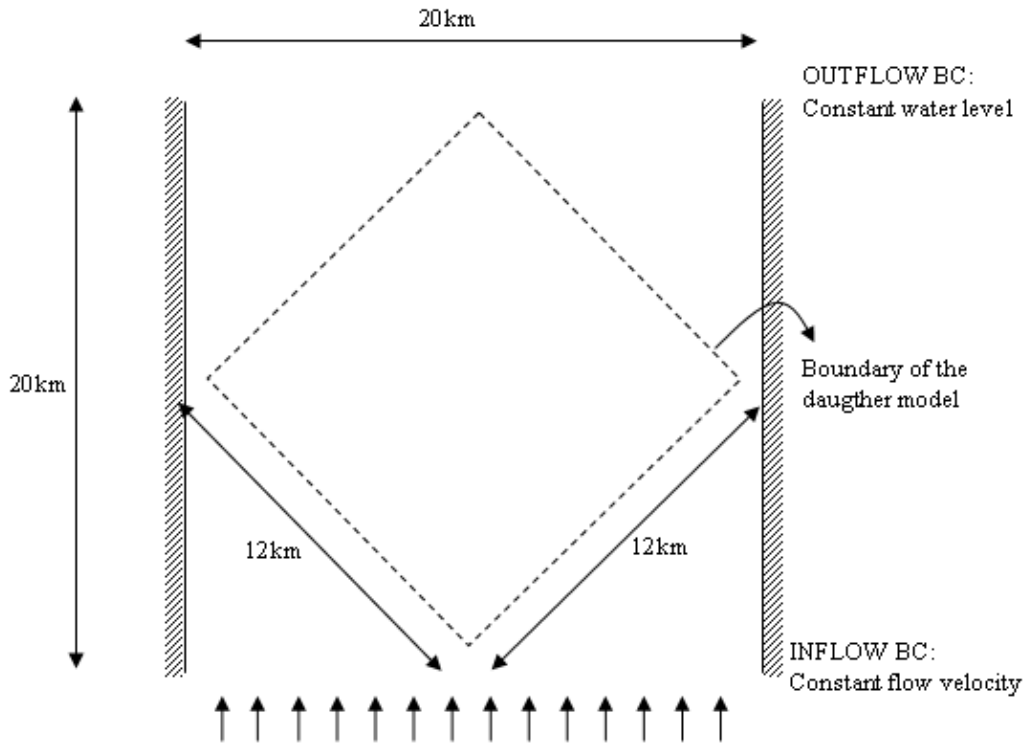

southern boundary and a constant water level is prescribed at the northern boundary. The results of this model are used for further comparisons an validations of the 'daughter model', where the tangential components of the flow velocity are prescribed. The setup of the model is defined according to the following data:

Table 20 – Data for the setup of the mother model

Parameter	Value	Remarks
Basin length	20 km.	
Basin width	20 km.	
Mean water depth		non-uniform bottom
Simulation time	1 day	
Number of rows	21	
Number of columns	21	
Number of vertical layers	10	
Grid size dx=dy	1000 m.	
Time step	30 sec.	
Roughness height	0.006 m.	
Initial flow velocity	0.00 m/s	
Initial water surface	0.00 m.	
Transport BC	1 m/s	constant flow velocity
WL BC	1.00 m	

The daughter model represents a domain within the mother model, that is rotated 45° (see Figure 114). Therefore, the results of the mother model can be decomposed according the direction of the boundaries of the

daughter model in order to obtain the normal and tangential components of the flow velocity. The setup of the model is defined according to the following data:

Table 21 – Data for the setup of the daughter model

Parameter	Value	Remarks
Basin length	12 km.	from mother model results
Basin width	12 km.	
Mean water depth		non-uniform bottom
Simulation time	1 day	
Number of rows	13	
Number of columns	13	
Number of vertical layers	10	
Grid size dx=dy	1000 m.	
Time step	10 sec.	
Roughness height	0.006 m.	
Initial flow velocity	0.00 m/s	
Initial water surface	0.00 m.	
Transport BC	normal + tang	INFLOW boundaries
Transport BC	normal + tang	OUTFLOW boundaries

5.5.3 Results

Two experiments are defined for testing this boundary condition type:

- tang_A: 2D test
- tang_B: 3D test

The discussion of the results corresponds the two models, the mother model and the daughter model.

Mother model

In this section is discussed the results of the mother model which are used for comparison and validation of the results of the daughter model.

The mother model simulates the flow in a basin with two open boundaries and steady and uniform flow. The boundaries are located at the southern and northern boundaries and water flows in the north direction. This basin presents a non uniform bathymetry which is depicted in Figure 115.

This non uniform bathymetry leads to a longitudinal variation of the flow velocity as seen in Figure 116 and Figure 117. The total water depth at the southern boundary is less than the depth at the northern boundary, which leads to a reduction o the flow velocity.

The calculated depth integrated flow currents (transport) at the points where the boundaries of the daughter model are located, are decomposed according to the direction of these boundaries and prescribed as boundary conditions (normal and tangential components).

Figure 115 – Top view of the non uniform bathymetry of the mother model

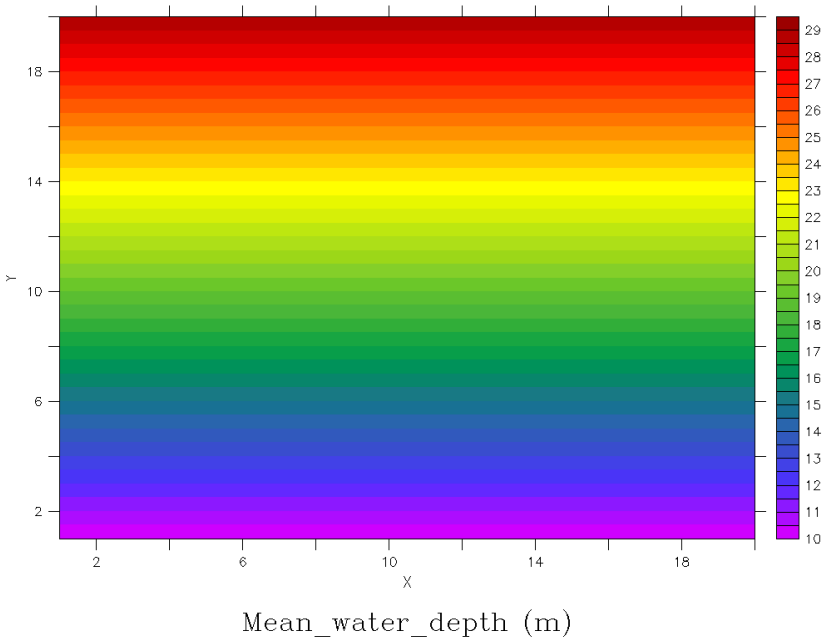

Figure 116 – Calculated flow velocities and water levels after 1 hour

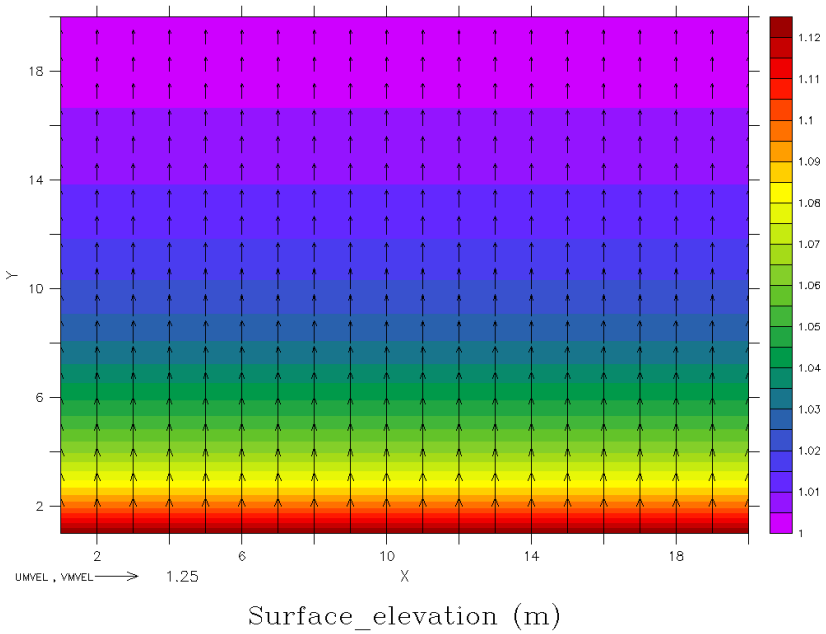

Figure 117 – Longitudinal view of the calculated flow velocities after 1 hour

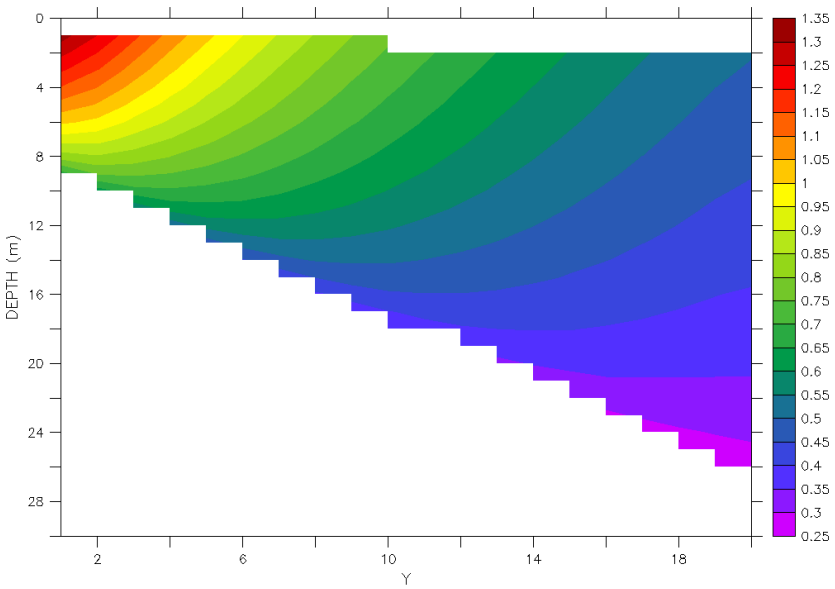

Daugther model

The daughter model represents a part of the domain of the mother model, being rotated 45° in relation to the boundaries of the mother model. Hence, the bathymetry of the daughter model is non uniform with gradients in both directions (see Figure 118).

Figure 118 – Top view of the non uniform bathymetry of the daughter model

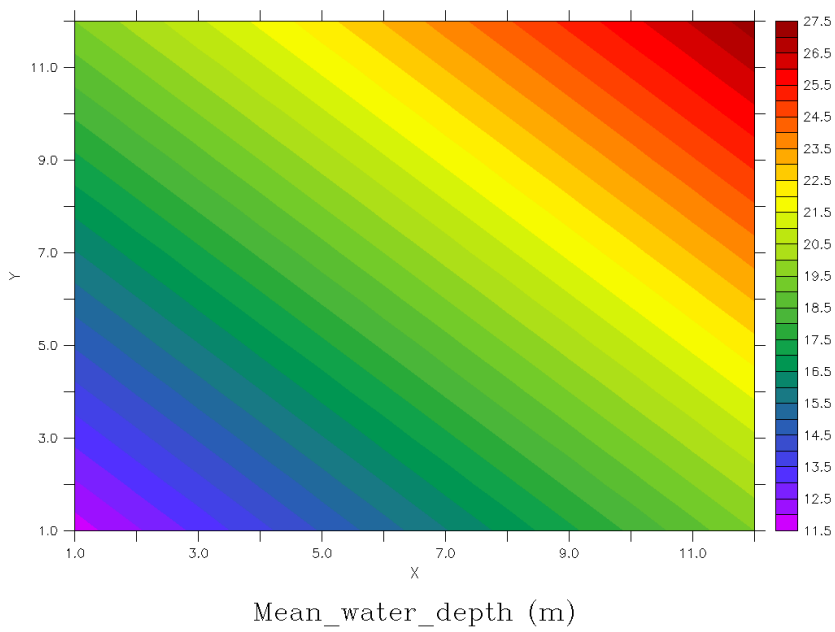

The normal and tangential components of the depth integrated currents are prescribed as boundary conditions. Since the flow velocity varies along the flow direction in the mother model, different values are obtained at the middle axis of the mother model. Moreover, there is no transversal variation of the flow velocity. The obtained depth integrated currents vary from $11.8m^2/s$ to $11.805m^2/s$. Then, the normal and tangential components presents the same value since the daughter model is rotated 45°, producing components that vary from $8.344m^2/s$ to $8.348m^2/s$. These values are prescribed as boundary conditions in the daughter

model.

Figure 119 depicts the calculated water levels and the flow velocities. Notice that the flow direction is rotated 45° in relation to the direction of the boundaries. The calculated water levels vary in the diagonal direction according to the flow direction in the mother model.

Figure 119 – Calculated flow velocities and water levels after 1 hour

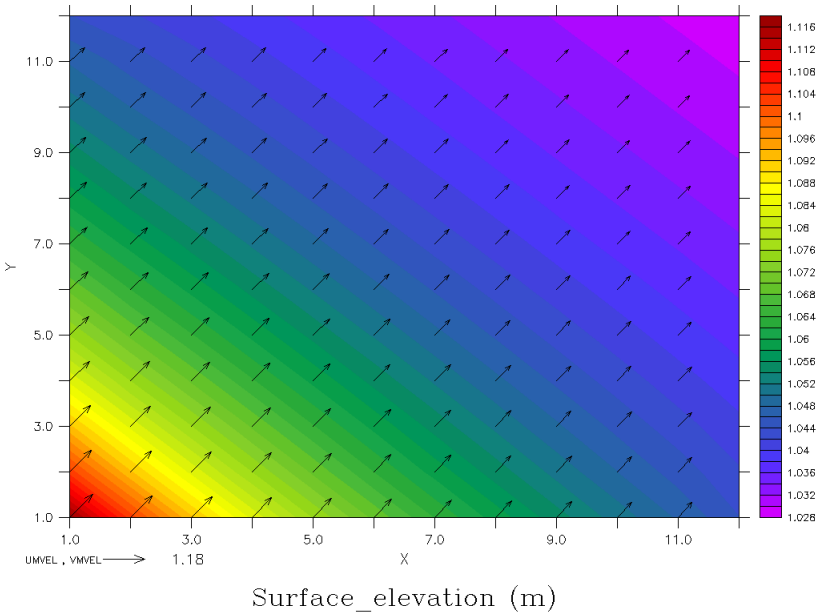

The calculated water levels of both models (mother and daughter) were compared to validate the performance of the prescribed boundary conditions. Figure 120 depicts a comparison of the calculated water levels, these levels correspond to the central axis of the mother model. The differences in the calculated water levels vary from $2cm$ to $5cm$ which represent a percentage of the water level of 2.5% and 5.4%.

Figure 121 and Figure Figure 122 depict the longitudinal view, in both directions, of the flow velocity. It is evident the presence of the bottom gradient in both directions.

The mass conservation was verified, this verification was done in order to determine if the prescribed boundary condition, fulfills the requirement of the mass conservation. The mass balance for water shows (see Figure 123) a mean mass balance of -0.034% of the initial water volume.

5.5.4 Conclusions

The implemented boundary condition type for tangential components of the depth integrated currents could reproduce in an acceptable way the obtained results of the mother model, small differences in the calculated water levels are observed. Additionally, the daughter model could take into account the non uniform bathymetry with bottom gradients in both directions for both modes (2D and 3D). Moreover, hte mass balance for water showed a low percentage deficit of the initial water volume, which remains constant along the simulation time.

As a preliminary conclusion, the tangential components boundary condition type showed an acceptable performance and constitute in an alternative for the prescription of boundary conditions in practical situations.

Figure 120 – Comparison of the calculated water levels of the mother and daughter model

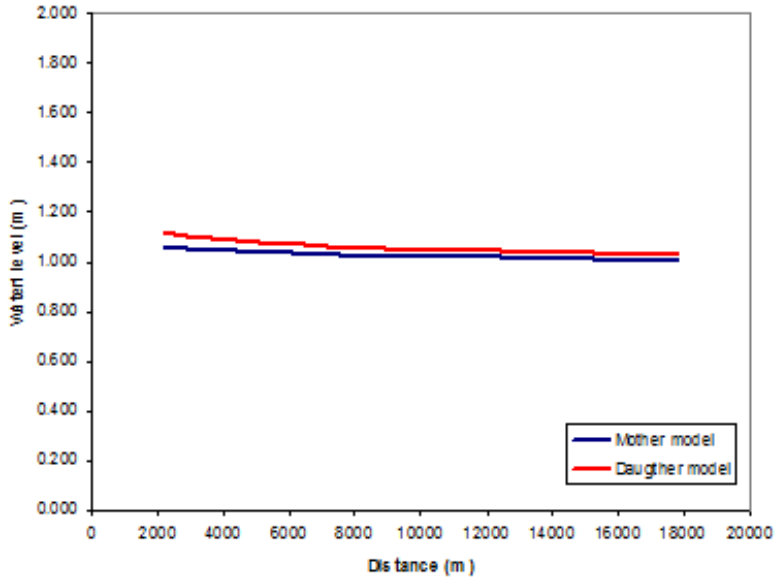

Figure 121 – Longitudinal view of the flow velocity in the X-direction

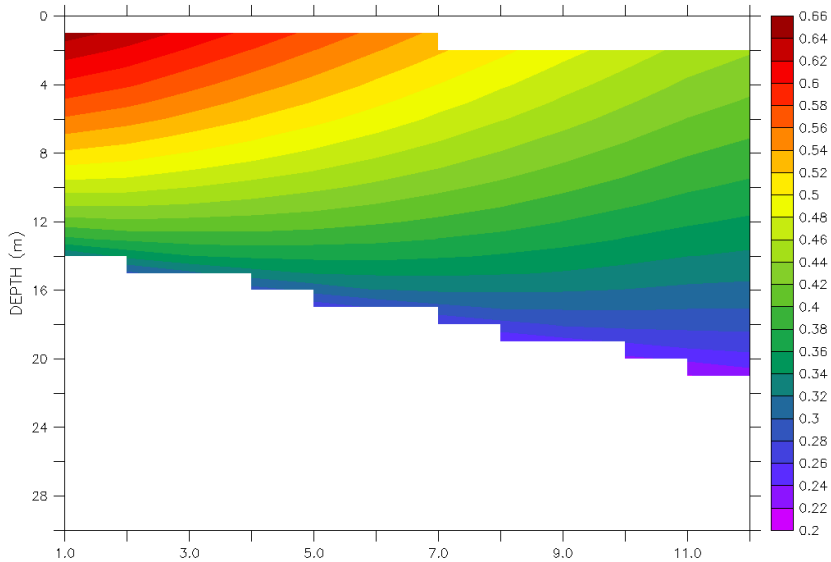

Figure 122 – Longitudinal view of the flow velocity in the Y-direction

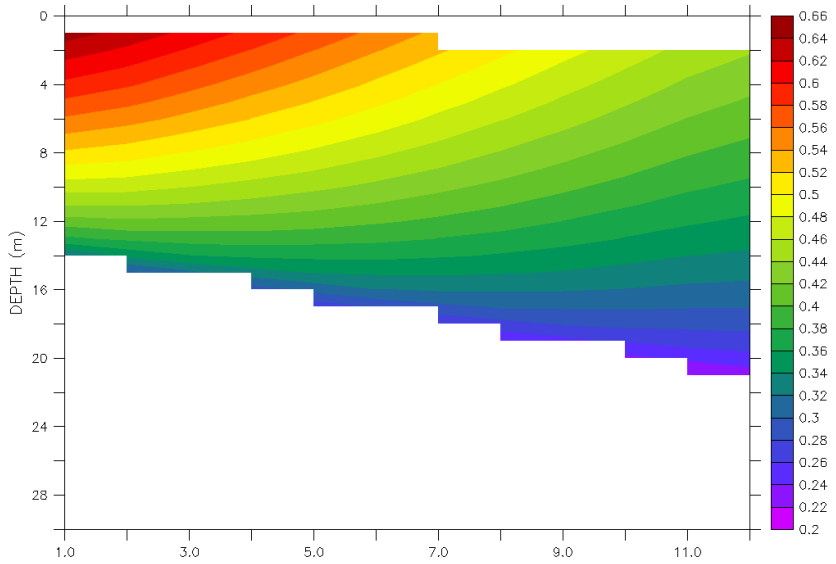

Figure 123 – Calculated mass balance for water, experiments A and B

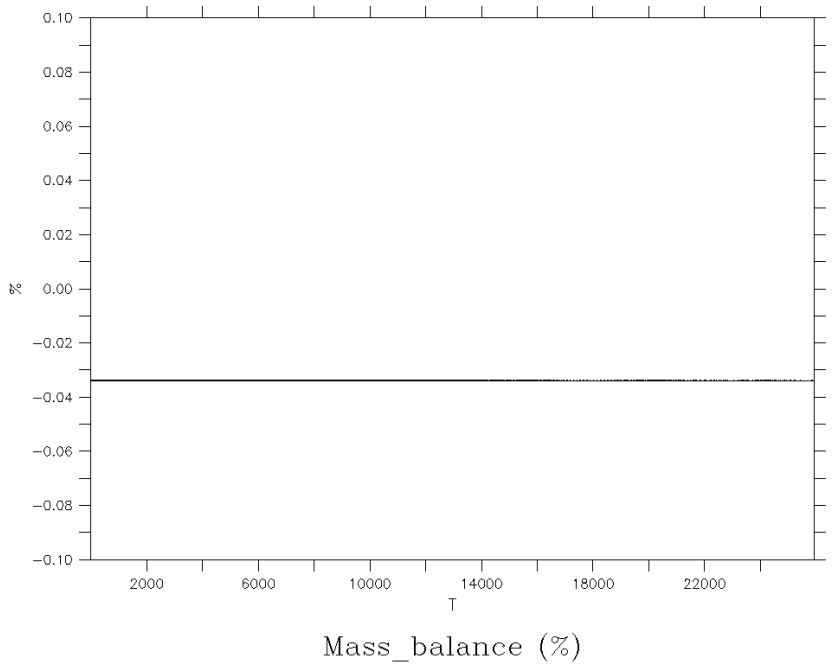

5.6 Conclusions

Regarding the functionality of the additional boundary conditions presented in this chapter, the following conclusions can be drawn:

1. using the distributed discharge boundary condition, the computed total discharge calculated at the open boundary is equal to the prescribed total discharge. Additionally, it was observed that the mass conservation for water and salinity present relative errors of 0.00001% and 0.01% respectively, which are low values considering that standard modeling practices suggest that mass balance errors below 1% are acceptable. Hence the distributed discharge doundary condition works acceptably.
2. Neumann boundary conditions give reliable results when used in combination with a prescribed water level boundary condition or a radiative condition. Mass conservervation is obeyed wel (relatiev deviation $\sim 0.0001\%$ or less).
3. the Thatcher-Harleman boundary condition is able to reproduce cyclic time behaviour of salinity near the boundary of a tidally dominated region. The mass balance for water and salinity is satisfied.
4. imposing a depth-integrated tangential velocity at the boundary reproduce results that are obtained with a larger scale model. The mass balance of water is satisfied with an overall relative accuracy ~ 0.03%.

6 Sediment

6.1 Introduction

In this chapter the functionality of the COHERENS sediment transport module is validated. To this end, five test cases have been investigated.

The first three validation cases are devoted to sediment profiles and consider the distribution of sediment throughout the water column only (i.e. no horizontal structure). These are effectively 1DV model. First the standard Rouse profile is considered in Sect. 6.2. Next, Sect. 6.3 studies the modification of this profile for high sediment concentrations when vertical mixing becomes damped. Finally, Sect. 6.4 considers the influence of hindered settling of sediment particles that occurs for high sediment concentrations.

Next Sect. 6.5 takes into account horizontal structure by simulation of a transition from a non-erodible to an erodible bed under a stationary flow. This is done for both 2D and 3D situations. The downstream sediment distribution is compared to results from literature.

Section 6.6 considers a gravity current that occurs when a plume of suspended partcles is released in a medium of lower density (clear water). Finally, in Sect. 6.7 the transport of both bed and suspended load in a bended flow is simulated and interpreted.

6.2 Rouse profile

6.2.1 Introduction

The objective of this test case is to assess the ability of COHERENS to simulate suspension transport by performing 1DV simulations. Computed longstream velocity and sediment concentration profiles are plotted against the analytical law of the wall and Rouse profile, respectively, given by:

$$u = \frac{u_*}{\kappa} \ln(z/z_0) \tag{158}$$

$$\frac{c(z)}{c_a} = \left(\frac{H-z}{z} \frac{a}{H-a} \right)^{\frac{w_s}{\kappa u_* \beta}} \tag{159}$$

where u is the longstream velocity, κ is the von Karman number = 0.4, u_* is the bed shear velocity given by $\sqrt{\tau_b/\rho_w}$ with τ_b the bed shear stress and ρ_w the water density, z_0 is the bed roughness coefficient, $c(z)$ is the suspended sediment concentration, c_a is the equilibrium sediment concentration near the bed at reference level a, w_s is the settling velocity and β is the ratio of the sediment diffusion coefficient to the momentum diffusion coefficient (inverse of the Prandtl-Schmidt number).
Simulations are performed for multiple values of the dimensionless parameter u^*/w_s – i.e. low settling velocity $\rightarrow u_*/w_s = 10$, medium settling velocity $\rightarrow u_*/w_s = 5$ and high settling velocity $\rightarrow u_*/w_s = 1$ – and two formulas for the bed boundary condition – i.e. Van Rijn, 1984 and Smith and McLean, 1977:

- Van Rijn, 1984

$$c_{a,i} = 0.015 \frac{d_i}{a_i} \frac{T^{1.5}}{d_*^{0.3}} \tag{160}$$

Here, $T = \tau/\tau_{cr} - 1$ and $d_* = d\left[(s_s - 1)\frac{g}{\nu^2}\right]^{1/3}$. The reference level a_i (either half the size of the dunes or the roughness length scale k_S) is limited to be between $0.01H$ and $0.1H$.

- Smith and McLean, 1977

$$c_{a,i} = 0.0024 c_{max} \frac{\theta}{1 + 0.0024\theta} \tag{161}$$

$$a = k_s + 26.3(\theta - \theta_{cr})d_i \tag{162}$$

$$k_s = 30 z_0 \tag{163}$$

Here, c_{max} is the maximum possible concentration, i.e. the concentration of a bed packed with sediment, k_s is the Nikuradze roughness length, z_0 the roughness length used in COHERENS and θ the non-dimensional Shields parameter.

In addition, the influence of the vertical grid resolution on result accuracy is tested by carrying out simulations with 5, 10, 15, 25, 50, 100 and 200 vertical grid layers, non-uniformly distributed over the water height (higher resolution at the bed).

Aims and requirements

It can be concluded that hydrodynamics and suspended sediment transport are simulated satisfactorily in COHERENS when difference between the numerical results and the respective analytical solutions is $< 10^{-3}$. Similarly, mass balance is achieved when the difference between the sediment in suspension and the cumulative net sediment transport through the bed is $< 10^{-3}$.

6.2.2 Model setup

The one-dimensional, uniform model grid consists of 1 computational cell of 10m by 10m, and the water depth is 10m. Hydrodynamics are calculated by COHERENS , with the flow field components initially set to zero. The eddy-diffusivity D_z is provided to the model as initial condition and has a parabolic shape:

$$D_z = \kappa H u_* \frac{z}{H}\left(1 - \frac{z}{H}\right) \tag{164}$$

A quadratic formulation of the critical bed shear stress is adopted, with a spatially uniform bed roughness z_0 set to $z_0 = 0.001m$, $d_{50} = 200\mu m$ and $\rho_s = 2650 kg/m^3$. The shear velocity u_* is set to $0.07 m/s$ (in case calculation of hydrodynamics is disabled, a user-defined value for u_* is used to explicitly calculate bottom stress in **usrdef_phsics**; otherwise a value for the pressure gradient is provided as data for 1D-forcing), the settling velocity w_s is calculated with the formula of Camenen:

$$w_s = \frac{\nu}{d} Re_* = \frac{\nu}{d}\left[\sqrt{\frac{1}{4}\left(\frac{A}{B}\right)^{2/m} + \left(\frac{4}{3}\frac{d_*^3}{B}\right)^{1/m}} - \frac{1}{2}\left(\frac{A}{B}\right)^{1/m}\right]^m \tag{165}$$

where $A = 24.6$, $B = 0.96$, $m = 1.53$ and d_* is determined by the following expression:

$$d_* = d\left[(s_s - 1)\frac{g}{\nu^2}\right]^{1/3} \tag{166}$$

Fluid density is considered uniform, with added density effects excluded from the model. The model settings are summarized in Table 22

Table 22 – Model setup for suspended sediment concentration test cases

Characteristic	Model setting
Model grid	1DV, 1 cell, $10m$ x $10m$
Vertical grid resolution	5, 10, 15, 25, 50, 100, 200 layers
Water depth	$10m$
Hydrodynamics calculation	Enabled
Turbulence formulation	Parabolic
Initialisation	zero flow, zero suspended sediment, parabolic diffusion coefficient
D_{50},ρ_s,z_0	$200\mu m$, $2650kg/m^3$, $0.001m$
Bed shear stress	Quadratic
Critical bed shear stress	Brownlie: $\theta_{cr} = 0.22d_*^{-0.9} + 0.06.10^{(-7.7d_*^{-0.9})}$
Bed boundary condition	Test case 2.2: Van Rijn
	Other: Smith and McLean
Settling velocity	Test case 1: $w_s = 0.007m/s$
	Test case 2: $w_s = 0.014m/s$
	Test case 3: $w_s = 0.07m/s$
Density	Uniform
Time step	$12s$
Simulated time	$12h$

6.2.3 Results

Longitudinal velocity profiles Fig. 124 plots the theoretical law of the wall of Eq. (158) against the velocity profile calculated by COHERENS , and this for the different values of vertical grid resolution.

Suspended sediment concentration profiles As described in the model setup, simulations were performed for three values of the parameter u_*/w_s. Figs. 125 and 126 plot the theoretical Rouse profile against the COHERENS results, with the formula of Smith and McLean and Van Rijn employed as bed boundary condition, respectively.

Figure 124 – COHERENS velocity profile versus the theoretical law of the wall

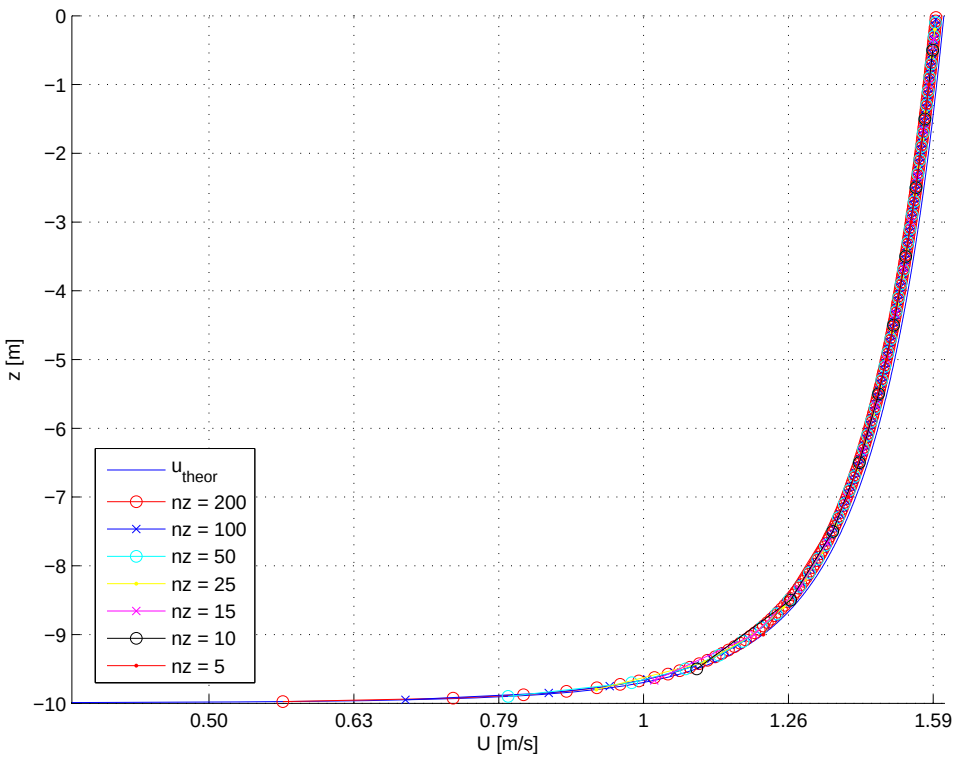

Figure 125 – COHERENS suspended sediment concentration profile versus the theoretical Rouse profile for $u_*/w_s = 5$ and bed boundary condition of Smith and McLean

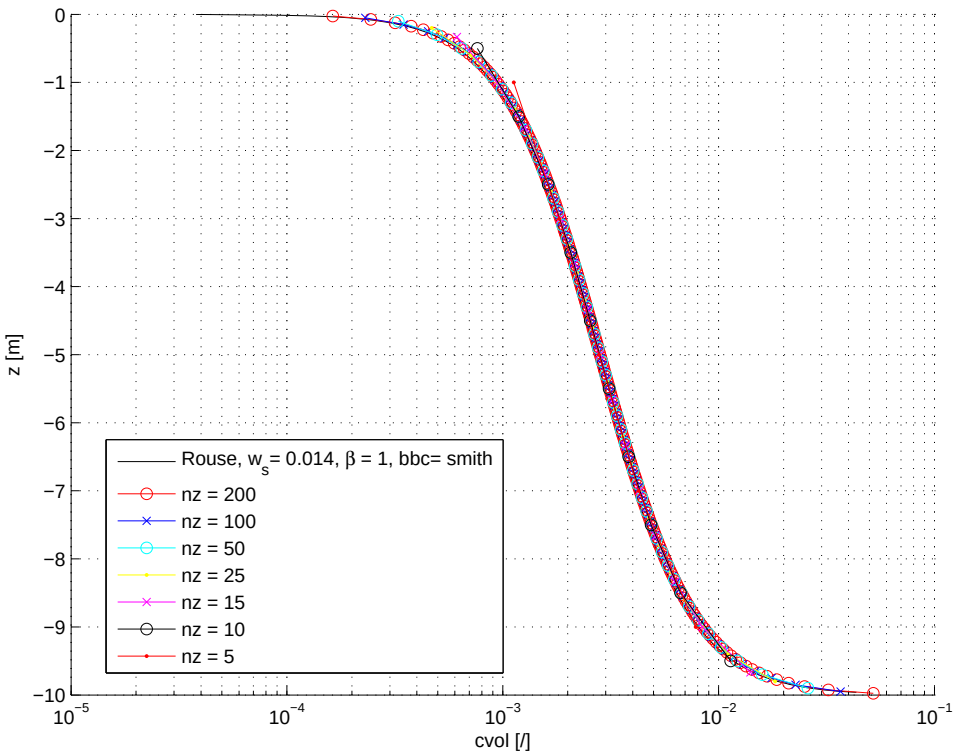

Figure 126 – COHERENS suspended sediment concentration profile versus the theoretical Rouse profile for $u_*/w_s = 5$ and bed boundary condition of Van Rijn

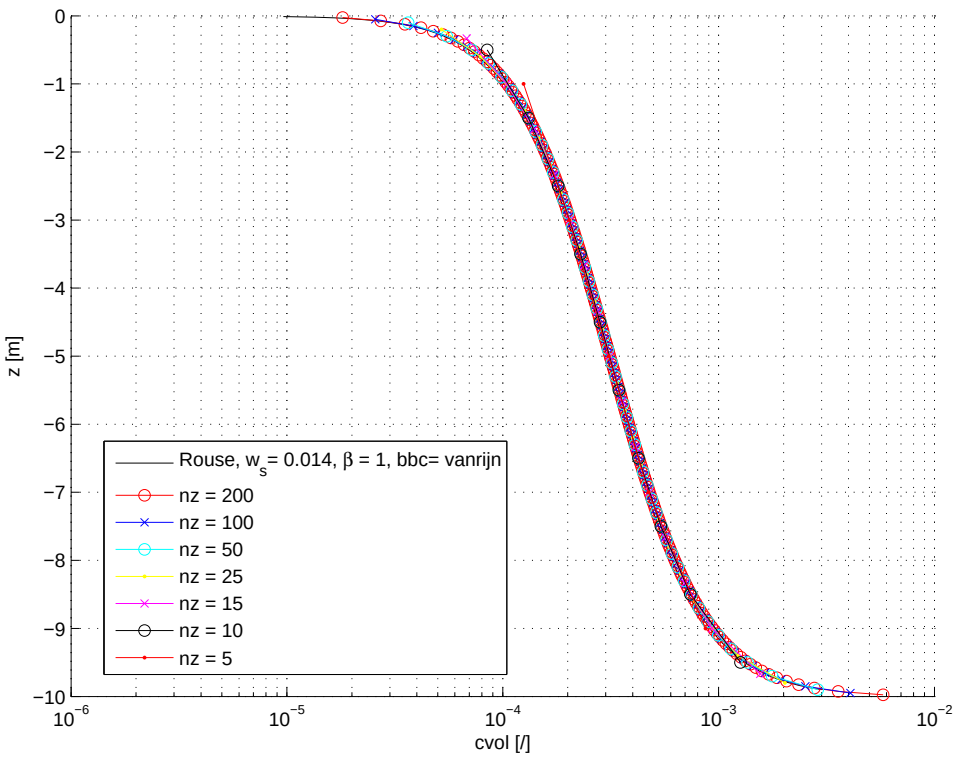

The suspended sediment transport concentration profiles for $u_*/w_s = 10$ and $u_*/w_s = 1$ are displayed in Figs. 127 and 128, respectively. The bed boundary condition of Smith and McLean was retained for these simulations.

Sediment flux through the bed Since an accurate determination of the net sediment transport at the bed is essential to the calculation of bed deformation and, thus, channel morphology, it is prudent to evaluate the performance of COHERENS in balancing sediment deposition and erosion fluxes through the bed with the amount of sediment in suspension. This balance is expressed by the following equation:

$$\int_0^t \left[E\left(t'\right) - D\left(t'\right)\right] dt' = \int_a^\zeta c\left(z,t\right) dz \tag{167}$$

in which the left hand side represents the net sediment transport through the bed [deposition flux $D = w_s c\left(z = a, t\right)$ and erosion flux E is related to the adopted bed boundary condition] and the left hand side represents the amount of sediment in suspension. Eq. (167) expresses that the difference of these two terms should be zero, or sufficiently small to be deemed negligible. Fig. 129 shows the temporal evolution of the net deposition and erosion flux through the bed, indicating that, indeed, the channel has reached a state of equilibrium and that the total amount of suspended sediment at the final time step can be compared to the sediment transport flux through the bed, integrated over time. Table 23 displays this comparison for different values of the vertical grid resolution.

6.2.4 Conclusions

- COHERENS approximates the theoretical longstream velocity profile very well. While increasing the vertical grid resolution improves accuracy for the lower vertical grid resolutions, this improvement becomes negligible from 50 layers onwards.

Figure 127 – COHERENS suspended sediment concentration profile versus the theoretical Rouse profile for $u_*/w_s = 10$

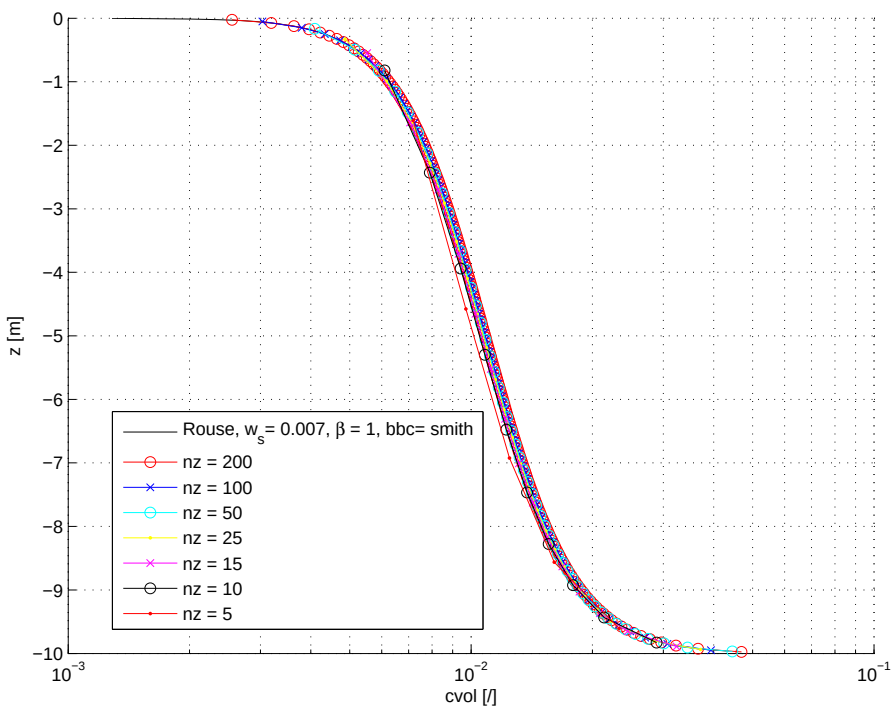

Figure 128 – COHERENS suspended sediment concentration profile versus the theoretical Rouse profile for $u_*/w_s = 1$

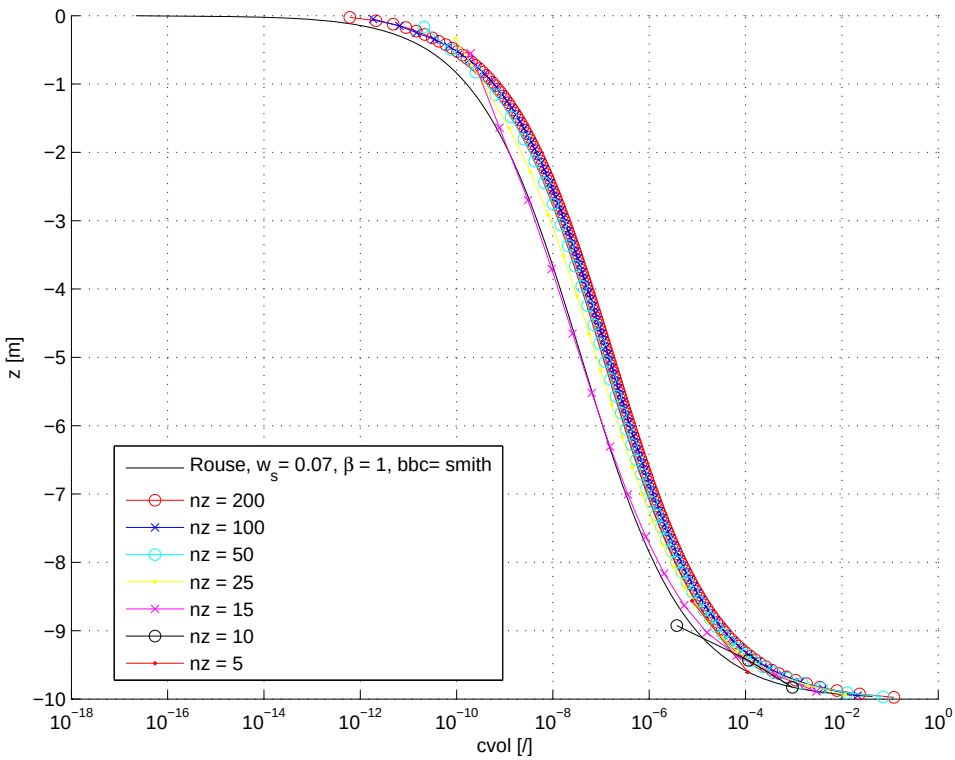

- There is a very good agreement between the theoretical Rouse profile and the COHERENS results for u_*/w_s=5 and u_*/w_s=10, while some inaccuracy occurs for u_*/w_s=1. This could be attributed to the high concentration gradient that occurs near the bed in cases of high settling velocity, which - even with the TVD scheme - introduces numerical diffusion into the model and in turn causes the computed concentrations to be higher than they are in reality. Nevertheless, considering that the numerical results are displayed on a logarithmic scale, the margin of error is reasonable. The lack of data points in the direction of the water surface in the $n_z = 5$ and $n_z = 10$ curves indicates that $c = 0$ for these points, an expected approximation error when employing low vertical resolutions in cases with high settling velocity.
- Table 23 shows a perfect agreement between the calculated total net sediment transport through the bed in time and the total amount of suspended sediment particles at equilibrium. An increase in vertical grid resolution yields a significant increase in both quantities for resolutions smaller than 50 layers, showing the importance of the grid resolution with respect to bed morphology calculations. At higher resolutions, this increase becomes negligible. Fig. 129 shows a logical evolution of the net sediment transport through the bed from the initiation of motion up to the equilibrium state. The calculated value for the flux at equilibrium equals $1.22\ 10^{-9}$ (or ca. 4cm/year), which is negligible.

Figure 129 – Temporal evolution of the net sediment transport flux through the bed ($n_z = 50$ layers)

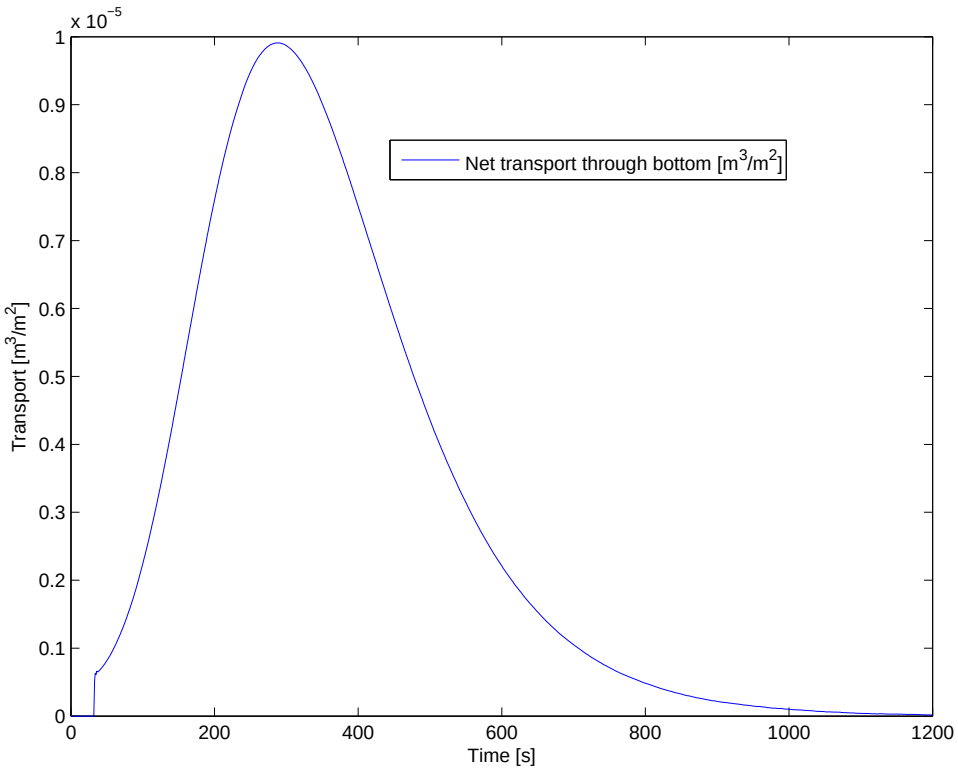

Table 23 – Comparison of total amount of suspended sediment with total net transport through the bed

	Vertical grid resolution						
Parameter	5	10	15	25	50	100	200
Cumulative net sediment transport through bed [m^3]	3.5624	3.8012	3.9127	4.0278	4.1456	4.2298	4.2891
Volume of suspended sediment [m^3]	3.5624	3.8012	3.9128	4.0278	4.1457	4.2298	4.2895
Difference [%]	$< 10^{-3}$	$< 10^{-3}$	0.0026	$< 10^{-3}$	0.0024	$< 10^{-3}$	0.0093

6.3 Density stratification

6.3.1 Introduction

Sediment suspended in turbulent flows of water over plane beds are known to influence the structure of the flows by which they are carried. This influence is called the stratification effect. A sediment-laden flow has a mean velocity profile with larger gradients than the corresponding profile in clear water flow. Consequently, the distribution of suspended sediment is affected as well, and differs from the sediment distributions presented in section 6.2.
The test cases under consideration are governed by the following momentum and sediment balance equations:

$$g\frac{\partial \zeta}{\partial x} = \frac{\partial}{\partial z}\left(A_z \frac{\partial u}{\partial z}\right) \tag{168}$$

$$\frac{\partial c}{\partial t} = \frac{\partial}{\partial z}\left(D_z \frac{\partial c}{\partial z} - w_s c\right) \tag{169}$$

where A_z and D_z denote vertical viscosity and diffusion. The main effect of density stratification will be a decrease of both A_z and D_z (i.e. turbulence damping). Consequently, Eq. (168) indicates that the flow velocity u will increase to keep the local shear stress fixed.

Aims and requirements

Performing a qualitative analysis, it can be concluded that stratification effects are implemented well into COHERENS when the shape of the numerical concentration profiles, velocity profiles and diffusion coefficients of simulations with enabled stratification effects significantly differ from the profiles associated with simulations without stratification effects. Specifically, stratification should yield a lower diffusion coefficient and higher flow velocities when compared to the expected profiles without stratification. Furthermore, decreasing critical shear stress should not only have an effect on the depth averaged suspended sediment concentration (as would be the case without stratification) but also on the slope of the concentration profile (representing the effect of stratification).

Table 24 – Model setup for density stratification test case

Characteristic	Model setting
Vertical grid resolution	50 layers (non-uniform)
Critical bed shear stress	$x\ 10^{-4}\, m^2/s^{2*}$
	* x= 1, 2, 5, 15, 1/2, 1/5, 1/15
Settling velocity	Test case 1: $w_{s,cst} = 0.021\, m/s$
	Test case 2: Camenen for sand (see Eq. (165))
Bed shear velocity	$u_* = 0.07\, m/s$
Bed boundary condition	Smith and McLean
Turbulence model	parabolic eddy viscosity profile
Density effects	Munk-Anderson equation
Time step	$12s$

Figure 130 – Comparison of velocity profile without and with stratification effects (model settings of section 6.2 with $nz = 50$)

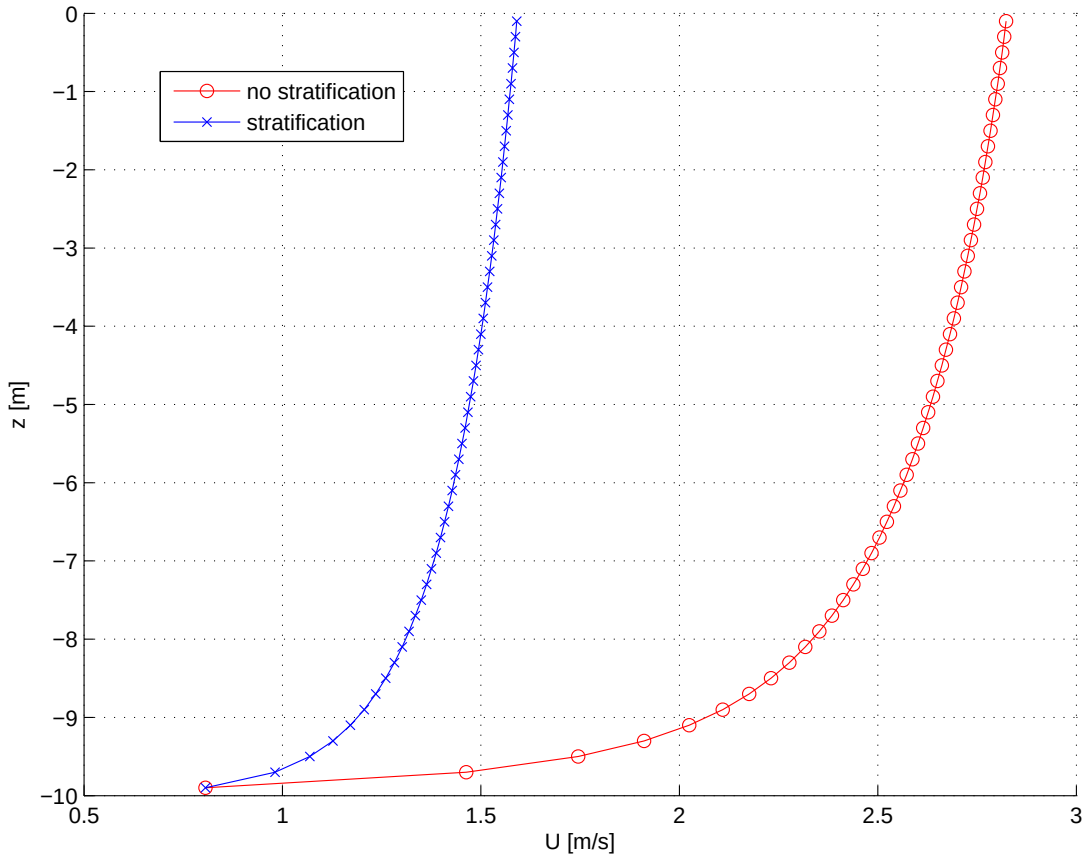

6.3.2 Model setup

The setup of the 1DV model is similar to the setup described in section 6.2, yet now with the inclusion of density stratification effects. Two different cases are simulated. In the first case, user-defined values for the critical kinematic shear stress ($\tau_{cr} = x\,0.0001\,m^2/s^2$, with $x = 1, 2, 5, 15, 1/2, 1/5, 1/15, 1/100$) and the settling velocity ($w_s = 0.0221\,m/s$) are supplied to the model. In the second case, the same values for the critical shear stress are used, yet the Camenen formula for sand particles is employed to calculate the settling velocity to include the effect of stratification on the settling velocity as a second influence for the sediment concentration profile. Vertical grid resolution for all the simulation is 50 layers, non-uniformly distributed over the water height (higher resolution near the bed). The model settings are summarized in Table 24

6.3.3 Results

Figs. 130 - 132 show the effects of enabling the calculation of stratification effects on the velocity profile, the diffusion coefficient profile and the concentration, respectively, whereas Figs. 133 - 135 display the added effect of calculating the settling velocity. Finally, Figs. 136 - 138 and Figs. 139 - 141 show the stratification results for test case 1 and test case 2, respectively.

6.3.4 Conclusions

The following conclusions can be drawn from the results presented in section 6.3.3:

- Stratification decreases the diffusion coefficient D_z. A decrease in critical shear stress τ_{cr}, and thus an increase in the amount of suspended sediment, yields a further decrease in D_z.
- When enabling the effect of stratification on the settling velocity w_s, the diffusion coefficient decreases slightly.
- The opposite holds for the longstream velocity U: when D_z decreases, U increases, and vice versa.
- The suspended sediment concentration shows behaviour similar to that of D_z. However, enabling the effect of stratification on w_s increases slightly the suspended sediment concentration, as w_s decreases with increasing c.

Despite the lack of analytical solution to serve as a reference for comparison, the results mirror the expected stratification effects. Therefore, it is concluded that stratification is implemented well within COHERENS .

Figure 131 – Comparison of diffusion profile without and with stratification effects (model settings of section 6.2 with $nz = 50$)

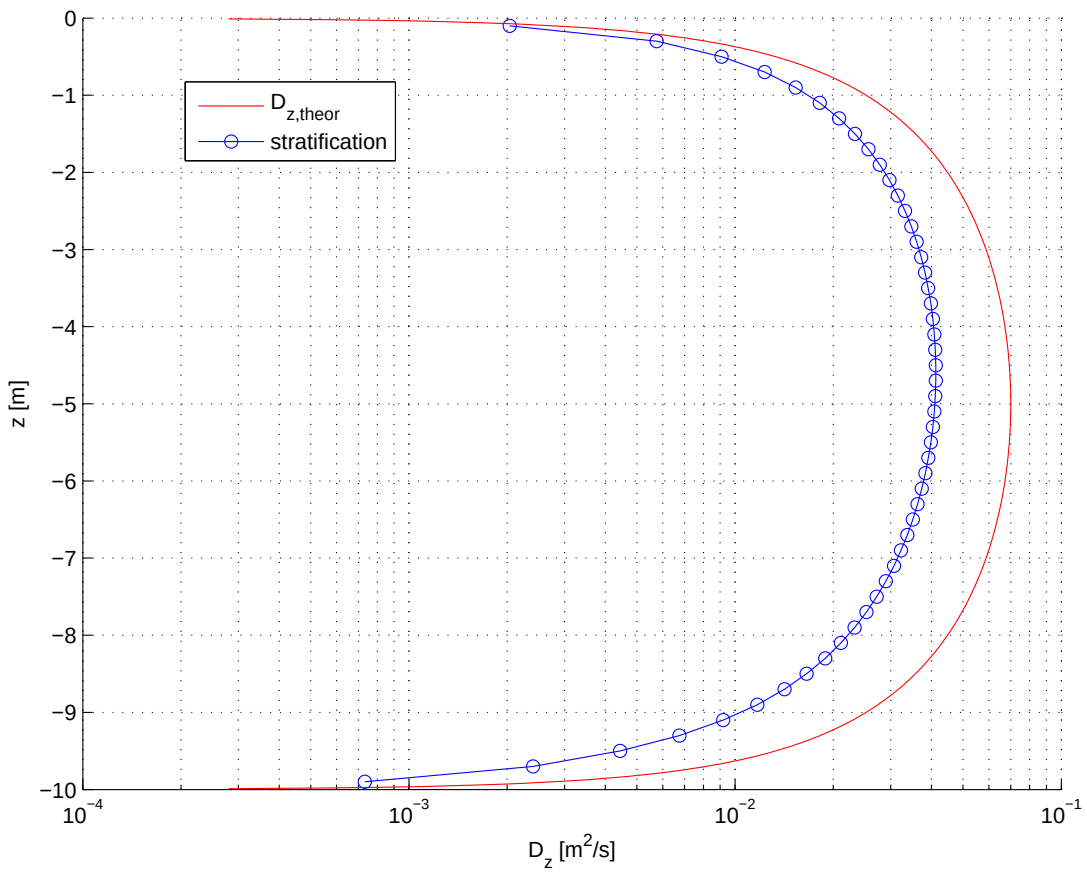

Figure 132 – Comparison of concentration profile without and with stratification effects (model settings of section 6.2 with $nz = 50$)

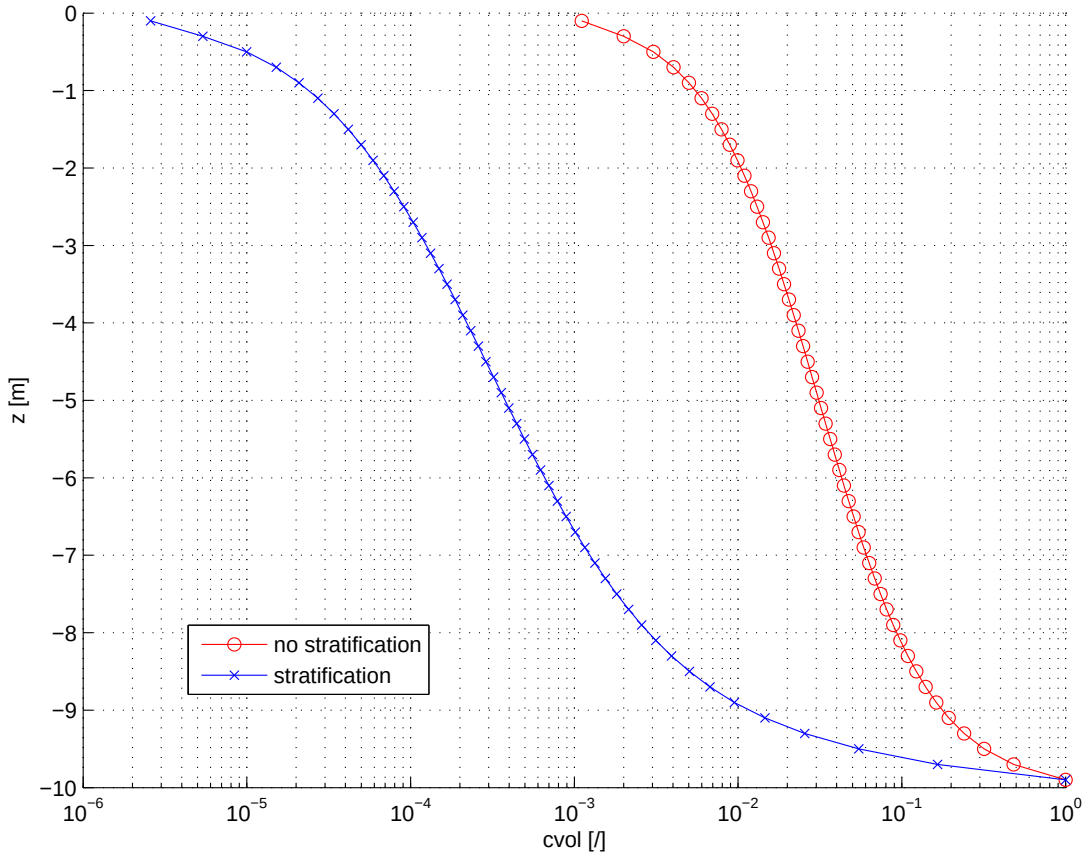

Figure 133 – Comparison velocity profiles of stratification test case 1 (w_s = cst) and stratification test case 2 (w_s = calculated) for $\tau_{cr} = 1/15\,10^{-4}\,m^2/s^2$

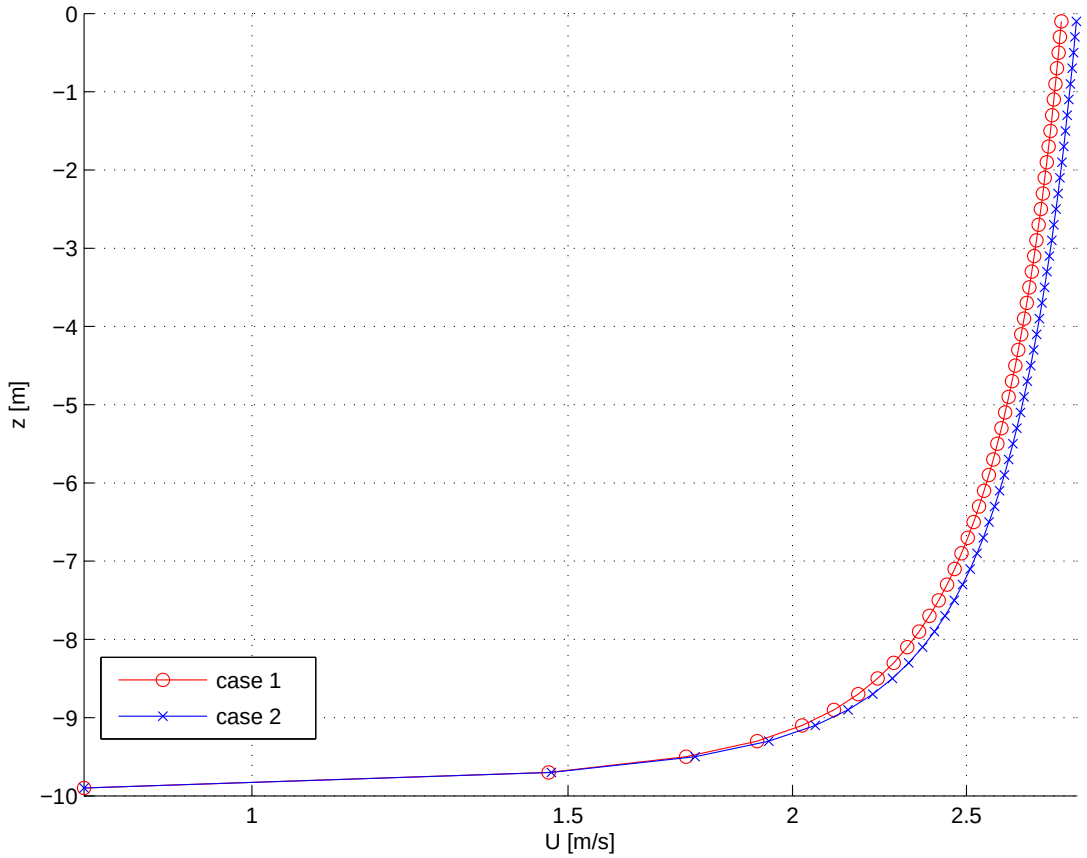

Figure 134 – Comparison diffusion profiles of stratification test case 1 (w_s = cst) and stratification test case 2 (w_s = calculated) for $\tau_{cr} = 1/15\,10^{-4}\,m^2/s^2$

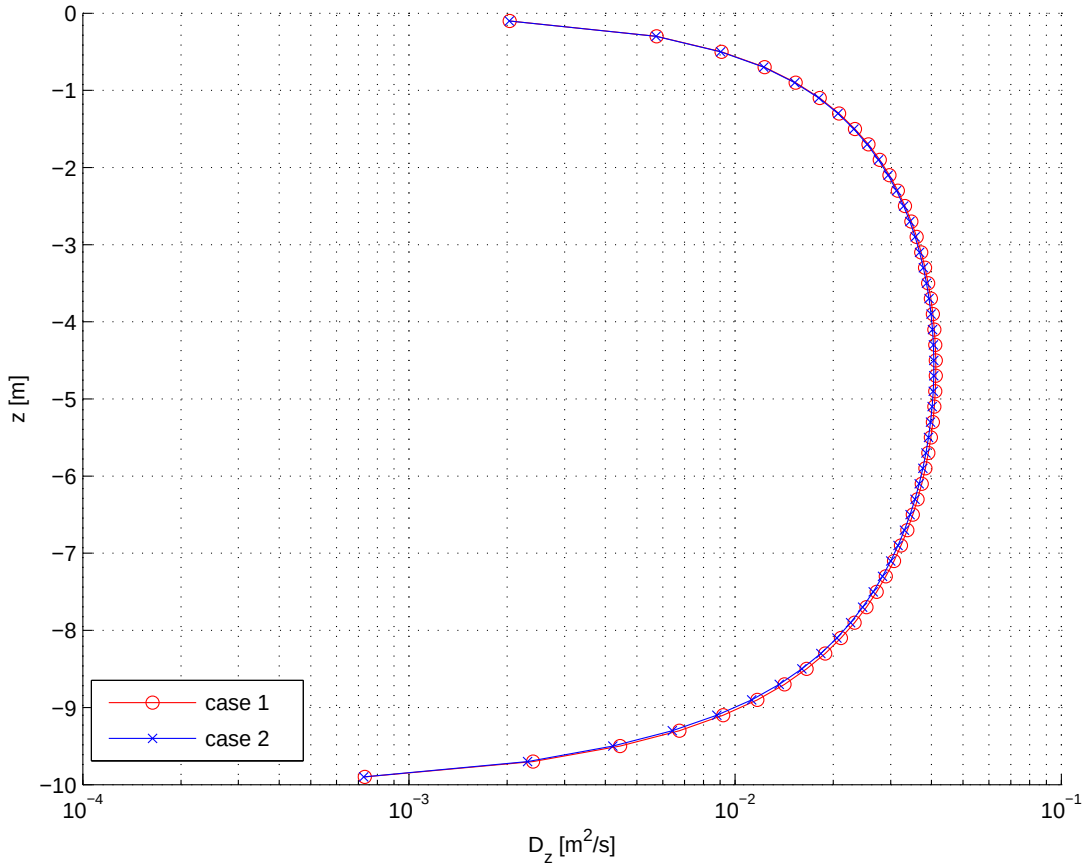

Figure 135 – Comparison concentration profiles of stratification test case 1 (w_s = cst) and stratification test case 2 (w_s = calculated) for $\tau_{cr} = 1/15\,10^{-4}\,m^2/s^2$

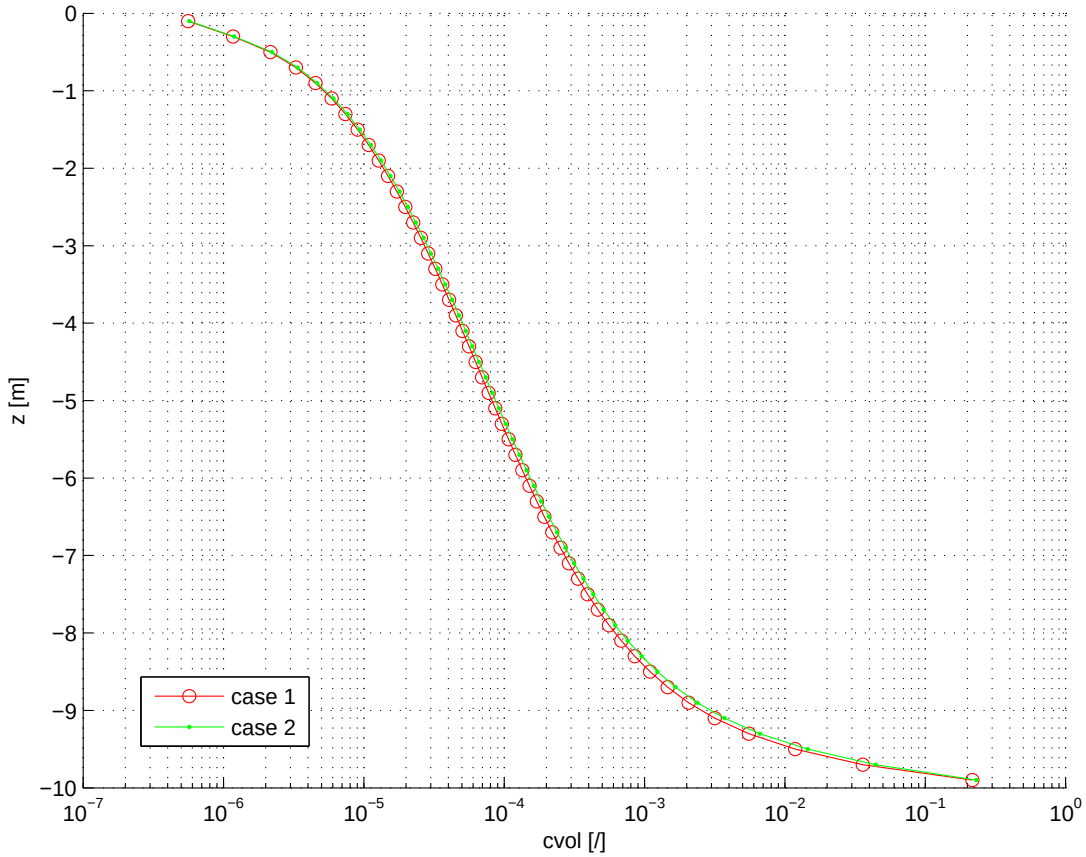

Figure 136 – Velocity profiles in case of stratification, with w_s = cst

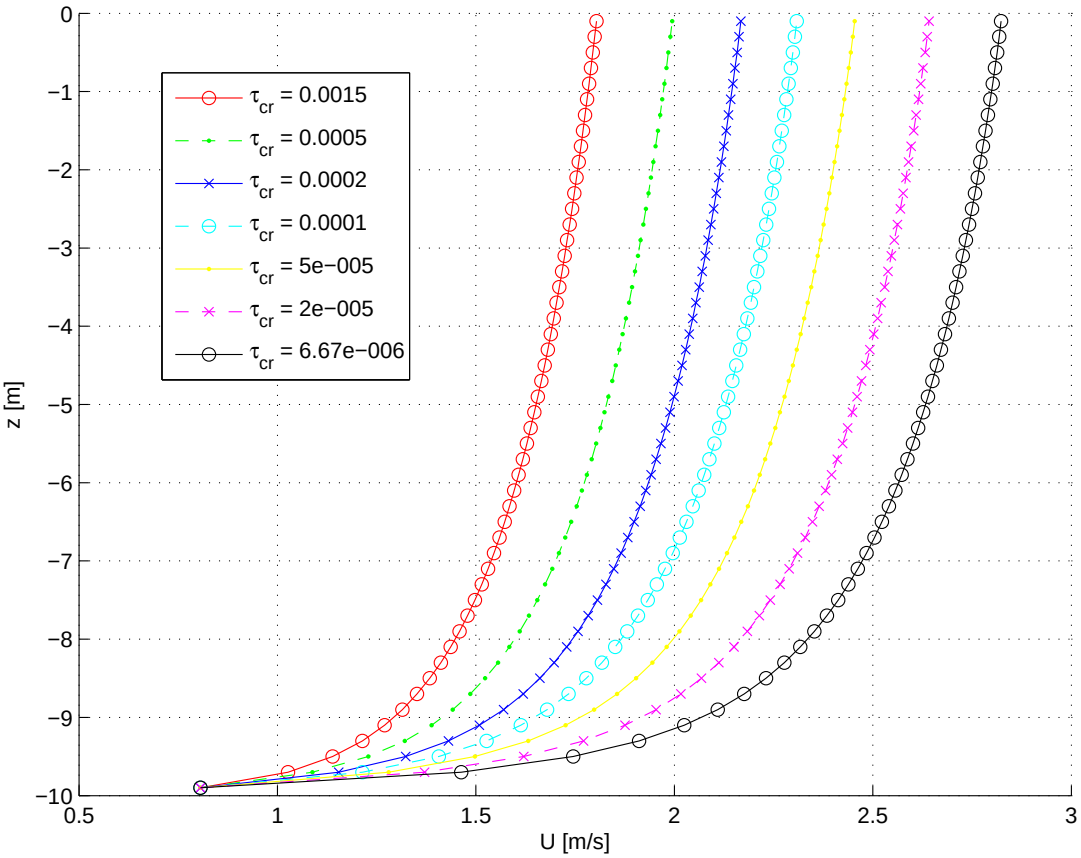

Figure 137 – Diffusion profiles in case of stratification, with w_s = cst

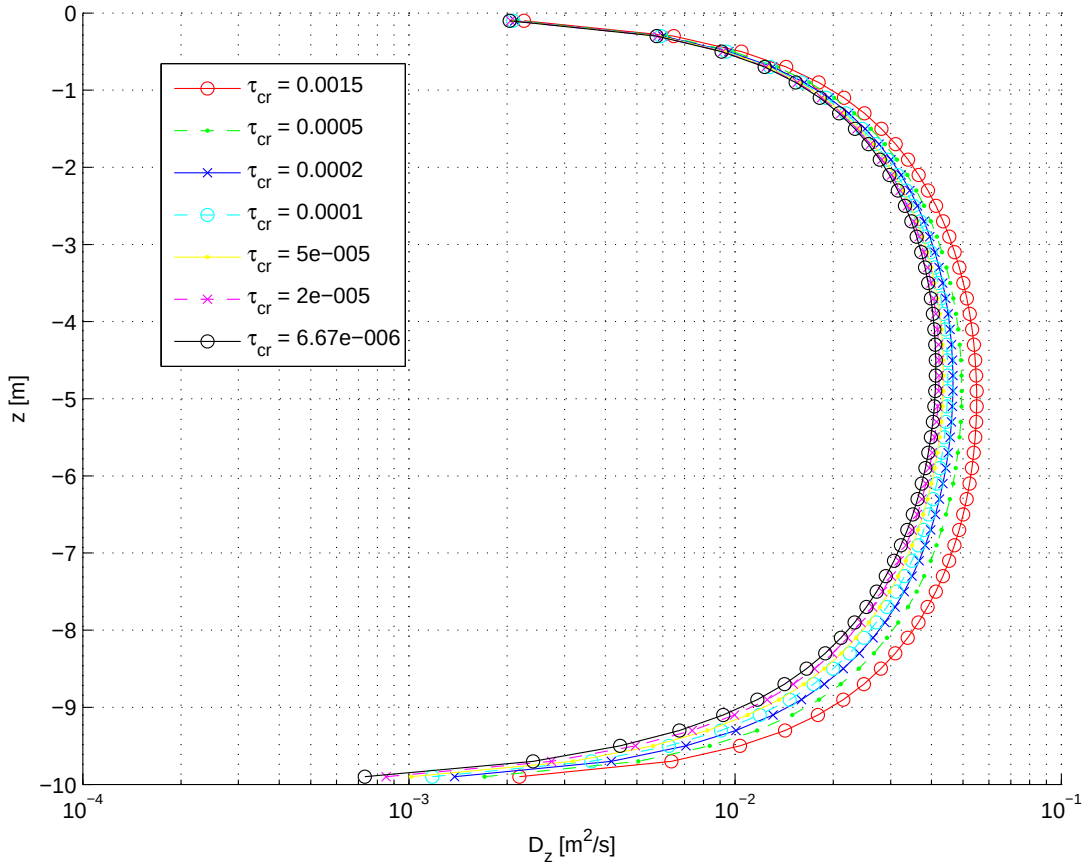

Figure 138 – Concentration profiles in case of stratification, with w_s = cst

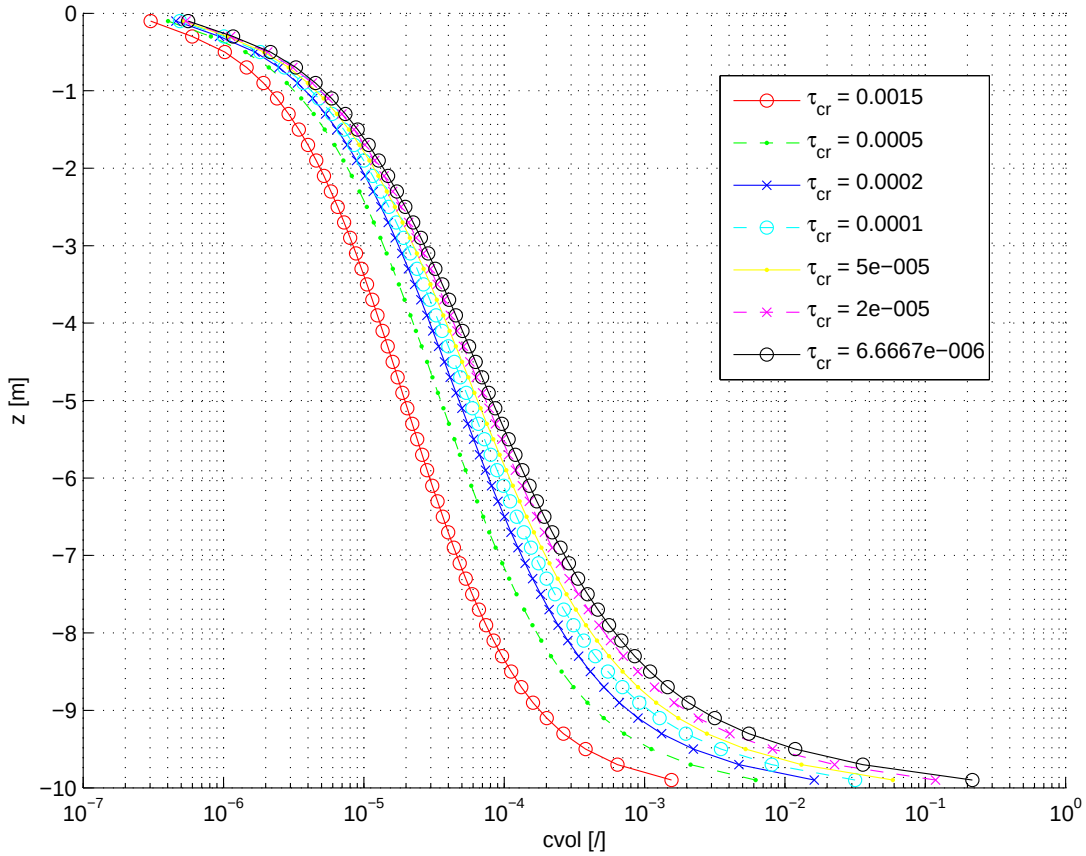

Figure 139 – Velocity profiles in case of stratification, with w_s = calculated

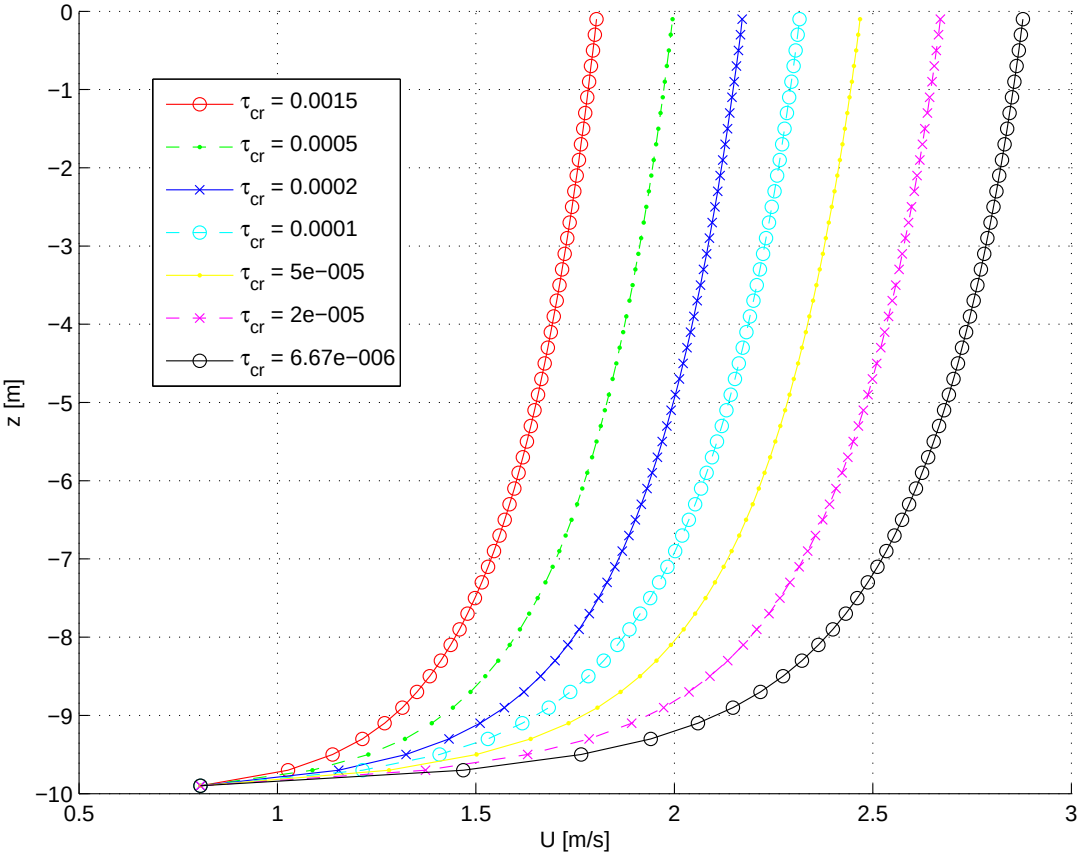

Figure 140 – Diffusion profiles in case of stratification, with w_s = calculated

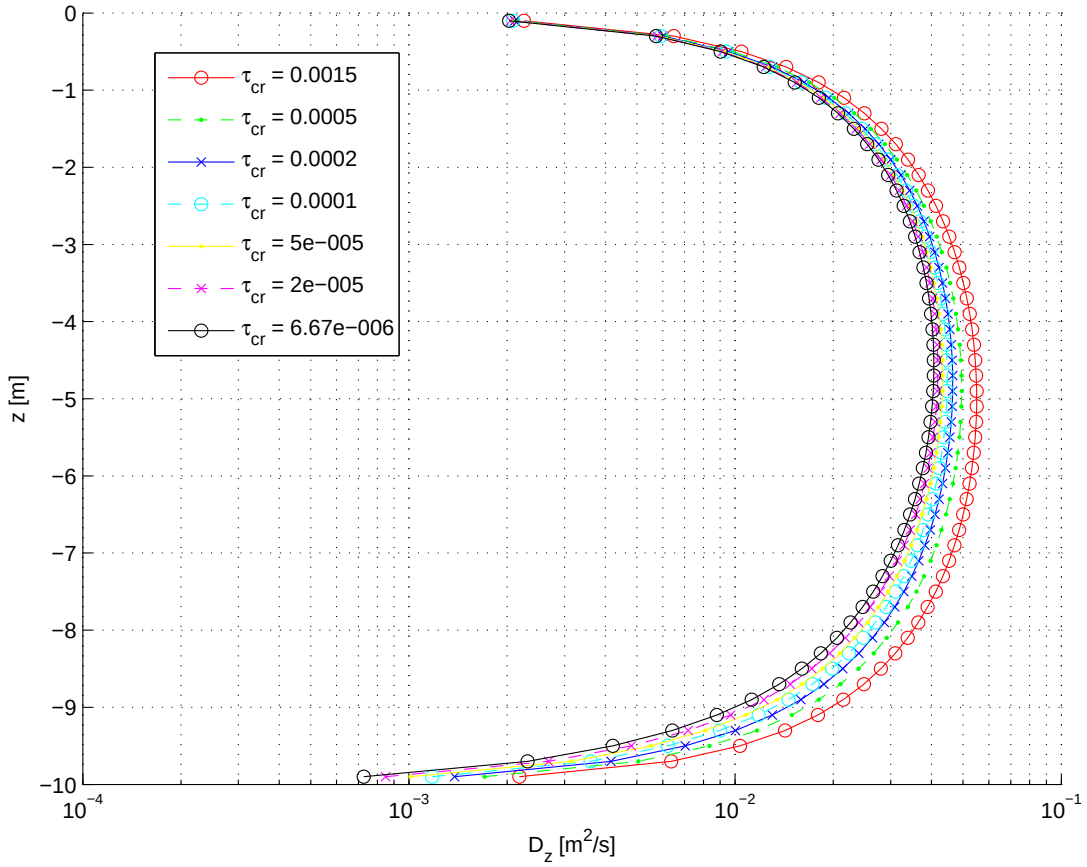

Figure 141 – Concentration profiles in case of stratification, with w_s = calculated

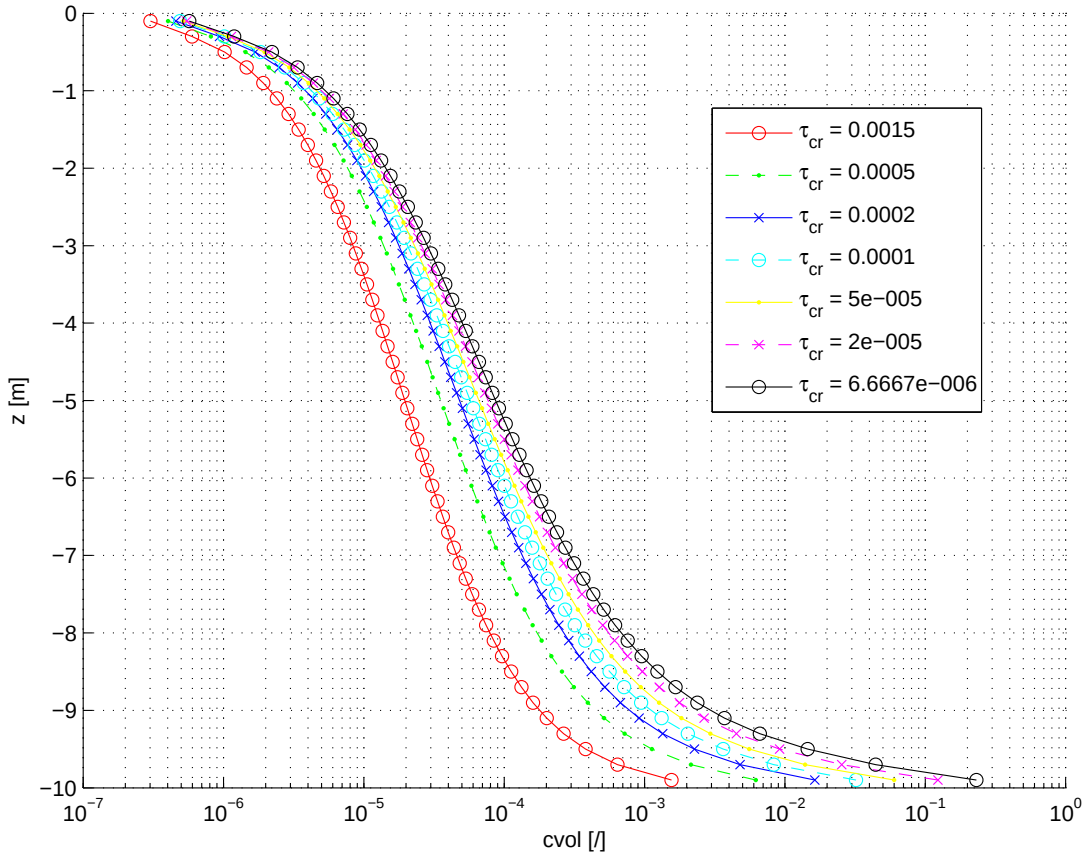

6.4 Hindered settling

6.4.1 Introduction

Hindered settling occurs when the settling of suspended sediment particles is obstructed by neighbouring particles in their downward trajectory toward the bed. This causes the particles to remain in suspension longer than would be the case without the hindering effect, and thus leads to a lower settling velocity for the suspended sediment particles.
In this section, the implementation by COHERENS of the formula of Richardson and Zaki, 1954 for sand, specifically designed to account for the effects of hindered settling, is tested. The formula describes the settling velocity in high sediment concentrations as a function of the sediment concentration, Re_p and the undisturbed settling velocity $w_{s,0}$:

$$w_s = w_{s,0}\,(1-c)^n \tag{170}$$

The model results are compared to a linearisation of the Richardson and Zaki, 1954 analytical solution for the suspended concentration profile with hindered settling:

$$\frac{c_z}{c_a} = \frac{-1}{\left(nc_a - 1\right)\left(\frac{C_R}{c_a}\right)^{-1} - nC_a} \tag{171}$$

Where C_R is the theoretical Rouse concentration at height z, c_a is the reference concentration employed in the Rouse formulation and n is a linearisation exponent in the Richardson and Zaki, 1954 settling equation with value $n = 4.6$. Calculations are carried out for two cases. In one case, different values for the critical shear stress τ_{cr} are provided alongside a constant value for the settling velocity w_s. In another case, w_s is calculated by providing a particle diameter, while again varying the value for τ_{cr}. This should result in an additional hindrance, as the increased the fluid density increases due to increased sediment concentration.

For calculating the uniform bed resolution, the following equation was used:

$$\sigma_i = 1 + \frac{\tanh \alpha i/n}{\tanh \alpha} \tag{172}$$

Table 25 – Model setup for hindered settling test case

Characteristic	Model setting
Vertical grid resolution	50 layers (non-uniform)
Hydrodynamics calculation	Disabled
Turbulence formulation	user-defined
Initialisation	Flow field: law of the wall
	Turbulence: parabolic profile
Settling velocity	Hindered settling formula Richardson and Zaki, 1954
Critical bed shear stress	$x\ 10^{-4}\ m^2/s^{2*}$
	* x= 1, 2, 5, 15, 1/2, 1/5, 1/15
Hindered settling	Enabled

Here, σ_i is the height of the i the layer (of a total of n layers), and α is a grid stretching parameter, which was set to 1.5.

Aims and requirements

It can be concluded that hindered settling is implemented well into COHERENS when the suspended sediment concentration profile with hindered settling enabled shows a higher depth-averaged concentration (yet similar slope) due to the decreased w_s compared to the general Rouse-profile (qualitative comparison)and the difference between the numerical results and the analytical solution is $< 10^{-3}$ (quantitative comparison). Similar behaviour should be observed when decreasing the critical shear stress (qualitative comparison).

6.4.2 Model setup

Model setup is similar to the setup described in section 6.2 - i.e. 1DV model with bed boundary condition of Smith and McLean - with the inclusion of hindered settling effects and user-defined values for the critical shear stress τ_{cr} as described in section 6.3. In addition, instead of the hydrodynamics being calculated by COHERENS , the law of the wall is provided as an initial condition for the longitudinal velocity field. The vertical grid resolution is 50 layers, non-uniformly distributed over the water height (higher resolution at the bed). The model settings are summarized in Table 25

6.4.3 Results

Fig.142 compares the numerical suspended sediment concentration profiles with and without hindered settling with each other, and with their respective theoretical profiles, while the effect of varying the critical shear stress τ_{cr} on hindered settling is shown in Fig 143.

6.4.4 Conclusions

The following conclusions can be drawn from the results presented in section 6.4.3:

- The numerical results calculated by COHERENS agree very well with the analytical solution. Hindered settling increases the suspended sediment concentration, as described in section 6.4.1
- Decreasing the critical shear stress yields a logical increase in suspended sediment concentration and decrease in concentration gradients (inclination of profile shape decreases).

Based on the above, it can be concluded that hindered settling is implemented well within COHERENS .

Figure 142 – The effect of hindered settling on the suspended sediment concentration

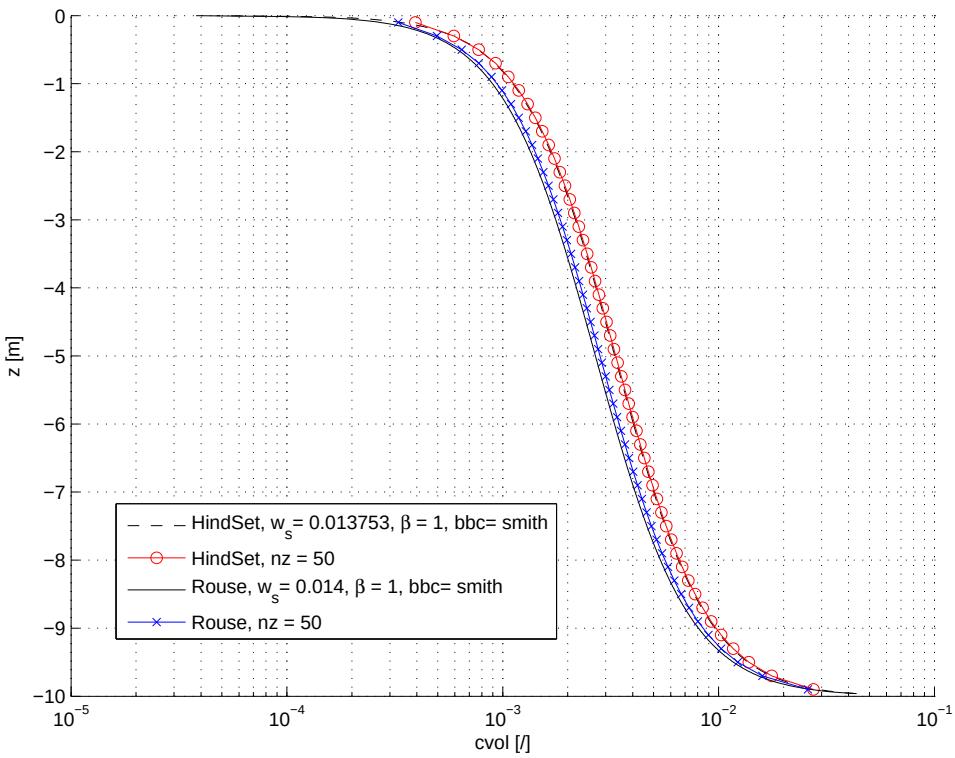

Figure 143 – The effect of varying critical shear stress on hindered settling

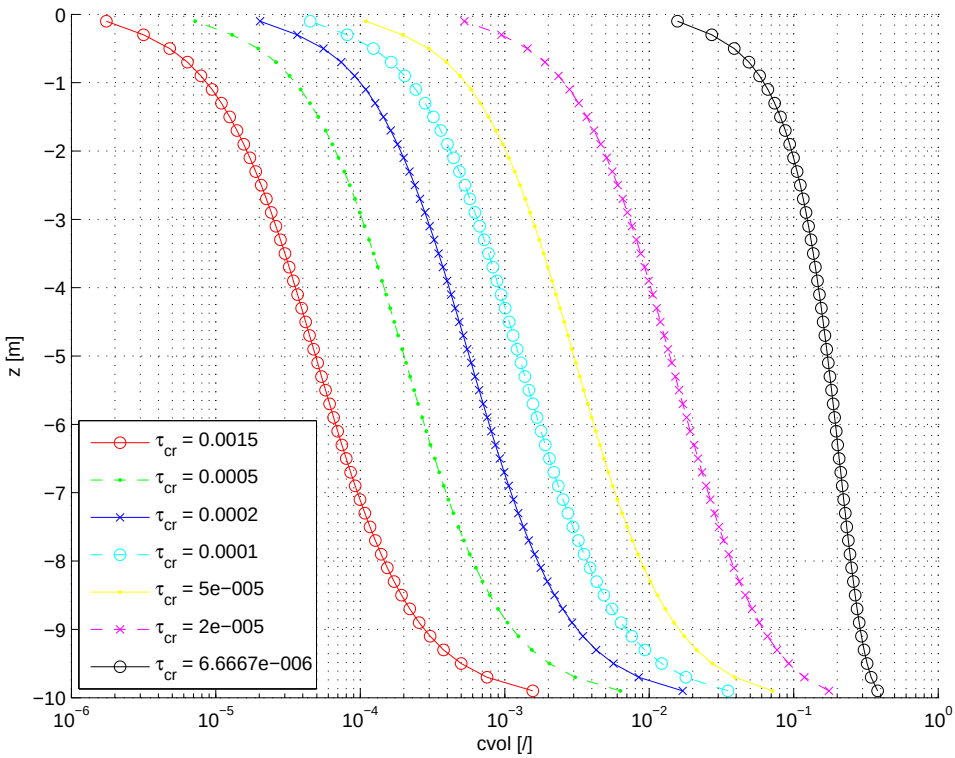

6.5 Comparison 2D/3D simulation

6.5.1 Introduction

In this test case, the development of the sediment concentrations from the transition between a non-erodible bed and an erodible bed is simulated. For this situation, an analytical expression for the sediment concentration profiles as function of the distance from the bed was derived by Hjelmfelt and Lenau, 1970. Only for the special case that $u_*/w_s = 5$, the analytical expression takes a simple form, using only elementary functions. The dimensionless sediment concentration, $\hat{c} = c/c_a$, is expressed as a function of the dimensionless terms $X = \frac{\beta\kappa u_* y}{UH}$, $Z = z/H$ and $A = z_a/H$ with U the depth averaged flow velocity. This results for this situation in:

$$\hat{c} = \sqrt{\frac{A}{1-A}}\sqrt{\frac{1-Z}{Z}} + \frac{\sqrt{A}}{\sqrt{Z}\sin^{-1}\sqrt{1-A}}\sum_{K=1}^{\infty}\frac{(-1)^K\alpha_K\sin\left[2\alpha_K\sin^{-1}\sqrt{1-Z}\right]}{\left(\alpha_K^2-\frac{1}{4}\right)}e^{-X\left(\alpha_K^2-1/4\right)} \tag{173}$$

With:

$$\alpha_K = \frac{K\pi}{2\sin^{-1}\sqrt{1-A}} \quad for \quad K = 1,2,3,... \tag{174}$$

In this solution, it was assumed that the velocity field is constant in space and time (also over the depth), while the eddy-diffusivity has a parabolic shape:

$$D_z = \beta\kappa z u_*\left(1-\frac{z}{H}\right) \tag{175}$$

Here, κ is the Von Kármán's coefficient, β is the ratio of the sediment diffusion coefficient to the momentum diffusion coefficient (inverse of the Prandtl-Schmidt number).

Aims and requirements

The objective of this test case is to compare the results of two-dimensional sediment transport (using an equilibrium concentration and an adaptation time scale) with a complete three-dimensional simulation. Moreover, it is the objective to compare the different available formulations to calculate the equilibrium concentration for two-dimensional sediment transport.

6.5.2 Model setup

In order to perform a simulation that can be easily compared to the analytical solution, the flow field and diffusivity were given as initial conditions in COHERENS , and the fixed values of these parameters were used in a simulation, in which only sediment concentrations were calculated.

Thus no simulation of the hydrodynamics was performed. The transition between a non-erodible and an erodible bed was simulated by applying an upstream boundary conditions for the sediment concentration of $0\ m^3/m^3$. All simulations were run staring from a zero initial concentration towards a stable equilibrium. Seven simulations were performed, six in 2D and one in 3D (30 layers). An overview is given in table 26 and 27.

Table 26 – Overview of model set up

Simulation	2D	3D
nc	3	3
nr	121	121
nz	1	30
dt [s]	10	10
u_* $[m/s]$	0.03	0.03
H $[m]$	10	10
d_p $[\mu m]$	89.48	89.48
w_s $[mm/s]$	6.0	6.0
iopt_vdif_impl	1	
theta_impl	0.0	

Table 27 – Overview of the 2D simulations

Simulation	Eq. concentration
1	Rouse profile, Gaussian quadrature (3 points)
2	Rouse profile, Gaussian quadrature (7 points)
3	Engelund and Hansen, 1967
4	Ackers and White, 1973
5	Wu *et al.*, 2000
6	Van Rijn, 2003

Figure 144 – Depth averaged concentration as function of distance from the boundary (for different sediment transport models). Equilibrium concentrations are shown with a dotted line

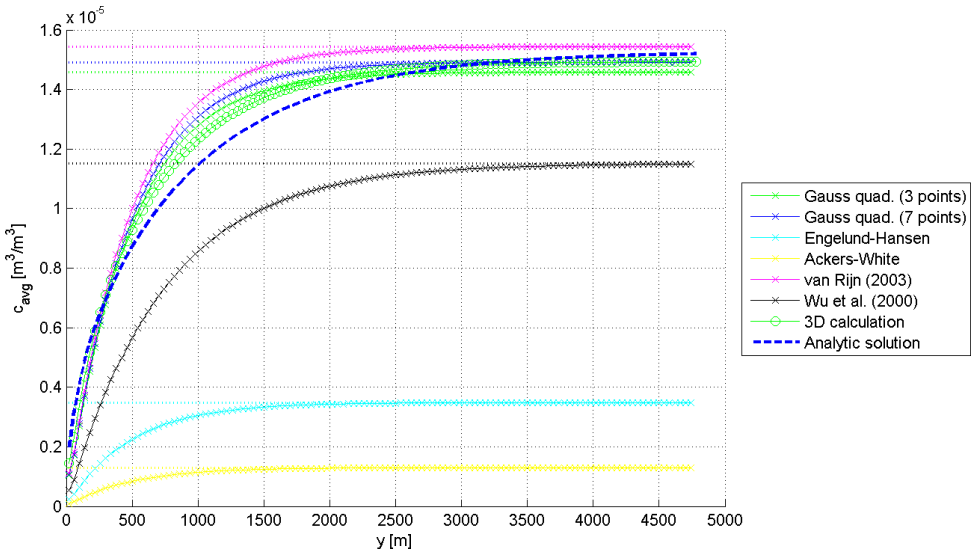

The equilibrium concentration c_{eq} was calculated from the sediment transport rate q_{sed}, using $c_{eq} = q_{sed}/UH$, except for the Rouse profile run. In this situation, the Rouse profile was integrated numerically using Gaussian quadrature, in order to obtain the depth averaged sediment concentration. Hence, in this situation, a value for the near bed sediment concentration was needed. For the near bed concentration, the equation of Smith and McLean, 1977 was used, which was also used for the 3D simulations. Further $z_a = 1.0mm$, $\beta = 1$ and $U = 0.59m/s$.

6.5.3 Results

In fig. 144, the depth averaged concentration is shown as function of the distance from the boundary, together with the equilibrium concentration calculated by COHERENS (for the two-dimensional simulations) and the analytical solution. For the three-dimensional simulations, the calculated concentration profiles at different distances form the boundary are plotted together with the analytical solution of Hjelmfelt and Lenau, 1970 in fig. 145. The analytical solution is plotted for reference purposes only, because the set-up used in COHERENS does not exactly represent the set-up that was used to derive the analytical solution. However, the equilibrium value of the analytical solution can be used, because for large enough distances from the source, this solution should be equal to the Rouse profile.

6.5.4 Conclusion

- The results of the two-dimensional and three-dimensional simulations compare well with each other at least for the Gaussian quadrature with seven points. The equilibrium concentration in 2D is approximated better than in 3D. The reason is that with 30 equidistant cells, the resolution near the bed is still not high enough in 3D to capture the concentration profile well. For the two-dimensional simulation, it seems that seven cells is sufficient for the Gaussian quadrature, while the equilibrium concentration is overestimated slightly when only three cells are used.
- The length scales needed for the adaptation in the two-dimensional and three-dimensional simulations compare well. This agrees with the fact that 3D simulations were used to determine the 2D parametrization for the adaptation time scale. The adaptation length in the model solutions are somewhat smaller than the one from the analytical solution, which is related to the fact that this represents a slightly dif-

Figure 145 – Calculated sediment concentration profiles (3D calculation; green) and analytical solution (black).

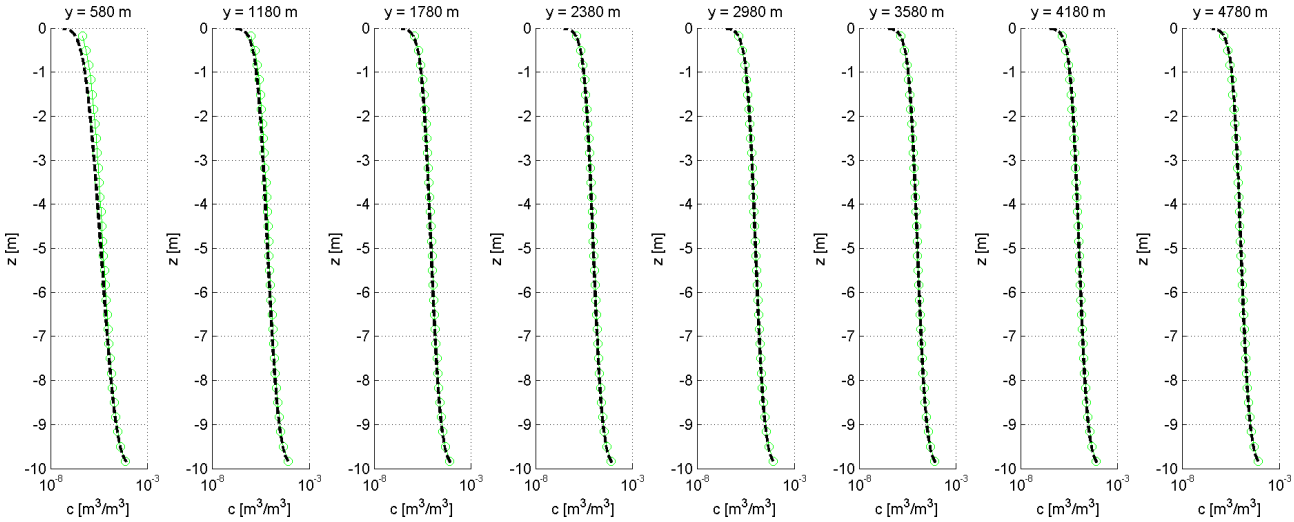

ferent situation

- The concentration profiles in the 3D simulation compare well with the analytical solution for the last observation points. The difference in the first observation point are exaggerated by the use of a logarithmic scale for the concentration.
- The model of Van Rijn, 2003 for the equilibrium situation give similar results as the use of the Rouse profile of the 3D simulation. This could have been expected, because the equation was derived from the same advection-diffusion approach.
- The models of Engelund and Hansen, 1967 (with iopt_sed_eha = 2) and Wu *et al.*, 2000 give equilibrium concentrations that are 30% lower than the advection diffusion approach.
- The model of Ackers and White, 1973 gives equilibrium concentrations that are an order of magnitude lower than the other models.

6.6 Gravity current

6.6.1 Introduction

Particle-driven gravity currents arise whenever suspensions of heavy particles are released into an ambient fluid. Because of the presence of the particles, the density of the suspension differs from that of the ambient, and a buoyancy force is induced which drives the flow. Fig. 146 displays a schematic picture of such a particle-driven gravity current.

The objective of this test case is to assess the ability of COHERENS to simulate density-driven gravity currents. The test case setup is based on the findings of Hogg *et al.*, 2000, who derived an asymptotic extension to the classic similarity solution for a theoretical 2D test case in which an initial volume of sediment creates a density current in the longitudinal direction, while sediment particles settle downward out of the gravity current. Note that only a qualitative comparison is possible due to the inherent differences between the two cases (e.g. the Hogg *et al.*, 2000 test case is frictionless, which is impossible to simulate in COHERENS) and the fact that the similarity solution is invalid for small times (singular behaviour at t = 0) and thus cannot be compared to the COHERENS results at the first time steps.

Aims and requirements

Due to the inherent differences in test case setup and limited validity of the similarity solution, it can be concluded that gravity currents are simulated satisfactorily in COHERENS when the numerical gravity current height and depth-averaged velocity profiles show trends similar to the profiles suggested by the similarity solution of Hogg *et al.*, 2000.

6.6.2 Model setup

The gravity current is simulated using a 2DV model. The simulation starts with a narrow sediment column of 1 m^3/m in a water column of 10m, containing an initial sediment concentration of 0.05. this leads to an initial sediment volume per unit width $v_d = 1m^3/m$, which facilitates comparison with the similarity solution of Hogg *et al.*, 2000. The dimensionless settling velocity $\beta = 0.005$, which yields a settling velocity $w_s = 4.5\ 10^{-3}$ m/s using the following expressions:

$$\beta = \frac{w_s}{U_r} \tag{176}$$

$$U_r = \sqrt{(L_r g_0')} \tag{177}$$

in which length scale $L_r = \sqrt{v_d} = 1$ and initial reduced gravity $g_0' = 0.80933 m/s^{-2}$. Due to the high water column to density current height ratio, a relatively high vertical grid resolution of 500 layers was chosen in order to maintain a high enough number of computational cells in the region of interest. There is no erosion of sediment at the bed, yet the calculation of sediment deposition from the gravity current onto the bed is enabled. Since the similarity solution is only valid for small settling velocities and time spans, w_s was set to be $4.5\ 10^{-3}$ m/s (calculated from a dimensionless settling velocity β=0.005) and the total time of simulation is 10s. The model settings are summarized in Table 28.

Figure 146 – Schematic picture of a particle-laden gravity current flowing along a horizontal boundary, under a deep and otherwise quiescent ambient fluid (Hogg *et al.*, 2000)

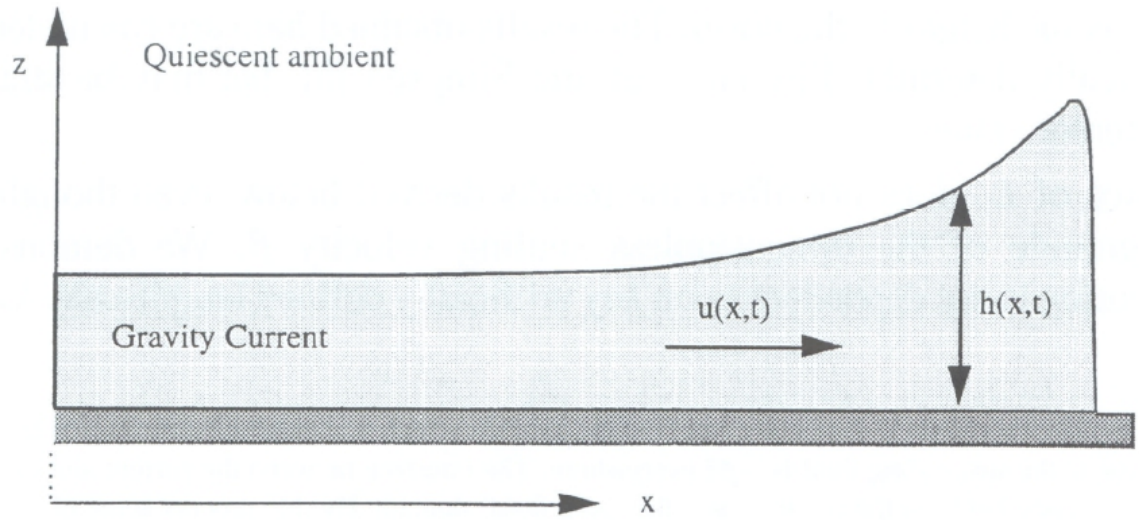

6.6.3 Results

The height profile of the density current (defined as the height where sediment concentration drops below 10^{-3}) and the depth-averaged velocity profiles as given by the similarity solution are presented in Figs. 148 and 150 for time t=1 to 10s. Their numerical counterparts are displayed in Figs 147 and 149. Results are presented for the lowest 10% of the water column. For ease of comparison, Figs. 151 and 152 show the gravity current height and depth-averaged velocity profiles, repectively, on the final time step $t = 10s$, for both solutions combined. Finally, Fig. 153 compares the cumulative proportion of sediment that has deposited out of the gravity current predicted by the similarity solution with the one predicted by COHERENS .

6.6.4 Conclusion

Based an a qualitative comparison of the results presented in section 6.6.3, the following conclusions can be drawn from :

- Disregarding the first time steps (as mentioned in the introduction), the position of the nose of the current predicted by COHERENS corresponds well with the position given by the similarity solution.
- The shapes and evolution of the velocity profiles from both solutions agree reasonably well.
- The evolution of the cumulative proportion of deposited sediment as calculated by COHERENS follows the same trend as the one described by the similarity solution, yet COHERENS underpredicts the analytical results by 60 %. This is possibly due to the turbulence that keeps the sediment in the current for a longer time, and the omittance of this effect in the similarity solution.

Keeping in mind the qualitative nature of the comparison to the similarity solution of Hogg *et al.*, 2000, it can be concluded that the treatment of gravity currents is implemented well in COHERENS .

Table 28 – Model setup for gravity current test case

Characteristic	Model setting
Model grid	2DV, $nr = 2$, $nc = 41$, $\Delta x = 0.2m$
Vertical grid resolution	n$nz = 500$ layers (uniform)
Water depth	$10m$
Hydrodynamics calculation	Enabled
Turbulence formulation	k-ϵ model
Turbulence buoyancy influence	Derived from RANS equations
Initialisation	Zero flow, zero turbulence
D_{50},ρ_s,z_0	$250\mu m$, $2650kg/m^3$, $0.001m$
Sediment transport	Deposition, no erosion
Initial sediment volume	$1m^3/m$, as narrow column of 1m height
Initial sediment concentration	0.05 m^3/m^3
Settling velocity	$w_s = 4.5\ 10^{-3}$ m/s
Density effects	Enabled
Time step	$0.01s$
Simulated time	$10s$

Figure 147 – Numerical profiles of the gravity current height

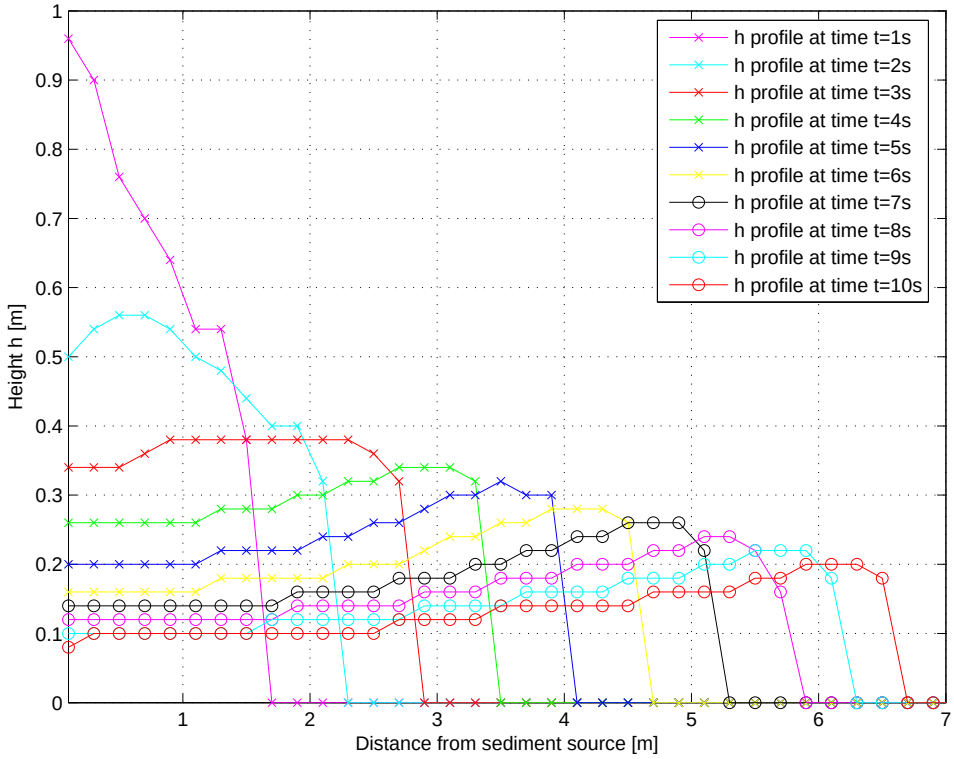

Figure 148 – Profiles of the gravity current height derived from the similarity solution

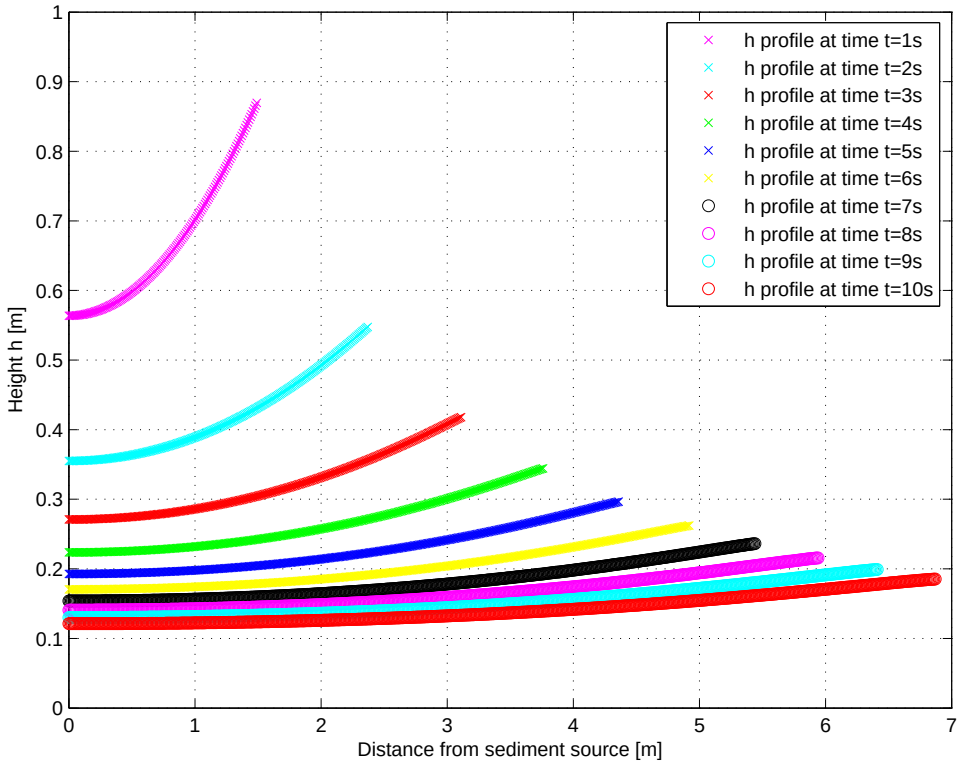

Figure 149 – Numerical longitudinal depth-averaged velocity profiles

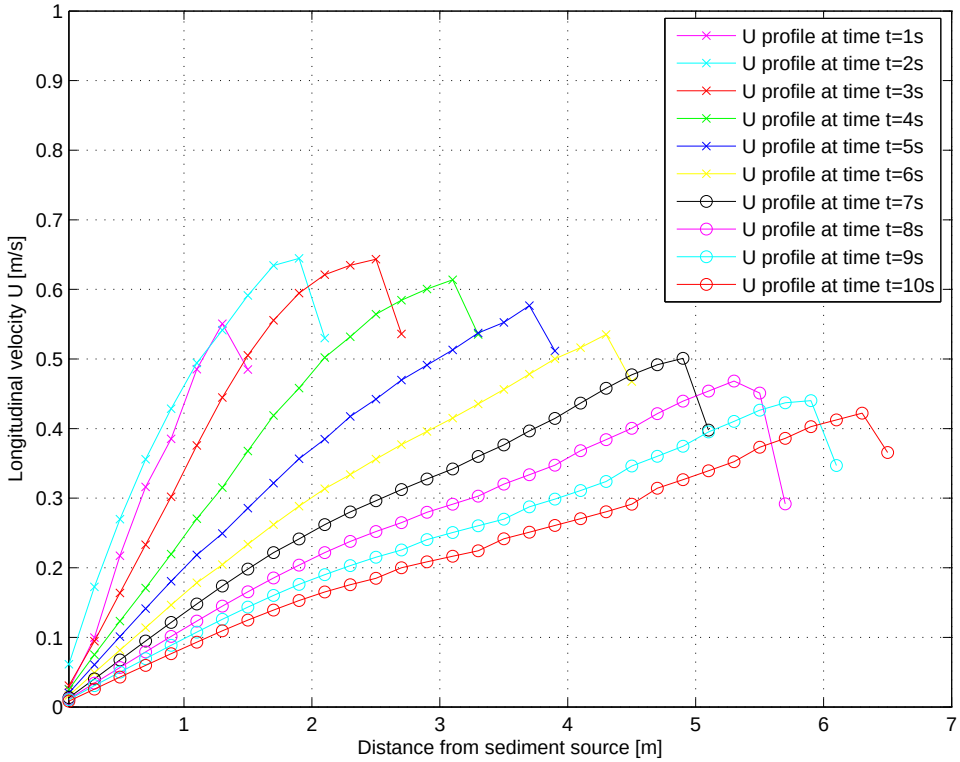

Figure 150 – Longitudinal depth-averaged velocity profiles derived from the similarity solution

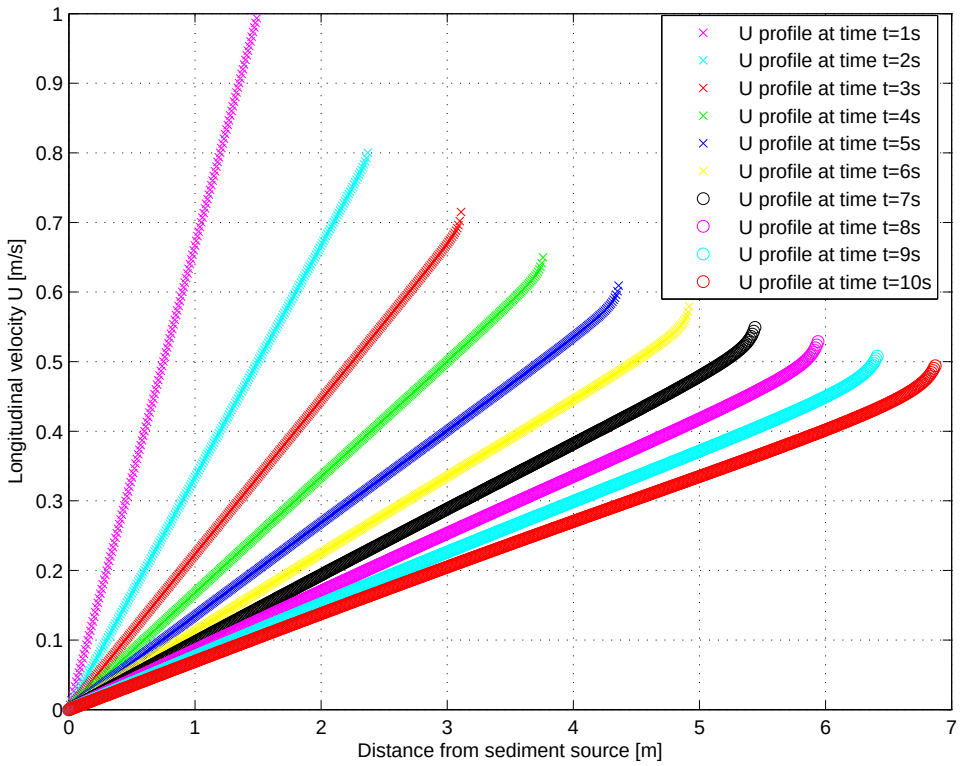

Figure 151 – Gravity current height for the similarity solution (red curve) and the numerical solution (green curve) at $t = 10s$

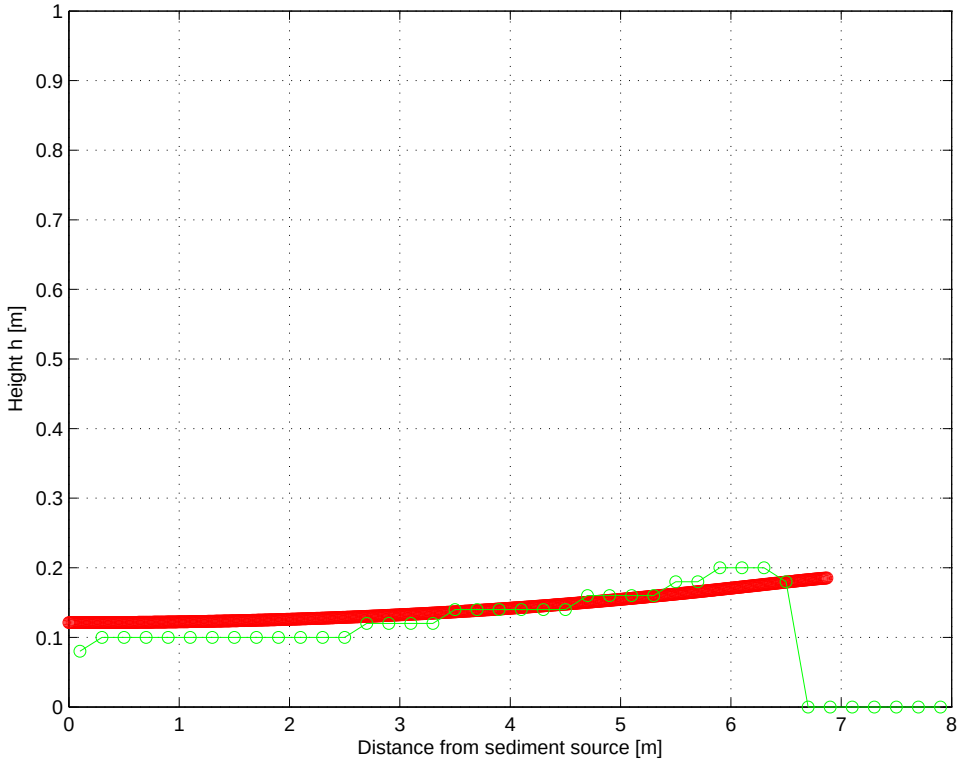

Figure 152 – Longitudinal depth-averaged velocity profiles for the similarity solution (red curve) and the numerical solution (green curve) at $t = 10s$

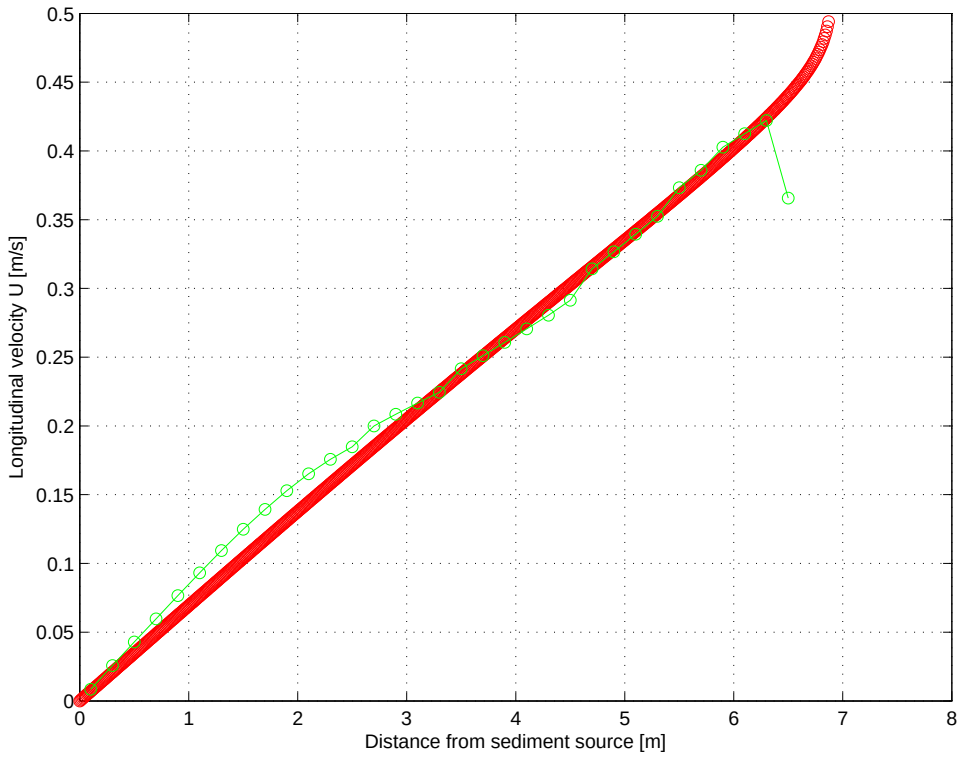

Figure 153 – Proportion of sediment that has deposited out of the density current

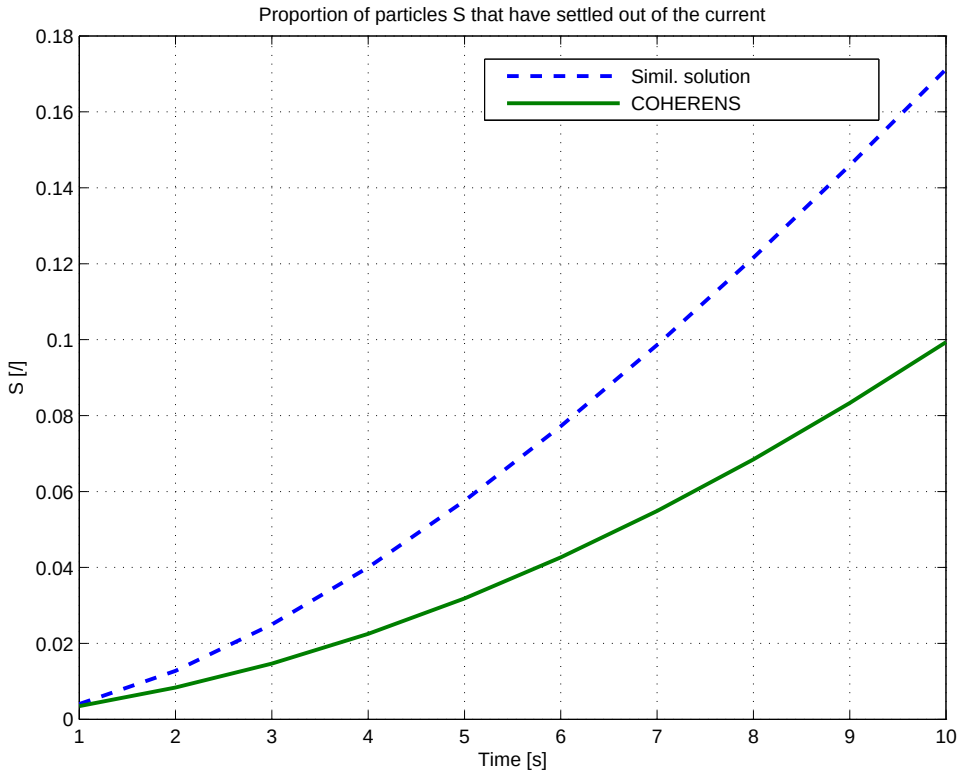

6.7 Bend flow

6.7.1 Introduction

The objective of this test case is to assess the performance of COHERENS in simulating flow in curvilinear geometries. The numerical experiment involves flow through a 180˚ sharp open-channel bend. Hydrodynamics and sediment transport are simulated, the latter separated into a case with only bed load transport, and a case with only suspended load transport. Due to a lack of physical data, results are qualitatively compared to common knowledge of bend flow and secondary current:

- Due to the non-uniformity in the vertical structure of the velocity distribution and the added curvature-induced pressure gradient, a redistribution of the flow field occurs in the bend. Aside from the primary flow a secondary current is initiated in the channel bend which is directed towards the outer bank at the water surface and towards the inner bank at the bed
- Maximum flow velocity occurs near the outer bank
- When local bed shear stress exceeds the critical shear stress for incipient motion, the sediment particles at the bed can be transported as bed load and suspended load. Scour of the bed typically occurs at the outer bank side of the channel, while bed aggradation occurs at the inner bank side due to sediment deposition. Bed load transport is directed towards the inner bank

Aims and requirements

It can be concluded that bend flow is simulated satisfactorily in COHERENS when the numerical results qualitatively display the theoretical phenomena presented in section 6.7.1.

6.7.2 Model setup

Flow is simulated through a channel with constant rectangular cross section and channel width $B = 4m$, consisting of straight in- and outflow sections of 20m and a 180˚ bend with a radius of curvature R of 20m. Water height in the channel is 2m, which makes $B/H = 2$ and $R/H = 10$. The flow rate at the inlet equals $1.7m^3/s$. The model settings are summarized in Table 29

6.7.3 Results

Figs. 154 and 155 show a vector plot and contour plot of the average velocity in the channel. The secondary current is visualised in Figs. 156 and 157, for 45˚ and 135˚ cross sections, respectively.
Under the influence of the flow field, sediment present at the channel bed is transported through bed load and suspended load transport. Figs. 158 and 159 show vector plots of the direction of the bed load transport, whereas Figs. 160, 161, 162 and 163 illustrate contour plots of the average suspended sediment concentration in the channel.

6.7.4 Conclusions

The following conclusions can be drawn from the results presented in section 6.7.3:

- The occurence of secondary current in the bend and the presence of maximum velocity near the outer bank is clearly visible in Figs. 154 - 157.

- Figs. 158 and 159 indicate that the simulated maximum bed load indeed occurs at the outer bank side, and that the sediment is transported towards the outer bank, where it will be deposited. Scour at the inner bank side is minimal.

Table 29 – Model setup for bend flow test case

Characteristic	Model setting
Model grid	3D, nc=161, nr=11
Vertical grid resolution	10 layers (uniform)
Water depth	$2m$
Hydrodynamics calculation	Enabled
Turbulence formulation	k-ϵ model
Initialisation	Zero flow, zero turbulence
Upstream boundary condition	Flow rate=$1.7m^3/s$
Downstream boundary condition	Water surface elevation=-0.01m
D_{50},ρ_s,z_0	$250\mu m$, $2650kg/m^3$, $0.001m$
Sediment transport	Test case 1: bed load transport
	Test case 2: suspended load transport
Initial sediment concentration	zero
Settling velocity	w_s=Camenen (see Eq. (165)
Time step	$0.01s$
Simulated time	$10s$

Figure 154 – Vector plot of average velocity in channel

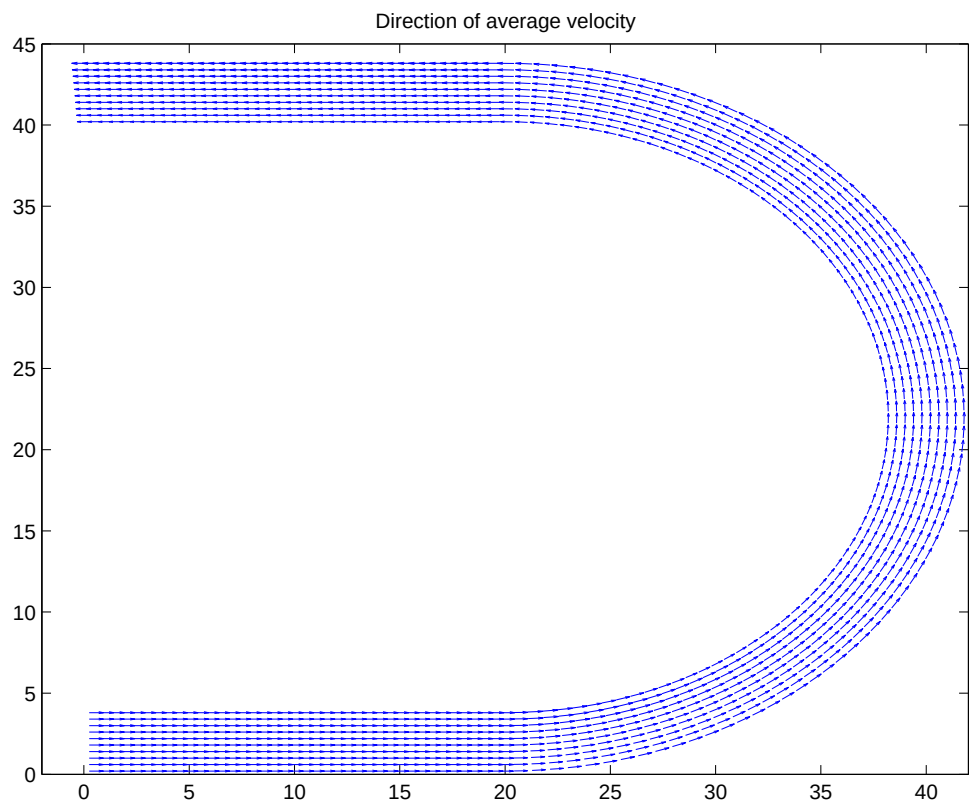

Figure 155 – Contour plot of average velocity in channel

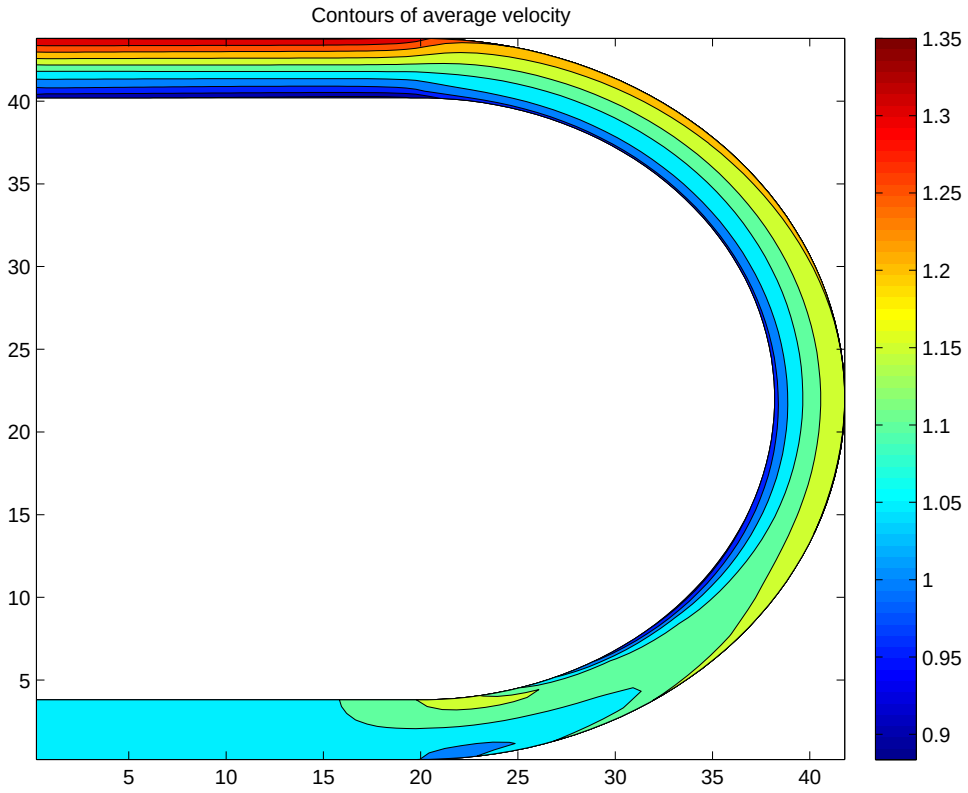

Figure 156 – Secondary current at 45° bend angle

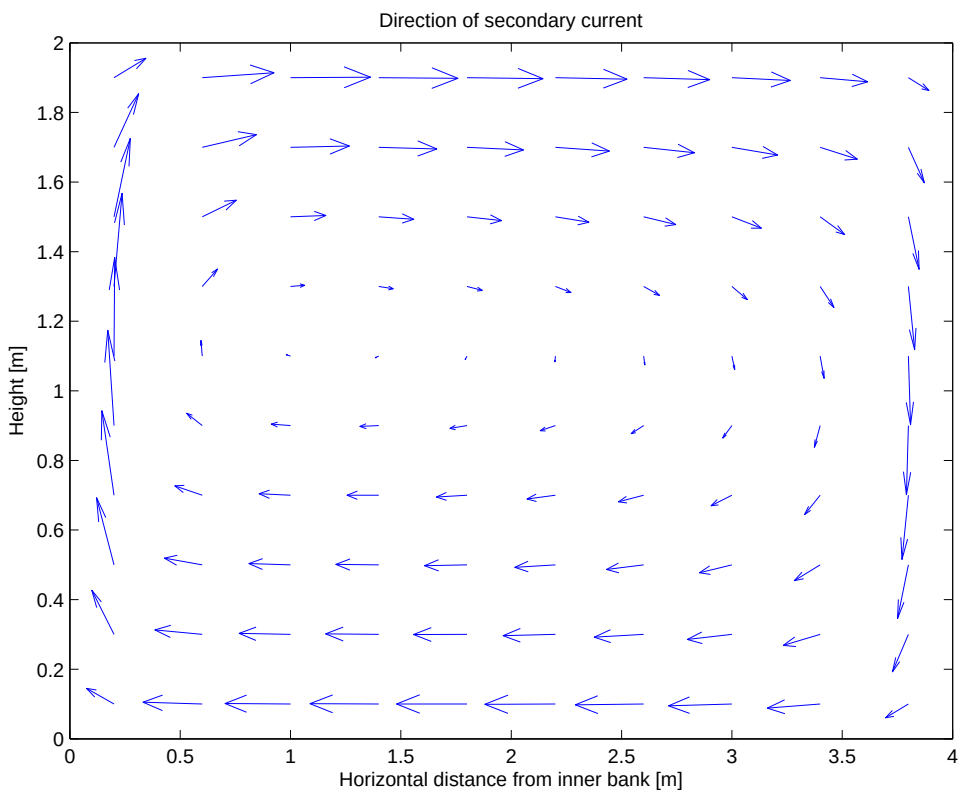

Figure 157 – Secondary current at 135° bend angle

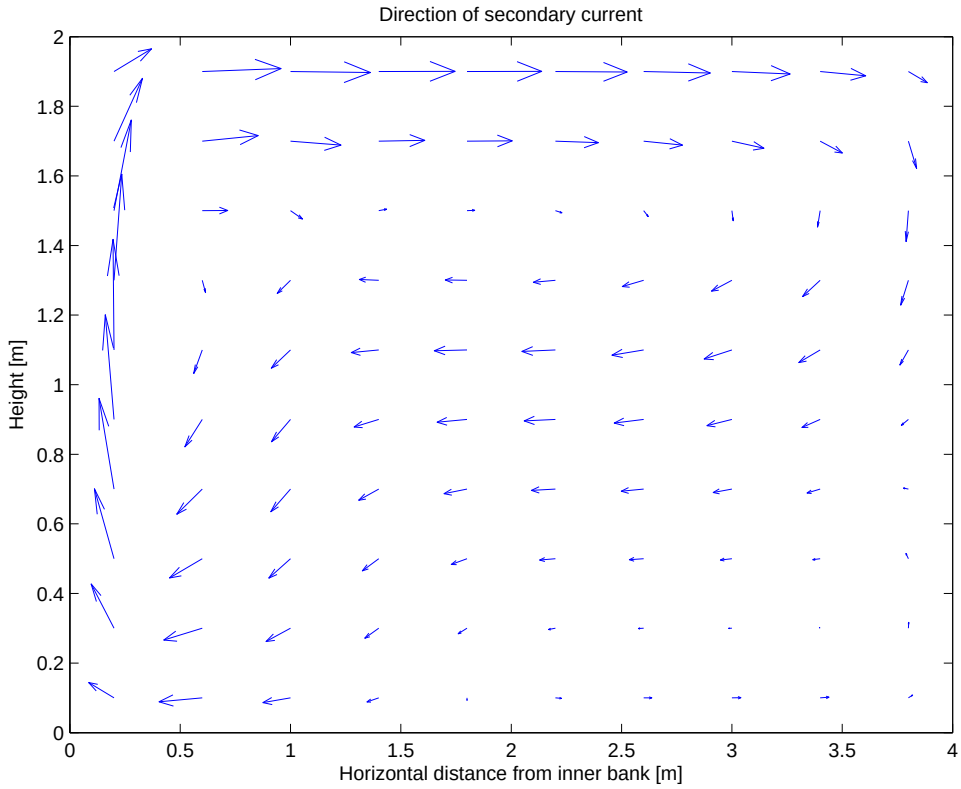

Figure 158 – Direction of bed load transport

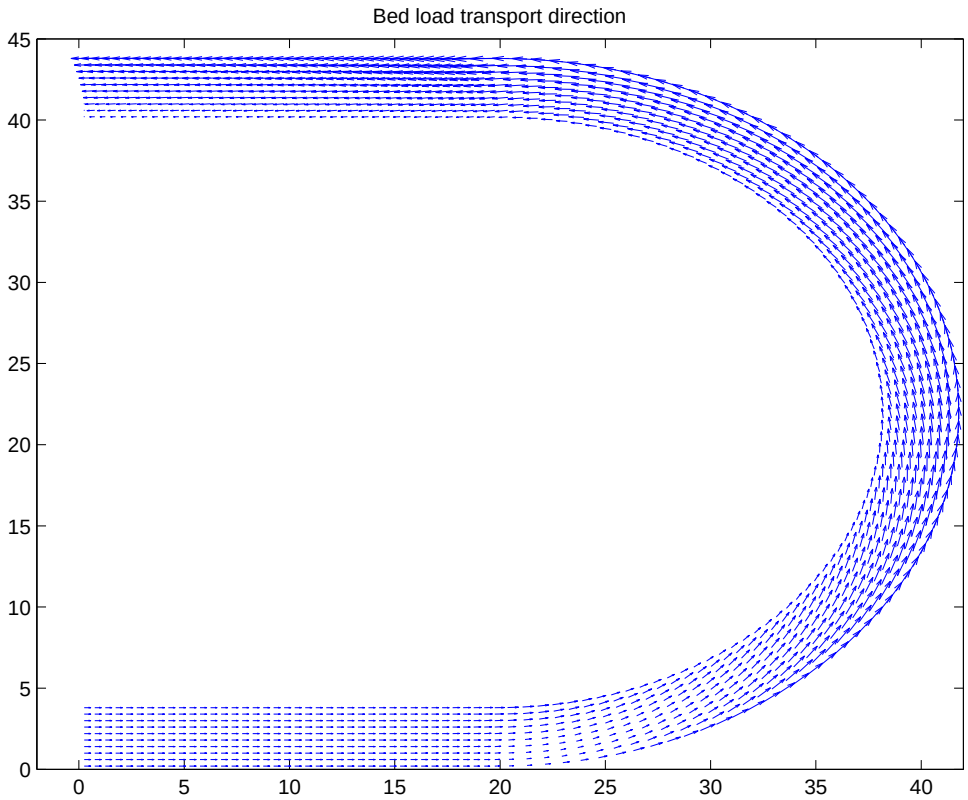

Figure 159 – Detailed view of the bed load transport direction

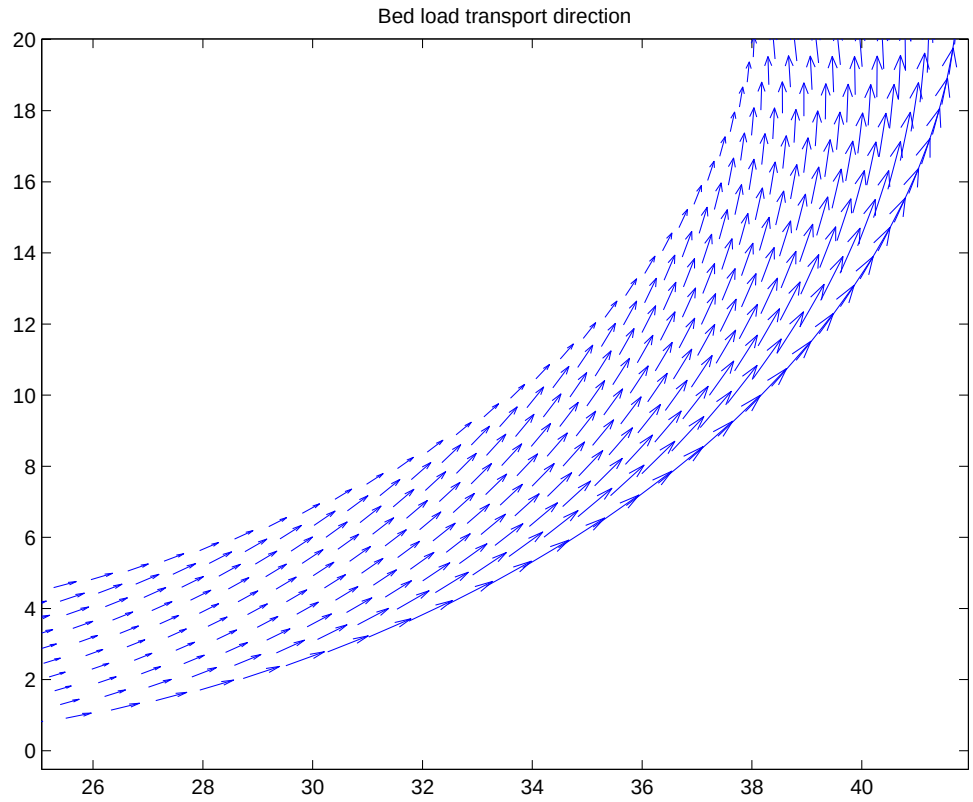

Figure 160 – Contour plot of depth-averaged suspended sediment concentration

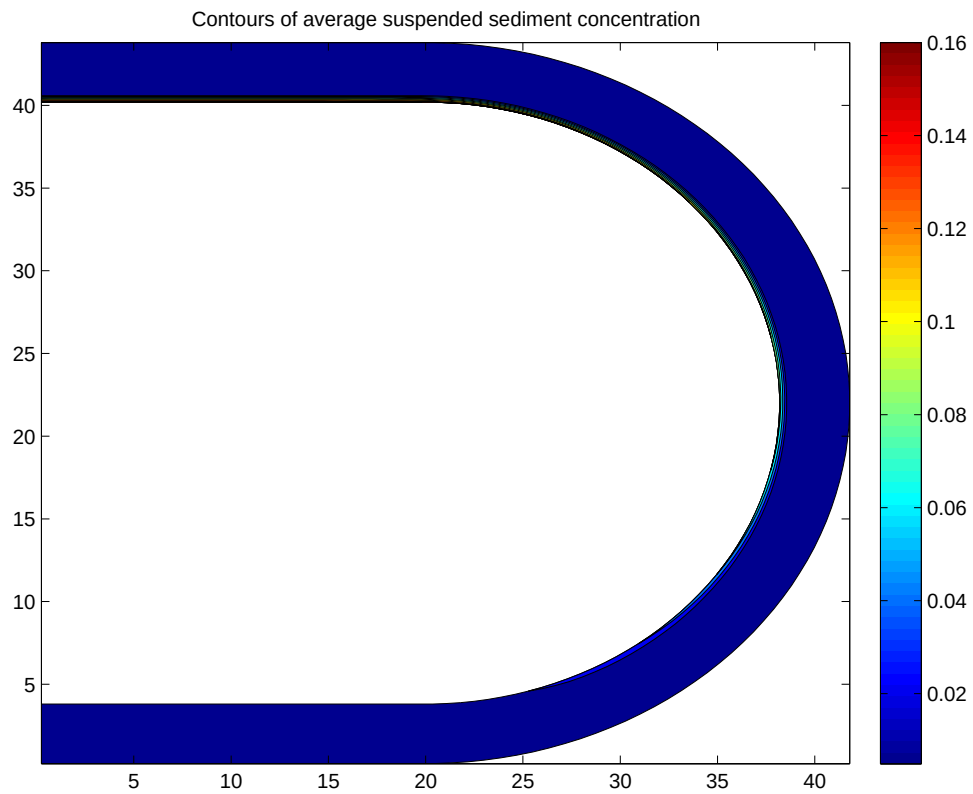

Figure 161 – Detailed view of the depth-average suspended sediment concentration

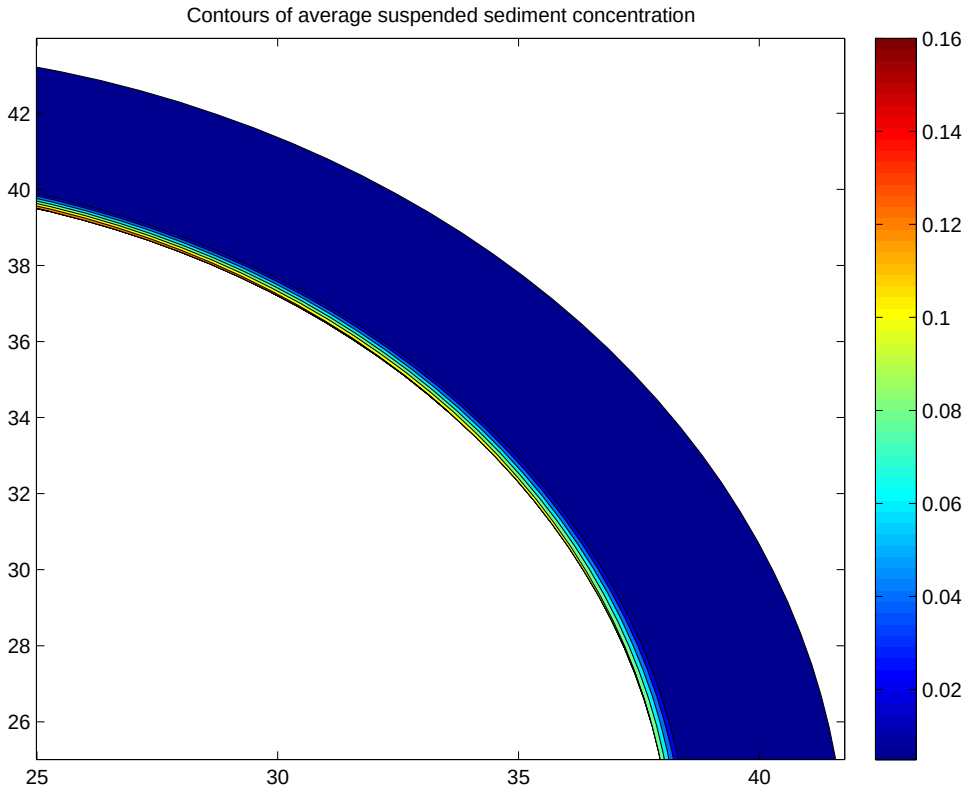

Figure 162 – Distribution of suspended sediment concentration at 45° bend angle

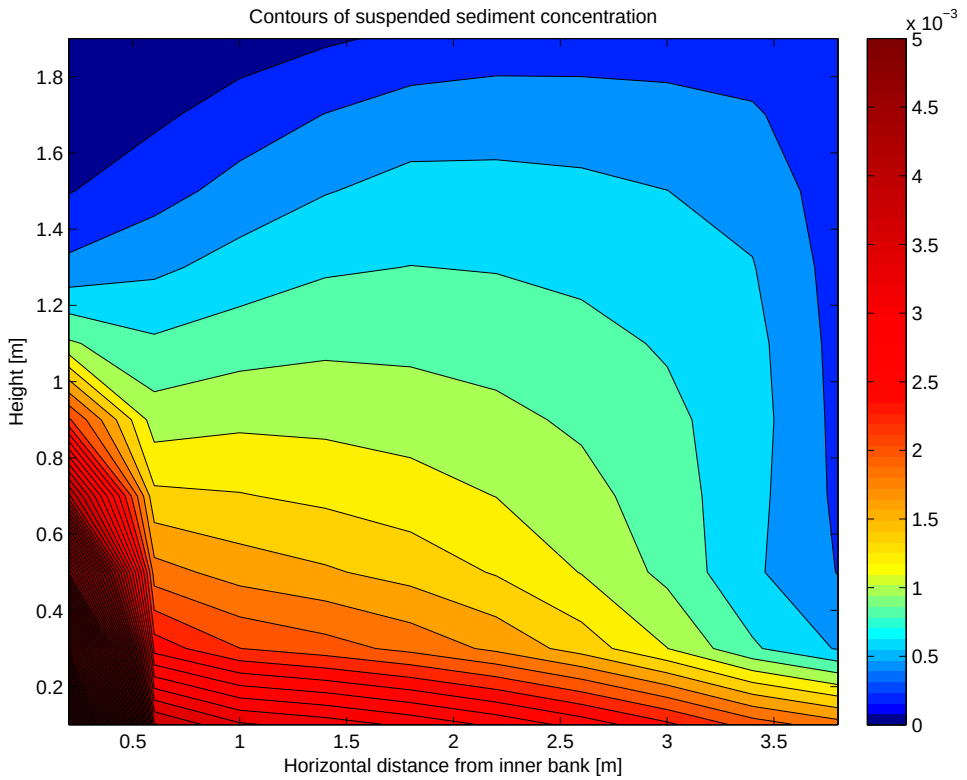

Figure 163 – Distribution of suspended sediment concentration at 135° bend angle

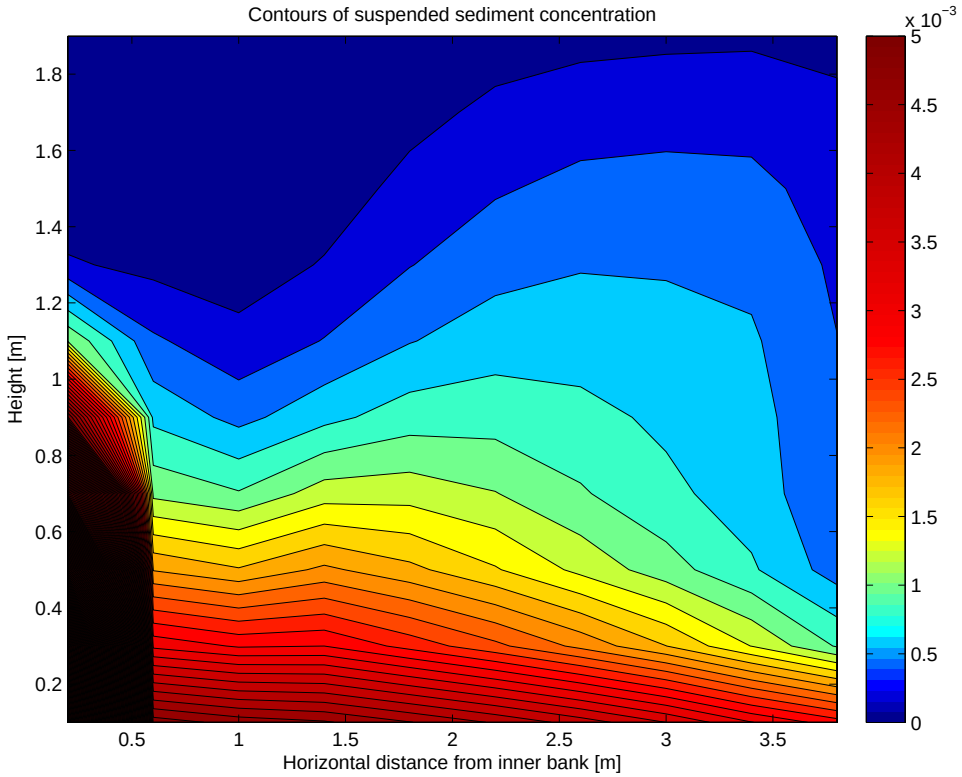

- Influenced by the structure of the flow field redistribution, suspended sediment near the surface is transported away from the inner bank and towards the outer bank, whereas suspended sediment near the bed is transported towards the inner bank. This explains the minimum concentration of suspended sediment near the water surface at the inner bank side, and the maximum concentration of suspended sediment near the bed at the inner bank side in Figs. 160 - 163

Despite the lack of an analytical solution or experimental measurements to serve as a reference for comparison, the results agree very well with the theories on flow and sediment transport in open channel bends. Therefore, it can be concluded that COHERENS is capable of simulating flow and sediment transport processes typical of curvilinear geometries qualitatively.

6.8 Conclusions

Regarding the testcases discussed in this chapter, the following conclusions can be drawn with respect to the sediment functionality in COHERENS:

1. using a parabolic vertical variation of diffusivity, both the logarithmnic velocity profile and the theoretical Rouse profile are reproduced very well in a stationary column model setting. Noticable deviations only occur at high values of the settling velocity, where an increased resolution of the vertical grid is required to obtain accurate results. The total (i.e. accumulative) amount of eroded sediment from the bed matches the total amount of sediment in suspension.

2. the qualitative effects of density stratification on the vertical variation of velocity and sediment are well reproduced within a stationary column model setting. Specifically, the dampening of vertical viscosity increases the horizontal velocity in order to keep the shear stress fixed. Likewise, for a given bed shear stress the dampening of vertical diffusion increases the relative importance of settling effects in the vertical sediment balance so that sediment concentrations in teh water column are lowered.

3. the effect of hindered settling on suspended sediment concentrations agrees well with the analytical solution for a stationary column model. As expected, the ampount of sediment is suspension increases as the critical shear stress is lowered.

4. the suspended sediment concentration in the transition from a non-erodible to an erodible bed is well described in stationary depth-averaged (2D) and depth dependent (3D) mode, albeit that results depend on the precise parameterisation of the near bed sediment concentration. The 3D results are somewhat less accurate because of the relatively low veritcal resolution (30 layers) that prevents an accurate description of the near-bed sediment profile. Also, the horizontal adaptation length (i.e. length scale to reach equilibrium concentrations) compare well between 2D and 3D. The vertical equilibrium sediment profile in 3D agress with teh analytical Rouse profile.

5. results from a 2DV model setup for a gravity current in a quiescent medium are compare qualitatively well with the similarity solution by Hogg *et al.*, 2000. Explicitly, the position of the nosie of the gravity current corresponds well with the similarity solution. The evolution of velocity (both in space and time) also agrees well while the temporal behaviour of the deposited sediment shows a similar trend as the similarity solution.

6. the qualitative features of a stationary bend flow are reproduced. The secondary current and the prescence of a velocity maximum near the outer bank are demonstrated. This gives maxmuim bed load towriads the outer bank, where sediment is deposited. Furthermore, suspended sediment at the surface (near the bed) is transported to the outer bank (to the inner bank)

7 Morphology

7.1 Introduction

This chapter presents two test cases that were used to validate the morphology functionality of COHERENS. First, in Sect. 7.2 the time evolution of an initially Gaussian bedprofile is simulated up to the point that it breaks due to non-linear effects. The second test case is elaborated in Sect. 7.3 and considers the implementation of vertical sorting of sediment within the bed.

7.2 Gaussian hump

7.2.1 Introduction

The test case reported in this section simulates a 1D flow which causes an initial so-called 'Gaussian hump' bed form to migrate through the channel. The propagation of the bed form can be considered similar to a wave propagation in a sense that it deforms because the top is moving faster than the front. After some time the hump breaks just like a wave would.

Aims and requirements

The aim of the test case is to assess the ability of COHERENS to simulate morphological flow problems such as the propagation of bed features. The comparison with the analytical solution presented above is valid only until the moment that breaking occurs. Furthermore, the propagation velocity of the hump is compared to expectations based on the velocities right before and after it. It should be noted that by default, a total agreement between analytical and numerical results is not expected as COHERENS solves a different equation. In the end, the comparison should be made by mainly focusing on the shape of the humps and their propagation velocities.

Analytical formulation

For the purposes of this test case an analytical solution (see equation (178)) is provided, based on the method of characteristics, which describes the displacement and position of gausssian humps prior to breaking (Kubatko and Westerink, 2007).

$$\eta_i(x) = \eta_0 \exp(-\frac{(x - x_{mean})^2}{2\sigma^2} \tag{178}$$

where η is the bed level, η_0 the initial bed level, x is the distance, x_{mean} is the half distance and σ is equal to 450 m.

As it is known from theory the bed level can be deduced from the following equation:

$$(1-\epsilon)\frac{\partial \eta}{\partial t} - \frac{\partial q_x}{\partial x} = 0 \tag{179}$$

where ϵ is the porosity and q_x is the sediment transport that in this case is calculated by the Engelund-Hansen equation referring to total load (see (180)).

$$q_x = mu^b \tag{180}$$

where

u is the propagation velocity defined equal to

$$Q/(H-\eta(x)) \tag{181}$$

where

H is the total water depth
η is the bed level
$b = 5.$
m is a constant defined as follows

$$m = 0.05\Delta^{-2}d_p^{-1}g^{-2}C_d^{3/2} \tag{182}$$

where Δ is the relative density
d_p is the grain size

g is the gravity acceleration 9.81 m/s^2
C_d is a constant

$$C_d = \left[\frac{\kappa}{\log(h/(ez_0))}\right]^2 \tag{183}$$

κ is the von Karman constant with a value of 0.4
h is the total water depth 10 m
z_0 is 0.001 m.

Using these equations one can obtain the following equation:

$$\frac{\partial \eta}{\partial t} + c(\eta)\frac{\partial \eta}{\partial x} = 0 \tag{184}$$

With:

$$c(\eta) = \frac{bmQ^b(H-\eta)^{-b-1}}{(1-\epsilon)} \tag{185}$$

This can be solved approximately using the method of characteristics giving:

$$\eta = \eta_i(\xi) \tag{186}$$

with

$$\xi = x + c(\eta_i)t \tag{187}$$

Note that several simplifying assumptions were made in deriving this equation, compared to the model in COHERENS . Most important, the hydrodynamics are calculated from the continuity equation only, and the force balance (including advection and bed friction effects) is not used. The latter will have a diffusive effect, which is not in the analytical solution. Further, the dependence of the bed friction coefficient on the depth is neglected. Finally, in the solution of the characteristic method, the change in the propagation velocity when the hump moves is neglected. Therefore, only a qualitative agreement is expected.

7.2.2 Model setup

A rectangular grid was applied of dimensions 2400x160 m^2 with a spatial resolution of 40 m. An initial hump is considered to exist on the bed of a height equal to 2 m. the flow discharge was 10 m^2/s. The effect of the morphological factor was also taken into consideration. The test cases were done with morfac=100 for the chosen discharge. the sediment transport was calculated with the Engelund Hansen equation using $\Delta = 1.58$ and $d_p = 150\mu m$

7.2.3 Results

In Figure 164 a comparison is made between the results extracted from the code and those calculated by the analytical solution. The evolution of the Gaussian hump is shown for several time steps, with each curve representing a different time step. In total nine moments are monitored from the start until the end of the simulation.

Figure 164 – Gaussian Hump Evolution under a constant discharge of $10\ \mathrm{m}^2/\mathrm{s}$ for different time steps.

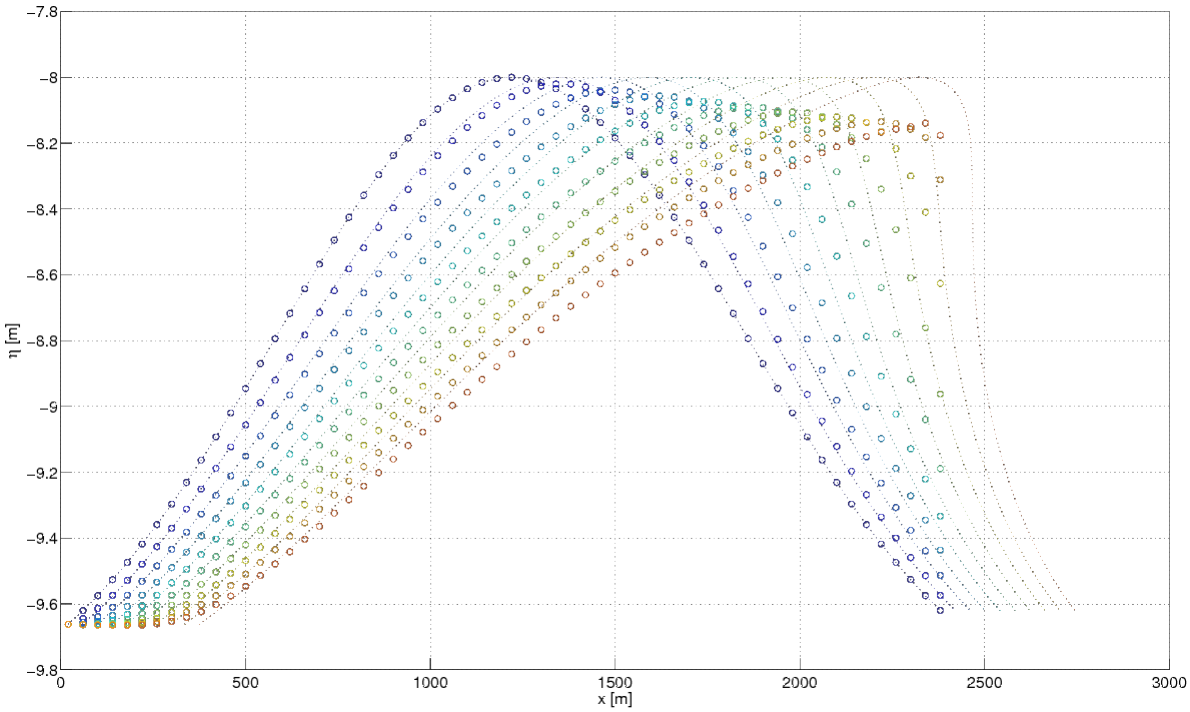

The analytical solution is shown as a dotted line, the numerical solution as markers.

7.2.4 Conclusions

The test case shows an acceptable agreement between the analytical solution and the numerical one. The numerical results seem to have a slightly larger propagation velocity, which is (at least partly) due to neglecting the depth variation of the drag coefficient in the analytical solution. the deformation of the hump is similar in both cases, although the exact details differ due to simplifications in the analytical solution. Finally, we some diffusion (with a decreasing the height of the hump) in the numerical solution, which is partly caused by the inclusion of bed friction and advection in the momentum equation in the numerical model, and partly by numerical diffusion of the used morphological scheme.

7.3 Vertical sorting

7.3.1 Introduction

When dealing with multiple types of sediment in the bed, the different grain sizes are seldom distributed uniformly along the depth of the bed. Rather, stratification occurs due to passing bed forms or changing flow regimes. This stratification or varying bed fraction distribution can be modeled numerically by adopting a vertical sorting model. Such a model has been implemented into COHERENS .

A test case was developed to assess the performance of COHERENS in simulating vertical sorting mechanisms in the bed. This test case does not mirror laboratory experiments or compare numerical results to an existing analytical solution, rather they are very simple setups designed to test the theoretical concepts.

Test case description

Consider a straight channel in which one transportable sediment fraction is covered by a larger, non-transportable sediment fraction [1]. If the non-transportable layer is thick enough (i.e. the thickness of the layer is larger than the active layer thickness [2] for the sediment mixture in that layer), it protects the underlying layer from being transported by the flow. This phenomenon is called armouring, and keeps the channel from eroding further until flow increases such that the larger sediment fraction becomes transportable. If, however, the thickness of the non-transportable layer is limited, the finer sediment particles can be filtered through the non-transportable layer and transported by the flow. The following describes a test case designed to simulate this armouring or filtering process.

Aims and requirements

The test case is said to be successful when the results reflect the correct behaviour of the bed according to the theoretical concepts of vertical sorting.

7.3.2 Model setup

The bed of a straight channel consists of three layers. The first layer and third layer are made up of fine, transportable sediment of diameter $d_{50} = 150\mu m$, the second layer of a much larger, non-transportable sediment of diameter $d_{50} = 25mm$ [3]. No sediment enters the channel at the upstream boundary, which is implemented by setting the bed layer thickness and all of the bed fractions in the most upstream cells to zero [4]. Using the formula for flat bed conditions (Armanini, 1995), the active layer thickness for a layer consisting of rough sediment then equals $\delta = 4.5d_{50} = 11.25cm$.

Two different scenarios are simulated:

- Case 1: layers 1 and 3 have a bed layer thickness of $10cm$, layer two has a bed layer thickness of $20cm$. The latter is larger than the active layer thickness for rough sediment.
- Case 2: All three layers have a bed layer thickness of $10cm$, which is smaller than the active layer thickness for rough sediment.

By applying the concepts of vertical sorting, the outcome of these test cases can be predicted. The start of the simulation should be the same for both cases: fine sediment starts to erode from the top layer until the second layer is reached. At this point, the paths diverge. In case 1a, the rough layer is thicker than the active layer thickness δ, which means that the rough sediment layer protects the underlying fine sediment layer from erosion. The end result of simulation 1a is that the top fine sediment layer is washed out, with the rough sediment layer and the fine sediment underneath remaining untouched. In case 1b, however, the active layer thickness is greater than the thickness of the rough layer. The fine sediment underneath is filtered through the rough sediment layer and transported by the flow. In the end, only rough sediment remains in the channel. The other model settings for this test case are summarized in Table 30.

[1] A fraction is considered transportable when the flow is large enough to transport said fraction. It is, therefore, not an absolute grain size characteristic, but should rather be seen in light of the flow regime in question

[2] The concept of the active layer thickness is discussed in the Conceptual Description Manual

[3] This grain size distribution might not be realistic, but it suits the purposes of this test case perfectly

[4] i.e. an application of the fixed layer mechanisms implemented in COHERENS

7.3.3 Results

The results for the armouring test case in the first three cells are shown in Figures 165 to 169, whereas the results for the filtering test case are shown in Figure 170 to 174. In these figures, the thickness of the separate bed layers, the overall availability of sediment and the volume fraction of the fine sediment are shown in one cell of the channel (red = 100% fine sediment, blue = 100 % rough sediment), with cell 1 the most upstream and cell 5 the most downstream cell.
Figure 166 shows that, initially, fine sediment is eroded from the top layer. The moment this sediment is depleted, an internal shift in the layer bookkeeping occurs: the new top layer becomes the old layer 2, the new second layer becomes the old layer 3, and the new layer 3 becomes a fixed layer (not displayed). At his point, no further sediment transport occurs, as the rough sediment protects the fine sediment from erosion. When looking at cell 3 in Figure 167, it can be seen that erosion of the top layer starts when erosion in the first layer has stopped, which indicates that the inflow flux of sediment in cell 3 equals the outflow flux of sediment during the primary phase of the test case. Eventually, the top layer sediment is washed out of all the cells, and the two underlying layers remain.
Figure 171 shows a slightly different situation. The moment at which the sediment in the top layer is depleted coincides with that of test case 1. Again, an internal shift of the layers occurs. However, since the active layer thickness is larger than the thickness of the rough sediment layer and, thus, acts as the limiting thickness, the active layer thickness becomes the new top layer thickness.

This is displayed clearly: fine sediment from new layer 2 infiltrates the new top layer (resulting in a top layer thickness of 0.1125 m and a second layer thickness of 0.8875 m) and is mixed over the rough sediment, resulting in a fraction distribution in the new top layer that is not quite 100% rough. The fine sediment is transported out of the bed and the new second layer thickness drecreases over time, while the top layer thickness remains fixed. This continues until the new second layer is depleted, at which point the fine sediment that is still in the rough layer is filtered out until a layer of 100% rough sediment with thickness = 0.10m remains.
Note that the first cell for both cases is included in the results to show that COHERENS accurately handles fixed layers: no sediment is present in cell 1, and consequently there is no sediment influx into cell 2.

7.3.4 Conclusions

The following conclusions can be drawn from the results presented in section 7.3.3:

Table 30 – Model setup for vertical sorting test case 1a and 1b

Characteristic	Model setting
Model grid	2D, nc=6, nr=2
Water depth	$10m$
Hydrodynamics calculation	Enabled
Turbulence formulation	Disabled
Initialisation	Zero flow
Upstream boundary condition	Flow rate=$10m^3/s$
Downstream boundary condition	Outflow
ρ_s, z_0	$2650kg/m^3$, $0.001m$
Sediment transport	Bed load transport formula (Wu *et al.*, 2000)
Time step	$1s$
Simulated time	$1h30min$

- The shifting of characteristics (i.e. bed layer thickness and bed fraction distribution) between layers in implemented well in COHERENS
- sediment mixing (i.e. mixing fine with rough sediment to produce a mixture of varying distribution) is implemented well in COHERENS
- Armouring and filtering depend on the ratio of bed layer thickness over active layer thickness. COHERENS is able to simulate both processes well, with armouring resulting in a full stop of sediment transport, while filtering has the sediment transport continue in deeper layers.
- Fixed layers are implemented well in COHERENS . No sediment is present in the fixed cell and no sediment is transported into the cell immediately downstream of it

Despite the lack of an analytical solution or experimental measurements to serve as a reference for comparison, the results agree very well with the expected outcome. Therefore, it can be concluded that COHERENS is capable of simulating vertical sorting processes adequately.

Figure 165 – Armouring simulation results in Cell 1 (case I)

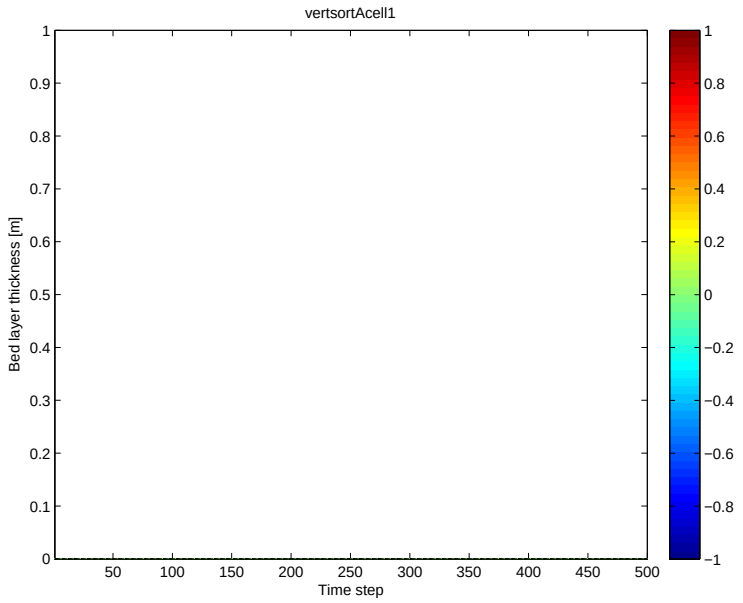

Figure 166 – Armouring simulation results in Cell 2 (case I)

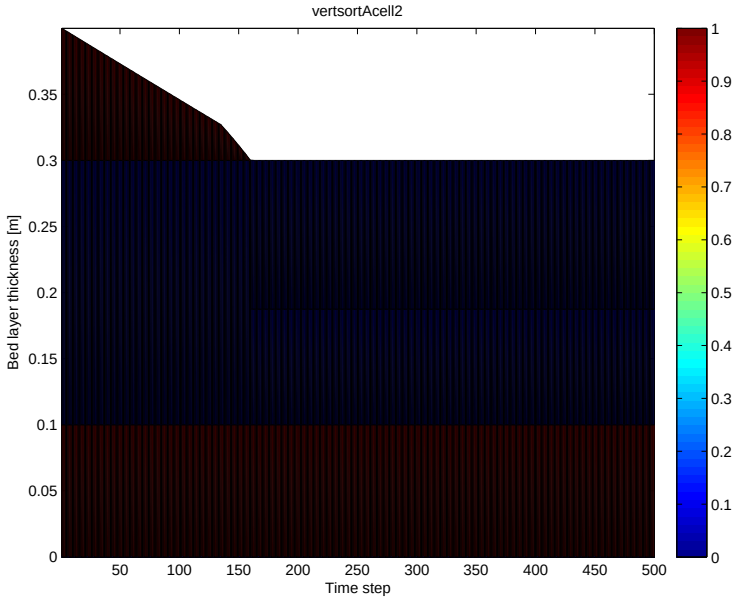

Figure 167 – Armouring simulation results in Cell 3 (case I)

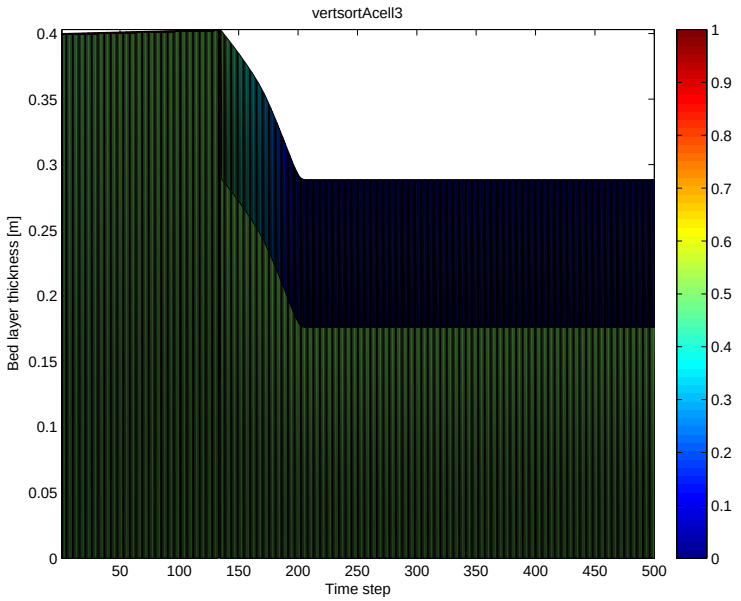

Figure 168 – Armouring simulation results in Cell 4 (case I)

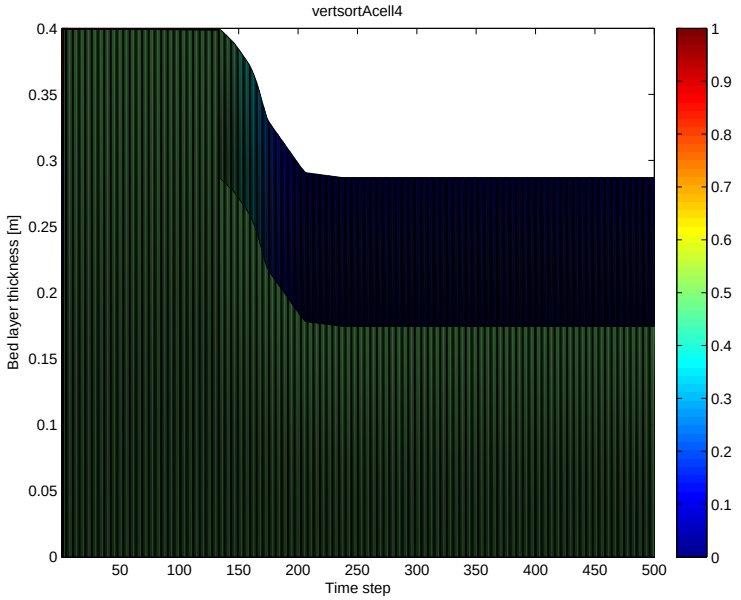

Figure 169 – Armouring simulation results in Cell 5 (case I)

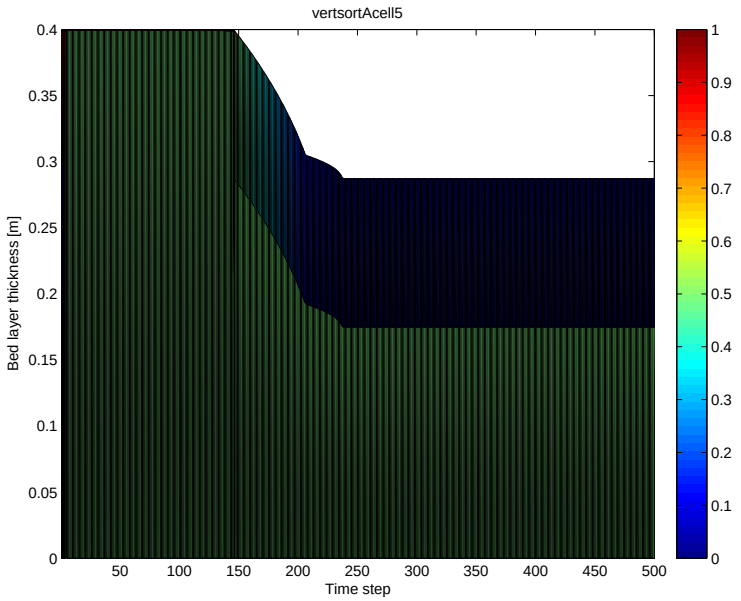

Figure 170 – Filtering simulation results in Cell 1 (case II)

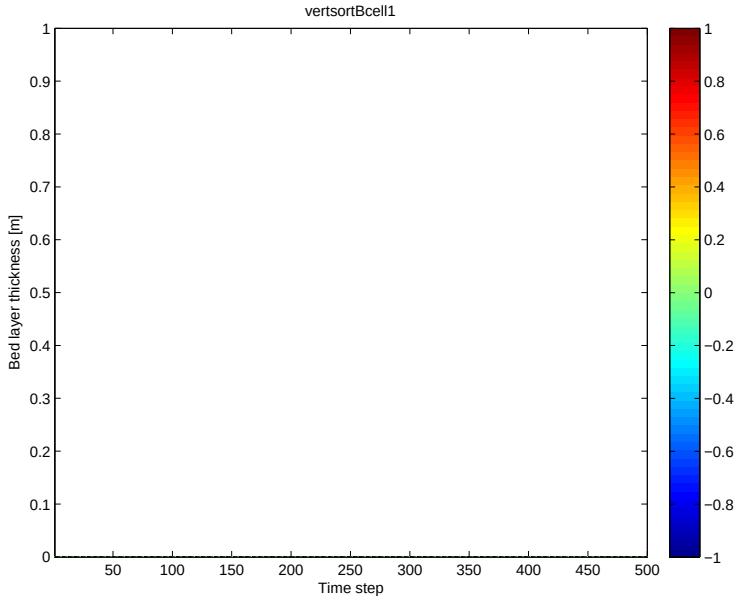

Figure 171 – Filtering simulation results in Cell 2 (case II)

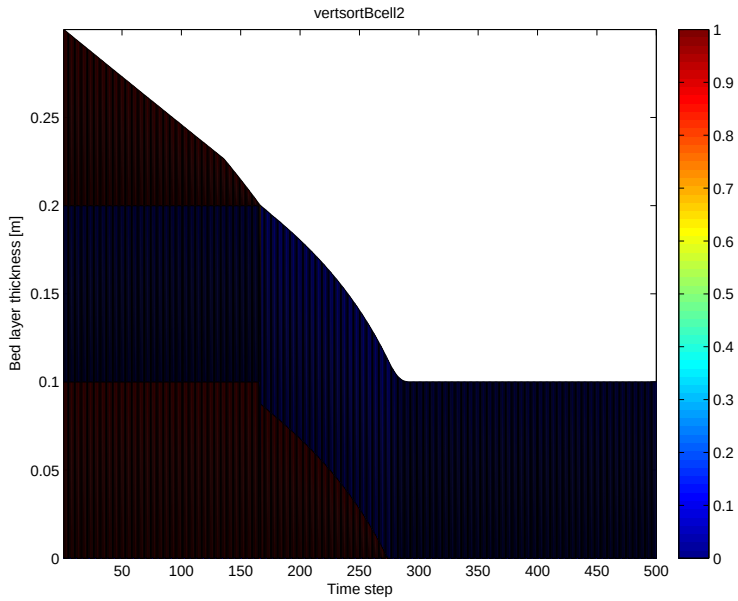

Figure 172 – Filtering simulation results in Cell 3 (case II)

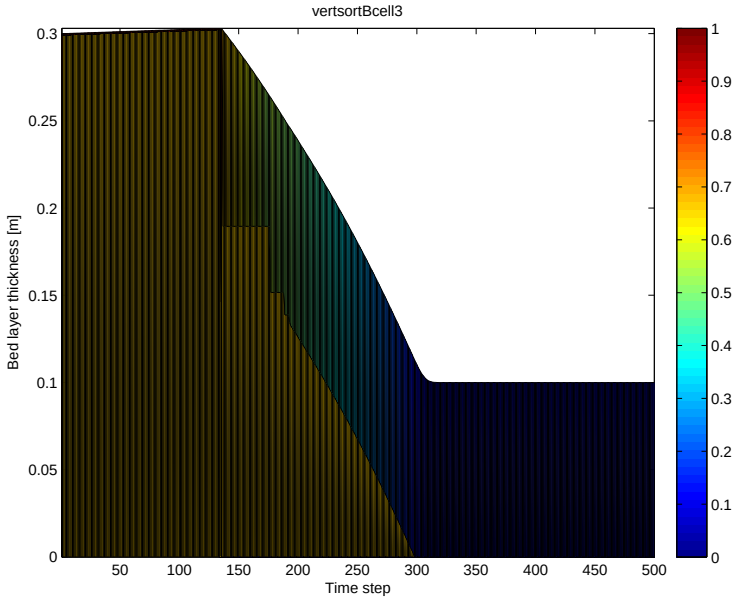

Figure 173 – Filtering simulation results in Cell 4 (case II)

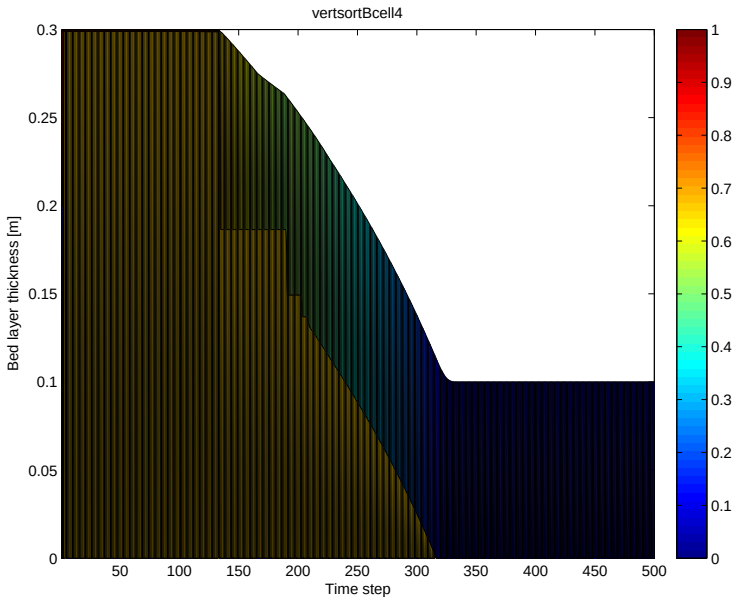

Figure 174 – Filtering simulation results in Cell 5 (case II)

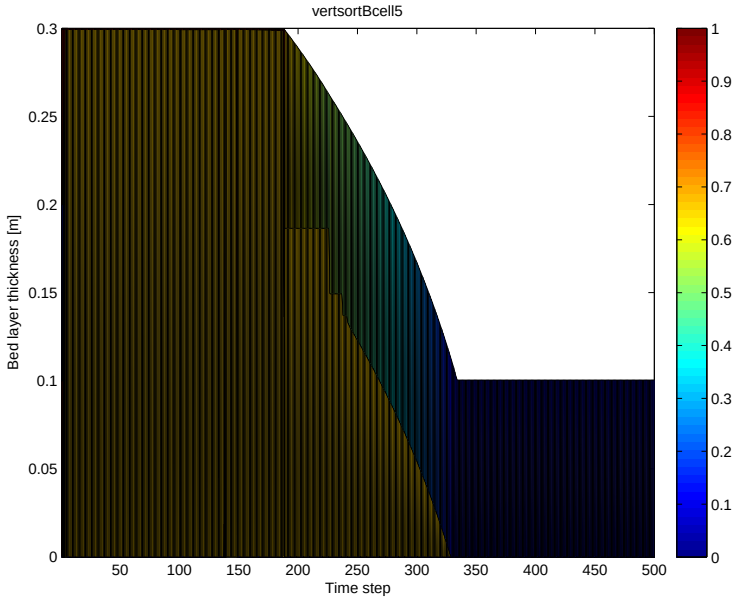

7.4 Conclusions

Regarding the two testcases presented in this chapter, the following conclusions can be drawn with respect to the morphology functionality in COHERENS:

1. the migration of bedforms in a stationary flow under the assumption of total load sediment transport shows an acceptable qualitative agreement between the analytical solution and the numerical one. The differences can be atrributed (at least in part) to a number of assumptions of the analytical solution that were not obeyed in COHERENS, e.g. the neglect of depth variation of the drag coefficient.

2. vertical sorting of sediment in the bed layer evolves according to qualitative expectations. More explicitly. Explicitly, he shifting of characteristics (i.e. bed layer thickness and bed fraction distribution) between layers is implemented well. Sediment mixing (i.e. mixing fine with rough sediment to produce a mixture of varying distribution) is ialso taken into account correctly. Armouring and filtering depend on the ratio of bed layer thickness over active layer thickness and are reproduced adequately. Specifically, with armouring resulting in a full stop of sediment transport while filtering has the sediment transport continue in deeper layers. Finally, fixed layers are implemented well in the code.

References

Ackers, **P.; White**, **W.** (1973). Sediment transport: new approach and analysis. *Journal of the Hydraulics Division 99 (11)*: 2041–2060

Armanini, **A.** (1995). Non-uniform sediment transport: dynamics of the active layer. *Journal of Hydraulic Research 33 (5)*: 611–622

Engelund, **F.; Hansen**, **E.** (1967). A monograph on sediment transport in alluvial streams. *MONOGR, DENMARK TECH UNIV, HYDRAUL LAB, 62 P, 1967. 30 FIG, 3 TAB, 31 REF.*

Hjelmfelt, **A.; Lenau**, **C.** (1970). Nonequilibrium Transport of Suspended Sediment. *Journal of the Hydraulics Division 96 (7)*: 1567–1586

Hogg, **A.; Ungarish**, **M.; Huppert**, **H.** (2000). Particle-driven gravity currents: asymptotic and box model solutions. *EUROPEAN JOURNAL OF MECHANICS SERIES B FLUIDS 19 (1)*: 139–156

Kubatko, **E.; Westerink**, **J.** (2007). Exact Discontinuous Solutions of Exner's Bed Evolution Model: Simple Theory for Sediment Bores. *Journal of Hydraulic Engineering 133*: 305

Richardson, **J.; Zaki**, **W.** (1954). Sedimentation and fluidisation: Part I. *Chemical Engineering Research and Design 32 (a)*: 35–53

Smith, **J.; McLean**, **S.** (1977). Spatially averaged flow over a wavy surface. *Journal of Geophysical Research-Oceans 82 (12)*

Talstra, **H.** (2011). 'Large-scale turbulence structures in shallow separating flows'. PhD thesis. TU Delft

Thacker, **W. C.** (1981). Some exact solutions to the nonlinear shallow-water wave equations. *Journal of Fluid Mechanics 107*: 499–508

Van Rijn, **L.** (2003). Sand transport by currents and waves; General approximation formulae. *unpublished*

Van Rijn, **L.** (1984). Sediment transport, Part II: Suspended load transport. *Journal of Hydraulic Engineering 110 (11)*: 1613–1641

Wu, **W.; Wang**, **S.; Jia**, **Y.** (2000). Nonuniform sediment transport in alluvial rivers Transport de sédiments non uniformes en rivière alluviale. *Journal of Hydraulic Research 38 (6)*: 427

DEPARTMENT **MOBILITY & PUBLIC WORKS**
Flanders hydraulics Research

Berchemlei 115, 2140 Antwerp
T +32 (0)3 224 60 35
F +32 (0)3 224 60 36
waterbouwkundiglabo@vlaanderen.be
www.flandershydraulicsresearch.be